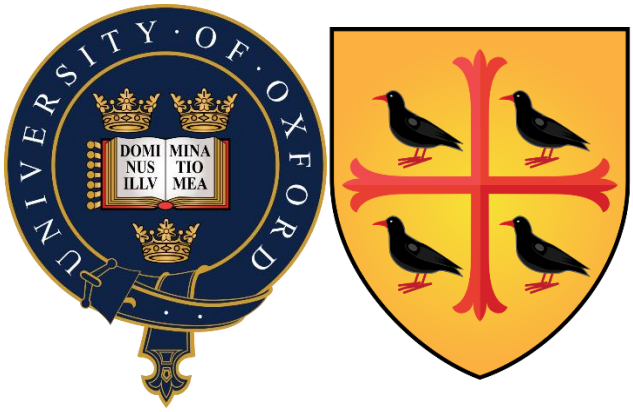
EXPERIMENTAL VALIDATION OF INTERGRANULAR STRESS CORROSION CRACKING PREDICTIVE MODELS



NAGANAND SARAVANAN

St Edmund Hall

University of Oxford

A thesis submitted for the degree of Doctor of Philosophy

Department of Materials

Hilary Term 2022

In a gentle way, you can shake the world.

-M. K. Gandhi.

PREFACE

This dissertation is the result of my own work carried out in the Department of Materials, University of Oxford, under the supervision of Prof. Sergio Lozano-Perez. No part of this thesis has been accepted, or is currently being submitted, for any degree or diploma or certificate or any other qualification at the University of Oxford or elsewhere. Work carried out in collaboration with other authors is dully acknowledged in the text. A list of references is given at the end of the dissertation.

Some of the work and content in the dissertation has been reported in the following publications:

Karamched, PS, **Saravanan, N**, Wilkinson, AJ, Lozano-Perez, S. *Effect of sample thinning on strains and lattice rotations measured from Transmission Kikuchi Diffraction in the SEM,* Ultramicroscopy, 2021, Volume 225 .

JOURNAL ARTICLE

Liu, J, **Saravanan, N**, Haley, JC, Karamched, PS, Yu H, Wilkinson,AJ, Lozano-Perez, S. *On the effects of step size on measurements of geometrically necessary dislocation density using transmission Kikuchi diffraction,* Ultramicroscopy, (under review).

JOURNAL ARTICLE

Saravanan, N, Karamched, PS, Liu, J, Rainasse,C, Scenini, F, Lozano-Perez, S. *Using local GND density to study SCC initiation,* Ultramicroscopy, October 2020, Volume: 217.

JOURNAL ARTICLE

Shen, Z, Chen, K, Yu, H, Jenkins, B, Ren, Y, **Saravanan, N**, He, G, Luo, X, Bagot, PAJ, Moody, MP, Zhang, L, Lozano-Perez, S. *New insights into the oxidation mechanisms of a Ferritic-Martensitic steel in high-temperature steam,* Acta Materialia, 1 August 2020, Volume: 194, pp. 522 – 539

JOURNAL ARTICLE

Saravanan, N, Karamched, PS, Le Faucheur, M, Burger, E, Scenini, F, Lozano-Perez, S. *Effect of local strain and GND density on crack initiation in alloy 600,* 19th International Conference on Environmental Degradation of Materials in Nuclear Power Systems - Water Reactors, EnvDeg January 2019, pp.457 – 465

CONFERENCE PAPER

Invited talk on '*Investigation of Stress Corrosion Crack initiation sites in Alloy 600 using 3D-EBSD and Local Model';* at 149th Annual meeting and exhibition held in San Diego, CA,USA. February 23-27, 2020.

ORAL PRESENTATION

Invited talk on "*Effect of Local Strain and GND density on crack initiation in Alloy 600"* in 19th International Conference on Environmental degradation of Materials in Nuclear Power Systems –Water Reactors held in Boston, MA, USA. August 18-22, 2019.

ORAL PRESENTATION

Invited talk on "*Experimental validation of Predictive Models"* in 10th year Materials Ageing Institute (MAI) day in EDF R&D labs, Les Renardieres, France. June 27, 2018.

ORAL PRESENTATION

ACKNOWLEDGEMENTS

First and foremost, I want to express my deep gratitude to my supervisor Prof. Sergio Lozano-Perez for being a guiding light through this journey. I have been extremely grateful for all the support, effort, and time that you have dedicated to me in teaching and discussing about EM. I am particularly thankful for all your patience you had on me and for innumerable humorous conversations. I can proudly say that you're the kind of supervisor every student wish to have and I am fortunate for having you as my supervisor.

Secondly, I want to thank Dr. Thierry Couvant from EDF France for supporting me and helping with all the shortcomings with the simulation studies. I express my gratitude to Dr. Claire Rainasse for providing all the support necessary at the crucial times. I am also grateful to Dr. Fabio Scenini for helping out with autoclave testing in University of Manchester.

I would express my utmost gratitude and respect to Dr. Phani S Karamched. You have been an inspiration to me from the day one of my time in Oxford. Thank you for supporting, caring, mentoring and for pushing me out of my comfort zone. Phani, thank you brother for being there all along the way.

Particular thanks are also due to my friends from Nanoanalysis group - Guanze, Ed, Zhao, Jack. A special thanks to Junliang Liu for the wonderful time and discussions we had. Thank you for all the guidance and for a fantastic time together. Additionally, I want to acknowledge the EM support team at Oxford Materials for all the help provided.

A big thank you goes to all of my OIS friends, cricket buddies and College mates; Bharat, Gulati, Abdullah, Lucky, Nidi, Raghav, Avni, Rubhan, Akshat, Shivani and others. Without you the experience would not have been the same. A special mention to Priya and Monisha for supporting me from the beginning and for being there. I am extremely grateful to my buddies Vineeth and Hari Prashanth for their support whenever needed and covering my back. I would like to specially mention Eric for being wonderful host and good friend whenever I visited France. A special thanks to Chandra Vadana for your unconditional support and being there whatsoever.

A devoted thank you to my Oxford family – Govind, Jagdish, Shaum, Tharini, Nikita, Ganesha and Nandi for putting up with me and never once to my knowledge tried to kill me :P Thank you very much for making my time in 8 Horwood close so exceptional which I would cherish.

Most importantly, a million thanks to my PARENTS, granddad and KMDT family members who always love, understand, and support me no matter what. I could not have done it without them.

ABSTRACT

Intergranular Stress Corrosion Cracking (IGSCC) has been one of the most important challenges to nuclear power plant operation worldwide. The degradation of alloy 600 (Ni-based alloy) and its susceptibility to Stress Corrosion Cracking (SCC) when exposed to primary water environment in pressurized water reactors (PWRs) has been a topic of interest for many decades among the SCC community. However, the understanding or prediction of SCC mechanisms remains questionable. To address this, an IGSCC predictive model called 'Local Model' has been developed in the framework of EDF's CSI project. The main focus of this research is to investigate IGSCC in alloy 600 and to experimentally validate a predictive model. Firstly, it is important to know whether stress corrosion cracking occurs in these materials, in the way presented in the existing experiments and models in the literature. These have shown a very large scattering for the needed for the crack initiation and crack propagation, indicating significant model uncertainties.

In this thesis, an experimental and modelling program has been developed for investigating SCC in alloy 600 for conditions simulating PWR conditions under constant load. The goal of the experiments was to find a reliable and quantitative determination of crack initiation and crack propagation for these conditions. For the modelling aspect, the aim was to determine the critical parameters of SCC by considering the phenomena in the local scale of grain boundaries and crack tips. The model requirements include the ability to predict the crack initiation and to model crack growth rate as a function of macroscopic and measurable parameters. This has been validated by experiment to ensure that the assumptions of the model are realistic enough to make sure of reliability for reactor safety applications. By doing this, the model allows for a better understanding of the underlying mechanisms of SCC. As such, it focuses on the phenomenological approach rather than the empirical approaches in other models.

CONTENTS

1. INTRODUCTION 16
1.1 Nuclear Power 16
1.2 SCC in Nuclear Power Plants 17
1.3 Alloy 600 20
1.3.1 Microstructure 22
1.4 Motivation 23
1.5 Aim & Objectives 24
1.6 Thesis Outline 25
2 LITERATURE REVIEW 27
2.1 SCC in Alloy 600 27
2.2 Influencing parameters 29
2.2.1 Nickel and chromium content 30
2.2.2 Carbon content and carbide distribution 34
2.2.3 Grain boundary type 38
2.2.4 Grain size 42
2.2.5 Cold work 43
2.2.6 Strain 46
2.2.7 Strain path 48
2.2.8 Stress 50
2.2.9 Primary water conditions 52
2.2.10 Temperature 54
2.2.11 Potential and Dissolved H_2 concentration 57
2.3 Models and Mechanisms 59
2.3.1 Film Rupture Model (FRM) 59
2.3.2 Surface Mobility Model (SMM) 63
2.3.3 Hydrogen based models 65
2.3.4 Internal Oxidation model 70
2.4 Modelling Component life 74
2.4.1 Index model 74
2.4.2 Local model 77
2.4.3 Intergranular Oxidation kinetics 80
2.4.4 Criteria for Initiation 83

2.4.5 Crack growth 84
2.5 Numerical Tools 87
2.5.1 Salome Meca 87
2.5.2 Code_Aster 88
2.5.3 Code_Coriolis 88
2.6 Preliminary results on SCC computation 93
2.7 Strategy for Validation 95
2.8 Summary 99
3 EXPERIMENTAL METHODS 103
3.1 Scanning Electron Microscopy (SEM) 103
3.2 Focused Ion Beam (FIB) 106
3.2.1 TEM/TKD sample preparation 108
3.2.2 3D FIB serial sectioning 111
3.3 Transmission Electron Microscopy (TEM) 113
3.4 Electron Back Scattered Diffraction (EBSD) 114
3.4.1 Transmission Kikuchi Diffraction (TKD) 115
3.5 3D Electron Back Scattered Diffraction (3D EBSD) 118
3.5.1 3D EBSD Data Acquisition Conditions 122
3.5.2 Limitations 127
3.5.3 Objectives of performing 3D EBSD experiments 127
3.6 Summary 128
4 MATERIAL USED AND SCC TESTS 129
4.1 Specimen Orientation 129
4.2 Metallurgical state 129
4.3 Mechanical Testing 133
4.4 Pre-characterization 133
4.4.1 Grinding and polishing procedure 133
4.4.2 Grain size estimation 135
4.4.3 Grain boundary characteristics 136
4.4.4 Grain Boundary Coverage (Carbide Coverage) 137
4.4.5 Misorientation Analysis 138
4.5 Stress corrosion cracking testing (SCC tests) 140
4.5.1 SCC test specimens 140
4.5.2 Autoclave conditions 141
4.6 Experimental Set-up 142

4.6.1 Water chemistry and loading conditions 144
4.7 Crack Identification and length analysis 145
4.7.1 First autoclave test specimen 145
4.7.2 Second autoclave test specimen 146
4.7.3 Third autoclave test specimen 147
4.7.4 Crack Analysis 148
4.7.5 Carbide Identification and Chromium Zone depletion 150
4.8 Summary 154
5 EFFECT OF LOCAL GND DENSITY TO STUDY SCC CRACK INITIATION IN ALLOY 600 155
5.1 Introduction 155
5.2 Materials and Experimental methodologies 156
5.2.1 Materials used 156
5.2.2 Site-specific sample preparation using FIB 156
5.2.3 TKD analysis 157
5.2.4 TKD patterns processing 159
5.2.5 Transmission Electron Microscopy (TEM) Characterization 160
5.3 Results 161
5.3.1 Cracked grain boundary 1 162
5.3.2 Uncracked grain boundary 1 163
5.3.3 As-Received grain boundary 165
5.3.4 Cracked grain boundary 2 167
5.3.5 Kernel Average Misorientation (KAM) characterization 170
5.3.6 Geometrically Necessary Dislocation (GND) Density calculation 172
5.3.7 Dislocations and Schmidt factor calculation 175
5.3.8 Effect of step size on the measurements of GNDs using TKD 181
5.4 Discussion 186
5.5 Summary 189
6 EVALUATION OF GLOBAL STRESS, STRAIN FIELDS AND LOCAL STRESS ALONG THE GRAIN BOUNDARIES 191
6.1 Finite Element Model of four-point bend test 191
6.1.1 Components 191
6.1.2 Mesh 192
6.1.3 Material Properties 196
6.1.4 Boundary conditions and Loading 196
6.1.5 FEM calculation 197

6.1.6 Convergence of the model 197
6.2 Results 198
6.2.1 Experimental results 199
6.3 FEM Modelling results 200
6.3.1 FEM analysis result for 0.5 mm displacement 201
6.3.2 FEM analysis result for 1 mm displacement 201
6.4 Discussion 205
6.4.1 Summary 207
6.5 Evaluation of Local Stress along the grain boundaries 208
6.6 Conversion of 3D EBSD data into aggregate mesh 208
6.7 3D EBSD dataset 1 209
6.7.1 3D Reconstruction of 3D EBSD dataset 1 210
6.8 Polycrystalline aggregate mesh generation 213
6.8.1 Assigning nodes and elements to the geometry 214
6.8.2 Smoothening of grain boundaries 214
6.9 Stress concentration at the grain boundaries 222
6.10 Results 224
6.10.1 3D EBSD Dataset 1 225
6.10.2 3D EBSD Dataset 2 227
6.10.3 3D EBSD Dataset 3 228
6.10.4 3D EBSD Dataset 4 230
6.10.5 Cracking criteria for oxidized grain boundaries 231
6.11 Misorientation analysis of the cracked grain boundaries 234
6.12 Discussion 236
6.12.1 Misorientation analysis 237
6.12.2 Stress to fail oxidised grain boundary 237
6.12.3 Statistical approach of estimating critical stress to failure and stress linear coefficient 'S' parameter for Local model 238
6.13 Summary 239
7 VALIDATION AND OPTIMISATION OF LOCAL MODEL 241
7.1 Validation of Initiation 241
7.1.1 Testing of Local Model Initiation 241
7.1.2 Results of Local Model Initiation 248
7.2 Validation of Propagation 249
7.2.1 Testing of Propagation 249

7.2.2 Results of Local Model Propagation 250
7.2.3 Comparison of predicted crack propagation and observed crack depths 252
7.3 Validation of Propagation Calibration of 'cgr1,cgr2,cgr3 & cgr4' parameters 253
7.3.1 Effect of 'cgr3' parameter 253
7.3.2 Effect of 'cgr2' parameter 255
7.3.3 Effect of 'cgr4' parameter 257
7.3.4 Effect of 'cgr1' parameter 259
7.4 Comparison of Crack Growth Laws 262
7.5 Effect of Temperature 262
7.6 Discussion 263
7.6.1 Ranking of model parameters 266
7.6.2 Limitations of the model 269
7.7 Summary 273
8 CONCLUSIONS 274
8.1 New experimental approaches 274
8.2 Summary of Results 275
8.3 Suggestions for future research 276
9 APPENDIX 282
10 REFERENCES 303

List of Abbreviations and Acronyms

ALPHABETICAL ORDER

3D EBSD	3D Electron Back Scattered Diffraction
3D FIB	3D Focused Ion Beam
AEM	Analytical Electron Microscopy
AIDE	Adsorption Induced Dislocation Emission
AISM	Adsorption Induced Slip Mechanism
APT	Atom Probe Tomography
BWR	Boiling Water Reactor
CEPM	Corrosion Enhanced Plasticity Model
CERT	Constant Extension Rate Test
CGR	Crack Growth Rate
CLSB	Coincident Site Lattice Boundary
CPFEM	Crystal Plasticity Finite Element Modelling
CRDM	Control Rod Drive Mechanism
CRSS	Critical Resolved Shear Stress
CSL	Coincident Site Lattice
CW	Cold Work
DH	Dissolved Hydrogen
DIC	Digital Image Correlation
DZn	Dissolved Zinc
EBSP	Electron Back Scattered Pattern
EcP	Electrochemical Potential
EDF	Électricité de France
EDM	Electric Discharge Machining
EDX	Energy Dispersive X-Ray Spectroscopy
EELS	Electron Energy Loss Spectroscopy
EFTEM	Energy Filtered Transmission Electron Microscopy
EGBD	Extrinsic Grain Boundary Dislocation
FAC	Flow Accelerated Corrosion
FE	Finite Element

FEGSEM	Field Emission Gun Scanning Electron Microscopy
FEM	Finite Element Modelling
FIB	Focused Ion Beam
FRM	Film Rupture Model
FSD	Forescattered electron Diodes
GB	Grain Boundary
GBC	Grain Boundary Carbide coverage
GBE	Grain Boundary Engineering
GEOM	Geometry Module
GIEM	Grazing-Incidence Edge Milling
GIS	Gas Injection System
GND	Geometrically Necessary Dislocation
HAC	Hydrogen Assisted Cracking
HAGB	High Angle Grain Boundary
HE	Hydrogen Embrittlement
HELP	Hydrogen Enhanced Local Plasticity
HR-EBSD	High Resolution Electron Back Scattered Diffraction
HR-TEM	High Resolution Transmission Electron Microscopy
IASCC	Irradiation Assisted Stress Corrosion Cracking
IGSCC	Intergranular Stress Corrosion Cracking
IPF	Inverse Pole *Figure*
IPFZ	Inverse Pole *Figure*
IQ	Image Quality
KAM	Kernel Average Misorientation
LAGB	Low Angle Grain Boundary
LDE	Liquid Droplet Impingement Erosion
LDZ	Lattice /Localized Deformation Zone
LISM	Low Incidence Surface Milling
LMIS	Liquid Metal Ion Sources
LPSCC	Low Potential Stress Corrosion Cracking
LT	Longitudinal-Transverse
MA	Mill Annealed

MO	Misorientation
OPS	Oxide Polishing Suspension
PFIB	Plasma Focused Ion Beam
PWR	Pressurized Water Reactor
PWSCC	Primary Water Stress Corrosion Cracking
RHAGB	Random High Angle Grain Boundary
ROI	Region of Interest
SAD	Selected Area Diffraction
SCC	Stress Corrosion Cracking
SEM	Scanning Electron Microscopy
SG	Steam Generator
SMM	Surface Mobility Model
SS	Stainless Steel
SSRT	Slow Strain Rate Tensile
ST	Short-Transverse
STEM	Scanning Transmission Electron Microscopy
t-EBSD	Transmission Electron Back Scatter Diffraction
TEM	Transmission Electron Microscopy
TKD	Transmission Kikuchi Diffraction
TSCC	Transgranular Stress Corrosion Cracking
TT	Thermally Treated

1. INTRODUCTION

1.1 Nuclear Power

According to a recent World Nuclear Association report, nuclear energy contributes to 10% of the world's electricity. This is from about 450 reactors; about 50 more are under construction – equivalent to about 15% of existing capacity. In 2018, nuclear power plants supplied about 2563 TWh of electricity compared to 2503 TWh in 2017. There is a global need for increasing the capacity of the nuclear energy in order to replace the fossil fuel plants and reduce carbon emission. This is evident from the construction of new nuclear projects both in developed and developing countries. In France, nuclear energy represents more than 70% of the total generated power. In UK, over 18% of the country's generated power is from the 15 operable nuclear reactors [1].

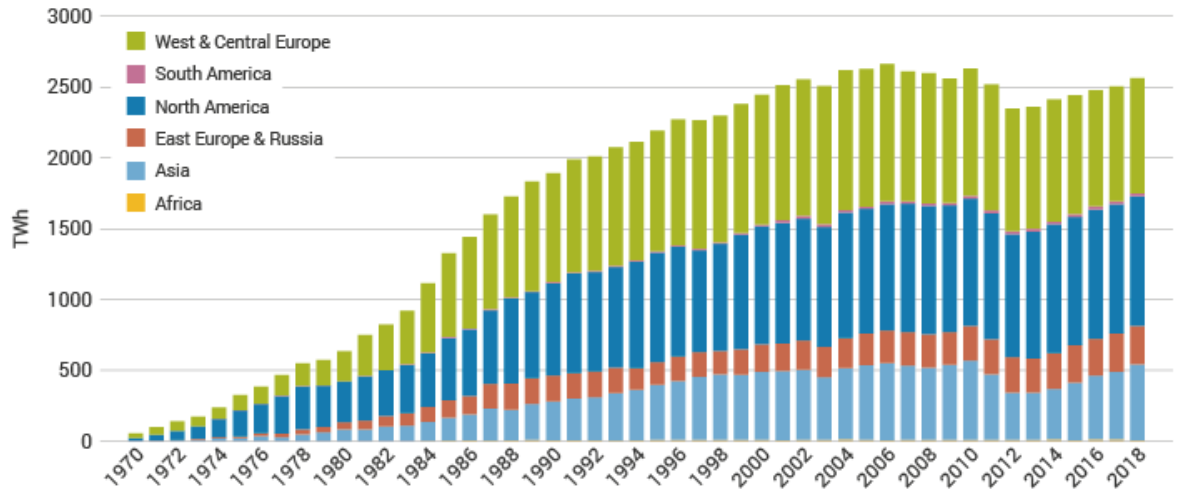


Figure 1 : Global Nuclear Electricity Production [1].

The performance of nuclear reactors has improved substantially over the last few decades. The average lifetime of nuclear reactors is 35-40 years, but in many cases this operational period has been extended by several decades. Due to this reason, predicting the long-term performance

of nuclear reactors and maximising their operating time has been one of the major goals of the nuclear industry. During operation, several nuclear components are subjected to a corrosive environment, high temperature, pressure, and radiation. Safety of these components is of utmost importance, not just because of the hazard it poses but also to economic performance [2]. The exposure of materials to aggressive environment harvests certain structural and microstructural faults. For instance, it may be in the form of hydrogen embrittlement, irradiation induced hardening or corrosion leading to severe catastrophic failures. The components of a nuclear power plant are affected by different types of corrosion such as General Corrosion, Stress Corrosion Cracking (SCC), Liquid Droplet Impingement Erosion (LDE) or Flow Accelerated Corrosion (FAC) [2]. Corrosion, especially Stress Corrosion Cracking (SCC) of these components has proved to be the most significant cause of failures in nuclear industry [3][4]. It has been estimated that failures caused by SCC in the nuclear industry have cost more than $5 billion since 1980 [5]. As a result, for over three decades, significant research and development efforts have been directed to determine the factors affecting SCC [6].

1.2 SCC in Nuclear Power Plants

Pressurized Water Reactors (PWRs) are the most common type of nuclear power plants worldwide. The PWRs usually consists of two major systems, (1) primary system and (2) secondary system. The primary system is where the nuclear fuel (usually uranium) undergoes fission reaction to generate the heat and this heat is then transferred to steam generator. The secondary system consists of the steam generators, condensers and feed water systems [7]. The schematic of the Pressurized Water Reactors (PWRs) is given in *Figure 2*. A typical PWR consists of various kinds of materials depending on whether they are in the primary circuit or

secondary circuit as shown in *Figure* 3. The materials are also classified based on the purpose as nuclear materials or structural materials [8]. The nuclear materials are the ones which come into contact with the fuel such as fuel cladding, control rods etc. The structural materials consist of the piping, divider plates, control rod drive mechanism (CRDM), pumps, internals, turbines heat exchanger etc. The safety of the nuclear plant mainly depends on the integrity of these materials during the service time.

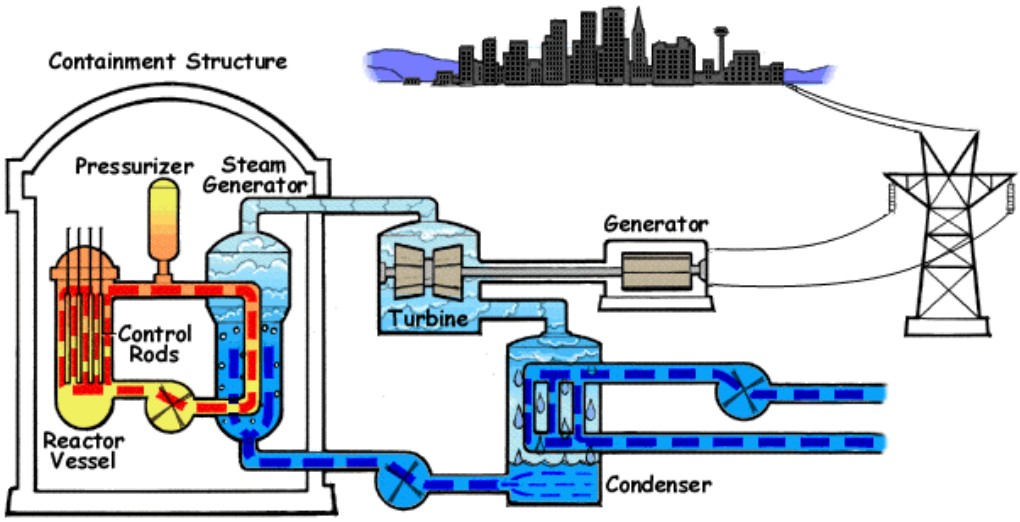


Figure 2: Schematic of Pressurized Water Reactors (PWRs) [9].

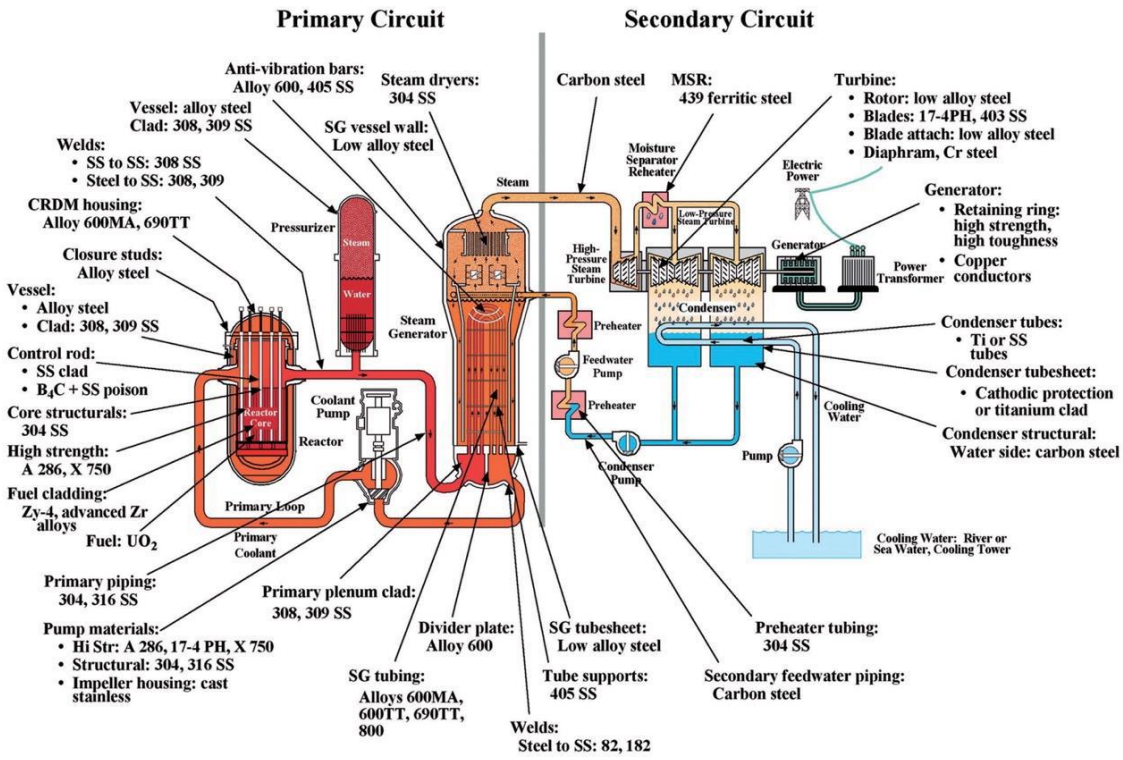


Figure 3: Outline of various kinds of materials used in PWRs [8].

Over a period of time, irrespective of the materials being in primary or secondary circuits, they undergo degradation due to exposure to extreme conditions. There are many forms of material degradation such as irradiation-induced hardening and environmentally assisted forms of failure such as stress corrosion cracking (SCC), flow accelerate corrosion (FAC), Liquid Droplet Impingement Erosion (LDE) etc. Of all these, SCC is a major concern for the nuclear industry as it is hard to detect and predict. The components that are reported to have failed by SCC are not only expensive to replace by also cause huge threat to the integrity of the structure [10].

Austenitic alloys due to their combination of excellent mechanical properties and high corrosion resistance have been extensively used in PWRs as structural components. However, many of these alloys can become susceptible to degradation due to the corrosive environment of the PWR primary water conditions [11]. Cracks appearing in various reported cases of failure in nuclear reactors are caused due to SCC. SCC is the synergetic effect of material

susceptibility, environment, and applied stress. The schematic representation of SCC phenomenon is shown in *Figure 4*.

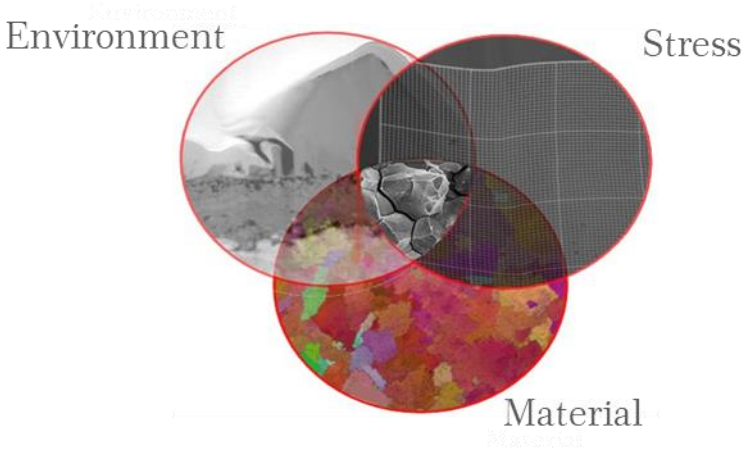


Figure 4: Various factors involved in Stress Corrosion Cracking (SCC).

The lifetime of the PWR, is usually 30-40 years. Nevertheless, most PWRs at present have been in their extended lifetime with 60+ years of service. Thus, studying and predicting the SCC behaviour of the structural materials (such as stainless steel and Ni-based alloys) is a prime interest to the nuclear industry in order to ensure the safety of the PWRs. In this thesis, SCC behaviour of Alloy 600 (Ni-based) used in the primary circuit is studied.

1.3 Alloy 600

The material under investigation in this study is alloy 600 or Inconel 600. It is a nickel, chromium and iron (Ni-Cr-Fe) alloy used in various applications which require good heat and corrosion resistance along with excellent mechanical properties [12]. The typical composition of this austenitic Ni-based alloy is presented in Table 1 and mechanical properties in

Table 2 [13].

Table 1: Limiting Chemical Composition of Alloy 600 in wt. % [13].

Element	Weight (%)
Nickel (NI)	**72 MIN**
Chromium (CR)	**14.0 – 17.0**
Iron (FE)	**6.00 – 10.00**
Carbon (C)	**0.15 MAX.**
Manganese (MN)	**1.00 MAX.**
Sulfur (S)	**0.015 MAX.**
Silicon (SI)	**0.50 MAX.**
Copper (CU)	**0.50 MAX.**

Table 2*: Mechanical Properties of Alloy 600* [13].

Mechanical properties	
YOUNG'S MODULUS	207 GPa
POISSON'S RATIO	0.3
TENSILE STRENGTH	550 - 690 MPa
YIELD STRENGTH (0.2 % OFFSET)	172 - 345 MPa

Alloy 600 is a standard material of construction for nuclear reactors. It is used in various parts of the PWRs (such as steam generator tubes, anti-vibration bards, divider plates and control rod driving mechanism, nozzles etc.) as illustrated in *Figure 5*. The higher nickel content in alloy 600 results in good resistance to chloride-induced stress corrosion cracking and an

excellent resistance towards corrosion in alkaline and reducing conditions. The main role of chromium is to act as solution strengthener, but it also enhances carbide formation and provides good oxidation resistance [14]. The presence of iron in this alloy makes the oxidation of nickel more difficult, by precluding the formation of Ni (IV) and reduces the thermal expansion. The addition of carbon, makes Ni-Cr-Fe alloy more resistant to corrosion, increases hardenability and toughness.

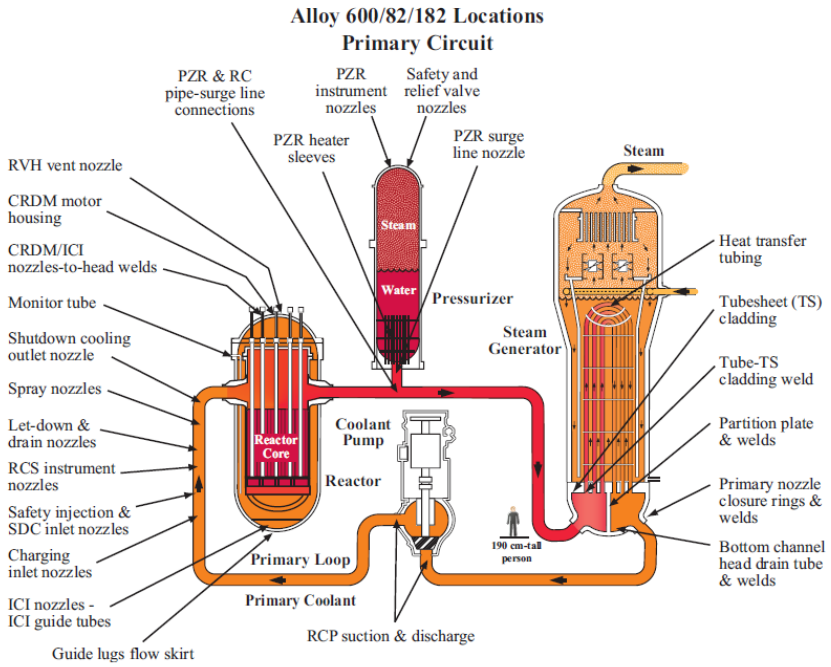


Figure 5: Applications of Alloy 600/82/182 in PWRs [14].

1.3.1 Microstructure

Alloy 600 is a stable austenitic alloy with face centred cubic nickel-based structure with high percentages of solid solution elements. Due to the stable austenite matrix, there is no major transformation in the microstructure at different temperatures. However, thermal treatment causes precipitation or dissolution of carbides. The precipitation of carbides in alloy 600 occurs readily due to the low solubility of carbon even at high temperatures [15,16]. The carbon precipitation diagram for alloy 600 is presented in *Figure* 6. The predominant type of

precipitate formed during thermal treatment of alloy 600 is M_7C_3 type carbide [17]. However, there are other precipitates such as $M_{23}C_6$ type carbides, titanium nitrides and carbonitrides [15,18,19]. This precipitation does not cause any change to the hardness of the alloy. Alloy 600 can be strengthened or hardened only by cold work.

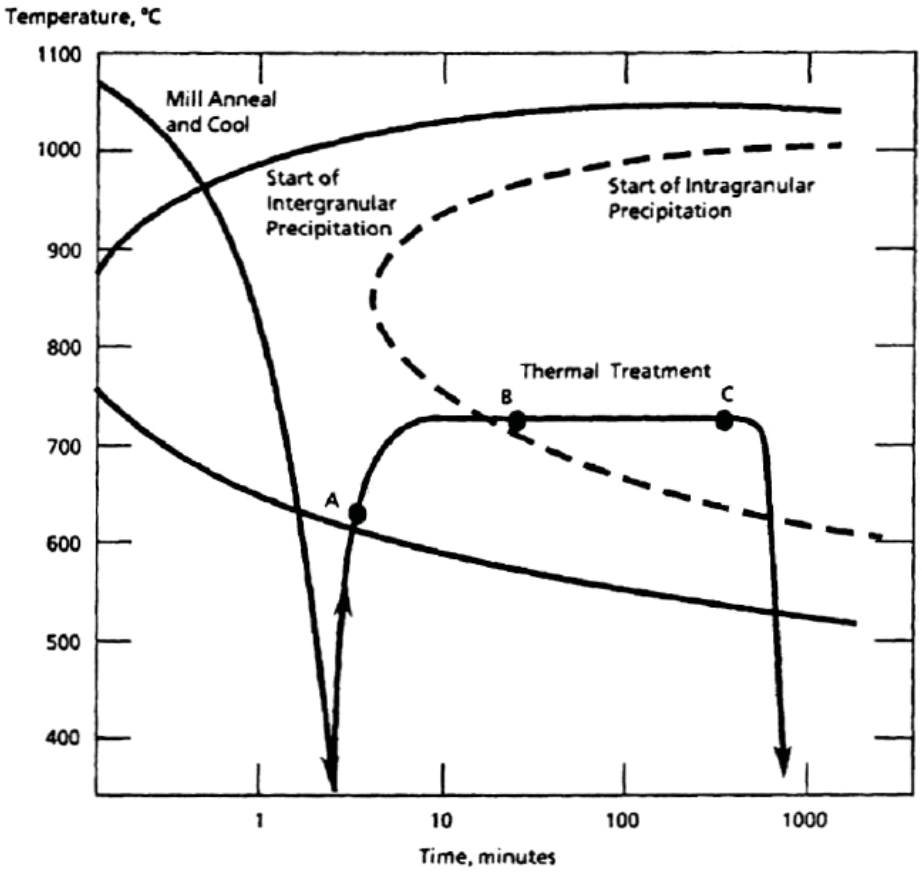


Figure 6: Precipitation diagram for alloy 600 [20].

1.4 Motivation

Extensive preventive maintenance and testing (surveillance) programs exist to ensure that nuclear safety-significant equipment functions when it is supposed to. In some cases, regulations called technical specifications may require the plant to be shut down if the

equipment is not corrected within a certain period of time. Shutting down and restarting power plants result in losses in millions of dollars and thousands of man hours.

In an attempt to allow a more practical prediction of SCC using engineering models, Électricité de France (EDF) has recently introduced a phenomenological-based model of SCC, which combines extensive experimental findings and simulations to address the challenges faced with predicting SCC. Direct comparisons between the experiments and simulations of the same grain morphologies and orientations and investigating the development of local strains and dislocation densities, will help in understanding the fundamental reasons for strain accumulation and crack initiation. Development of a more reliable model will reduce the expensive and time-consuming lab trials, test methods and more importantly shutting and restarting power plants.

1.5 Aim & Objectives

An Intergranular Stress Corrosion Cracking (IGSCC) predictive model called 'Local Model' has been developed as a part of "CORIOLIS", an EDF project. Validation is an important part of the model development process. The focus of this project is to investigate IGSCC in Alloy 600 (Ni-based alloy) which is widely used in Pressurized Water Reactors (PWRs) and experimentally validate the Local Model.

Firstly, it is important to know whether stress corrosion cracking occurs in these materials, in the way presented in the existing experiments and models in the literature. These have shown a very large variation in the behaviour needed for the crack initiation and crack propagation, indicating significant model uncertainties. In this thesis, an experimental and modelling program has been conducted for investigating stress corrosion cracking in alloy 600 for

conditions simulating PWR conditions under constant load. The goal of the experiments is to find a reliable and quantitative determination of crack initiation and crack propagation for these conditions. High Resolution Electron Back Scattered Diffraction (HR-EBSD) and Transmission Kikuchi Diffraction (TKD) have been systematically used to determine the local strains and dislocation densities at the crack initiation sites.

For the modelling aspect, the goal is to determine the critical parameters of stress corrosion cracking in this alloy by considering the phenomena in the local scale of grain boundaries and crack tips. The model requirements include the ability to predict the crack initiation and to model crack growth rate as a function of macroscopic and measurable parameters. This also needs to be validated by experiments, to ensure that the assumptions of the model are realistic enough to be reliable for application to reactor safety purposes. By doing this, the model allows a better understanding of the underlying mechanisms of stress corrosion cracking. The aim is to eliminate the empirical approaches of the other models and focus on phenomenological approach.

1.6 Thesis Outline

The remainder of this report is organised as follows:

Chapter 2 deals with a comprehensive review of SCC-related literature, various existing mechanisms, and models.

Chapter 3 presents an overview of experimental methods and techniques used in the study to extract the required inputs to validate the model.

Chapter 4 gives detailed information on the selected Alloy 600, details of the autoclave experiments and a comparison of crack growth for different time durations.

Chapter 5 deals with the local strain aspect around the oxidized grain boundary to cause crack initiation. These investigations were made on the alloy exposed to simulated PWR conditions under constant load.

Chapter 6 deals with the Finite Element Modelling of the experiment and extracting the global stress and strain and Crystal Plasticity Finite Element Modelling (CPFEM) of the polycrystalline aggregate extracted from the autoclave samples. 3D EBSD is used to extract the 3D morphology and orientation of the grains.

Chapter 7 deals with the validation aspect of the model; the relevant parameters of the model are identified, the results are compared to the experiments and limits of the model are discussed.

Chapter 8 summarizes the major conclusions of this thesis and includes suggestions for future work that could further improve the understanding and performance of the model.

2 LITERATURE REVIEW

2.1 SCC in Alloy 600

Coriou et al. [21] first identified stress corrosion cracking in alloy 600 in 1959. Ever since, there have been many reports of SCC occurrences in alloy 600 component parts (such as steam generator tubes, divider plates etc.) in nuclear power plants [22,23]. SCC is a mode of corrosion with various submodes. SCC of alloy 600 in primary water conditions is the low potential stress corrosion cracking (LPSCC) as it is occurring near the Ni/NiO equilibrium shown in *Figure 7* (or otherwise in region below or near the standard hydrogen equilibrium). It is also known as primary water stress corrosion cracking (PWSCC) as the SCC occurs in the primary water PWR conditions. SCC of alloy 600 is also known as intergranular stress corrosion cracking (IGSCC) as the cracking is most extensively intergranular for alloy 600 in nuclear power plants [24].

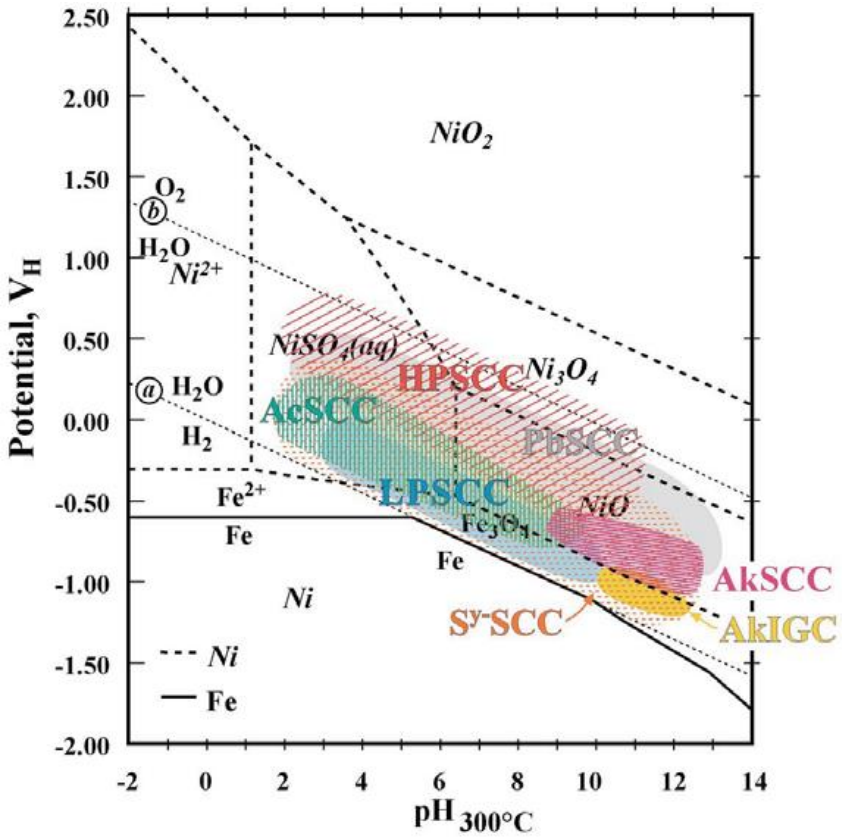


Figure 7: Pourbaix diagram showing the various sub modes of SCC cracking for alloy 600 [24].

SCC in alloy 600 is not instantaneous, there are various stages involved as shown in *Figure 8*. The main steps involved in SCC are Incubation, Initiation and Propagation. During the incubation period the intergranular oxides reach penetration depths of several microns. Several short cracks can initiate in the incubation period, but they are mostly smaller than the detection threshold. The incubation period can last from many hundreds to thousands of hours. The cracks then propagate by slow crack growth regime. At this time, the cracks are visible and can be detected using optical microscopy. The transition from initiation to propagation occurs for the crack length 1-10 µm. This slow regime of crack propagation transits into fast crack growth regime after several thousands of hours during which the rate of the deepest crack increases at least by an order of magnitude [14]. The transition of slow crack to fast crack propagation occurs when the stress intensity factor K becomes greater than the critical stress intensity factor

(K_{IGSCC}) [25]. SCC in alloy 600 occurs mostly intergranular with the oxides becoming brittle. In some cases of fractured surfaces, pseudo intergranular kind of appearance of cracking was reported.

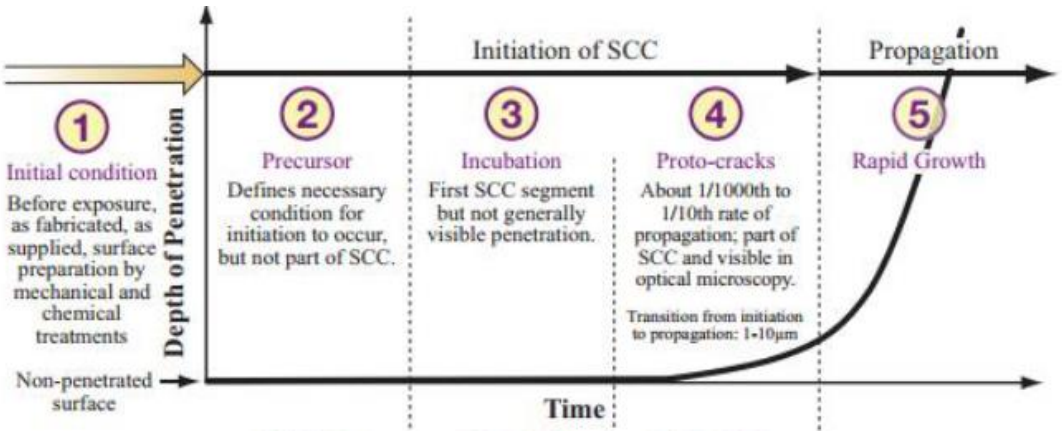


Figure 8: Steps involved in Stress Corrosion Cracking (SCC) process [14].

IGSCC of alloy 600 is a complex process as it involves various influencing parameters at large. Alloy 600 can also be affected by transgranular stress corrosion cracking (TSCC) in primary water depending on the percentage of dissolved hydrogen content or in secondary water environment. The cracking process is still a topic of debate amongst the SCC community even after extensive studies carried out over the last four decades. The following section largely focuses on the influencing parameters of SCC and their effects reported.

2.2 Influencing parameters

SCC is a phenomenon which occurs due to the synergistic effect of material susceptibility (nickel and chromium content, carbon content and carbide distribution, grain boundary type, grain size, strain path), environment to which the material is exposed (primary water conditions, temperature, potential and H_2 concentration) and stress (applied and residual). This

section summarizes the various studies carried out to understand the factors influencing SCC by research groups across the globe.

2.2.1 Nickel and chromium content

To understand the effect of two important elements in the alloy, a large number of studies were conducted across the world. It is quite complicated to present the impact of these two elements individually as the change in the composition of each element correspondingly changes the mechanical and microstructural properties. In 1969, Coriou performed a general investigation of SCC of austenitic stainless steel in pure and chlorinated water. *Figure 9,* shows the behaviour of Fe-Cr-Ni alloys in both pure and chlorinated water. It is interesting to note that alloys with higher Fe-content only have transgranular SCC (TSCC) susceptibility in chlorinated water. However, alloys with high Ni-content are susceptible to intergranular SCC (IGSCC) in both the environments [26][21][27].

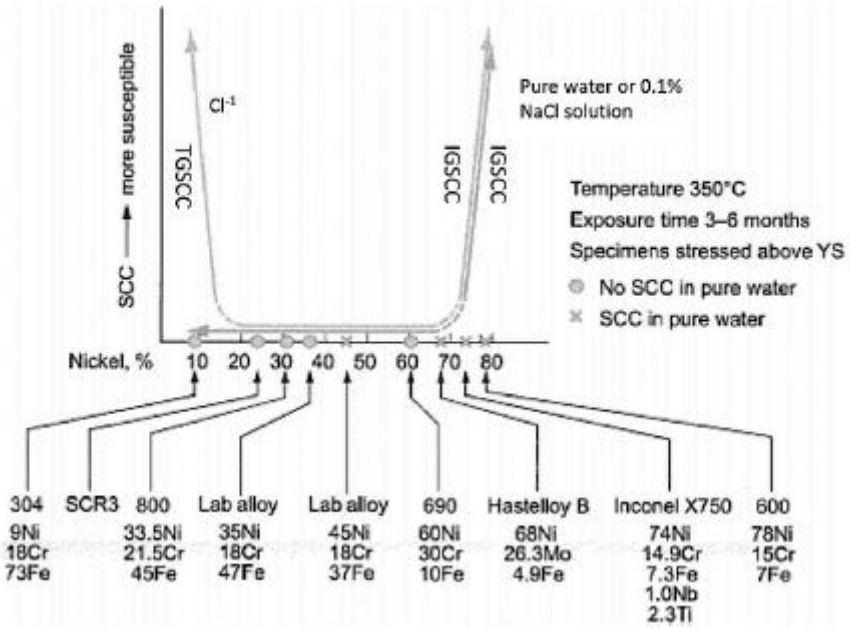


Figure 9: SCC susceptibility vs Ni-content for Fe-Cr-Ni alloys at 350 C in pure deoxygenated water and pure water with 0.1% NaCl [27].

The alloys with Ni-content in the range between 20 and 65% exhibit a very high resistance to SCC. The alloys such as Inconel 800 and 690 fall in this range and hence they are used in SG tubes as replacement to Inconel 600 [10][28]. Arioka [29] performed similar experiments with the potential near to Ni/NiO, this favoured the formation of external stable NiO on the Ni-rich alloy surface. It was presented in further research studies by Arioka [30], that Ni-rich alloys showed higher susceptibility towards SCC whereas Fe-rich alloys showed lower susceptibility. It was also reported that alloys in the middle region of Ni-content presented better SCC resistance[29][30]. *Figure* 10, shows the results from Arioka's experiments conducted at constant load at different temperatures ranging from 290°C to 360°C in simulated primary water conditions.

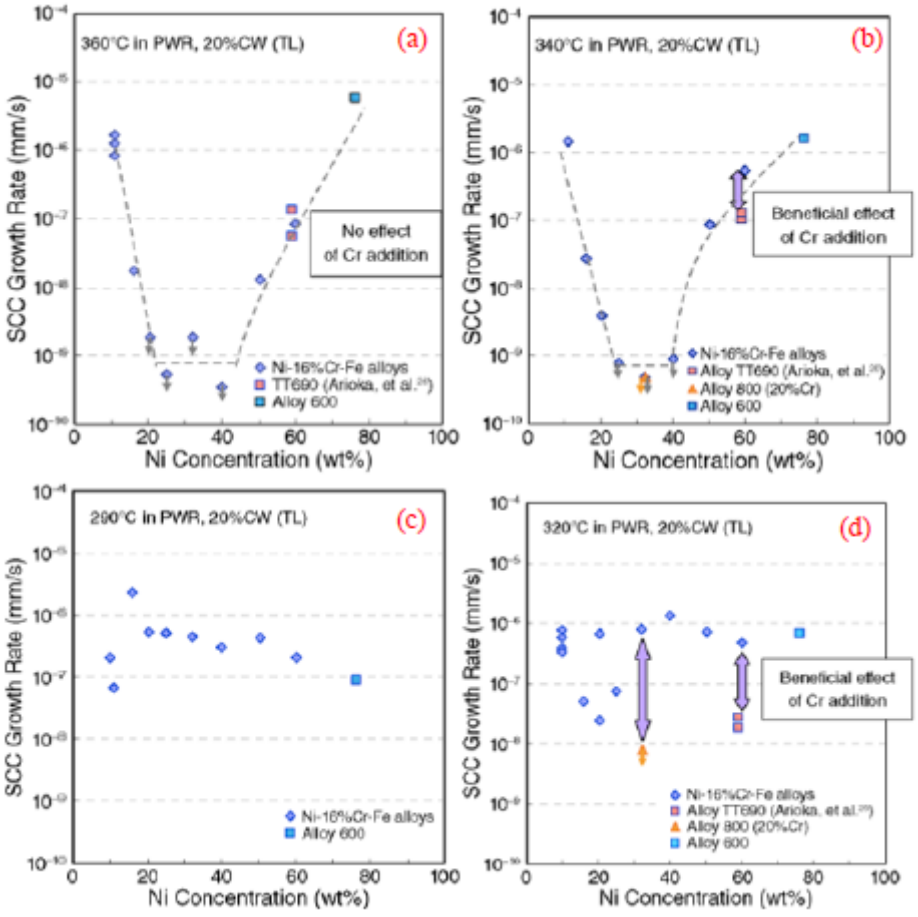


Figure 10: SCC crack growth rates (CGR) vs Ni-concentration in simulated PWR primary water conditions at various temperatures. (a)360°C; (b) 340°C; (c)290°C; (d)320°C [29].

It is interesting to note that samples tested at higher temperatures (340°C & 360°C) exhibited similar trend with regards to SCC susceptibility as reported by Coriou. However, the samples tested at lower temperatures (290°C & 320°C) showed almost negligible effect on SCC susceptibility with change in Ni-concentration. Staehle et al., [10,31] has reported similar results to Coriou about the effect of Ni-concentration in SCC susceptibility in austenitic alloys. Staehle performed his experiments on U-bend specimens in deaerated pure water at 350°C. Yonezawa et al.,[32] found that effect of Ni-concentration had a limited influence in SCC crack initiation as shown in *Figure* 11. It is important to note that previous studies from Arioka and Staehle mainly focused on SCC crack growth rate (CGR). The results are therefore not comparable. Recent studies from Meisnar et al., [33,34] on SS316 steels and Shen et al. [35] on alloy 600 showed that in case of SS316 CGR increases with increase in temperature from 250°C to 320°C and then exhibits a sudden drop from 320°C till 360°C. However, in alloy 600 there is a steep increase in CGR from 320°C onwards. There is no concrete explanation as to why this behaviour was observed.

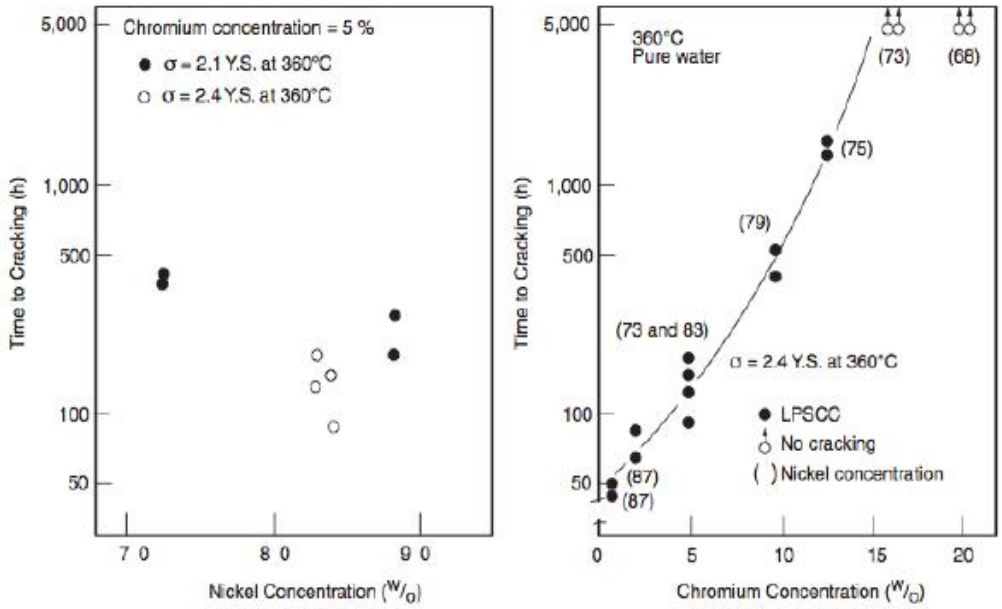


Figure 11: Effect of Nickel and Chromium concentration on SCC susceptibility in primary water environment at 360°C [32].

Yonezawa et al. [32], initially reported that increasing the Cr-content proportionally increases the SCC resistance of Ni alloys. It is seen from *Figure* 11, that in alloy 600, there is a significant rise in SCC resistance as the chromium concentration increases from 3 up to 17%. Many researchers later confirmed this. Nagano et al [36] observed maximum susceptibility to SCC for Ni-10Fe-xCr alloys with 5-10% Cr, a sharp increase in SCC resistance for 10-17% Cr concentration and no cracking for alloys with 17-30% Cr concentration. Similarly Arioka [30] observed that the SCC susceptibility in austenitic alloys decreased by increasing the Cr-concentration. He also reported that the beneficial effect of Cr becomes negligible at 360°C mainly due to the temperature dependent solubility of Cr oxide (Cr_2O_3). It is well known that when Cr concentration is more than 10%, Cr readily reacts with oxygen to form a protective layer on the surface preventing the base materials from corrosive environments [37]. Many researchers explained the positive influence of the increased Cr-content on SCC resistance [29,30,36,38–42]. The results from numerous studies show the improved resistance of alloy 690 to SCC compared to alloy 600. Further research carried out by Terachi et al [40] showed

that the thickness of the protective oxide layer becomes constant when the Cr-concentrations are over 15%. This means that constant thickness from the oxide layers provides uniform protection therefore reducing the SCC susceptibility. This beneficial role of chromium is complex to explain because of synergetic influence of many other parameters influencing SCC. Angeliu [43] and Vaillant [42] reported that for increased concentration of chromium there is a strong reduction in creep mechanism. This was later confirmed by Was [41], who reported that Cr acts as a strong solid strengthener of Ni, which reduces the creep and deformation rates by preventing slip and blocking dislocations in nickel-based alloys. Lozano-Perez [44], performed high resolution microanalysis on the crack tips of SUS304 with 18.2% Cr and 15% Cr to thoroughly understand the effect of Cr in SCC behaviour. He found that the oxidised region ahead of the crack tip in 15% Cr SUS304 sample is larger than the 18.2% Cr concentration one. This proves that due to the lower Cr-content the formation of oxide layer ahead of the crack tip in 15% Cr-sample is delayed causing more aggressive corrosion attack.

2.2.2 Carbon content and carbide distribution

Earlier study by Bandy et al. [45] on U-bend test specimens showed that there is a possible effect of carbon content in alloy 600 on crack initiation and temperature. The results from testing tubes with 0.01-0.05% carbon content in temperature range of 325°C to 360°C exhibited an increase in SCC crack initiation activation energy with increase in carbon content. However, the effect of carbon content is usually associated with carbide precipitation and distribution. Similar to chromium, carbon acts as solid solution strengthener. By increasing the carbon content, the creep resistance of the material increased. The creep resistance has a huge detrimental effect on SCC crack initiation and propagation, meaning higher the creep rate faster the crack initiation and propagation [38][39][46][47].

The carbon concentration in the base metal controls the carbide precipitation. The carbides can generally be precipitated along the grain boundary as intergranular carbides or inside the grain as intragranular carbides. The carbide precipitation mainly depends on the thermos-mechanical history of the material. However, heat treatment temperatures, duration, grain size and carbon content also strongly affect the precipitation of carbides. Lower carbon content shifts the precipitation to longer time thus improving the conditions for intergranular precipitation. It is also reported that for too high carbon content (> 0.063%) and too low carbon content (< 0.012%), the material tends to become highly susceptible to SCC [20]. There are two different types of carbide precipitates in austenitic alloys, $M_{23}C_6$ (FCC structure) or M_7C_3 (HCP structure) type. Most predominant type of carbide precipitate in alloy 600 is M_7C_3 type carbide with M being chromium as alloy 600 is rich in Cr. Cr_7C_3 has the most favourable microstructure to precipitate along grain boundaries [48,49]. These precipitates can be intergranular or intragranular or both.

Further studies [8,50–55] showed that networks of intergranular carbides (continuous or semi-continuous) improved the SCC resistance. On the contrary, the intragranular carbides increase the SCC susceptibility. Norring et al [56] demonstrated that increased grain boundary carbide density increased resistance to SCC in SG U-bend tubes.

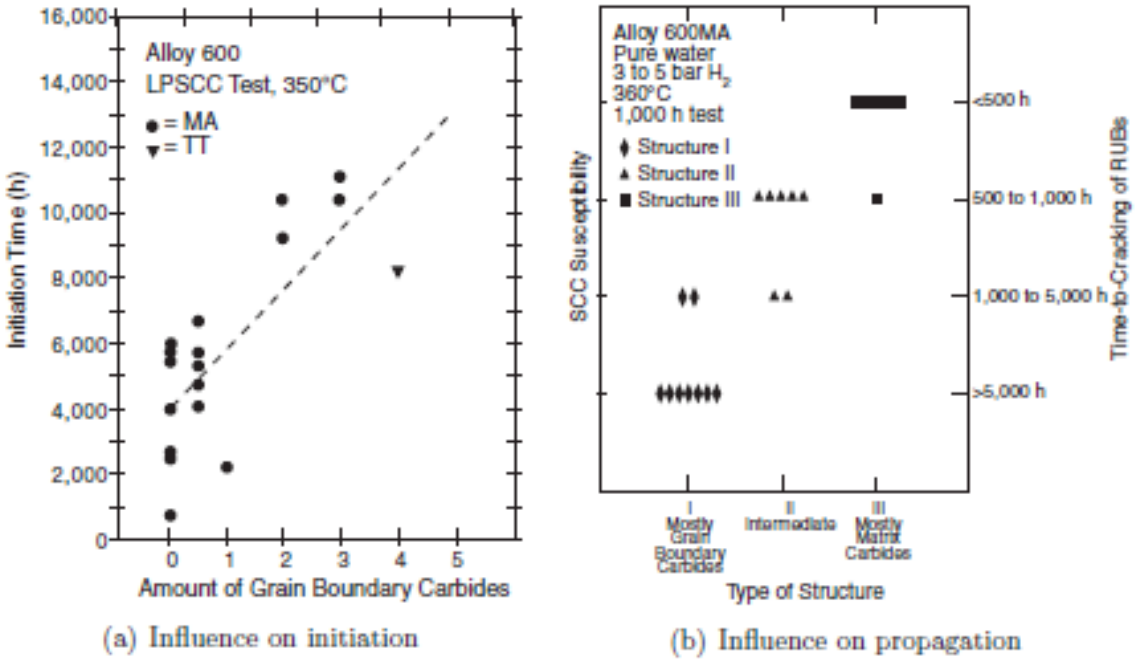


Figure 12: Influence of Carbide distribution on SCC initiation and propagation [23].

Depending on the carbide distribution, the microstructure of alloy 600 used in SG tubes are classified into three types and they are shown in *Figure* 13. Type I microstructure shows beneficial effect of intergranular carbides and thus better resistance to SCC. Type II and III microstructures show the deleterious effect of intragranular carbides and thus higher SCC susceptibility [57].

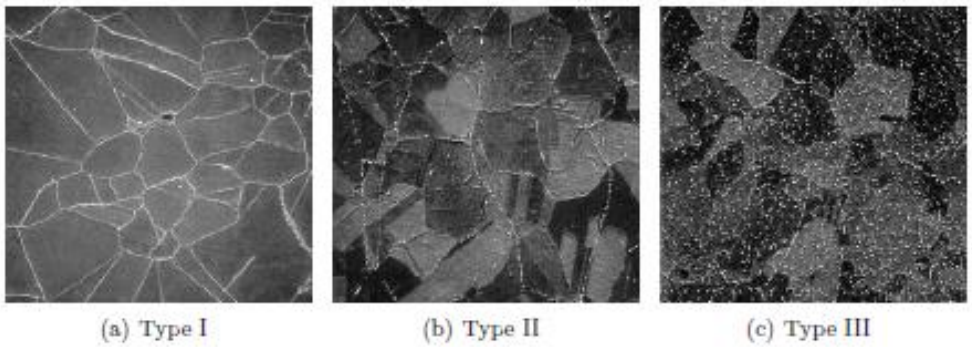


Figure 13: Examples of Carbide distributions

The intergranular carbide distribution acts as an obstacle to grain boundary sliding by reducing the amplitude and number of grain boundaries sliding. This hugely reduces the time to crack initiation and crack growth rates [38,42,58]. Boursier et al. [47] reported that intergranular carbides lower the creep resistance in alloy 600, even though the interdependency of microstructure, creep and IGSCC susceptibility is complex. Bruemmer et al [59] proposed that intergranular carbides could reduce the stress state at the crack tip and thus enable the crack tip blunting. As the radius of the crack tip increases, there is a consequent reduction in the crack growth rate.

High-resolution analysis carried out on the crack tip of alloy 600 by various researchers [15,17,19] show that Cr-carbide precipitates arrest the oxygen from further diffusing into the material and largely reduce the SCC growth rate. However, the formation of Cr-carbides at the grain boundaries leads to a formation of chromium-depleted zone next to the grain boundary as shown in *Figure* 14. This phenomenon where chromium depletion occurs close to the grain boundary is called sensitization and the corresponding microstructure is referred as sensitised [15].

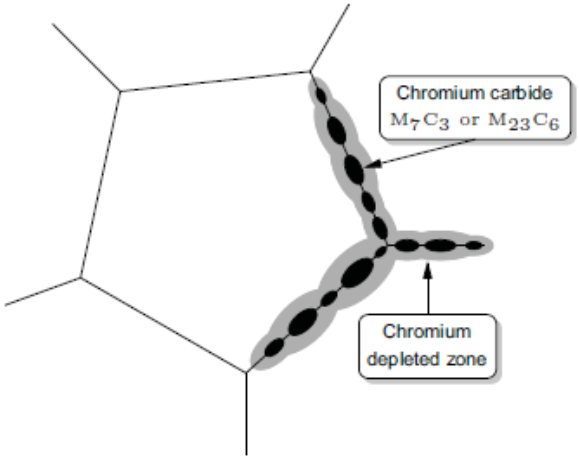


Figure 14: Schematic of Sensitised grain boundary.

The thermodynamics of carbide formation and differences in the diffusivities of chromium and carbon hugely influence the depletion. This occurs for the temperature range where the carbide formed is thermodynamically stable and the diffusivity of chromium is rapid to nucleate carbide [60,61]. Micromechanical testing carried out by Dugdale [53] et al. on oxidized grain boundaries indicated that presence of carbides along the grain boundaries modified the SCC crack paths. It was also seen that the chromium-depleted region around these carbides are preferentially oxidized.

Studies [15,62,63] show that Cr-depletion enhances SCC susceptibility especially in oxygenated water, in low temperature acidic environments or in presence of sulphur species. Contradictory results were observed by Arioka [39] in hydrogenated water even with the obvious Cr-depletion at the grain boundaries. This was later confirmed by Andresen et al. [64], that in high temperature hydrogenated water environment, SCC was mainly controlled by carbide distribution rather than the chemical distribution at the grain boundaries. Nevertheless, the influence of chromium depletion is yet to be properly demonstrated in primary water environment. However, if the chromium depletion is detrimental to IGSCC, its effects are largely compensated by the beneficial effect of grain boundary carbides (IG carbides) [38].

2.2.3 Grain boundary type

Ever since the grain boundary hardening and segregation in alpha iron-tin alloy studied by Watanabe [65], the effect of grain boundary character (type) on SCC has become an area of interest for many researchers. Watanabe et al. [65] proposed a concept of grain boundary engineering (GBE) to design and control the type of grain boundary, to better understand the intergranular stress corrosion resistance. The grain boundary type usually depends on the orientation of the neighbouring crystals and it seems to have a crucial role in distribution of

stress intensity along the grain boundary. Depending on the degree of misorientation of the neighbouring crystals (atomistic point), the grain boundaries are classified as Low Angle Grain Boundaries (LAGBs) and High Angle Grain Boundaries (HAGBs) [66,67]. The LAGBs have misorientation < 15° and the HAGBs have misorientation >15°. Since some high angle grain boundaries can have high symmetry, a new classification method was introduced. For a better understanding of the effect of various grain boundary types on SCC, Grimmer et al. [68] first used a model called the Coincident Site Lattice (CSL) model proposed by Kronberg [69] in 1949. According to this model, a value is given to each grain boundary depending on the reciprocal of the frequency of coincident lattice site points. If the number of coincident sites are higher in a grain boundary (low number of bonds broken) then the energy of grain boundary is low. These values given to the CSL boundary (CSLB) are often denoted by $\sum$ and called special boundaries. Any grain boundary with $\sum > 29$ can be considered as a random grain boundary because of their low symmetry. From now on in this manuscript high angle grain boundaries will assume to have low symmetry. Alexandreau et al. [70] proved these CSLB value to be associated with the energy stored in the grain boundary. His work on alloy 600 IGSCC in simulated primary water environment as function of CSL boundary fraction, carbon content and grain boundary coverage suggested that the grain boundaries with low energy have better resistance to SCC. His results also showed that regardless of the testing conditions, random grain boundaries with lower symmetry crack more than the CSLBs. Alexandreau and Was [71,72] found that SCC cracks tend to propagate mainly along the HAGBs, with those separating grains have different orientations. His work also suggested that these grain boundaries are subject to higher concentration of deformation.

Gertsman [73] did an extensive study of the grain boundary character along IGSCC crack paths in austenitic alloys and found that $\sum 3$ grain boundaries (annealed twin boundaries) are more

resistant to SCC cracking shown in *Figure 15*. It was reported that grain boundary orientation concerning the applied stress is also important.

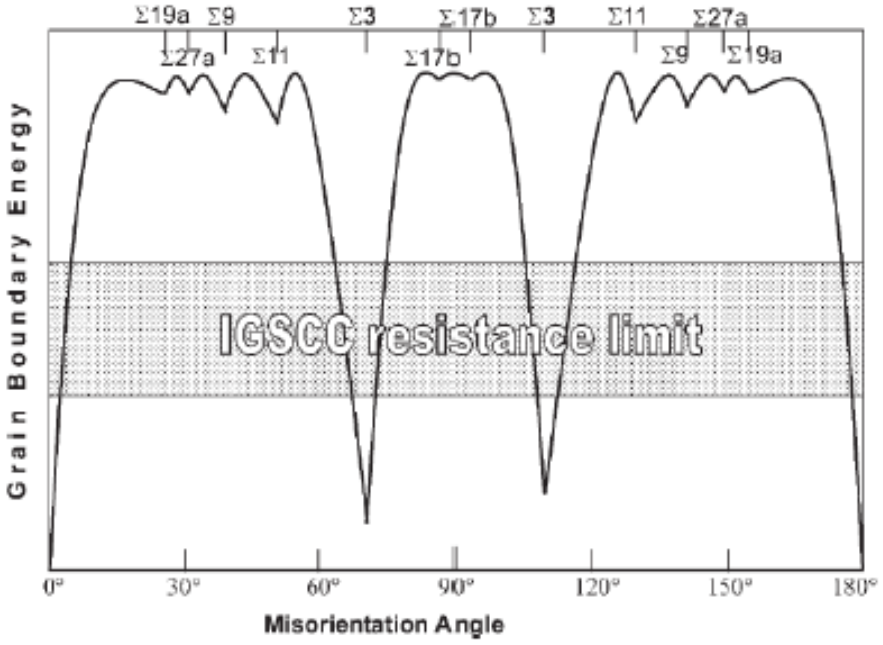


Figure 15: Schematic representation of IGSCC susceptibility as a function of Grain boundary energy and misorientation [73].

Lehockey [74,75] performed experiments to improve the service performance of Fe-based and Ni-based super alloys by grain boundary engineering (GBE). He reported that sensitization had a huge impact on the grain boundary character and that SCC susceptibility changed on varying the proportion of the different grain boundaries. By increasing the percentage of CSLBs, the SCC resistance increased drastically. Similar results were reported by Kokawa [76] and Michiuchi [77] that GBE of increasing the CSLBs, proved more resistance to SCC. Kokawa [78] conducted high resolution analysis using TEM to study the effect of GBE on carbide precipitation and found that CSLBs require more time for intergranular carbide precipitation than random high angle grain boundaries (RHAGBs) [79].

Several other studies were conducted to address this phenomenon of superior crack resistance of ∑3 boundaries compared to other HAGBs [71,80–82]. Thaveeprungsriporn [81] conducted

slow strain rate tensile (SSRT) experiments to understand the underlying dependence of dislocation absorption at the grain boundaries in SCC. The results from the experiments show that the better SCC behaviour of CSLBs are due to the extrinsic grain boundary dislocations (EGBDs). These dislocations are created as a result of the interactions between the lattice dislocations and grain boundaries at high temperature deformation. Also, based on the type and structure of the grain boundaries these dislocations might be absorbed, trapped, or dissociated at the grain boundaries. Thus, due to the high uniformity of CSLBs it is more difficult for the dislocation to be absorbed and hence they show higher density of EGBDs compared to other HAGBs. HAGBs have three times higher annihilation rate of EGBDs than CSLBs. Alexandreau et al.[71] , later confirmed this behaviour of slower absorption rate kinetics of dislocations and thus reducing the creep rate. Stratulat et al. [83] performed micro cantilever bend tests on oxidised alloy 600 grain boundaries in order to establish a relation between critical stress intensity factor and grain boundary character. However, there has not been a direct correlation between the obtained values in the range of 0.73 – 1.83 MPa $m^{1/2}$ and grain boundary character.

All these studies suggest that CSLBs have better SCC resistance as they impede the absorption kinetics of dislocations into the grain boundary. This results in increased lattice hardening and reduced creep rate for materials with higher CSLB density [71].

It is known that M_7C_3 and $M_{23}C_6$ carbides precipitate at GBs in Alloy 600 after aging at about 700 °C, and that M_7C_3 carbide dominates in generally [84]. However, the current work reveals only $M_{23}C_6$ carbides precipitating at Σ3 and Σ9 GBs, while M_7C_3 carbides were not observed. $M_{23}C_6$ carbide has the same crystal structure and the coherent orientation relationship with the nearby matrix, while M_7C_3 carbide does not [85]. Hence, the nucleation energy for $M_{23}C_6$ carbide is lower than that of M_7C_3 carbide. So $M_{23}C_6$ carbide is prone to precipitate at low

energy GBs, e.g., Σ3 and Σ9 GBs, while M_7C_3 carbide is prone to precipitate at random GBs in the case of alloy 600.

2.2.4 Grain size

The grain size of alloy 600 has been shown to influence the behaviour of IGSCC. Results from Gorman [86] presented in *Figure 16* indicate that grains which are smaller have a greater propensity for cracking. However, the analysis is quite complicated as the parameters such as grain size, thermal treatments, carbide distribution and mechanical properties. For instance, a high yield strength material obtained after thermomechanical treatments will result in fine grain microstructure.

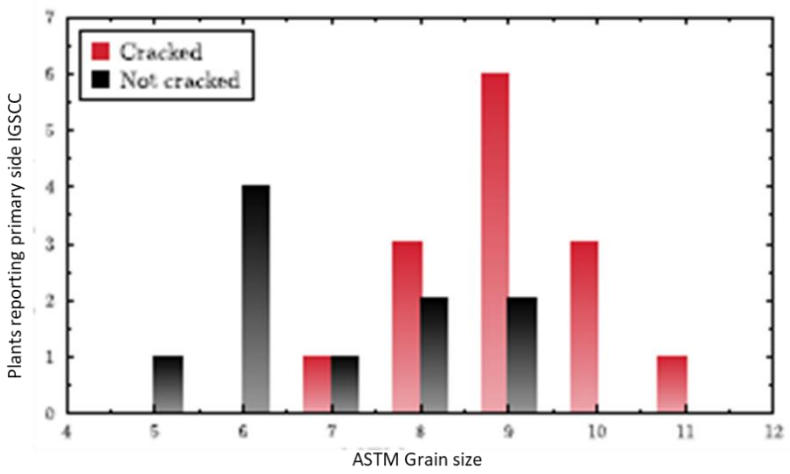


Figure 16: Effect of grain size on IGSCC behaviour.

Norring [56,87] in his studies reported that there is a drastic decrease in time to cracking with increased yield strength, which is contradictory to the results of Gorman [86]. Therefore, it is better to say that results from Gorman are related to the relationship between carbon in the solution and grain boundary coverage more than grain size. The effect of grain size and yield strength follows opposite trends and it is difficult to interpret which is the primary factor [87].

2.2.5 Cold work

Cold work (CW) is the process by which materials are work hardened. Work hardening usually happens due to the changes introduced in the microstructure of materials due to the application of external stresses. A large number of defects and dislocations are generated in the materials by cold work, thus making the material harder. The strengthening effect is due to the introduction of dislocations and consequently reducing the dislocation movement in the materials. This result in high defect density which causes delay in the onset of plastic deformation, in other words, more stress is required to deform plastically. Many researchers across the globe studied the effects of CW in austenitic alloys and reported that there is a detrimental effect on the resistance to cracking [25,38,44,88–101].

The amount of CW has been found to have an effect on the behaviour of IGSCC in alloy 600 and other austenitic stainless steels. These alloys are mainly used as structural materials in nuclear power plants especially in the primary side and hence CW is introduced into these alloys during the forming process. Machining process such as reaming have been shown to decrease the resistance to cracking in service parts [102]. It is also reported that increase in yield strength and CW have increased the crack growth rates in alloy 600 [59]. However, the quantification of the effect of these parameters individually proves to be challenging.

Couvant et al. [98] conducted tests on the low carbon stainless steels used in the heater of the PWR pressurizer. They observed that SCC cracks seem to occur preferentially in the high strain-localized areas of the heater. This strain localization happens due to the cold work. Similar SCC failure in austenitic stainless steels in the primary water inlet nozzle welds of SG was reported [100].

Lozano-Perez et al [44,103] using high resolution microanalysis observed that CW induced large number of deformation bands along the grain boundary microstructure. These

deformation bands as shown in *Figure* 17 have highly localized stress which could assist the diffusion of oxygen into the crack opening during crack propagation leading to higher crack growth rates (CGRs).

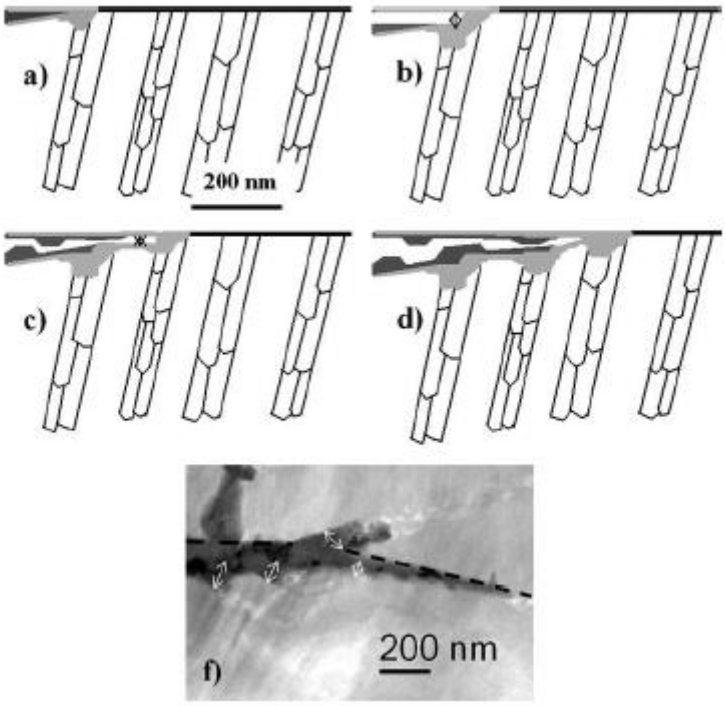


Figure 17: Schematic representation of Crack growth in 316SS cold work [44].

Similar trends were observed in alloy 600 depending on the extent of cold work. Bandy et al. [90] observed a decrease in SCC resistance for cold worked alloy 600 compared to as-received alloy tested in the same environment. Later studies confirmed this observation [25,91,92]. Rebak et al. [91] carried out constant extension rate tests (CERT) on U-bend specimens of alloy 600 at two different temperatures by varying the extent of cold work. The results show that increasing the degree of CW consequently increases the crack growth rate (CGR) as shown in *Figure* 18. Complementary results were observed later by Totsuka et al. [92] on specimens with a cold-pressed hump which exhibited an increase in order of magnitude faster crack growth when the level of cold work is increased from 6 to 35%.

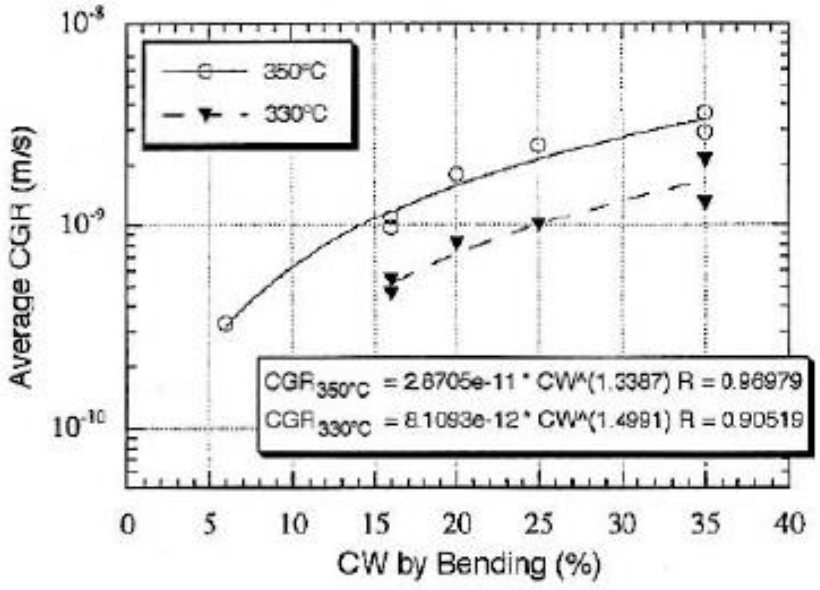


Figure 18: Average crack growth rate (m/s) vs extent of cold work (%) [91].

Le Hong [25] studied the influence of CW on crack initiation in alloy 600 and reported that there is a decrease in initiation times for capsule tests performed at similar strain levels for different levels of CWs ranging from 0-20%. He also reported that stresses are much higher than yield stress for cold worked materials to initiate cracking as shown in *Figure 19*. It could be seen that the effect of CW is beneficial as it increases the stress level to initiate SCC crack. However, CW reduces the value of ratio between applied stress and yield strength. This confirms the observations of Bandy [90] that specimens with lower cold work (5%) fractured earlier than the specimens with higher cold work (20%). Another study on crack initiation conducted by Airey [104] in hydrogenated and pure water showed that a reducing area reduces the SCC initiation time for both mill annealed (MA) and thermally treated (TT) alloy 600. Cold work clearly has a detrimental effect on IGSCC behaviour; however, it cannot be fully eliminated for alloys in service.

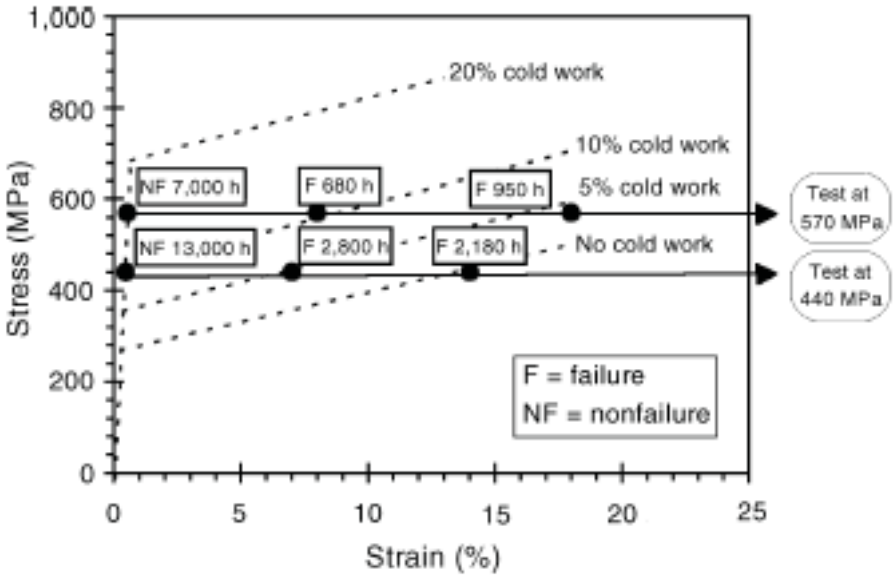


Figure 19: Effect of Cold work on SCC crack initiation time [25].

2.2.6 Strain

It was pointed out by Richey et al. [105] that plastic strain might be a crucial parameter than stress to characterize SCC initiation time. The authors reported a correlation between plastic strain to SCC initiation for no-cold work as well as cold worked materials as shown in *Figure 20.*

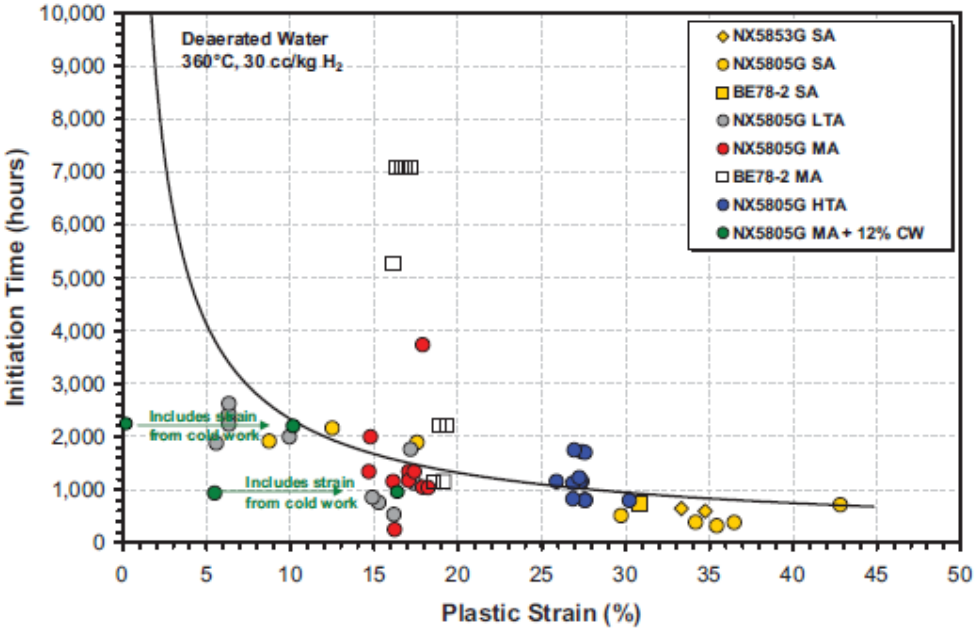
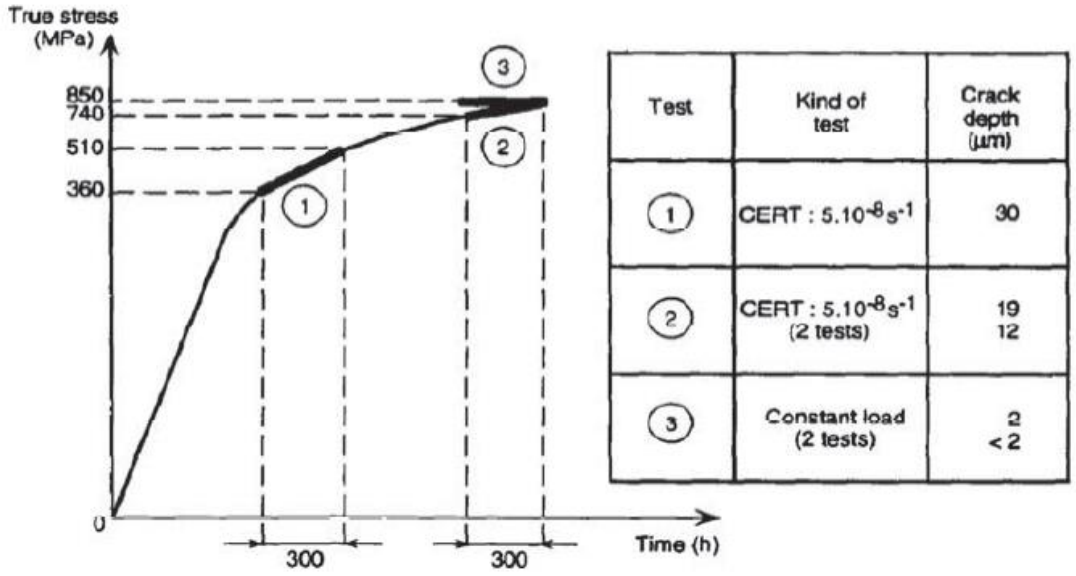


Figure 20: Plastic strain vs Initiation time [105].

Boursier et al. [47] performed constant load and slow strain rate tests on alloy 600 and found that there is a correlation between strain rate and crack growth rate during propagation. From *Figure 21*, it appears that maximum crack depth is obtained for the highest strain rates irrespective of the applied stress. It was also seen that there was no cracking for high stress levels in case of constant load tests. The authors felt that strain rate is a more suitable parameter defining IGSCC compared to stress. However, it is important to note that stress levels on the materials should be above yield stress in order to generate creep during the service.



Test	Kind of test	Crack depth (μm)
1	CERT : $5.10^{-8}s^{-1}$	30
2	CERT : $5.10^{-8}s^{-1}$ (2 tests)	19 12
3	Constant load (2 tests)	2 < 2

Figure 21: Comparison of crack depths for SSRTs and constant load tests [47].

2.2.7 Strain path

The strain path refers to the deformation history of specimen due to successive loadings. The influence of processing orientation on the crack growth rate was first reported by Moshier and Brown [106,107]. The tests were carried out on cold rolled alloy 600 in longitudinal-transverse (LT) and short-transverse (ST) directions using wedge opening loading and compact tension specimens at 316°C. The schematic of specimen orientation is shown in *Figure* 22. It was reported that ST orientation crack growth rates were an order of magnitude higher than LT orientation, results are presented in *Figure* 23. Andresen et al. [108] later observed high crack growth rates in SL and ST oriented specimens compared to TL and LT oriented specimens of unidirectionally cold worked alloy 690.

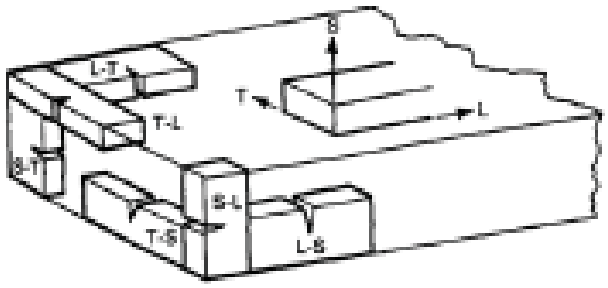


Figure 22: Schematic of specimen orientation [108].

These results confirm a correlation between the CGR and specimen orientation relative to the direction of cold work. Morton et al. [105] conducted tests to study this effect on SCC initiation and found that S oriented specimens had a slightly shorter initiation time than the T oriented specimens when tested in the same autoclave.

However, these studies did not mention any possible explanations for the observed behaviour about strain path. Couvant et al. [109,110] carried out few experiments to address this issue and proposed that complex strain paths induce higher stress concentration along the grain boundaries, thus promoting IGSCC due to stress localization rather than the high levels of strain.

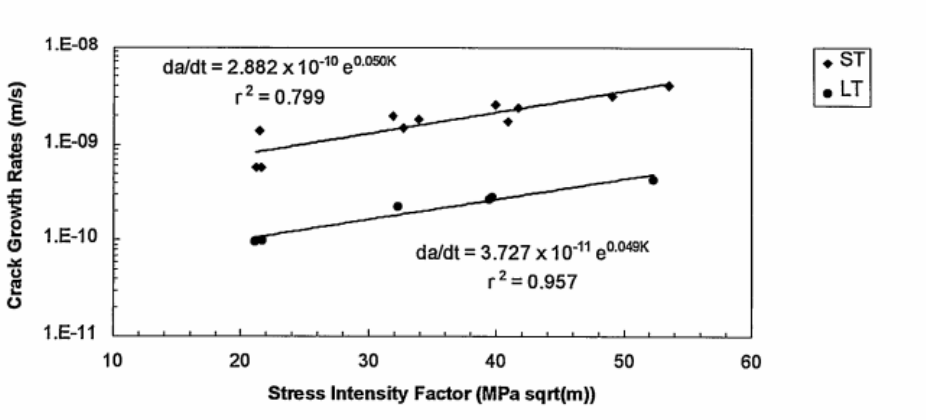


Figure 23: Effect of processing orientation (ST vs LT) on SCC growth rate behaviour of cold rolled alloy 600 with yield strength of 827 MPa tested at 316°C [107] .

2.2.8 Stress

Stress or external applied stress is one of the important parameters for IGSCC to happen. It plays a crucial role in crack initiation as well as crack propagation in the material. Staehle et al. [31] reported that SCC rate increases with increasing stress as presented in *Figure* 24. The relationship between the time to failure (t_f) under a constant load and tensile stress is based on the following equation (4) [45]:

$$t_f = k \cdot \sigma^{-n} \quad \text{.....(1)}$$

where, t_f is time to failure, k is a constant that depends on the susceptibility of the material, the chemical composition and testing temperature and σ is the applied stress.

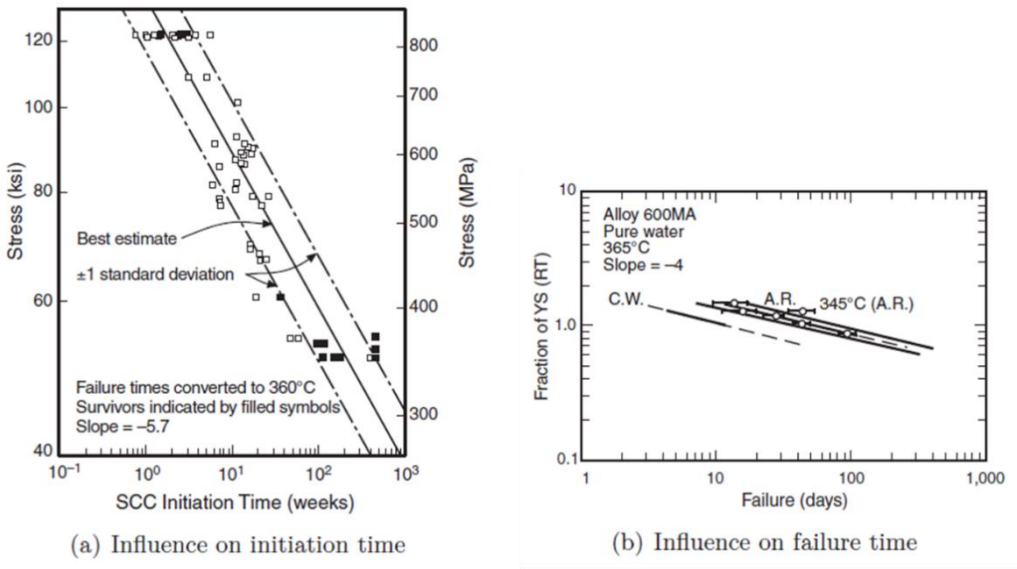


Figure 24: Influence of stress on initiation time and failure time [31].

The stress intensity factor (K) in fracture mechanics is generally used to describe the stress state at the crack tip caused by the applied stress (external/residual/both). This factor is a function of total stress and crack length by three different cracking modes. Various modes of

cracking are illustrated in *Figure 25*. The crack propagation occurs only when the critical stress intensity factor (K_c) is reached.

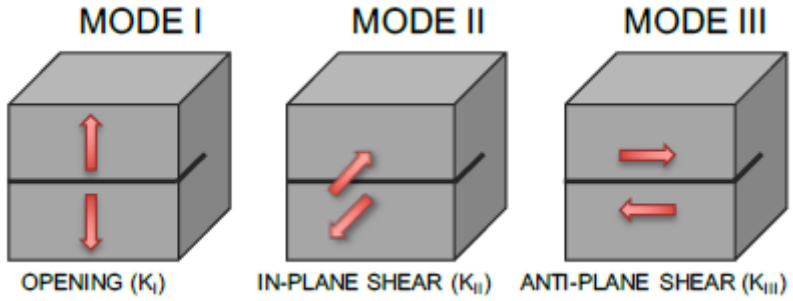


Figure 25: Various modes of cracking.

In mode I, the most common type of SCC, cracking occurs perpendicular to the applied stress. This is mainly because the critical stress intensity factor for mode I (K_{IC}) is usually lower than K_{IIC} or K_{IIIC}. However, bifurcation of cracks can locally occur in shear mode (mode II) or mix of modes I & II due to the activation of local plasticity. Chopra et al. [111] did an extensive study to correlate the crack growth rate to stress intensity factor and determine the threshold critical stress intensity factor (K_{ISCC}) for SCC in alloy 600 and 690. A significant amount of dependency on crack growth rates for stress intensity factors between 5-25 MPa $m^{-1/2}$ was reported, which reaches a plateau for values over 25 MPa $m^{-1/2}$ as presented in *Figure* 26. It is important to note that, during the initiation stage, K_I value is needed to combine to subcritical proto cracks in the materials to reach K_{ISCC} and cracks propagate. This means that as long as the stress intensity factor (K_I) is less than the critical stress intensity factor (K_{ISCC}), SCC can be prevented. It is widely agreed in the SCC community that this value of critical stress intensity factor is between 5 – 10 MPa $m^{-1/2}$. Raja et al. [112] reported the threshold stress intensity K_{ISCC} = 9 MPa $m^{-1/2}$ at 330°C.

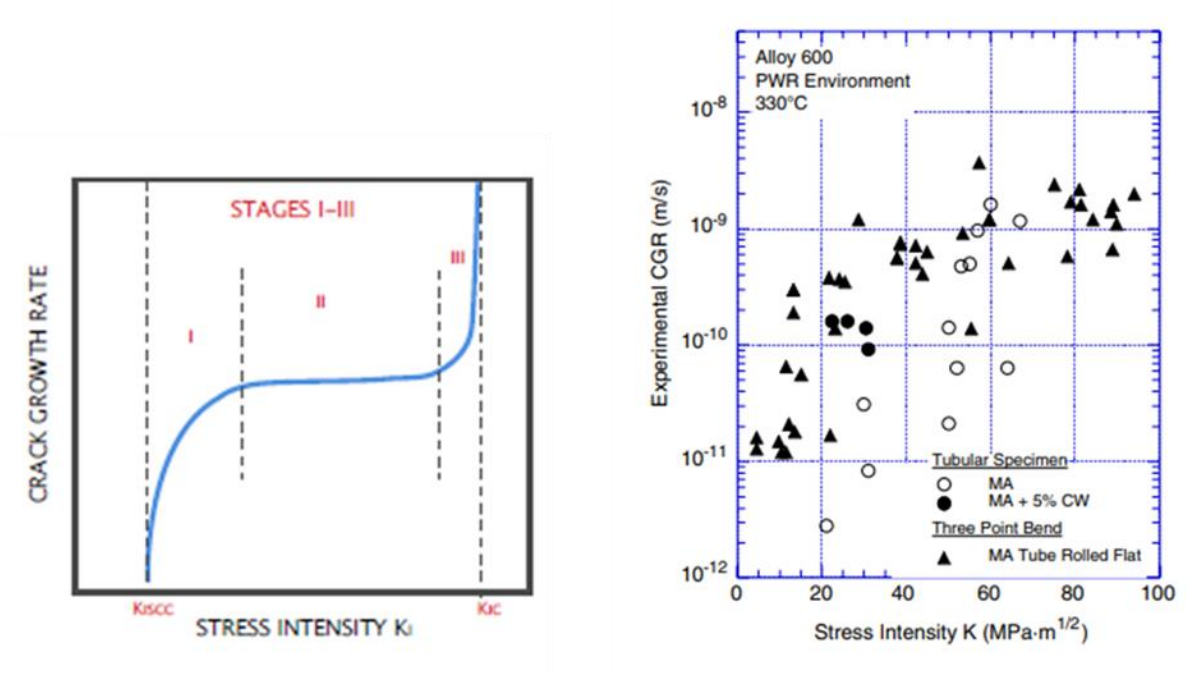


Figure 26: Crack growth rate vs Stress intensity factor: theoretical behaviour (left); observed behaviour (right) [111].

Couvant et al, [113] pointed out that SCC being a local and microscopic phenomenon, it is difficult to differentiate crack initiation to crack propagation stage on a macroscopic scale. The authors also felt that there is a need to obtain more data about local conditions that will give an accurate evaluation of stress intensity required for the grain boundary to fail. From this, it is hard to say that there is a unified value for threshold stress intensity factor. This value seems to vary depending on stress levels and synergetic effect of other influencing parameters.

2.2.9 Primary water conditions

The primary environment used in PWRs typically constitutes pure deaerated water (dissolved O_2 < 10 ppb) with addition of boron (from H_3BO_3), lithium (from LiOH) and hydrogen. Boron is usually added to control the neutronic reaction whereas lithium and hydrogen are added to maintain the pH of the solution between 6.8 and 7.4. This solution is generally kept at a temperature between 290°C and 345°C [62]. Several studies were carried out to understand the

influence of boric acid, lithium hydroxide and pH. However, the researchers found it difficult to separate the effect of lithium hydroxide and boric acid from the influence of pH [114,115]. Szklarska-Smialowska et al. [116] carried out SSRT experiments on alloy 600 in simulated primary water conditions at different pH levels and temperatures. The results showed that CSR tends to be minimum for the pH values in the range 6-7 but slightly increases for the acidic and alkaline pH levels. Jacko and Gold [117] observed contradictory results, crack propagation was found to be independent of pH level and shorter initiation times were observed in the case of 7.2 pH environment.

In a recent study by Norring et al. [87] focussing mainly on the effect of lithium on crack initiation time of alloy 600, it was concluded that an increase in lithium concentration from 2.25 to 3.5 ppm reduced the initiation time by 50%. However, this increase in lithium correspondingly increases the pH of the solution and it was difficult to differentiate both the effects. This is illustrated in *Figure 27.* Couvant et al. [118] found that CGR increased when decreasing concentration of lithium from 3.5 to 2.2 ppm while keeping the values of pH, boron and H_2 constant. The effect of boron on crack initiation and propagation is still to be investigated.

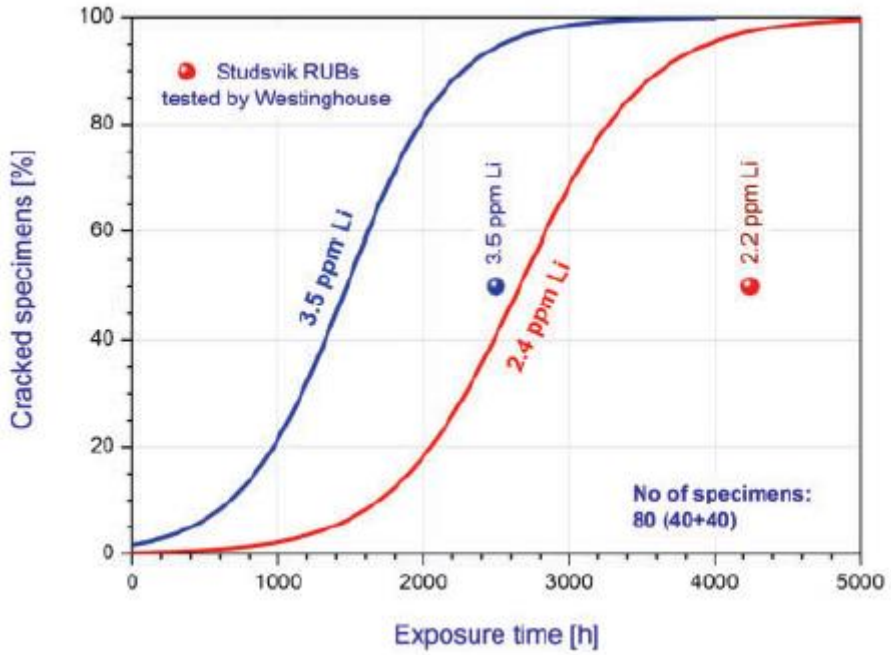


Figure 27: Influence of Lithium on crack initiation [116].

2.2.10 Temperature

The effect of temperature on SCC proved to be a hot topic of study in the SCC community for the past few decades. No cracking occurs for temperatures below 250°C and the service components in the hot leg of the SG tubes at 345°C are the ones severely affected by SCC. This phenomenon is consistent with the laboratorial results as well.

As temperature affects various other factors such as oxidation rate, diffusion rates of metal and oxides, pH of water and mechanical properties of alloys, it is important to study the crucial interdependency of temperature and SCC susceptibility. As SCC is a thermally activated phenomenon, an Arrhenius equation (1) is used to represent it.

$$k = C \cdot \exp\left(\frac{-Q}{RT}\right) \quad \text{..... (2)}$$

where, k is the reaction kinetic, C is the constant, Q is the apparent activation energy, R is the ideal gas constant and T is the absolute temperature.

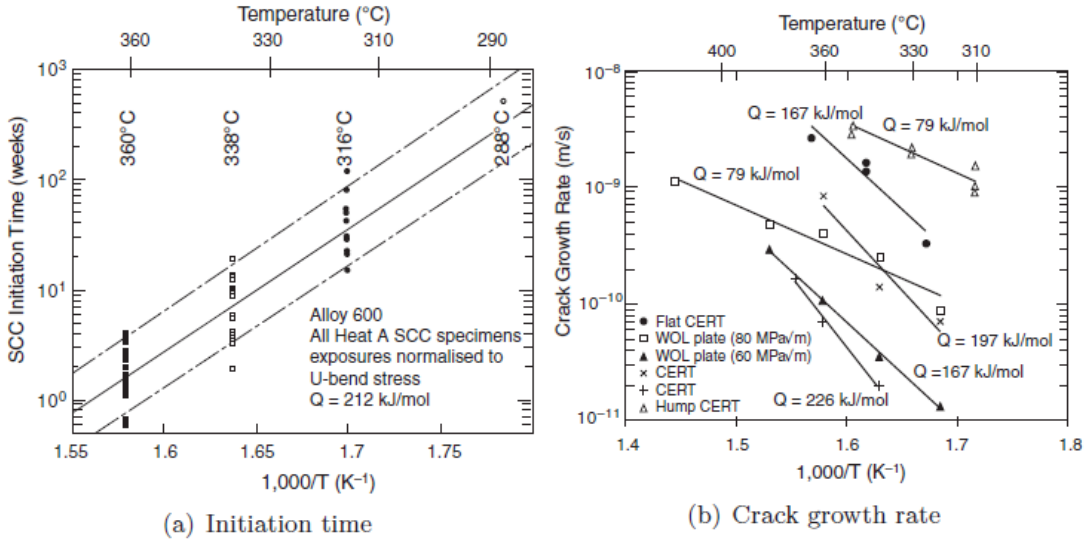


Figure 28: Arrhenius plot for SCC initiation time and Crack growth rate (CGR) [119].

From *Figure 28*, it is clear that SCC susceptibility is hugely influenced by temperature in both the initiation and propagation stages [119]. Cowan et al. [120] conducted tests on alloy 600 in high temperature aerated water and found a fivefold decrease in time to crack initiation as the temperature increased from 290°C to 340°C. Further studies on the failed samples during SSRTs showed that failures caused by IGSCC at 365°C, 345°C and 325°C are about 60%, 40%, 1.5% respectively [121]. In order to thoroughly understand the dependence of temperature on IGSCC in 316SS, 304SS, alloy 690 and alloy 600 a series of tests were conducted by Arioka [30,101,122]. He observed that both the steels had increasing CGRs with increase in temperatures. Arioka suggested that diffusion of vacancies would have caused the increasing trend of CGRs on increasing temperature from 250°C to 330°C. He also reported that for temperatures above 330°C there is a decline in the CGR with a distinct peak occurring between 320°C and 340°C. Andresen [123] studied the effects of temperature on stress corrosion crack growth rates on three heats of sensitized type 304 stainless steel (SS) and one heat of sensitized alloy 600. He reported that all heats and materials had similar temperature dependence and showed a peak in crack growth rate at ≈ 200°C, which typically was a factor

of 30 to 100 times higher than at 288K or 25°C. Growth rates decreased rapidly above 250°C compared to those between 25°C and 200°C. However, the trend of peak temperature was not observed for alloy 600. Economy et al. [124] made contradictory claims by reporting a linear relationship between time to initiation and reciprocal of temperature from hydrogenated steam to water as shown in *Figure* 29. The dissolution of metal does not occur at steam environment thus it is difficult to say that dissolution is the only parameter controlling IGSCC. Hence, there is a need for more studies on IGSCC on alloy 600 to understand the effect of temperature.

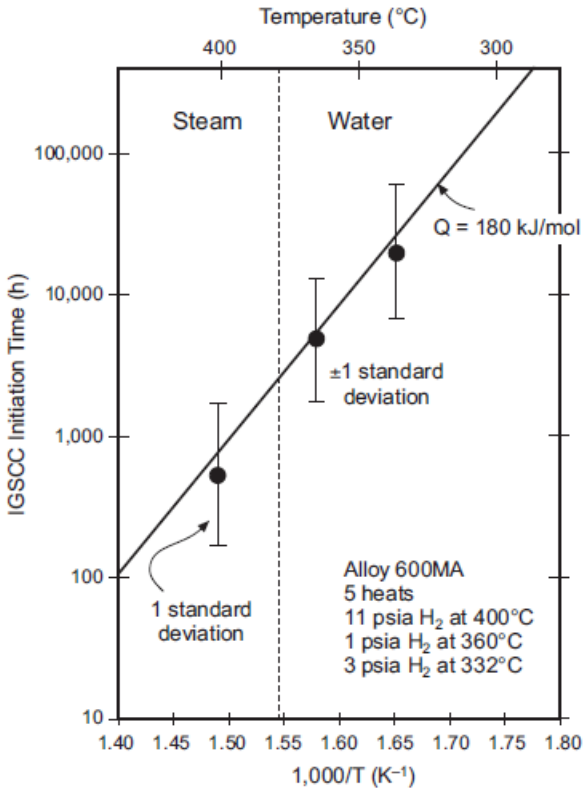


Figure 29: IGSCC initiation time vs Reciprocal temperature (1/T) [124].

According to a recent results reported by Meisnar et al. [33], the peak temperature phenomenon occurring in 316SS was the result of two rate-controlling mechanisms. One being a diffusion-based (thermally activated) mechanism, the other one a mechanical deformation-based mechanism as illustrated in *Figure 30*.

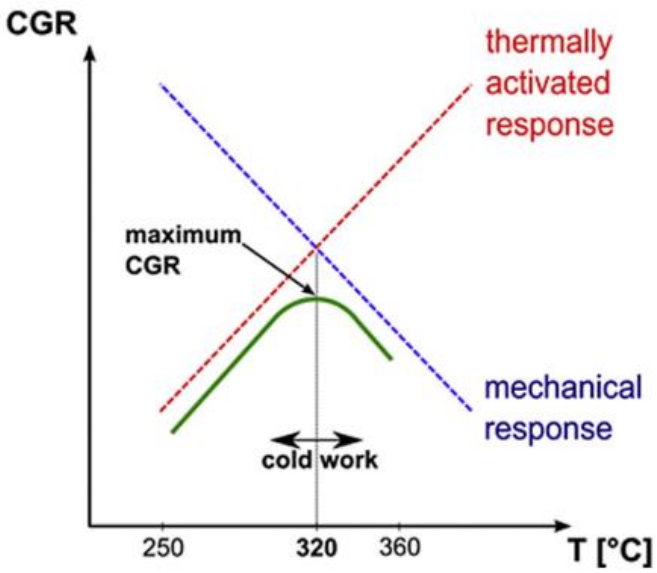


Figure 30: Phenomenological diagram illustrating the combined effects of thermally activated diffusion and mechanical response-based mechanisms on the temperature dependence of the SCC CGR in SS316 [33].

2.2.11 Potential and Dissolved H_2 concentration

The IGSCC behaviour is strongly affected by the corrosion potential in primary water environments. Corrosion potential is usually governed using oxygen and dissolved hydrogen. SCC susceptibility is often assumed to be affected by the main two electrochemical reactions happening in the high temperature primary water environment. These reactions are given by the following equations;

$$H_2 \rightarrow 2H + 2e^- \text{..... (3)}$$

$$O_2 + H_2O + 4e^- \rightarrow 4OH^- \text{..... (4)}$$

In order to compensate for the high corrosion potential due to the dissolved oxygen (which favours SCC), a required amount of hydrogen is added to lower the corrosion potential. Many researchers carried out SCC experiments and reported the results for lower concentration of dissolved oxygen [125]. IGSCC in Ni-based alloys is more favourable for the potential around

Ni/NiO equilibrium in primary water conditions as represented in the Pourbaix diagram [23] in *Figure* 31. The first study of galvanic couples of alloy 600 connected with more active or nobler metals to observe the sensitivity of low potential stress corrosion cracking (LPSCC) for small changes in electrochemical potential (EcP) was carried out [31]. After that, many researchers studied the effects of hydrogen potential on LPSCC. Economy et al [126] studied the influence of hydrogen partial pressure on IGSCC behaviour of alloy 600 tubing in 360°C water or 400°C steam and reported lowest time to crack initiation for hydrogen partial pressure in the range of Ni/NiO equilibrium. This was later confirmed by other studies carried out in simulated primary water conditions [127,128].

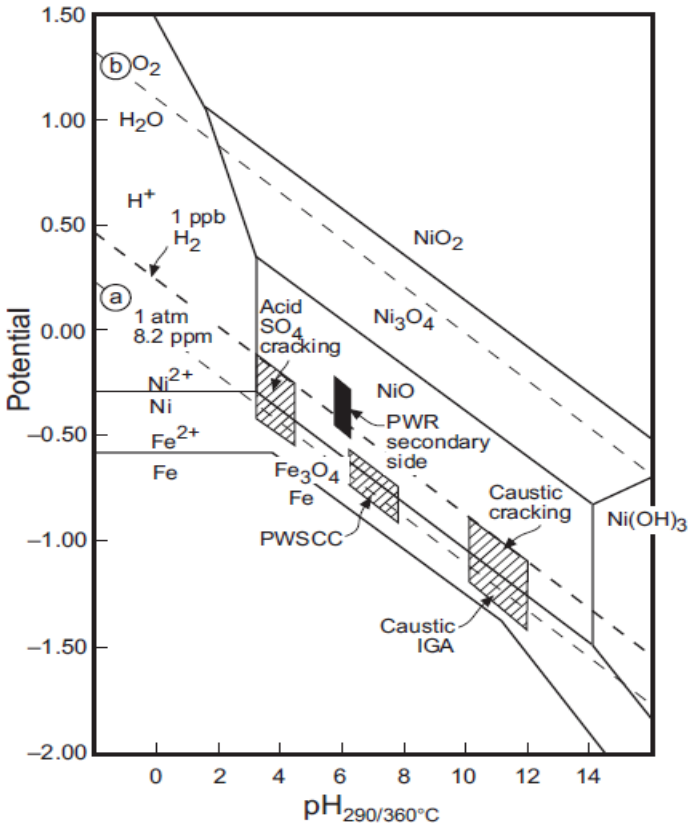


Figure 31: Pourbaix diagram showing the domains of cracking in alloy 600 at 290/360°C [23].

2.3 Models and Mechanisms

IGSCC has shown to affect the alloy 600 in PWR primary water conditions. Many researchers all over the world have studied the cracking behaviour of alloy 600 and other austenitic alloys with respect to a number of important parameters for the past four decades. However, till date there is not a single accepted model or mechanism explaining the full understanding of SCC behaviour amongst the SCC community. Several possible mechanisms have been proposed by researchers and the most recognised ones are presented in this part and broader review of other mechanisms can be found in [129].

2.3.1 Film Rupture Model (FRM)

The film rupture model is often referred as slip-dissolution or slip-oxidation model. It was first formulated by Logan in 1952 [130]. Many researchers in the following decades developed this model [131–140]. This model was successfully employed to predict SCC of sensitised or cold worked stainless steels and Ni-based alloys in boiling water reactors (BWRs). Andresen proposed the extension of this model from BWR to PWR conditions [141]. This model is based on the fact that crack growth proceeds due to a cyclic process of passivating film rupture, dissolution and film repair. There are four steps involved in crack propagation based on FRM and these steps are illustrated in *Figure 32*. They are as follows;

1. A sufficiently high-localised plastic strain is reached at the passivated crack tip.

2. This localised strain now rips apart the protective oxide layer and exposes the unprotected material to the environment.

3. On coming into contact with the environment, the exposed material undergoes anodic dissolutions (corrosion) before the repair (protective oxide) layer is formed.

4. The consequent advancement of the crack repeats as mentioned above with corrosion and strain working together.

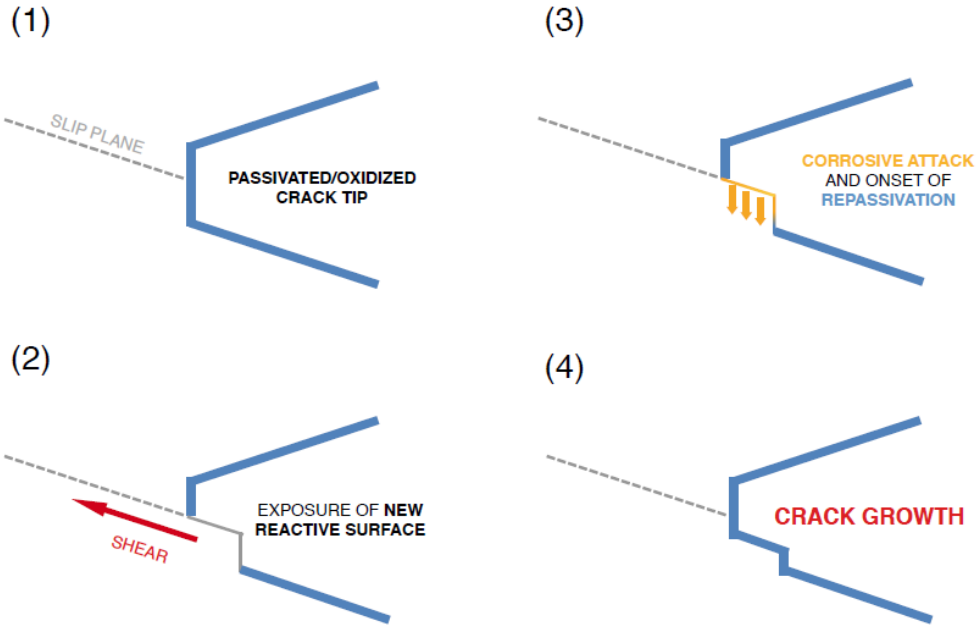


Figure 32: Schematic representation of crack propagation in FRM model [142].

Ford and Andresen developed an empirically predictive model based on the concept of slip-dissolution [134]. The key point of Ford-Andresen approach is that the crack propagation rate depends on the increase in crack length following each film rupture event (mass loss) and the frequency of the rupture events. The mass loss depends on anodic charge density, which passes due to the dissolution process, and frequency of the rupture events depend on the function of crack tip strain rate and the film fracture strain. Therefore, based on Faraday's law of electrolysis, the following relation (5) for crack propagation rate was presented [134]:

$$\overline{V_t} = \frac{M}{\rho z F} \cdot \frac{Q_f}{\varepsilon_f} \cdot \dot{\varepsilon}_{ct} \quad \text{..... (5)}$$

where, $\overline{V_t}$ is the average crack propagation rate, M and ρ are respectively the atomic weight and density of the crack tip metal. z is the number of electrons in the overall oxidation of a

metal atom, F is the Faraday constant, Q_f is the oxidation charge density, ε_f is the oxide fracture strain, and $\dot{\varepsilon}_{ct}$ is the crack tip strain rate.

As the repassivation, response generally follows a power law decay of a fixed slope n. Ford [133] used the power law behaviour for repassivation current ($i_t = i_0 \left[\frac{t}{t_0}\right]^{-n}$) and further distilled down the formulation that derives from the periodicity of strain and the repassivation response as follows [141,143,144] :

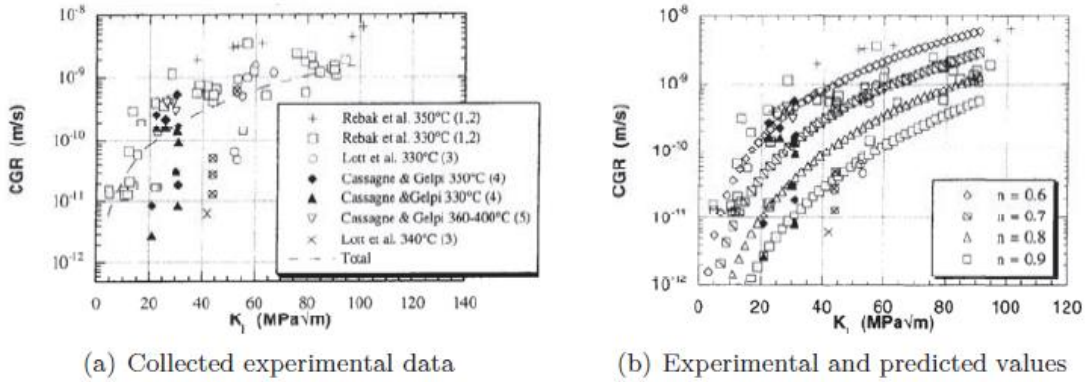
$$\bar{V}_t = \frac{M}{\rho z F} \cdot \frac{i_0 \cdot t_0^n}{(1 \quad -n)\varepsilon_f^n} \cdot (\dot{\varepsilon}_{Ct})^n \text{..... (6)}$$

where, i_0 is the bare surface dissolution current density, t_0 is the time for repassivation, n is a value that accounts for the reaction rate at the crack tip. This is the starting point of quantitative capabilities of the model, but the main limitation is that there is no link to measurable engineering and operational parameters. This equation (6) was further simplified by Andresen [141] as (7):

$$\bar{V}_t = A \cdot (\dot{\varepsilon}_{Ct})^n \text{..... (7)}$$

where, $\bar{V}_t$ is the average crack propagation rate, A and n are constants which represent the effects of the environment and material chemistries, and $\dot{\varepsilon}_{ct}$ is the crack tip strain rate.

Rebak [142] in this review paper demonstrated the model's capability to predict crack growth rates for alloy 600 SG tubes tested in open circuit condition in water at 330°C - 360 °C under constant load. It was reported that this model predicted a decrease of threshold stress intensity factor K_{ISCC} with increase in environmental effects (lower value of n) which is presented in *Figure 33*.



(a) Collected experimental data (b) Experimental and predicted values

Figure 33: Comparison of CGR predicted by FRM and experimental data [142].

Combrade et al. [145] observed the consistency of the strain rate during SSRT experiments on alloy 600 and regarded it as one of the strongest candidate to explain SCC. This model provides quantitative and simple analytical expression of average crack propagation rate. Hall [138,140] published few papers evaluating Shoji's approach and included variable stress intensity factor as a new parameter in the model [139]. Vankeerberghen et al. [146] used as the base to model propagation rates for 316 SS in PWR conditions.

However, there are a number of limitations to this model. It does not accurately predict various observed parametric effects. The model assumes that the strain causing SCC is always constant, whereas in practical point of view it is non-constant.

To overcome this problem, Vermilyea [147] assumed that the crack propagation occurs through dissolution at the crack tip and plastic deformation does not occur during the repassivation stage, but through creep mechanism afterwards as strain and corrosion are mutually simulated. The drawback of this approach is that crack should be large to obtain enough plastic deformation around the crack tip to fail. Nevertheless, if the crack depth is large, the crack opening should be wide causing heavier crack flank corrosion. However, this was not experimentally observed.

Another serious flaw in the model is that there is a lack of correlation between the potential dependence of SCC and film repair kinetics. It does not take into account sensitisation at the low corrosion potential in the case of PWR water environment. The crack advancement described by the model is more suitable for more oxidising environment such as BWRs, as the Cr-depleted grain boundaries will oxidise much faster than in PWR primary water environment.

Most importantly, this model does not describe the crack initiation. Combrade et al. [145] stated that it is unlikely for the thick films (>100 nm) to rupture by strain due to creep relaxation under static loading. In 2007, Gutman [148] indicated his scepticism about the model's ability to predict SCC and suggested that there is more than one mechanism involved in SCC crack propagation. He concludes that there is *no such thing as a unified mechanism or theory.*

Lozano et al. [149] in their review paper presented the main experimental observations necessary and required for the validation of this model. They are (1) Bare metal exposed to the crack tip or some oxide ahead of the crack tip as there is not enough time for the oxide to form prior to the sample extraction for characterization (2) Series of slips on the crack flanks associated with crack advancement leading to step like appearance on the fracture surface. Only when these conditions are satisfied, IGSCC occurs.

2.3.2 Surface Mobility Model (SMM)

In 1987, Galvele [150,151] proposed a model called Surface Mobility Model (SMM), which is heavily criticised across the SCC community. This model suggests that due to the high surface mobility of the corrosive environment, the vacancies move along the crack flank and get injected into the highly stressed crack tip causing the crack to propagate further. Galvele's [150] idea is based on the surface diffusion coefficient (D_s). This coefficient in aqueous

environment is a function of surface contamination. The model stated that if the value of D_s was high, a vacancy would replace an atom at the crack tip by lowering the local stress that leads to relaxation of the lattice. *Figure* 34 illustrates the concept of this mechanism. Even though Galvele claimed SMM is an outstanding model due to the accuracy in his experimental results, Sieradzki et al. [152] heavily criticised it as there are a number of errors in Galvele considerations for surface mobility based on thermodynamics of the stressed alloys. Sieradzki reported that this model overestimates SCC in fcc materials by 14 orders of magnitude [152]. They conclude saying that SCC propagation in principle could occur based on surface mobility; however, the effects of other mechanisms of cracking are more dominant. Gutman [153] in his critical review stated that SMM was developed mainly on "contradictions and mutually excluding statements". He proposed an approach of sub dividing the SCC process into separate phenomena acting at the crack tip and studying the underlying SCC mechanisms. However, he did not mention how this can be done [154]. Galvele responded to these claims and defended his model mainly emphasising on the fact that SCC is not simply caused by mechanical deformation/fracture, hence more attention must be given to electrochemical aspect if a general SCC model was to be developed [155,156]. Thus, SMM highlights the importance of electro-chemistry in developing a suitable model even though it is not perfect enough.

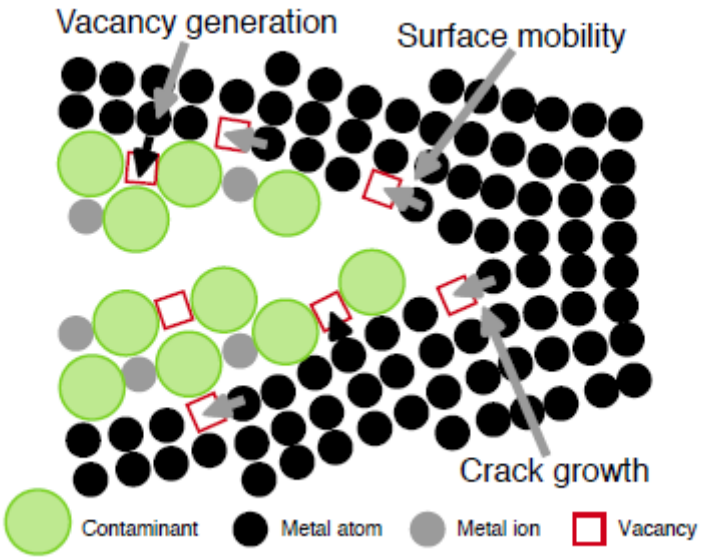


Figure 34: Illustration of Surface Mobility Model concept by Galvele [150].

2.3.3 Hydrogen based models

Hydrogen embrittlement (HE) is a form of environmental assisted material degradation similar to SCC [157]. Sub-critical cracking of materials in gaseous hydrogen or hydrogen sulphide, and cracking due to internal hydrogen resulting from pre-exposure of materials to hydrogen-bearing environments are considered to be forms of hydrogen embrittlement (HE) rather than SCC [158–160]. However, SCC in some materials can involve generation and ingress of hydrogen at crack tips. In addition, characteristics and mechanisms of SCC and HE have a lot in common. In case of Ni-based alloys in primary water environment, several studies show that H_2 has a detrimental effect on SCC behaviour [161]. Alloy 600 is generally prone to HE and the carbide precipitation in alloy 690 tends to significantly contribute to the HE effect [162,163]. It is believed that the metal/carbide interface acts as the major trapping site for H_2. Studies from Troiano [164], Beachem [165], Hirth [158] reported that HE was observed to increase at high temperatures and slow strain rates which leads to hydrogen assisted cracking (HAC).

2.3.3.1 Adsorption Induced Dislocation Emission (AIDE) Mechanism

In 1988, Lynch [166] proposed a model based on the similarities of SCC and HAC. In this paper he believes that SCC and HAC follows the same adsorption induced slip mechanism (AISM). This was later named as adsorption induced dislocation emission (AIDE). According to this model, solute hydrogen gets adsorbed to the crack surfaces near the crack tips. These adsorbed hydrogen atoms weaken the inter-atomic bonds and give rise to a high dislocation density at the crack tip. Localised strain fields formed at crack tip due to the dislocation density lead to growth of microvoids. The coalescence of these voids with the crack tip by alternating slip mechanism results in macroscopic crack growth as illustrated in *Figure* 35. Lynch made this hypothesis based on a number of studies on fracture surfaces (planes and directions) and distribution of the slip systems around the crack tips [167]. This was supported by Liu [168]. He also emphasis that there are some systems where adsorption is not responsible for HAC or SCC, in those cases he supports FRM [169].

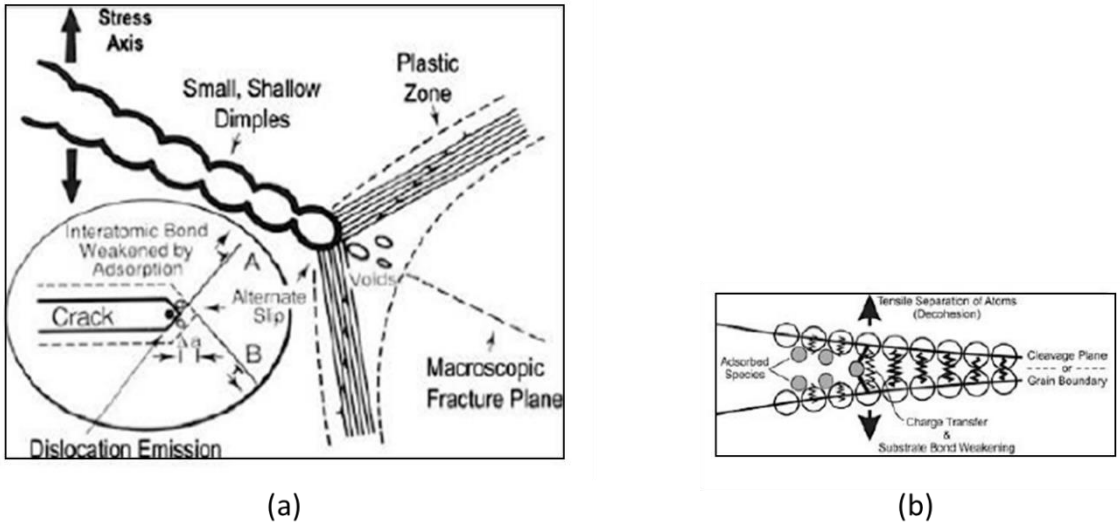


Figure 35: Schematic representation of AIDE model proposed by Lynch [166] (a) Adsorption inducing dislocations due to weakening of metal bonds. (b) Interatomic bonds weakened by adsorbed species.

2.3.3.2 Hydrogen Enhanced Local Plasticity (HELP) mechanism

In 1994, Birnbaum [170] studied the interaction between hydrogen in the matrix metal and the mobile dislocations present during deformation and proposed the Hydrogen Enhanced Local Plasticity (HELP) mechanism. At PWR operating conditions (300 – 400°C), deformation in alloy 600 is mainly controlled by glide and climb motions of dislocations. When these mobile dislocations encounter an obstacle [171], they tend to pile-up with a separation distance dependent on the short-range stress field. Hydrogen reduces the short range stress fields caused by obstacles which has been confirmed by computer simulations [172]. With the lower stress fields, dislocations can pass obstacles easily and move closer to each other allowing increased deformation [173]. This effect was later confirmed by many studies carried out at different experimental conditions [174–177].

2.3.3.3 Corrosion Enhanced Plasticity Model (CEPM)

Barth et al. [178] based on Troiano's [164] suggestion that hydrogen in the lattice will reduce the cohesive strength of the metal bonds claimed that if hydrogen concentrates in the regions of high stress fields around the crack tip, it may weaken the metal bonds and lead to crack growth. This process is then repeated with hydrogen diffusing into the new position of crack front. This hypothesis was named as Troiano-Oriani decohesion hypothesis [159,160]. They assumed that the cohesive force between atoms decrease with increase in hydrogen concentration. Lee used this approach to evaluate the pointwise relation between hydrogen concentrations in the cohesive zone [179]. Scheider et al. [180] and Raykar et el. [181] performed FE simulations supporting decohesive model and improved it by combining with an analytical approach. Even though decohesive approach seems promising, the main drawback is that it could not be applied to systems without voids observed experimentally ahead of crack tip.

Magnin et al. [182] combined the idea of decohesive hypothesis with Jones [183] suggestion of introducing brittle element instead of electrochemical dissolution to FRM postulated a new model called Corrosion Enhanced Plasticity Model (CEPM). CEPM is a crack propagation mechanism based on the interaction of hydrogen with dislocations very near the crack tip [172,184–186]. Based on CEPM, the crack propagation occurs in 5 steps described as follows and is illustrated in *Figure* 36:

1. Formation of a small, sharp crack allows for the injection of hydrogen into a localized region near the crack tip.

2. The injected hydrogen interacts with dislocations present in the alloy, specifically on the {111} slip planes, leading to a region of more mobile dislocations and a softened zone ahead of the crack tip (locally enhanced plasticity).

3. The softened zone extends till it reaches an obstacle. The mobile dislocations then pile up and create a region of high stress concentration.

4. Due to the hydrogen adsorption in {111} planes, the critical stress intensity is reduced thus forming a small cavity or new crack embryo.

5. Hydrogen lowers the cohesion energy of the (111) micro facets and stress normal to these facets is sufficient to open the crack along {111} planes.

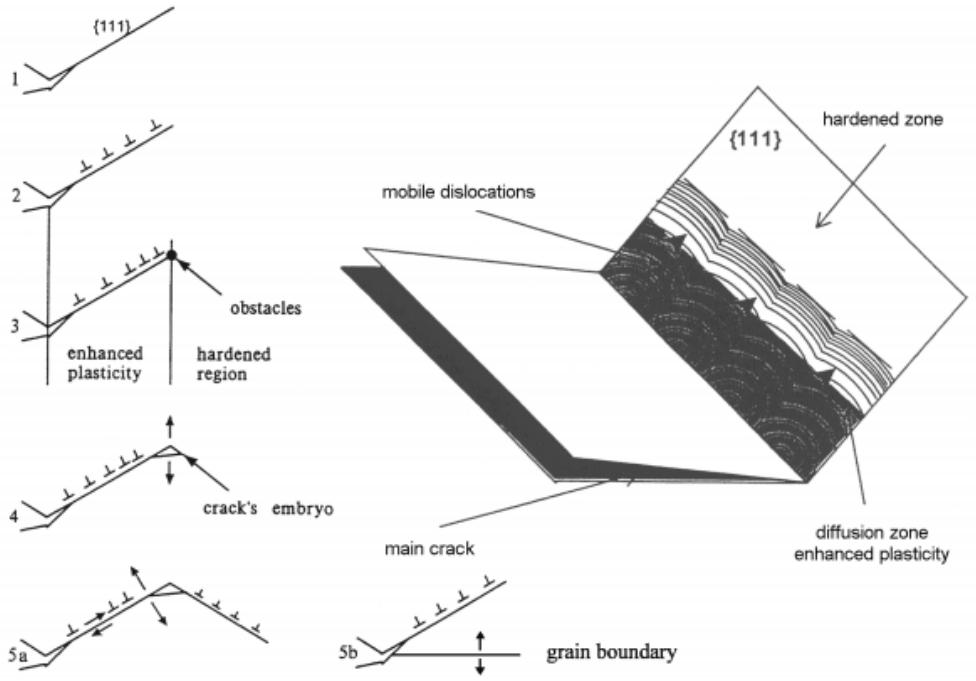


Figure 36: Schematic of different steps involved in CEPM model and of the mobile obstacle [186].

One of the key features is that as cracking occurs along the crystal planes, this model can be used to explain the observance of cracking in single crystal samples. Unlike HELP mechanism, CEPM model tries to explain exactly how crack propagation occurs rather than just the role of hydrogen in deformation behaviour.

Lozano et al. [149] in their review paper presented the main experimental observations necessary and required for the validation of this model. They are (1) Sufficient amount of H is trapped at the crack tip vicinity depending on the local stress and chemistry, this provides a correlation between the CGR and H concentration. (2) A local change in the mechanical and diffusion rate properties. (3) Presence of voids in front of the crack tip. Even though, this model addresses various parameters concerning IGSCC, it fails to be related to the higher dislocation region.

2.3.4 Internal Oxidation model

Scott and Le Calvar [187] proposed a plausible model called Internal Oxidation model also known as Selective Internal Oxidation model after studying the thermodynamics and kinetic characters in IGSCC mechanism of alloy 600 in 1993. This model is based on the phenomenon of preferential oxidation of alloy 600 along the grain boundaries in the temperature range (350 – 800). This involves an inward diffusion of oxygen and less noble alloying elements preferentially oxidising below the metal/oxide interface resulting in brittle oxide formation along the grain boundaries [188–190]. *Figure* 37 shows the schematic representation of the Internal Oxidation model. These brittle oxides, which are rich in Cr, fail under stress that leads to intergranular micro cracking and crack extension proceeds with the stress intensity value extending the critical value. Dugdale et al. [53] and Fujii et al. [191] have experimentally proved the brittle nature of the oxidized grain boundary by directly measuring and comparing the mechanical strength of oxidized and intact grain boundaries. As the crack extends, oxygen is diffused deeper into the alloy resulting in the oxidation of deeper grain boundaries. Consequently, these grain boundaries undergo cracking. Scott and Le Calver argued that this mechanism is favourable for Ni-based alloys in low partial pressures of oxygen as the Ni/NiO equilibrium is at a higher potential than the respective equilibria for typical alloying elements. They also suggested that the grain boundary embrittlement due to oxidation may also be due to gas bubble formation and oxygen adsorption at the grain boundaries [187].

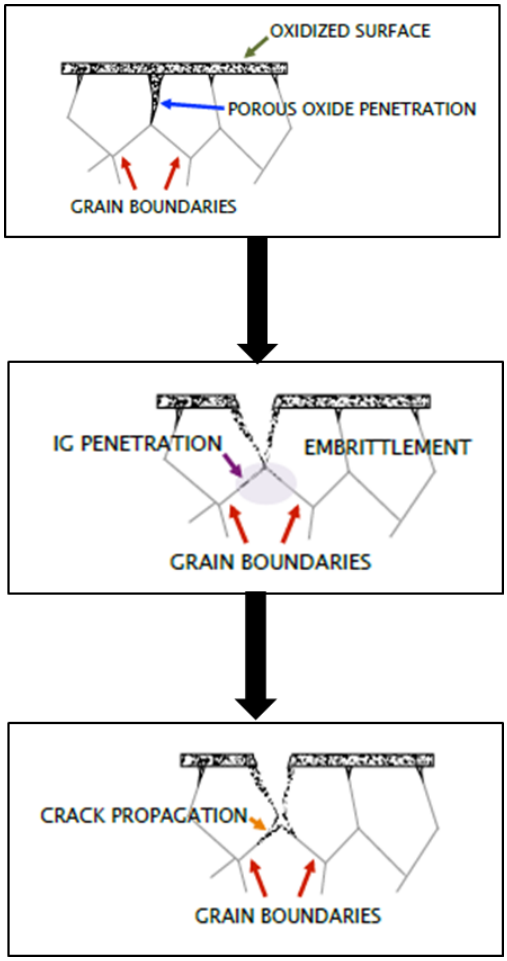


Figure 37: Schematic representation of Internal Oxidation model [189].

In the modified mechanism proposed by Laghoutaris et al. [189], defects such as dislocations and vacancies were assumed to assist diffusion of oxygen and chromium. When compared, the diffusion rate of oxygen is much faster than the diffusion rate of chromium. Hence, the latter should be the rate-limiting factor. It is also postulated that once chromium reacts with oxygen at the metal/oxide interface, it leaves behind a Cr-depleted region in the diffusion area and Ni-enrich region ahead of the crack tip as illustrated in *Figure 38*.

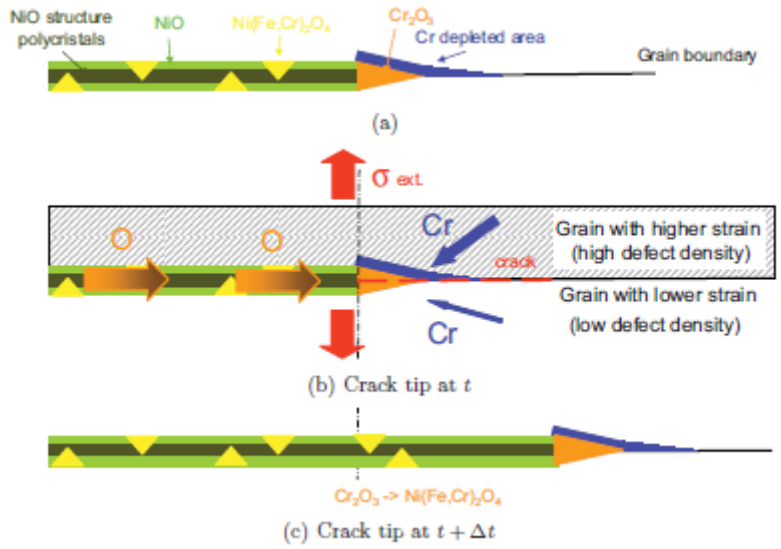


Figure 38: Schematic representation crack propagation using Internal Oxidation model [189].

Rebak et al. [142] criticised that the equation provided for the first case of CGR is proportional to stress intensity factor and the predicted CGR is too high compared to the observed one. There were many studies carried out to answer to this criticism [60,61,192–194]. Scott and Le Calver later assumed that diffusion of oxygen is stress independent and consequently obtained CGRs. These predicted CGRs appear to be close to observed ones in alloy 600. Lozano et al. [54] performed TEM investigations of intergranular stress corrosion cracking in austenitic alloys in PWR environmental conditions and observed that dislocations and stress seem to play a crucial role in enhancing diffusion in the crack tip region. Further studies confirmed this observation.

Recent studies from Scenini et al. [192] and Bertali et al. [60,194] confirmed the preferential intergranular oxidation of the alloy 600 SA. They observed a distinct grain boundary migration on the surface and beneath the surface, suggesting that HAGBs are susceptible to migration in the early stages of oxidation as shown in *Figure* 39. Microanalysis revealed that there are Cr-

rich oxide regions in the migrated zone. They reported that grain boundary migration massively reduced the local compressive stresses along the grain boundaries.

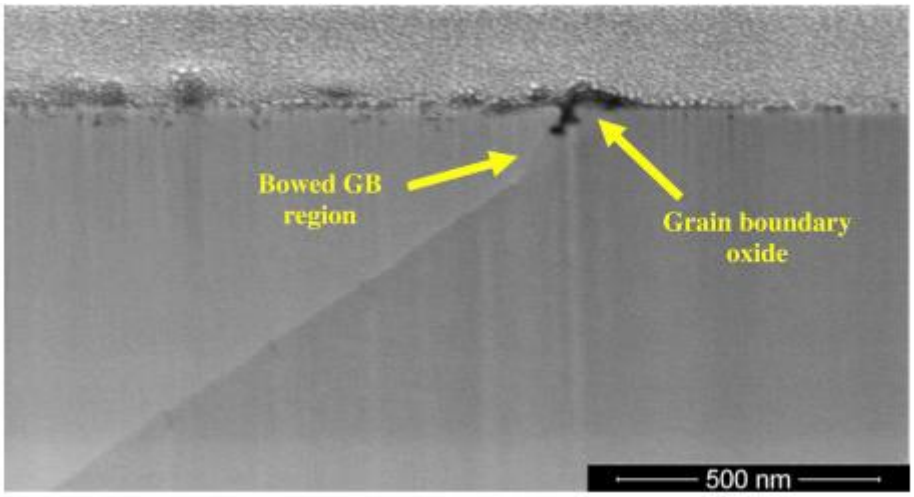


Figure 39: SE image of Grain boundary migration along the cross section [194].

Lozano et al. [147] in their review paper presented, if measured along GBs and deformation bands only, localized deformation (high dislocation density) seems to have an accelerating effect on intergranular oxide penetration depths and that applied stress further accelerates this process. This contribution of localized plasticity is however not accounted for by the original internal oxidation mechanism. The main experimental observations necessary for the validation of this model are (1) A brittle oxide (2) presence of oxidation ahead of the crack tip, which implies the rate of intergranular oxidation should be faster than crack growth rate (CGR). Due to these experimental observations in support of the internal oxidation mechanism, this model has to be considered as the plausible explanation for IGSCC. However, it cannot explain all the observations made in the experiments especially the localized plasticity near the crack tips, role of hydrogen and local microstructure.

2.4 Modelling Component life

2.4.1 Index model

Predictive equations for IGSCC in alloy 600 were first established for steam generator (SG) tubes and later extended to pressurizer nozzles, and upper head CRDM penetrations [11]. Various empirical models used both deterministic and probabilistic methods. However, the modelling of alloy 600 components invariably was based on the same empirical equation. As SCC of alloy 600 in PWR conditions depends on the three main parameters – temperature, material susceptibility and applied stress, the empirical equation governing the modelling of alloy 600 component life was given by the equation (8) [195] as follows :

$$t_f = C \cdot \frac{\sigma^{-4}}{I_m} \cdot \exp\left(\frac{E}{RT}\right) \quad \text{..... (8)}$$

where, t_f is the failure time (in hours), C is a constant, σ is the applied stress (in MPa), I_m is a material susceptibility index, E is the apparent activation energy, R is the universal gas constant, and T is the absolute temperature.

Framatome and EDF came up with an engineering model called Index model, based on the system of material indices I_m in order to assess the alloy 600 component life. The most influencing parameter is the temperature as IGSCC in alloy 600 is a thermally activated phenomenon based on the Arrhenius equation dependency. EDF used 180kJ/mol for crack initiation and 130kJ/mol for crack propagation as the apparent activation energy [31,196]. To address for the applied stress a power to the fourth is consistent with creep based processes or processes combining parabolic diffusion kinetics with stress intensity threshold for cracking was used [197].

As the component's temperature and operating stress can be measured or calculated, the material susceptibility index cannot be assessed easily. In order to overcome this shortcoming,

a system of material susceptibility indices was determined based on the minimum time to failure of the plant components. In cases where there was not any failure reported, laboratory corrosion test and engineering judgement of manufacturing process and microstructure examinations were used [198].

The reference of the material index of alloy 600 for the system is adjusted in such a way that a material susceptibility index of unity corresponds to a minimum failure time of 10,000 hours at a temperature of 325°C and applied stress of 450 MPa [199]. The constant C in the equation was then adjusted and two other indices were defined according to the reference conditions, (1) temperature index I_θ and (2) stress index I_σ given respectively in the following equations (9) & (10):

$$I_\theta = \exp\left[\left(\frac{-E}{R}\right)\left(\frac{1}{T} - \frac{1}{598}\right)\right] \text{.....(9)}$$

where I_θ, is the temperature index, E is the apparent activation energy, R is the universal gas constant and T is the absolute temperature.

$$I_\sigma = \left(\frac{\sigma}{450}\right)^4 \text{..... (10)}$$

where I_σ, is the stress index, σ is the applied stress.

By combining these three equations (8),(9) & (10) Scott and EDF, defined the Index model [200] by equation (11) :

$$t_f = \frac{10000}{I_m \cdot I_\theta \cdot I_\sigma} \text{..... (11)}$$

where t_f is the failure time, I_m is a material susceptibility index, I_θ is a temperature index, and I_σ is a stress index. In this way, the minimum time to cracking for various alloy 600 components were assessed and shown in *Table 3*:

Table 3: Predicted minimum time of failure for Alloy 600 component in PWR primary circuits [200].

Ref.	Alloy 600 parts	Material index	Stress index	Temperature index	Overall index	Time (hours)	Observation *
1	Hydraulic expansion	0.2	0.4	1	0.08	80000	NC
2	Divider plate	0.5	0.3	0.9	0.14	80000	NC
3	Hard rolling on cold leg (Ringhals 2)	2	2.2	0.1	0.44	48000	C
4	Pressurizer nozzle (San Onofre 3)	0.5	0.1	3.3	0.17	56000	C
5	Nozzle (San Onofre)	0.5	0.9	3.3	1.49	8000	C
6	Pressurizer nozzle (ANO1)	0.5	0.3	3.3	0.5	84336	C
7	Pressurizer nozzle (Palo Verde 1)	0.5	0.4	3.3	0.66	33320	C
8	Nozzle (Palo Verde 2)	0.5	1.5	1.1	0.83	25000	C
9	Explosive expansion Fessenheim 1	1	0.4	1	0.4	75000	C
10	Hard rolling on SG hot leg (Gravelines 6)	0.5	2.2	1	1.1	30000	C
11	Hydraulic expansion (Doel 2)	2	0.4	1	0.8	30000	C
12	Small U-bends Vallourec	2	2.2	0.3	1.32	30000	C
13	Small U-bends Westinghouse	2	10	0.3	6	6000	C
14	Sensitive hard rolling on SG hot leg	1	2.2	1	2.2	20000	C
15	Very sensitive hard rolling on SG hot leg	2	2.2	1	4.4	8000	C
16	1300 MW Pressurizer Nozzle	0.5	3.2	3.3	5.28	8000	C
17	Mechanical pluggs	0.5	1	1	0.5	40000	C
18	French CRDM Nozzles	0.5	1.5	0.5	0.4	80000	C
		0.5	1.5	0.5	0.4	26800	C
		1.1	2.8	0.08	0.24	72909	C
		1.1	2.5	0.08	0.22	48427	C
		1.1	2.5	0.08	0.22	58868	C
		1.1	2.5	0.08	0.2	90777	C

*: NC: non cracked; C: cracked.

This model has been useful in ranking the cracking susceptibility of the components and predicting the early cracking. It was employed to rank the different alloy 600 zones and then to rank the different components within the given zone and establish the appropriate surveillance and maintenance strategies. However, Valliant et al. [201] first pointed out the incapability of the Index model to properly assess the components for the strong deleterious effect of complex strain or monotonic strain paths and susceptibility variations between the different specimens tested in similar conditions. De Curieres et al. [202] later confirmed this on their study on comparison between model and experience. Hence, it is considered inefficient for the assessment of life of the components as the model is incomplete.

The main drawback of the Index model is that it is not possible to incorporate any new material parameters into it. It does not give the crack depth (length) associated with time. All the parameters used in Index model are macroscopic whereas the IGSCC is more of a local phenomenon. These findings clearly indicated the need for the improvement of the Index model towards the prediction of the stress corrosion cracking based on the effects of the material history for more quantitative assessment.

2.4.2 Local model

This section provides the detailed description of the local model which is been studied in this thesis. It also discusses a series of phenomena associated with the degradation as well as the main equations for calculating the initiation time and crack growth rates.

Most of the stress corrosion cracking models developed so far and discussed in this chapter describe mainly the possible mechanisms involved for degradation are usually qualitative. However, these models use the same empirical equation in modelling the alloy 600 components [198]. Researchers in EDF developed a numerical approach to predict SCC kinetics and location in 3D because of the operational experience on alloy 600 and to understand the observed in-service cracking of components. It is also important to take into consideration and evaluate the mitigating factors in operating PWRs such as changes in water chemistry (dissolved hydrogen concentration and zinc injection), changing the surface finish of the components (introducing stresses), material compatibility (chromium content) or changes in design of the components in order to reduce the stress concentrations. These mitigating factors are aimed at increasing the lifetime of the components largely. For this, EDF proposed an empirical approach called 'Index model'. It aimed to predict IGSCC of alloy 600 based on two isolated stages of cracking namely, initiation and fast crack growth.

The Index model, which is the quantitative empirical model trying to predict crack initiation and crack growth rates for alloy 600 exposed to primary water PWR conditions, does not describe the possible physical mechanism involved for cracking and hugely lacks accuracy. Index model seems to be more sophisticated and developed with high degree of complexity compared to other existing engineering models to predict SCC, it does have some limitations. The main drawbacks of 'Index model' are as follows:

1. It is difficult to incorporate new material parameters (such as dissolved hydrogen, zinc injection, cold work, and strain path) that are relevant, in order to improve the predictions.

2. There is a lack of association between crack depth and predicted time to initiation. Due to this, the link between initiation stage and fast crack growth stage is only possible if the time to initiation is assumed to be the same time to reach critical stress intensity factor (K_{IGSCC}).

3. All the parameters used in Index model are macroscopic parameters, whereas IGSCC is more of a local phenomenon. Hence, there is an absence of underlying mechanisms involving IGSCC such as incubation, initiation, and crack growth.

All these limitations clearly indicated the need for improvement of the Index model towards prediction of stress corrosion cracking based on the effects of the material history for a more quantitative assessment. Couvant et al. [203–205] felt the need for addressing these issues and proposed a more reliable engineering model to predict crack initiation, crack growth rate and intergranular oxidation kinetics. It is called Local model, as it considers IGSCC as a local phenomenon happening at the grain boundaries and takes into account all the microscopic parameters. Unlike other models discussed which mainly concentrates on the mechanisms involved in crack propagation, the authors also recognised the need to study crack initiation behaviour as they felt that initiation is the first step towards component failure.

2.4.2.1 Theory and Assumptions

Local model relies primarily on the cracking scenario and local parameters. When there is no crack present the term local refers to the grain boundaries where the degradation happens[205]. This occurs mainly during the incubation and initiation stage as illustrated in *Figure 40* . Once the crack occurs, the term local refers to the intergranular crack tip.

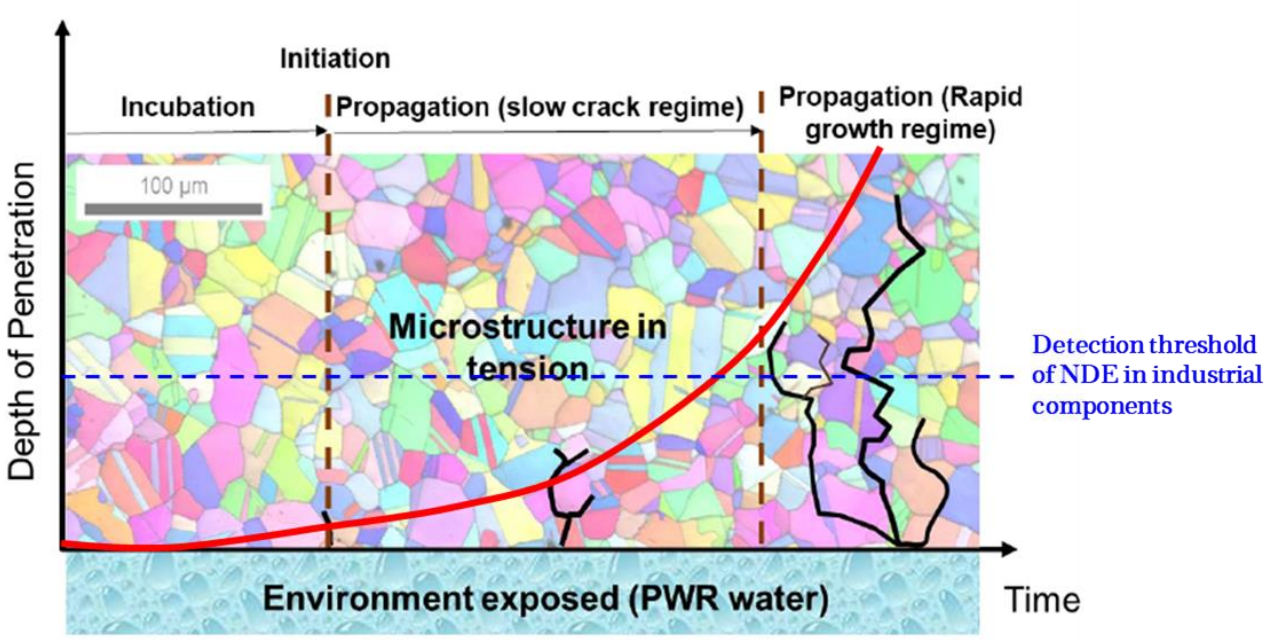


Figure 40: Schematic of various stages and levels of degradation considered in Local model (note: the cracks shown in the *Figure* are more likely to be intergranular).

The model scenario of cracking is based on the following assumptions [203]:

Incubation: The assumption is that once the material is exposed to the primary water environment the oxidation of the grain boundaries takes place and this oxidation strongly decreases the local stress to failure of the grain boundaries. This is given by the intergranular oxidation rate kinetics and for alloy 600 it depends on temperature, dissolved hydrogen in the primary water and grain boundary coverage of the material. All these parameters once combined give the time necessary to reach a critical oxidation depth.

Initiation: The assumption is that once the critical depth of oxidation (p_{oxc}) is reached, a critical stress to fail called as local stress (σ_c) is reached to cause the initiation of the crack.

Crack extension: Once the crack is initiated, crack propagation is governed by sigmoidal crack extension law to reach the slow crack growth rate (CGR) and then transits into fast crack growth rate (CGR). *Figure* 41 presents all the parameters used in the local model.

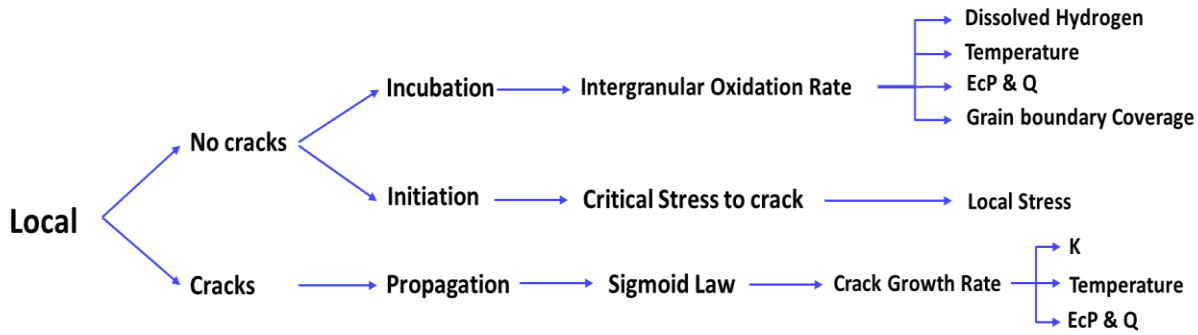


Figure 41: Parameters used in Local Model based on [203–206].

Theoretically, the Local Model seems to be the most reliable in terms of prediction of crack initiation and evolution of crack depth over time. Though it considers all the microscopic parameters and has room to incorporate new parameters into the equation, it is necessary for any engineering model to be experimentally validated. The main objective of this thesis is to experimentally validate the Local Model, better calibrate it and identify areas that can be improved, so that the usage of this model can be extended to all the other alloy types. In the following section, the details of the various parameters used in the local model, their influence on the prediction and the strategy used for experimentally validating the local model are described.

2.4.3 Intergranular Oxidation kinetics

The intergranular oxidation rate is the combination of the oxidation of three phases in a grain boundary which are:

- A grain boundary with a chromium nominal content referred to as ‘nom’ phase where the average level of chromium is present in the material (16.3% in case of alloy 600). This average value is from the matrix, where there are no carbide precipates formed.

- An intergranular chromium rich phase referred to as ‘carb’ phase where the chromium rich carbides are present. This value is quantified by the grain boundary coverage with chromium carbides.
- A chromium depleted grain boundary phase (close to the carbide precipitate regions) referred to as ‘depl’ phase where the chromium carbide precipitation causes local depletion in level of chromium.

For each of these phases i, the maximum oxidation depth p_i (in nm) is assumed to have a logarithmic dependency to the time t (hours) of exposure to primary water and is given by equation (13):

$$p_i = x_i + \frac{1}{b_i}\ln(1 + C_i \times t) \times g(\Delta EcP) \times \exp\left(\frac{-oxQ}{R \times T}\right) \dots\dots\dots\dots (13)$$

where, p_i depends on dissolved hydrogen (DH) content in primary water and is given by the term $g(\Delta EcP)$, ΔEcP refers to the potential difference of the electrochemical potential of the alloy, EcP, and the potential of the Ni/NiO transition, $EcP_{Ni/NiO}$. Lastly, p_i depends on temperature and is given by the term $\exp\left(\frac{-oxQ}{R \times T}\right)$ where oxQ refers to the activation energy in J/mol.

$$g(\Delta EcP) = oxg_1 + oxg_2 \times exp(-oxg_3 \times \Delta EcP) \dots\dots\dots (14)$$

$$\Delta EcP = 1000 \times \frac{R \times T}{2 \times F} \times \ln\left(\frac{DH}{DH_{N_i/N_iO}}\right) \dots\dots\dots\dots (15)$$

where, F = 96500 C. mol^{-1}, T is the temperature (in K) and DH_{N_i/N_iO} is the hydrogen content in Ni/NiO equilibrium (ml/kg). oxg_1, oxg_2 and oxg_3 are oxidation constants.

The oxidation rate is calculated as follows:

1. Random sampling of the 3 phases with given grain boundary properties such as grain boundary coverage (GBC), mean size of the chromium carbides (r_c x 2) and mean length of the chromium depletion zone (z_{cr}) with each chromium carbide.

2. Discretization of total grain boundary length in segments of 1 mm.

3. Incremental calculation time to oxidize the discretized grain boundary as;

a) The time to oxidize the grain boundary portion composed of a given phase with oxidation kinetics of the same phase.

b) When the oxidation front reaches the new phase at a depth p (transition from phase i to j), the new oxidation rate is the oxidation kinetics of phase j for p, assuming that the formed oxides are similar irrespective of the phase in which they grow. A direct transition between the kinetics is assumed as soon as the oxide front meets a new phase.

Using all these criteria, in the previous works of Couvant [113,203] and Wehbi [204], they simulated the oxidation process of the three phases. *Figure* 42 illustrates the kinetics of oxidation following nominal Cr phase, Cr carbide phase and Cr depleted phase and are given in blue, green and red respectively. The random grain boundary, including one Cr carbide and two associated depleted areas is shown on the right. The simulated oxidation rate along the grain boundary is the dark curve: it matches first with the oxide growth rate of the nominal Cr phase, following which a short increase in oxidation rate is experienced when the oxidation reaches the chromium-depleted zone, until the oxide front reaches the Cr carbide. This last transition is followed by a large decrease in oxidation rate.

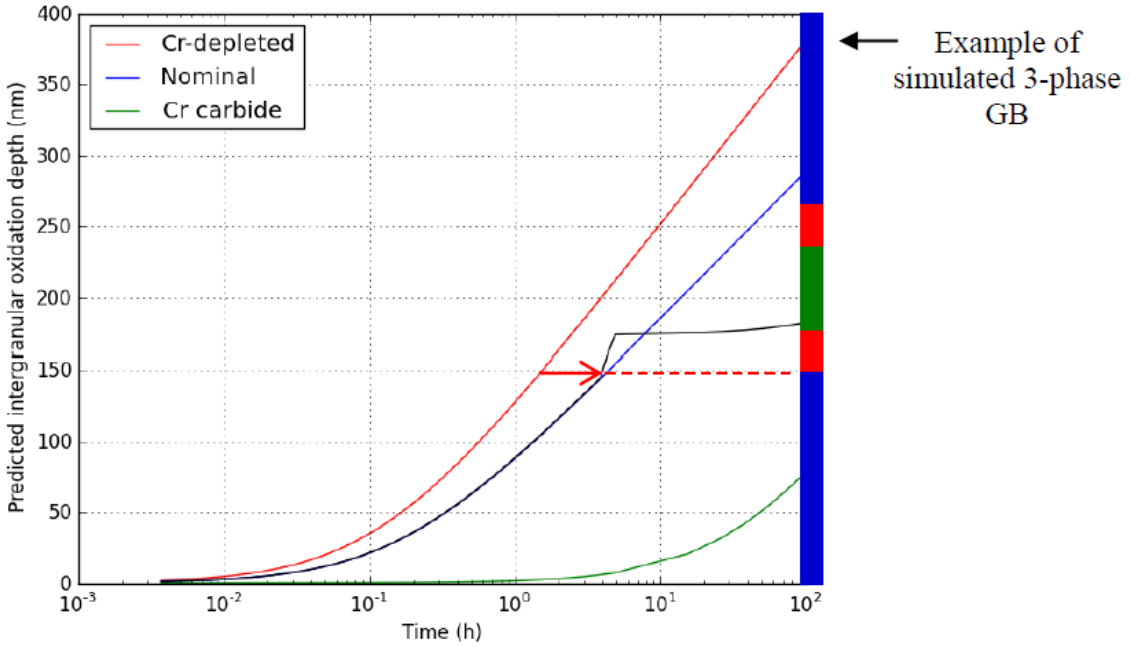


Figure 42: Simulated oxide growth (dark curve) along a grain boundary (on the right) with Cr carbide (green portion) surrounded with two Cr-depleted zones (red portions). The blue portions correspond to a nominal Cr content. The red arrow illustrates the change in oxidation rate as soon as the intergranular oxidation front reaches the first interface (nominal/depleted). The change corresponds to the simple shift in time of the oxidation kinetics along the depleted phase up to the current time. Oxidation rates given at 320°C with DH = 30 ml.kg-1 water [203].

With this approach, Couvant et.al. [205] calibrated b_{nom}, b_{depl} and b_{carb} values for alloy 600 as 3.14 $x10^{-15}$ nm^{-1}, 2.42 $x10^{-15}$ nm^{-1} and 4 $x10^{-14}$ nm^{-1} respectively. The C_{nom}, C_{depl} and C_{carb} values are calibrated as 3.35 h^{-1}, 0.1 h^{-1} and 1 h^{-1}.

2.4.4 Criteria for Initiation

Initiation is referred to as the failure (rupture) of an oxidized grain boundary. It is assumed to occur when both of the following conditions are reached:

1. A grain boundary is sufficiently oxidised: the oxidation depth is deeper than the critical oxidation depth (p_c) based on the evaluation from intergranular oxidation.
2. When the local stress experienced by the grain boundary is higher than the critical opening stress (σ_c) to fail an oxidized grain boundary.

If these two conditions are satisfied, then the initiation occurs. Once the initiation occurs, sigmoidal crack extension law now controls the crack propagation.

2.4.5 Crack growth

The local model is integrated into Code_Coriolis which is a numerical tool developed by EDF. To establish a link between initiation and crack growth regime, the crack growth rate is assumed to have a sigmoidal dependence to stress intensity factor (K). This kind of dependency allows considering both slow and fast crack growth regimes. The numerical tool allows choosing between the three sigmoidal crack extension laws [207] namely:

1. cgr_sigmoid
2. cgr_sigmoid_cw1
3. cgr_sigmoid_cw2_h

which will be explained next.

2.4.5.1 cgr_sigmoid

In this crack extension model, the maximum crack growth rate is given by the sigmoidal dependence on the stress intensity factor (K) and effect of temperature (T). This is given by the following equation (16):

$$cgr = cgr1 \times f(K) \times exp\left(\frac{-cgr5}{R \times T}\right) \dots\dots\dots\dots (16)$$

where,

$$f(K) = \frac{K^{cgr2}}{1 + \exp[\,-cgr3\ \times (K - cgr4)]} \dots\dots\dots\dots . (17)$$

The parameters cgr1, cgr2, cgr3, cgr4 are constants obtained from analytical function to K and cgr5 depends on the activation energy and they control the shape of the maximum crack depth vs time curve. K is the stress intensity factor of total deformation and R is the gas constant (R = 8.3144621 J mol^{-1} K^{-1}).

2.4.5.2 cgr_sigmoid_cw1

In this crack extension model, the maximum crack growth is given by the sigmoidal dependence on the stress intensity factor (K), total plastic deformation (ε_t) and temperature (T). This is given by the following equation (18):

$$cgr = cgr1 \times f(K) \times g(\varepsilon) \times exp\left(\frac{-cgr9}{R \times T}\right) \dots\dots\dots\dots (18)$$

where,

$$f(K) = \frac{K^{cgr2}}{1 + \exp[-cgr3 \times (K - cgr4)]} \dots\dots\dots\dots (19)$$

$$g(\varepsilon) = \frac{(\varepsilon + |cgr8|)^{cgr5}}{1 + \exp[-cgr6 \times (\varepsilon + |cgr8| - cgr7)]} \dots\dots\dots.. (20)$$

The parameters cgr1, cgr2, cgr3, cgr4, are constants obtained from analytical function to K cgr5, cgr6, cgr7 and cgr8 are constants obtained by homogenous work hardening before loading and cgr9 represents the activation energy. K is the stress intensity factor of total deformation and R is the gas constant (R = 8.3144621 J mol^{-1} K^{-1}). These values are calibrated for alloy 600 and provided by EDF [207].

2.4.5.3 cgr_sigmoid_cw2_h

In this crack extension model, the maximum crack growth rate is given by the sigmoidal dependence on the stress intensity factor (K), potential difference (ΔEcP), total plastic deformation (ε_t) and temperature (T). This is given by the following equation (21):

$$cgr = cgr1 \times f(K) \times g(\varepsilon) \times h(\Delta EcP) \times exp\left(\frac{-cgr11}{R \times T}\right) \ldots\ldots\ldots\ldots (22)$$

where,

$$f(K) = \frac{K^{cgr2}}{1 + \exp[-cgr3 \times (K - cgr4)]} \ldots\ldots\ldots\ldots (23)$$

$$g(\varepsilon) = 1 + cgr5 \times (\varepsilon + |cgr7|) + cgr6 \times (\varepsilon + |cgr7|)^2 \ldots\ldots\ldots\ldots (24)$$

$$h(\Delta EcP) = 1 + cgr8 \times exp\left(\frac{-1}{2}\left(\frac{\Delta EcP + cgr9}{cgr10}\right)^2\right) \ldots\ldots\ldots\ldots (25)$$

$$\Delta EcP = 1000 \times \frac{R \times T}{2 \times F} \times \ln\left(\frac{DH}{DH_{N_i/N_iO}}\right) \ldots\ldots\ldots\ldots (26)$$

$$DH_{N_i/N_iO} = ecp1 \times \exp(ecp2 \times T) \ldots\ldots\ldots\ldots (27)$$

The parameters cgr1, cgr2, cgr3, cgr4 are constants obtained from analytical function of K, cgr5, cgr6 & cgr7 are constants obtained by homogenous work hardening before loading and are calculated by code_aster, cgr8, cgr9 and cgr10 are constants obtained from the pourbaix diagram for different potentials of Ni/NiO equilibrium and cgr11 represents the activation energy. K is the stress intensity factor of total deformation and R is the gas constant (R = 8.3144621 J mol^{-1} K^{-1}).

The numerical tools developed by EDF provides finite element post analysis allowing to simulate SCC. Using these numerical tools, it is possible to generate global and aggregate meshes for testing. The local model along with the crack extension models are integrated to Code_Coriolis platform. This allows a proper transition between the initiation and crack growth regimes (slow and fast). The SCC crack growth computation involves an algorithm, which is explained in the following section.

2.5 Numerical Tools

In order to generate a global mesh for testing, visualizing and performing post analysis on both aggregate and global sample datasets three numerical simulation tools have been used: Salome Meca, Code_Aster and Code_Coriolis.

2.5.1 Salome Meca

The simulation needs are growing, both on the fidelity of numerical modelling of the physical problem (calculation codes) and on the implementation in interactive environments allowing to build datasets (Pre-Processor) and interpret the results (Post-Processor). On the other hand, developments in coming for engineering issues will increasingly involve multi-physical couplings. Salome Meca is a platform dedicated to mechanical simulation. It provides a software environment making it possible to carry put the complete chain of computer aided designing (CAD), calculation, meshing and visualization of results.

The Salome Meca platform offers the use of Code_Aster in an integrated platform presenting pre and post-processing modules; allowing the easy construction of business tools linking the production of geometries and parametric meshes with Code_Aster calculation sequences predefined and offer the community of mechanics access to all its simulation needs, beyond Code_Aster, in a unique and homogeneous environment. Salome Meca is therefore an ideal receptacle for the construction of chaining/coupling diagrams of codes, for example with Code_Saturne for thermo-hydraulics and Code_Coriolis of SCC computation. More details on this can be found in [208].

2.5.2 Code_Aster

Code_Aster is an in-house numerical simulation software developed by EDF for structural analysis. This tool covers a large range of applications: 3D thermal analyses and mechanical analyses in linear and non-linear statics and dynamics, for machines, pressure vessels and civil engineering structures. Beyond the standard functionalities of a FEM software for solid mechanics, Code_Aster compiles specific research in various fields: fatigue, damage, fracture, contact, geo-materials, porous media, multi-physics coupling etc. Justifying quality labels required by nuclear industry, most of the fields of the software have been validated by independent comparisons with analytical or experimental results, benchmarks towards other codes. Moreover, 2000 tests are managed in configuration: they are devoted to elementary qualification. Further details of Code_Aster can be found in [209,210].

2.5.3 Code_Coriolis

Code_Coriolis is a numerical tool developed by EDF to simulate SCC using finite element modelling (FEM) post analysis. The development of new SCC model (local) integrated along with crack extension models in Code_Coriolis platform provides a methodology to easily apply them on selected specimens and PWR components. The multiscale integration takes up during the initialising stage (Pre-processing) where the cracking criterion and stress assignment to grain boundary take place by random sampling of grain boundaries on a particular node in macroscopic specimen. This offers a 3D study of components closer to actual cases than the traditional 1D or 2D approaches. This allows better evaluation and calibration of the SCC model and thereby provides proper transition between initiation and crack propagation at larger scales (nms to cms).

Code_Coriolis follows a three-step algorithm in SCC computation as shown in *Figure* 43. The first step is *Pre-processing*. In this step, the SCC model (for initiation and crack growth) is selected. The model parameters for each material is assigned during this step. The components that are to be tested are first designed and meshed using GEOM and SMESH modules of the Salome Meca numerical platform. This mesh of the component is then subjected to finite element modelling (FEM) using Code_Aster FEM code to obtain the global stress and strain fields. The SCC computation in Code_Coriolis uses the mesh designed for the component and corresponding stress and strain fields obtained from the Code_Aster simulation as input. During this step, the environmental parameters such as the surface in contact with water, dissolved Hydrogen (DH), dissolved Zinc (DZn) and temperature are assigned. The material parameters such as grain boundary coverage (GBC), grain size, size of the carbides (r_c) and size of chromium depletion zone (z_{cr}) are given as input. For using the local model to predict initiation, a grain boundary sampling is fed. The critical local stress (σ_c) is statistically estimated from CPFEM computations performed on polycrystalline aggregate mesh using Code_Aster. The time and maximum crack depth are initialized as zero and criteria to stop the computation is assigned (such as maximum final time and maximum crack depth).

The second step of the algorithm is *SCC Initiation*. During this step, the minimum time to initiate crack on the nodes in contact with water is computed. In case of Local Model, random sampling of stress to each grain boundary and evaluation of initiation criterion for each grain boundary is carried out. For the link to happen and computation to continue into the SCC crack growth regime, the time is assigned as the time to initiation and maximum crack depth is assigned as the critical oxidation depth (p_{oxc}).

The third step of the algorithm is *SCC Growth loop*. During this step, the evaluation of stress intensity factor for assigned maximum crack depth is executed. This is followed by computation of crack extension length, evaluation of K for maximum crack depth + crack

extension length (total crack depth), evaluation of mean crack growth rate (CGR) along the crack extension length and time to crack along crack extension. The SCC computation ends when the computation reaches either the maximum final time or maximum crack depth during the pre-processing step.

Once the SCC computation is completed, it is possible to visualize sites of SCC initiation on the component and the crack path followed by the main crack tip within the model. Thus, kinetics and crack growth paths are predicted along with statistics on initiation time and cracking location. This gives evolution of crack depth to time. The graphical user interface (GUI) along with the required type of input in Code_Coriolis is shown in *Figure* 44.

Figure 43: General algorithm of SCC computation using Code_Coriolis for Local Model adapted from [203].

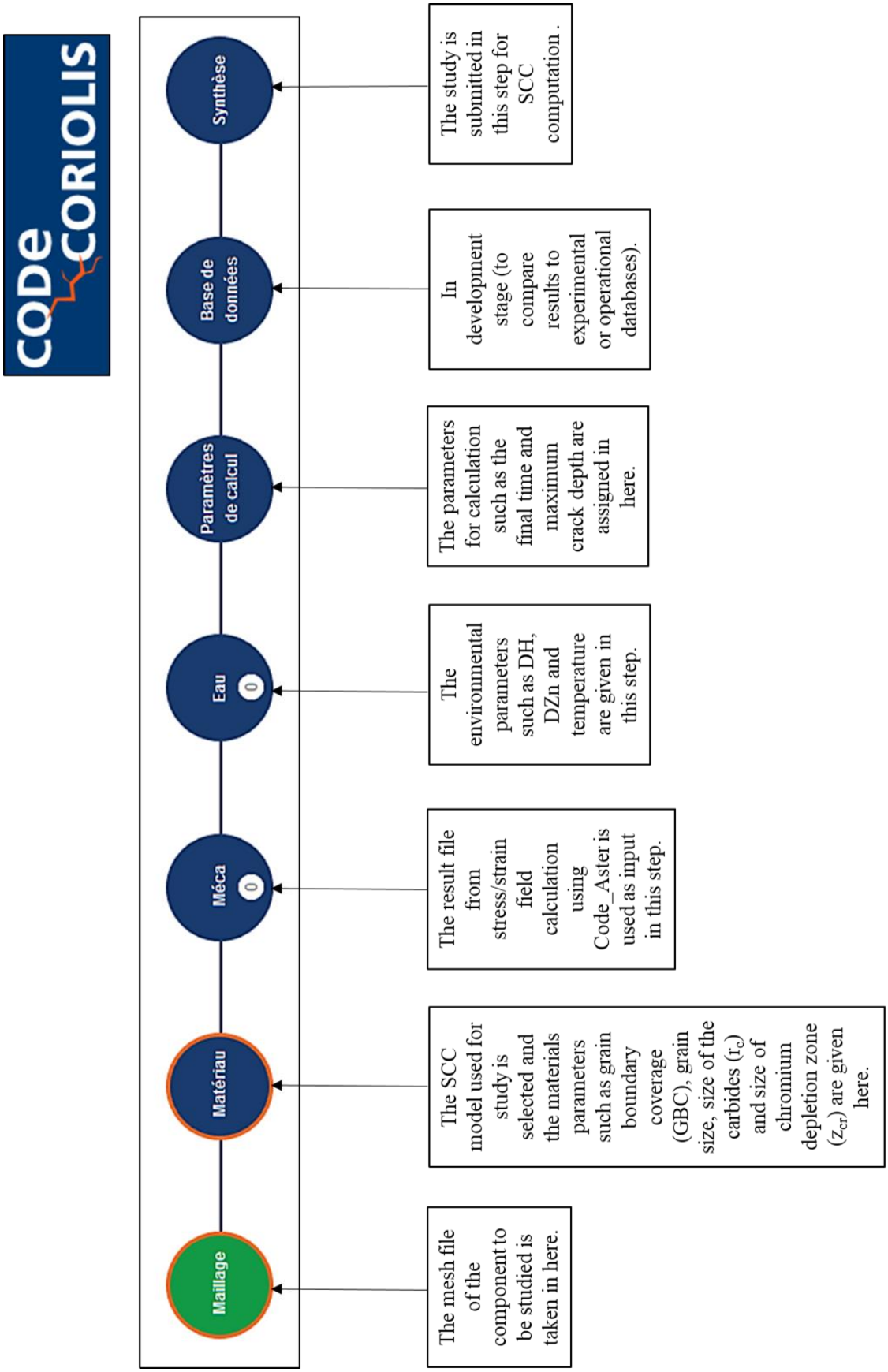


Figure 44: GUI of Code_Coriolis with required type of input at each step.

2.6 Preliminary results on SCC computation

Couvant et al. [206] performed SCC computation on various Alloy 600 heats simulating SCC laboratory scale and component tests. The simulation of an initiation test on Open C-Ring (OCR) specimen designated as 1650-42 (*Figure* 45) cut in Alloy 600 designated as RND-M-B-369 is illustrated. First, stresses at the testing temperature (360°C) were calculated (*Figure* 46), taking into account the prior loading at room temperature. Local model with parameters fitted for Alloy 600 designated as RND-M-B-369 (TT820°C) and CGR sigmoid law with parameters fitted for Alloy 600 (TT820°C) designated as RND-M-B-369 was selected as SCC behaviours. The predicted time to initiation is given in *Figure* 46.

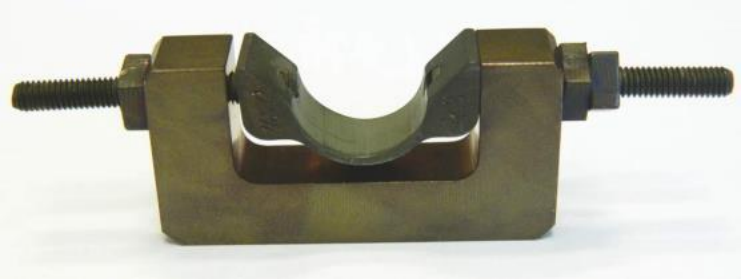


Figure 45: Open C-ring specimen [1650-42].

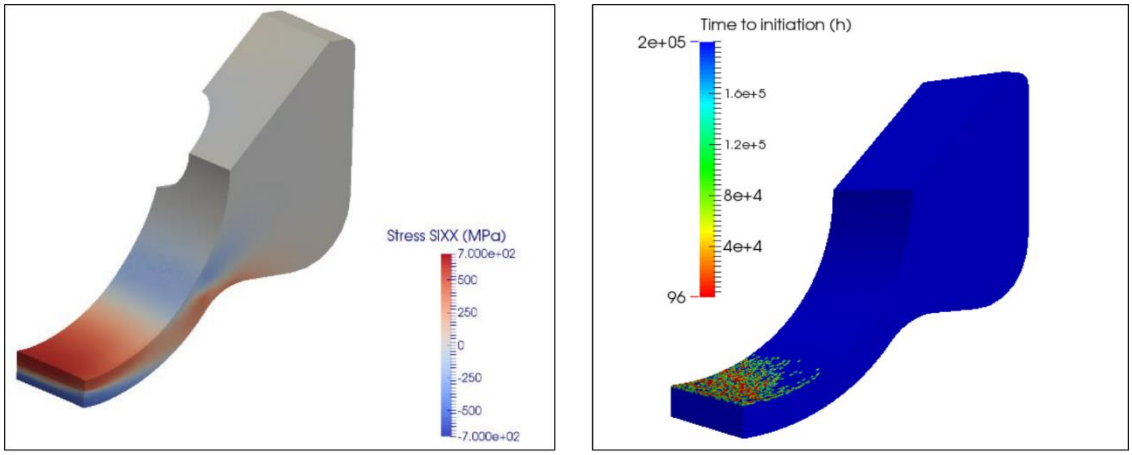


Figure 46: (a) Stress field at the end of the final loading of the OCR designated as 1650-42. (b) Map of the predicted times to initiation (with the local model) at the surface of the specimen designated 1650-42 (Alloy 600) [206].

The parameters used for this study were obtained from the test carried out in an aggressive environment. As a consequence of this, the SCC crack depth observed were much higher than 800 µm. Also, the stresses calculated as reference for local stress was obtained from the microstructure simulated with a polycrystal aggregate with random orientation. As a result, as shown in *Figure* 47, there was a lack of accuracy of the cracking kinetics in the slow crack regime and transition to fast crack regime and in the cracking criteria of oxidized grain boundaries. In the slow crack regime (up to 10 µm), the intergranular oxidation kinetics plays the major role and for the fast crack regime (> 10 µm), the mechanical aspect takes dominance than the oxidation kinetics. Also, the initiation using local model occurred much ahead of the observed SCC initiation.

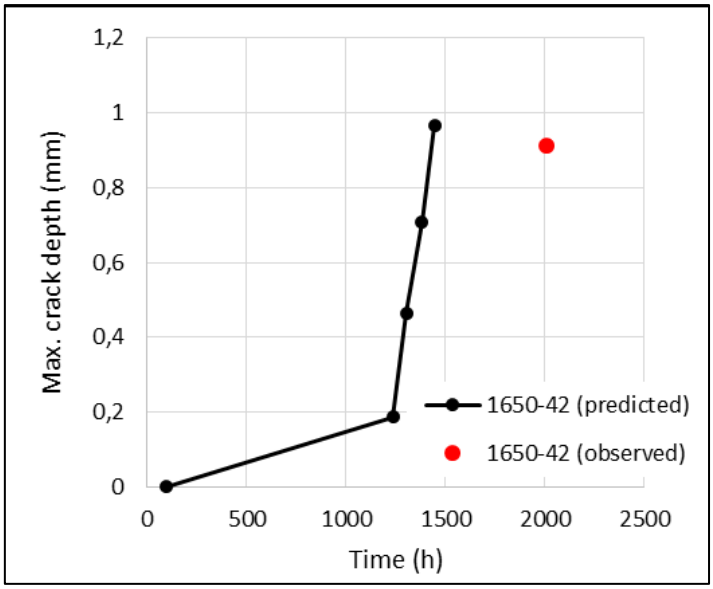


Figure 47: Comparison between predicted (with the local model) SCC kinetics of the specimen designated 1650-42 (Alloy 600) and observed final SCC depth [206].

Thus, these discrepancies and inconsistencies between SCC prediction and real components demand a solid systematic strategy in order to validate, evaluate and optimize the local model. Once the model is calibrated and validated for Alloy 600, it can be expanded to other alloy systems. The strategy used in this thesis to validate the local model is discussed in the following section.

2.7 Strategy for Validation

The comprehensive approach of the Local Model to predict crack initiation and evolution of crack depth over time should make it the most reliable. It also considers all the microscopic parameters and has room to incorporate new parameters into the equation. However, it is necessary for any engineering model to be experimentally validated before it is used on real components. The strategy for validation used in this work is described as follows and the schematic presentation is given in *Figure* 48:

Step 1 – Pre-characterization: Prior to subjecting the as-received alloy 600 to SCC tests, pre-characterization is carried out to obtain few input parameters such as grain size, grain boundary coverage (GBC), size of carbides (r_c) and size of chromium depletion (Z_{Cr}). The grain size and grain boundary types are obtained using EBSD analysis, the size of the carbides is measured using TEM and SEM.

Step 2 – SCC laboratory test: The sample was cut in the form of beams (60mm x10mm x7 mm) that were subjected to SCC test in autoclave with primary water conditions (DH= 30 ml $H_2.kg^{-1}$ water) at 345 °C. The tests were carried out for three different durations – 325 hours, 800 hours and 2000 hours and the samples subjected to a constant load of 5500 N (20% above yield stress) using four-point bend test. The load was applied by displacing the central rods by 1mm. The goal of performing these SCC tests at different test durations and same stress level is to make sure cracks are initiated in the susceptible grain boundaries, obtain the crack depth data and perform statistical assessment on this data. Finally, combine the test results, determine the average crack growth rate, and compare with the prediction of the model.

Step 3 – Global FEM simulation: The simulation of SCC test is the better way to calibrate the model. In this case, the four-point bend test is modelled using GEOM and SMESH modules in Salome Meca numerical platform [209] and finite element modelling (FEM) simulations are performed on them using Code_Aster tool [209] using the exact autoclave loading conditions. The goal of this step is to obtain the global stress and strain fields and use them as input to SCC computation in Code_Coriolis which will be then be chained with local stress.

Step 4 – 3D EBSD: Extraction of volume of interest after autoclave exposure by performing sequential sectioning of volume of interest, including imaging and EBSD mapping will obtain the 3D description of grain morphologies and crystallographic orientations. The goal of this step is to obtain the set of parameters to perform simulation to evaluate the local stress

concentration at the grain boundaries. This will facilitate the correlation of local stresses and crack initiation sites of predicted and observed cases.

Step 5 – Evaluation of local stress: The 3D aggregate obtained from 3D EBSD is converted into a mesh to perform crystal plasticity finite element modelling (CPFEM) simulation using Code_Aster. This is to obtain the stress concentration on the grain boundaries. The goal of this step is to statistically determine the local stress required for initiation by comparing with the experimental crack grain boundary fraction and use it as input for SCC computation in Code_Coriolis.

Step 6 – SCC computation: All the parameters obtained in the earlier steps are fed into the GUI of Code_Coriolis with Local model and SCC computation is carried out. The goal of this step is to obtain the predicted time to initiation, sites of crack initiation, maximum crack growth rate, evolution of crack depth with respect to time, evolution of stress intensity factor etc.

Step 7 – Validation and optimization: The goal of this step is to correlate the prediction with observed SCC tests to identify the limitations and rank the driving parameters and optimize it. This will provide better calibration for the model.

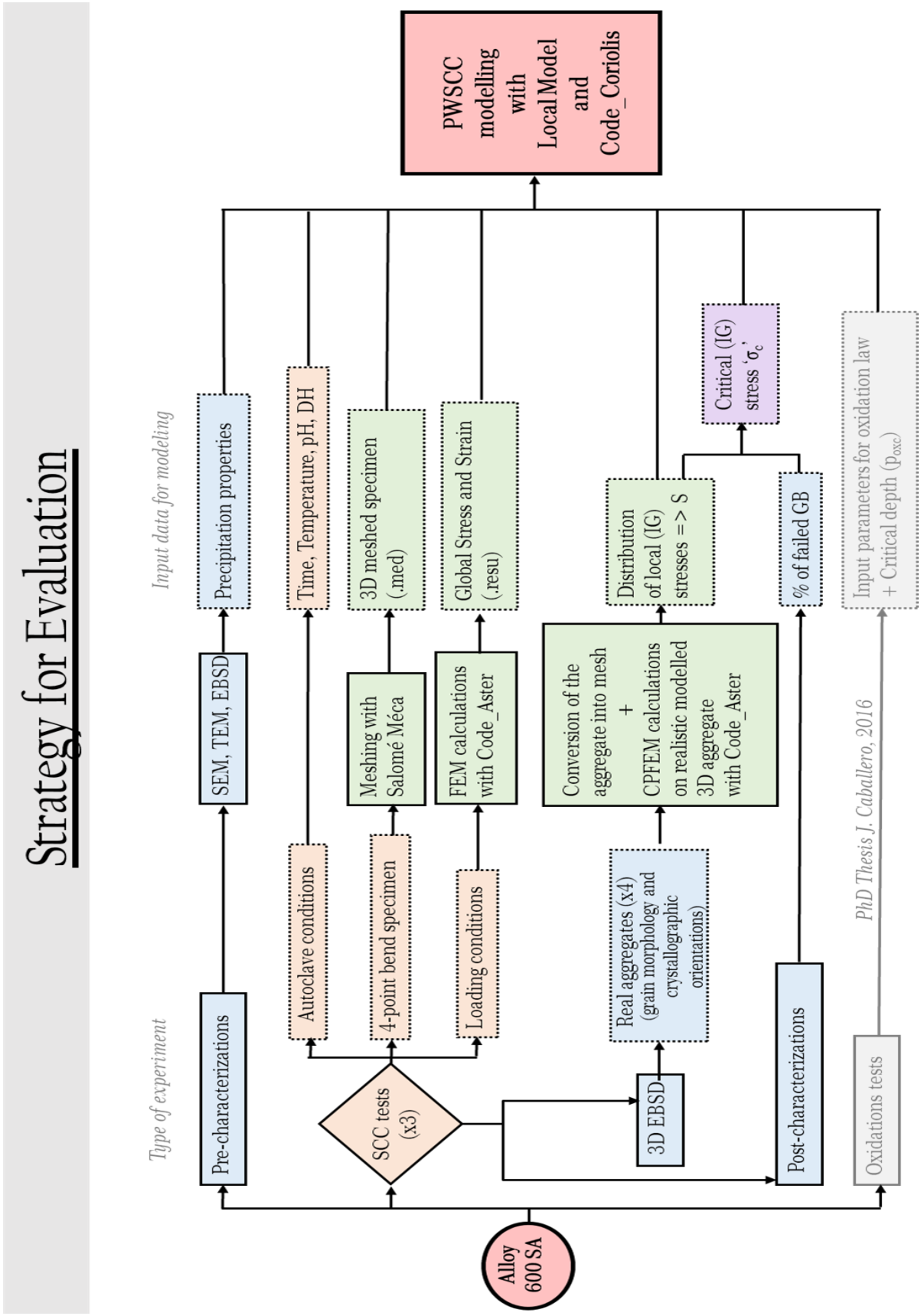


Figure 48: Schematic representation of the strategy for validation of Local model devised in this thesis.

2.8 Summary

The main conclusions coming from the detailed literature review on the influencing parameters and models are discussed and summarised in this section.

The Nickel and Chromium content has a huge impact on the IGSCC susceptibility. The alloys with Ni-content in the range between 20 – 65% exhibit a very high resistance to SCC. Hence, alloy 600 which has a Ni- content > 65% is highly susceptible to SCC. When comes to Cr-content, the resistance to SCC in alloy 600, proportionally increases as the chromium concentration increases from 3 -17%. The maximum susceptibility to SCC is observed for alloys with 5 -10 % Cr.

The carbon and carbide distribution plays an important role in affecting the SCC susceptibility. For alloys with 0.01 – 0.05% carbon content in the temperature range of 325°C to 360°C exhibited an increase in SCC crack initiation activation energy with increase in carbon content. As the alloy is thermally treated, the effect of carbon content is usually related to carbide precipitation and distribution. There are two different types of carbide precipitates in austenitic alloys, $M_{23}C_6$ or M_7C_3 type. The most predominant carbide precipitate type in alloy 600 is M_7C_3 type with M being chromium as alloy 600 is rich in Cr. These precipitates can be either intergranular or intragranular or both. The intergranular carbide distribution improved SCC resistance whereas intragranular carbide made alloy 600 more susceptible.

The grain boundary type have a crucial role in the distribution of the stress intensity along the grain boundaries and usually depends on the orientation of the neighbouring crystals. The CSL grain boundaries with $\sum < 29$ exhibited better resistance to SCC with $\sum 3$ grain boundary (annealed twin boundaries) showed higher resistance. The boundaries with $\sum > 29$, called as random high angle grain boundaries (RHAGBs) exhibited higher susceptibility to SCC.

The cold work and strain have shown to induce SCC susceptibility in austenitic alloys especially in primary water PWR conditions. The deformation of the austenitic alloys and microstructural heterogeneity can be linked to SCC initiation. This is observed by the evidences of enhanced oxidation along the deformation bands, crack initiation between grains with strain mismatch mainly due to the orientation, formation of cracks due to the intersection of shear bands with the grain boundary. There is evidence that strain path (macroscopic strain heterogeneity) also influences the SCC behaviour with the correlation between the rolling direction and the preferred crack initiation and propagation path. However, the complex strain paths induce higher stress concentration along grain boundaries, thus promoting IGSCC due to stress localization.

SCC increases with increasing stress, the stress intensity factor (K) describes the stress state at the crack tip caused by applied stress. As, SCC is microscopic phenomenon, it is difficult to differentiate the crack initiation and crack propagation time with respect to the macroscopic applied stress.

The best attribute of the Film rupture model is that it is experimental and combines a theoretical approach with data fitting. This model has been successfully employed to predict crack growth rates in both BWR and PWR environments but the crucial lack of experimental support for important things such as potential dependence, temperature, sensitisation tends to discriminate against this model.

The corrosion enhanced plasticity model was initially developed for transgranular cracking and was later extended to cracking of grain boundaries favourably oriented vs crack tip. However, the CEPM so far misses important input that could explain the implementation from trans to intergranular (such as obstacles capable of creating dislocations pile-ups). The critical point to

assess the corrosion enhanced plasticity model remains the evaluation of the hydrogen activity at the metal/oxide interface.

The internal oxidation model explains most of the known major thermodynamic and kinetic trends observed experimentally. The incubation time, continuous IGSCC mechanism between sub-cooled water and superheated steam, influence of carbon content and microstructure, and activation energy range all support an internal oxidation process. The stress and temperature dependency, even though not specific to an oxidation process, are consistent with the IO model. A similar remark can be made for the effect of potential which is unclear although similar to other cases of internal oxidation.

An engineering model called Index model was proposed by EDF, based on the system of material indices I_m in order to assess the alloy 600 component life. The most influencing parameter is the temperature as IGSCC in alloy 600 is a thermally activated phenomenon based on the Arrhenius equation dependency. EDF used 180kJ/mol for crack initiation and 130kJ/mol for crack propagation as the apparent activation energy [31,196]. To address for the applied stress a power to the fourth is consistent with creep based processes or processes combining parabolic diffusion kinetics with stress intensity threshold for cracking was used.

This model has been useful in ranking the cracking susceptibility of the components and predicting the early cracking. It was employed to rank the different alloy 600 zones and then to rank the different components within the given zone and establish the appropriate surveillance and maintenance strategies.

The main drawback of the Index model is that it is not possible to incorporate any new material parameters into it. It does not give the crack depth (length) associated with time. All the parameters used in Index model are macroscopic whereas the IGSCC is more of a local phenomenon. These findings clearly indicated the need for the improvement of the Index model

towards the prediction of the stress corrosion cracking based on the effects of the material history for more quantitative assessment.

To overcome the lack of accuracy of Index model and to predict the crack initiation, crack growth and intergranular oxidation kinetics, the Local model was proposed by EDF. The main objective of this thesis is to experimentally calibrate the Local Model predictions, so that the usage of this model can be extended to all the other alloy types. Local model relies primarily on the cracking scenario and local parameters. The failure of an oxidized grain boundary is assumed to be possible as soon as the both of the following conditions are satisfied: (1) a grain boundary is sufficiently oxidized (i.e., the oxidation depth is deeper than the critical oxidation depth, p_{oxc}) (2) the local stress experienced by the grain boundary is higher than the critical opening stress (σ_c). Once initiated, the crack propagation is governed by sigmoidal crack extension law. The details of various parameters used in the local model, their influence on prediction and the strategy used for experimentally validating the local model are important.

The local stress concentration at the grain boundaries are evaluated using CPFEM computation on 3D aggregate mesh. The stress levels are usually observed to be higher in the grain boundaries, hence in local model the tail of the Gaussian stress distribution is assumed to be responsible for initiation. Initiation is assumed to occur when grain boundary is sufficiently oxidised, and the local stress experienced by the grain boundary is higher than the critical opening stress (σ_c).

The strategy for validation employed in this thesis involves Pre-characterization, SCC laboratory test, Global FEM simulation, 3D EBSD and evaluation of local stress concentration followed by SCC computation in Code_Coriolis and validation.

3 EXPERIMENTAL METHODS

As discussed in the previous chapter, SCC in Ni-based alloys is a diverse phenomenon that occurs in various combinations of materials and environment under different external mechanical conditions. To have a better understanding of SCC, a thorough investigation of grain boundaries and crack area in the sample across different length scales – from millimetres to nanometres is required. For this multiscale approach, a range of complementary microscopy techniques have been used in this thesis. This chapter introduces each microscopy technique and their associated sample preparation techniques. The main techniques used in this work are Scanning electron microscopy (SEM), Focused Ion Beam (FIB), Electron Back Scattered Diffraction (EBSD), Transmission Kikuchi Diffraction (TKD) and 3D Electron Back Scattered Diffraction (3D EBSD).

3.1 Scanning Electron Microscopy (SEM)

Scanning electron microscope (SEM) uses a highly focused electron beam with an accelerating voltage between 5 to 30kV to scan over the sample surface [211]. The primary electron beam on interacting with the sample leads to different types of interactions between electrons and the solid such as; (a) elastic large-angle scattering, interaction with the nucleus of the target solid atoms, including the backscattering; inelastic scattering. The inelastic scattering causes plasmon excitation, electron-electron binary collisions and ionization [212]. Most of the SEM images used in this thesis were obtained using a dual beam Carl Zeiss Crossbeam 540 FEG SEM equipped with Oxford Instruments EDX detector and EBSD system. As illustrated in the *Figure* 49, the SEM column typically comprises of the electron source, double condenser lens, objective lens, deflection/astigmatism unit and a series of apertures. *Figure* 50 shows the schematic cross section of the interaction volume in XZ plane of the bulk sample under the

impact of the electron beam and various signals coming out for imaging at different positions of the interaction volume.

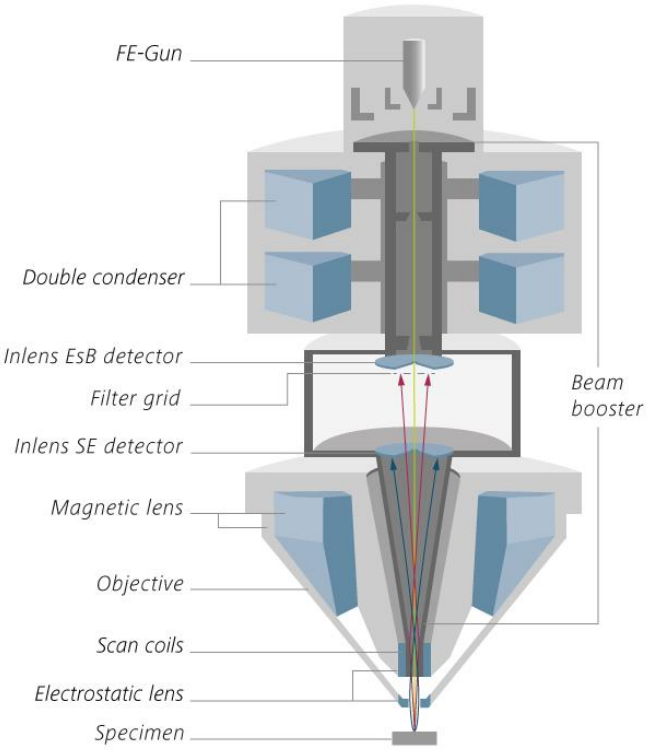


Figure 49: Schematic of Zeiss Crossbeam 540 electron beam column (courtesy by Carl Zeiss Company) [213].

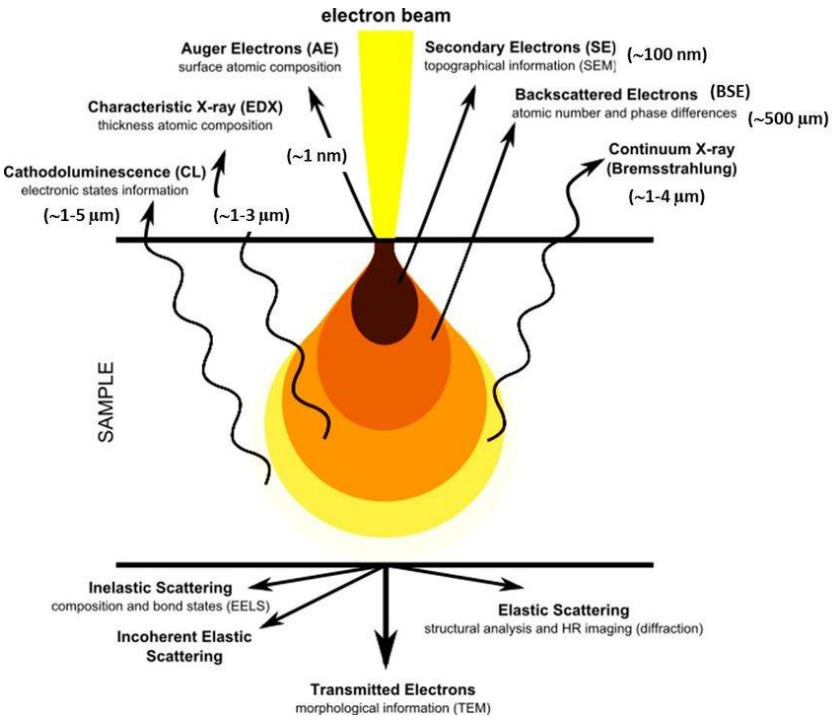


Figure 50: Schematic of interactions between electron beam and sample adapted from [211].

Figure 51 shows the energy distribution of the electrons emitted from the sample surface after interaction. The SEMs were used for identifying cracked grain boundary and intergranular carbide coverage. One example is presented in *Figure 52.*

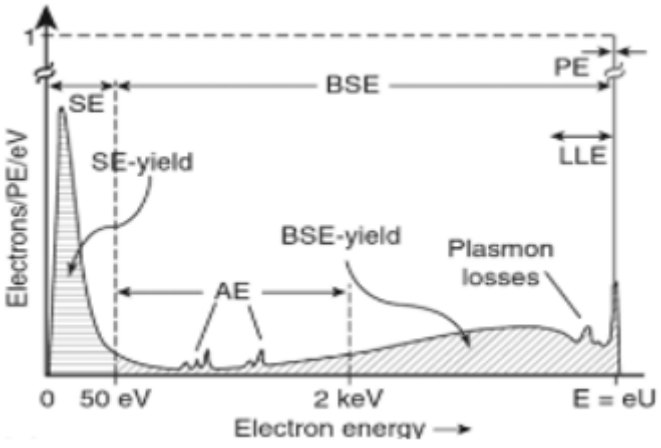


Figure 51: Energy distribution of electrons after interaction [212].

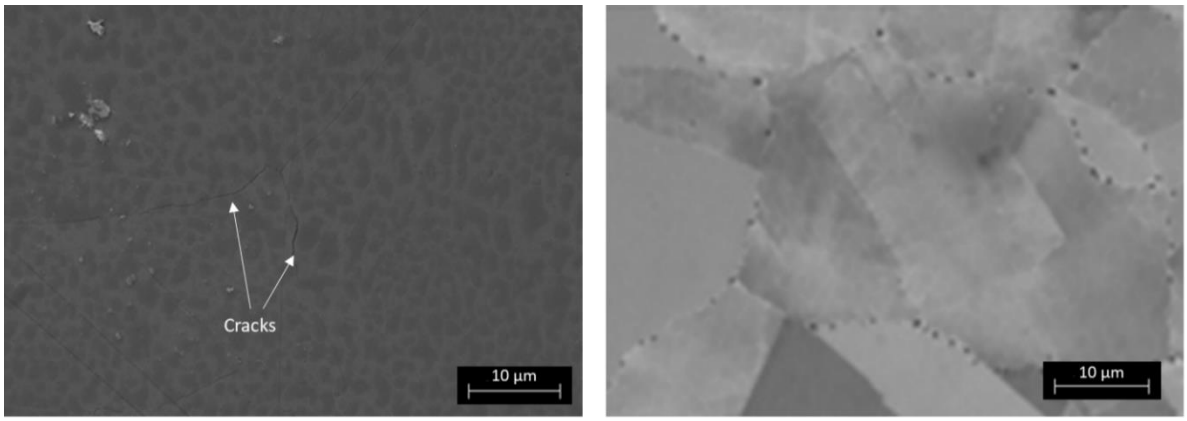


Figure 52: Preliminary examination of cracks and intergranular carbides using SEM; (a) SE image (b) Backscattered (BSE) image using Zeiss Crossbeam 540.

3.2 Focused Ion Beam (FIB)

The Focused Ion Beam (FIB) is very similar to SEMs, but instead of using electrons FIB uses Ga^+ ions to image. From the ion source, Ga^+ ions are accelerated down the FIB column and it is focused to a very small point on the sample. There are various types of ions sources; the most common one is Liquid Metal Ion Sources (LMIS). In order for the ion beam to be used, the samples must be highly compatible with high vacuum to prevent any kind of contamination [214]. The LMIS gives an advantage of smaller probe sputtering and its emission area is very small approximately 10 nm and the intensity is around 105 A/cm^2. The most commonly used LMIS is Ga^+, as it has a very low melting point, good vacuum and mechanical properties [214][215]. The schematic image of the dual beam SEM-FIB column is presented in *Figure 53.* The emission current of the source is usually 2.1 µA. Once the beam is generated, it goes down through the column and an aperture controls the beam current. The beam is then focused on the sample surface and astigmatism is corrected through the electrostatic lens unlike

magnetic lens used in SEM [214][215]. FIB has various applications such as lithography, milling, deposition, TEM sample preparation and serial sectioning etc.

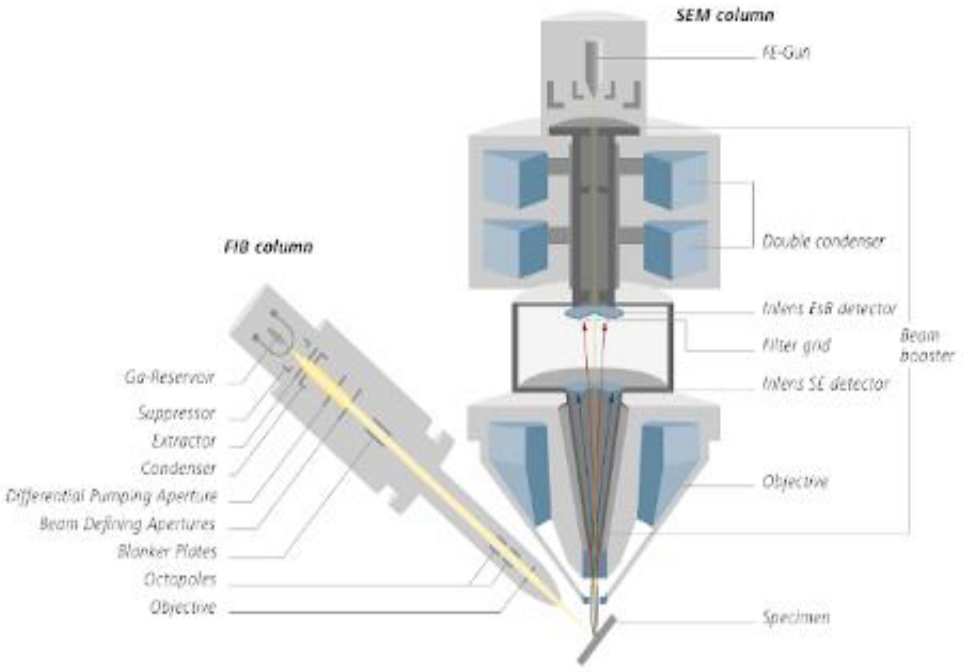


Figure 53: Schematic of dual beam SEM-FIB column in Zeiss Crossbeam 540 (courtesy Carl Zeiss Company) [213].

A dual beam system, Zeiss Cross Beam 540 was mainly used during this thesis. This equipment is fitted with an electron gun and Ga^+ source. The stage is five axis eucentric, meaning it can be used to tilt, rotate or move the sample in the x, y and z directions. The SEM operates between 100 V to 30 kV and has a resolution of 1.1 nm at 20 kV. The FIB operates between 1 kV and 30 kV with milling apertures from 1 pA to 100 nA. The system is fitted with the gas injection system (GIS) with W, Pt, C, Au to perform the deposition. In addition to GIS, the system has Kleindiek micromanipulator to perform in-situ TEM foil liftouts. It is necessary to prepare electron transparent TEM foils for high-resolution characterization of SCC crack tips and other site specific regions [44,54]. This system can be used for complex milling because the specimen can be imaged in real time using the SEM beam. As most of the phenomena related

to SCC occur in 3D, it is necessary to have a realistic observation in 3D. A new approach of 3D characterization technique has been lately used and reported [103,216]. The FIB 3D serial sectioning can be used to acquire 3D information around the SCC crack tips and grain boundaries. The TEM sample preparation and FIB 3D serial sectioning were performed using this equipment.

3.2.1 TEM/TKD sample preparation

Traditionally TEM samples were prepared by mechanical grinding, ion-beam milling or electro-polishing. With the development of FIB, the TEM samples were carefully milled out from specific small regions without any major change to their microstructure or chemistry. The TEM samples can be produced from two orientations depending on the feature for investigation [217]. (1) Plan view orientation samples are extracted with their face parallel to the sample surface. The samples from this orientation are usually used for APT studies, more details on this can be found in [217,218]. (2) Cross sectional view samples are extracted perpendicular to the sample surface. The samples from this orientation are usually used to investigate the surface oxides, crack tips and regions around crack tip. In this thesis, all the TEM/TKD samples have been extracted in this orientation and using in-situ FIB lift out method [217]. The steps (1-10) involved in TEM/TKD sample preparation process used in this thesis are described below and also presented in *Figure 54*.

1. Selection of interesting area in the sample (Crack or oxidised grain boundary).

2. Deposition of protective platinum (Pt) layer (20 x 3 x 3μm^3 thick) to avoid damage to the sample surface during imaging by 30kV Ga^+ beam.

3. Removal of material from both sides of the Pt layer by milling trenches of ~20µm length and 10 µm in depth.

4. Sample is tilted to 0° then the bottom and side part of the lamellae are cut.

5. Free corner of the lamella is welded to the in-situ micro manipulator.

6. Now the side attached to the sample is milled so that the lamella is completely detached.

7a- 7b. Micro manipulator attached with the lamella is lifted out and then positioned to the side of the omniprobe Cu grid.

8a- 8b. The lamella is then welded to the Cu grid and the link with the micromanipulator is cut.

9a- 9b. To get electron transparency the lamella is gradually thinned from both sides with milling current of 1500 -300 pA at 30 kV.

10. Uniform thickness of 50-100 nm can be reached using low energy of 5 kV, 200 pA at 40°. This low energy cleaning can also be used to reduce FIB damage and to estimate the thickness of sample by the transparency of the foil at 5kV.

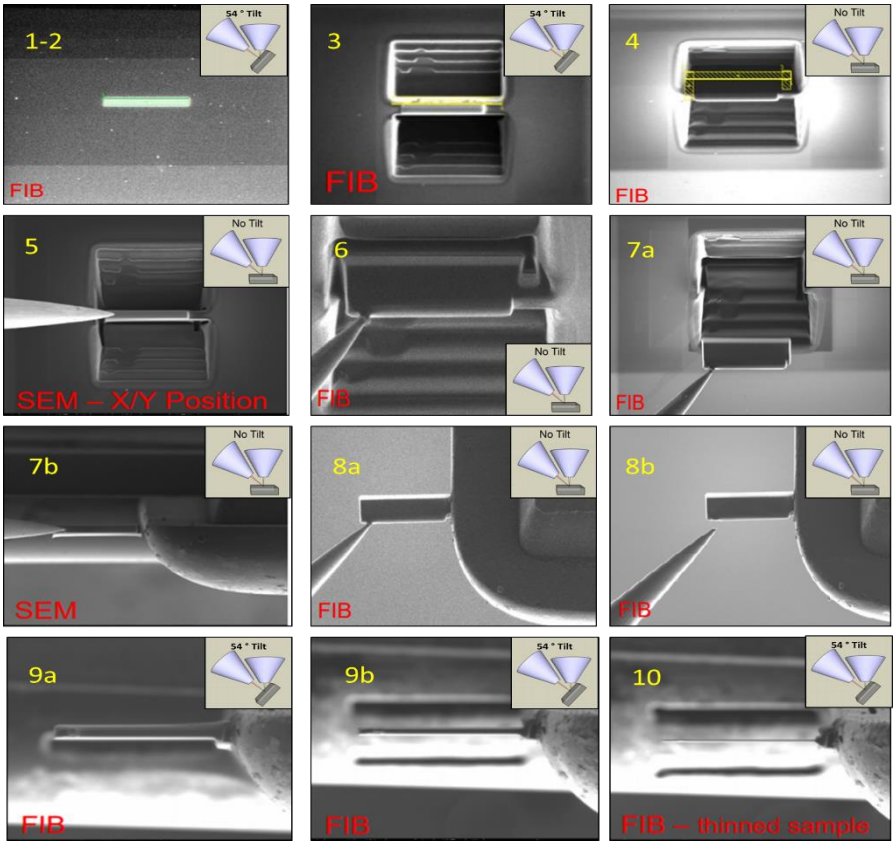


Figure 54: Systematic process for TEM/TKD sample preparation using FIB.

The main drawback of welding the sample to only one side is that during the thinning process the sample is exposed to high flux and it tends to bend. This bending can induce artefacts like local deformation mainly along the grain boundaries. Thus, an alternative welding strategy has been employed in order to improve the TEM/TKD lamella stability [219]. As shown in *Figure 55b*, the lamella is welded on two sides in V-shaped post on the Cu-grid instead of the traditional single post *Figure 55a*. By this approach, during thinning the sample is prevented from bending by leaving the thicker frames on both the sides as presented in *Figure 56*.

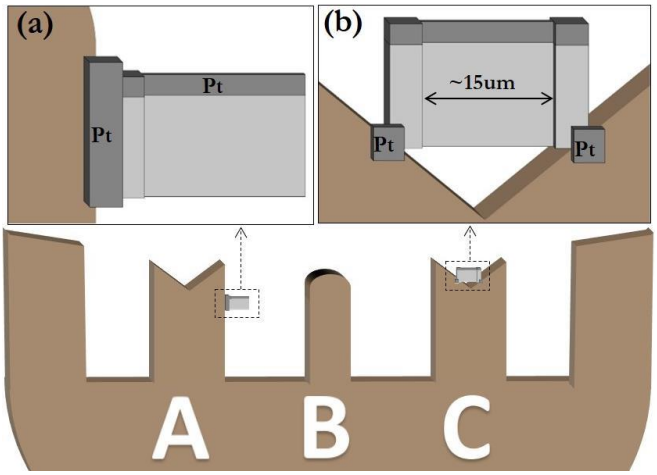


Figure 55: Schematic welding geometries on a 3 mm Cu grid. (a) one-side welded geometry on the centre post and (b) both sides welded geometry on the V-shaped post adapted from [219].

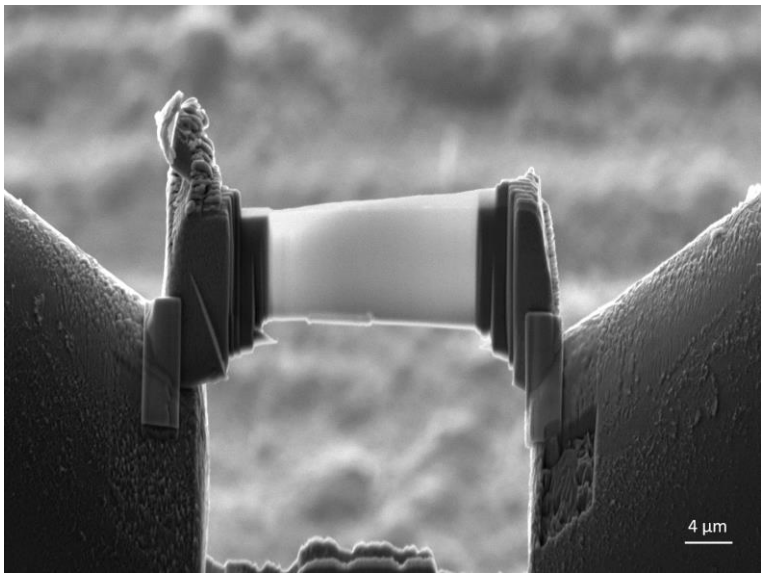


Figure 56: Example of TEM/TKD sample prepared using FIB.

3.2.2 3D FIB serial sectioning

Lozano et al. [103], have used 3D FIB sequential slicing to characterize surface oxidation (3D information) with high spatial resolution, improved statistics and minimum sample preparation. Since then, it has been proved to be a promising technique for investigating the retardation

effect of grain morphology, intergranular carbides on SCC, Cr depleted region on the grain boundaries, SCC crack path and morphology. In this thesis, 3D FIB serial sectioning was carried out using the Zeiss Crossbeam 540 dual beam FIB instrument. The recent development of Zeiss Atlas 5 software package enables high resolution and imagining continuously. This allows us to analyse huge volume of sample (up to several 100 cubic micrometres) with nanometre resolution in all three dimensions. The steps involved in high resolution 3D milling and imaging of alloy 600 microstructure with cracks is described as follows and an example is shown in *Figure 57:*

1. A protective layer of Pt was deposited and five fine lines were milled on the top of the Pt layer as shown in *Figure 57*.

2. A layer of carbon was deposited over these milled lines in order to enhance the contrast. These lines are used as markers for drift correction, auto focus, auto stigmatism and dynamic 3D tracking during the sequential sectioning.

3. A trench with a depth of 20 µm was then milled in front of the deposited layer. To obtain a better image quality, the cross-section surface was cleaned with 300 pA beam current.

4. The image was acquired for every 25 nm slice thickness with imaging resolution of 2nm pixel size. For every 30 seconds drift correction, stigmation, focus and dynamic 3D tracking were performed automatically till the sequential sectioning completed.

5. The 3D dataset was later visualized and reconstructed using Avizo 9.5 software.

This technique proves effective in revealing the tomography of the alloy 600, e.g. surface oxides, crack path, grain boundaries, Cr carbides, Cr-depleted region, crack distribution on the oxide layer etc. *Figure 57* shows the 3D reconstructed dataset.

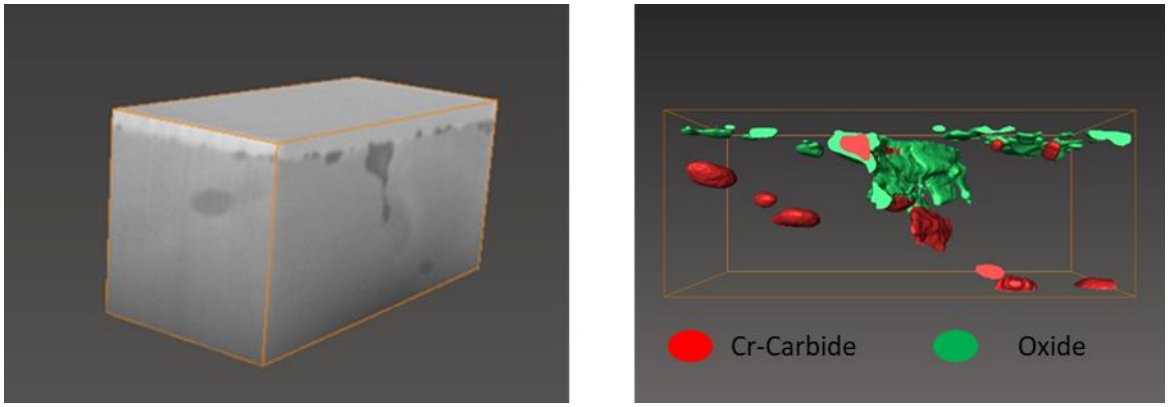


Figure 57: An example of 3D FIB sequential sectioning of Alloy 600.

3.3 Transmission Electron Microscopy (TEM)

Transmission Electron Microscopy (TEM) enables microstructural characterization of materials down to nanoscale. The incident electron beam generated by an electron source is accelerated to 200-300kV and transmitted through the sample [220,221]. In the TEM column there are a set of magnetic lenses and apertures which help in focussing the electron beam on to the sample. To facilitate the transmission, the samples are generally 50-100 nm thin (electron transparent). Due to the different scattering mechanisms (such as elastic and inelastic scattering), different signals are emitted by the interaction of electron with the sample volume. A detector (objective lens) is placed below the sample to collect the transmitted electrons which possess microstructural and crystallographic information. This can be used to generate image on the image plane or diffraction pattern on the back focal plane. By focussing on the image plane or back focal plane, we can switch between image mode and diffraction mode. Also, by changing the objective aperture in the diffraction plane, bright and dark field imaging and selected area diffraction (SAD) can be performed. By assembling the appropriate detectors to the TEM, a number of electron-base spectroscopy such as energy filtered TEM (EFTEM), energy dispersive x-ray spectroscopy (EDX) and electron energy loss spectroscopy (EELS) can be performed. TEM analysis can be performed in various forms, like high resolution

transmission electron microscopy (HR-TEM), scanning transmission electron microscopy (STEM) and analytical electron microscopy (AEM). More detailed information regarding each of this technique can be found in [220–222]. In this thesis, HR-TEM analysis was performed using JEOL 3000F microscope at 300kV to capture dislocations close to the SCC crack tips and grain boundaries. STEM analysis along with EELS was performed using JEOL ARM200F (cold-FEG) at 200 kV equipped with a Gatan GIF spectrometer to study the local chemical composition at the SCC crack tips and grain boundaries, and to measure the size of the Cr-depleted region.

3.4 Electron Back Scattered Diffraction (EBSD)

EBSD is a characterization technique that has been widely used to investigate the microstructure of crystalline samples. They are also used to acquire the texture, phase, crystal orientation, defects, grain morphology and local deformations [223–225]. This technique is based on the principle that the electron beam on interacting with the lattice planes of the sample at correct diffraction angle forms sets of parallel lines in the diffraction pattern. These lines are called Kikuchi bands and the pattern formed is called Kikuchi diffraction pattern. These patterns are collected and recorded on the phosphor screen by a CCD camera (EBSD detector) and later indexed using EBSD software. The centre lines of each bands which are thick corresponds to the gnomonic projections of the crystal lattice planes and the width is indicated by Bragg's law and the specimen to phosphor screen distance. Inverse Pole *Figure* (IPF) maps are generated by comparing the positions and angles between the Kikuchi patterns. EBSD can also be used to evaluate the relative elastic strain within the grain with respect to the reference point [226,227].

The Kikuchi patterns from the sample can be recorded using three different setups as shown in *Figure 58*. They are conventional EBSD, off-axis transmission Kikuchi diffraction (TKD) and on-axis transmission Kikuchi diffraction (on-axis TKD).

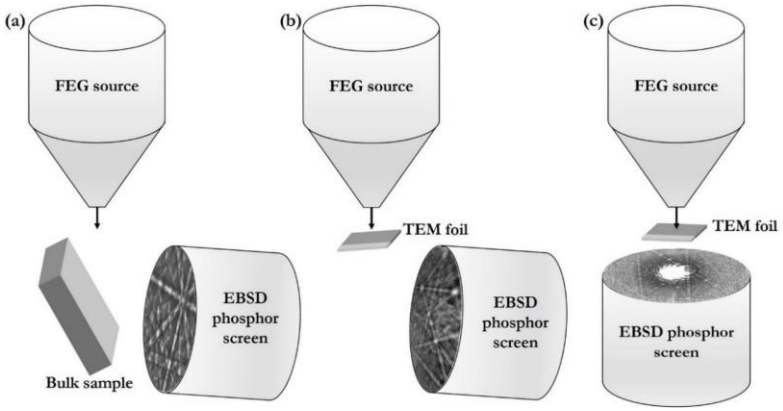


Figure 58: Schematic diagram of (a) Conventional EBSD (b) off-axis TKD and (c) on-axis TKD on TEM foil adapted from [219].

For a conventional EBSD measurement, the mirror polished bulk sample is positioned at an angle of 70° with respect to the horizontal and the incident electron beam is scanned across the surface. This way of positioning the sample towards the detector increases the backscattering yield and improves the quality of the Kikuchi patterns. The spatial resolution obtained is the combination of the size of the incident beam and the interaction volume for the Kikuchi pattern formation [228]. This resolution is usually ~20-100 nm for conventional EBSD. In this thesis, all the EBSD measurements were carried out using Zeiss Crossbeam 540 FEG-SEM equipped with Oxford Instrument (OI) EBSD NordlysMax detector at a working distance of 14 mm, accelerating voltage of 20-30kV and beam current between 10-20nA.

3.4.1 Transmission Kikuchi Diffraction (TKD)

When the spatial resolution of EBSD is not enough, an alternative technique known as transmission electron backscatter diffraction (t-EBSD) or TKD (preferred name) is used

[229,230]. Instead of the bulk sample, a TEM foil is used which allows the electrons to pass through it. This will reduce the interaction volume and thus provide a better spatial resolution. The traditional TKD or off-axis TKD uses the same hardware as the conventional EBSD. The off-axis TKD was carried out using Zeiss Crossbeam 540 FEG SEM equipped with an Oxford Instruments EBSD NordlysMax 3 detector system. The TEM sample is mounted on 45° pre-tilt holder and the stage is tilted by 25° in order to obtain a net tilt of 70° as shown in *Figure 59a*. The sample to detector distance was kept at 14 mm and working distance was 6 mm. An accelerating voltage of 20-30kV and probe current of 1 nA was used. The patterns were recorded at 400 x 300 resolution for a step size of 10 nm.

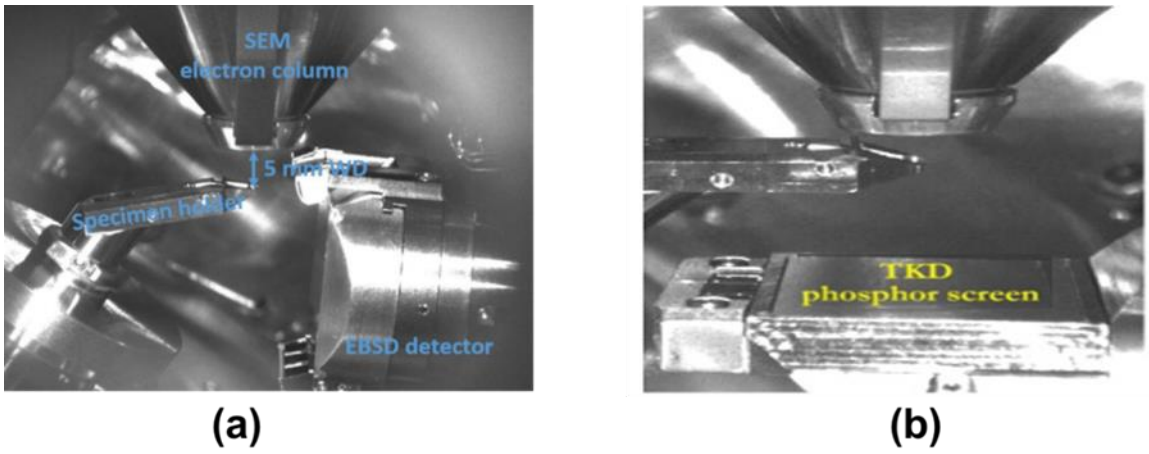


Figure 59: Geometrical setup (a) Off-axis TKD (b) On-axis TKD.

In case of On-axis TKD, the TEM foil mounted on the 45° pre-tilt holder and the stage is tilted by 45° so that the sample is placed beneath the electron gun in a transmission geometry as shown in *Figure 59b*. The TKD patterns are collected by the EBSD phosphor screen placed on-axis with the electron gun. Kikuchi patterns acquired in this configuration have less gnomonic distortion and the signal yield is maximum, thus the acquisition time of diffraction with similar quality as compared to the off-axis geometry is reduced by 50 times [229]. This provides a better spatial resolution of just few nanometres and can be used to characterize the

very small nanocrystalline oxides, cracks etc [34,190,231]. The high resolution TKD patterns obtained can be used to evaluate the elastic strain in the materials and thus calculate geometrically necessary dislocations (GNDs) density more accurately [232]. In this thesis, conventional EBSD was used to characterize the as-received alloy 600 and obtain the grain size, grain boundary types etc. On-axis TKD was used to investigate the local deformation, elastic strain, GNDs density and misorientations of the crack grain boundaries.

In previous SCC initiation and propagation studies [187,233–235], various electron microscopy techniques such as scanning electron microscopy (SEM), transmission electron microscopy (TEM) [54,236], electron back scattered diffraction (EBSD) and off-axis transmission Kikuchi diffraction (TKD) [237] have been used to study oxide structure, chemistry, crack morphology, matrix and deformation around the crack tip, orientation of the grains around the crack etc. Kernel average misorientation (KAM) after EBSD mapping has been traditionally used to identify regions of high strain and correlate them with SCC initiation. Lattice rotations are measured locally and differences smaller than a degree can be detected. As an example, Ehrnsten [238] used it to reveal the effect of cold work on creating local high-strain areas which facilitates initiation.

However, this method remains qualitative, since it is highly dependent on the parameters used for EBSD acquisition (e.g. step size) and cannot offer a lateral resolution better than the technique itself (>100nm). Some researchers [239–241] used Digital Image Correlation (DIC) to correlate the microstructural scale plastic strain and misorientation. Even when performed in a SEM, DIC has a limited lateral resolution (e.g. 5 µm mesh in [14]) which conditions its strain measurements and might not highlight key regions of high strain localization.

In previous SCC initiation and propagation studies [187,233–235], various electron microscopy techniques such as scanning electron microscopy (SEM), transmission electron

microscopy (TEM) [54,236], electron back scattered diffraction (EBSD) and off-axis transmission Kikuchi diffraction (TKD) [237] have been used to study oxide structure, chemistry, crack morphology, matrix and deformation around the crack tip, orientation of the grains around the crack etc. Kernel average misorientation (KAM) after EBSD mapping has been traditionally used to identify regions of high strain and correlate them with SCC initiation. Lattice rotations are measured locally and differences smaller than a degree can be detected. As an example, Ehrnsten [238] used it to reveal the effect of cold work on creating local high-strain areas which facilitates initiation.

However, this method remains qualitative, since it is highly dependent on the parameters used for EBSD acquisition (e.g. step size) and cannot offer a lateral resolution better than the technique itself (>100nm). Some researchers [239–241] used Digital Image Correlation (DIC) to correlate the microstructural scale plastic strain and misorientation. Even when performed in a SEM, DIC has a limited lateral resolution (e.g. 5 μm mesh in [14]) which conditions its strain measurements and might not highlight key regions of high strain localization.

3.5 3D Electron Back Scattered Diffraction (3D EBSD)

Most of the SCC studies until date usually involve 2D metallographic techniques for characterization. To better understand the SCC mechanism, it is necessary to gain insight into the 3D aspects of the microstructure. For example, in case of conventional EBSD, the misorientation between the grains can be obtained but the spatial orientation of the grain boundary plane is missing and the orientation of the boundary plane with relation to the crystal lattice separated cannot be determined. This information is very crucial in better understanding the underlying mechanism of SCC. Thus, for the first time in this thesis, a novel approach of

3D EBSD was used to extract information on grain morphology and orientations in 3D that will later be used in generating 3D aggregates for simulation studies.

In this thesis, 3D EBSD was performed using two different approaches in two different instruments. They are (1) Rotation setup and (2) Tilt setup [242–244]. *Figure* 60 shows the schematic of both the set up. The rotation setup approach was employed in FEI Plasma FIB fitted with an Oxford Instruments EBSD NordlysMax 3 detector. Using the plasma FIB several hundreds of microns of volume can be investigated. The tilt setup approach was employed in Zeiss Crossbeam 540 equipped with an Oxford Instruments EBSD NordlysMax 3 detector system. As it is a Ga^+ ion FIB, only a small volume (tens of microns) can be investigated. However, the electron backscattered pattern (EBSP) quality is much better than the ones obtained using plasma FIB. The main reasons for this one is that, small step size was used for Ga^+ FIB compared to PFIB and pattern resolution used also better.

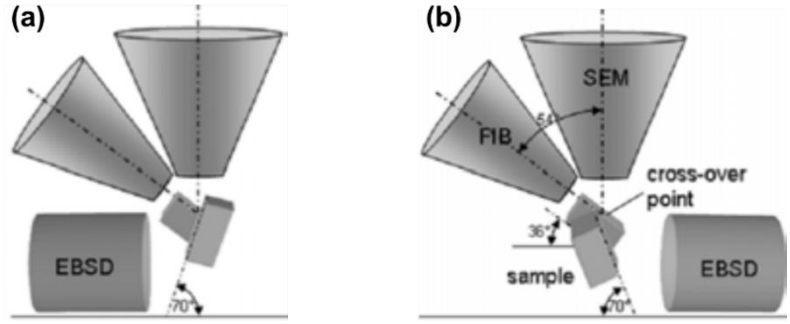


Figure 60: Different geometrical setup for 3D EBSD: (a) Rotation setup (b) Tilt setup [244]

Zaefferer et al. [243], presented two possible sectioning strategies for 3D EBSD. The first method is known as the grazing-incidence edge milling (GIEM) method. In this approach, a sharp rectangular edge is produced on the sample at one side. Sectioning is carried out by milling the rectangular edge at a grazing incidence to one surface of the sample edge. The advantage of this method is that it is trivial to setup and very large volumes of datasets can be investigated in a shorter time. However, the main drawback of this method is that the region of

interest for investigation in the microstructure should be on/close to the rectangular edge. The second method is known as low incidence surface milling (LISM) method. In this approach, the ion beam is made to enter the sample surface at a low incidence angle due to the stage tilt between 10°-20°. The advantage of this method of sectioning is that it provides greater flexibility in investigating any feature on the sample surface. However, the main drawback of this method is that the milling area should be larger than the imagining area in order to avoid the effects of shadowing on the EBSD detector.

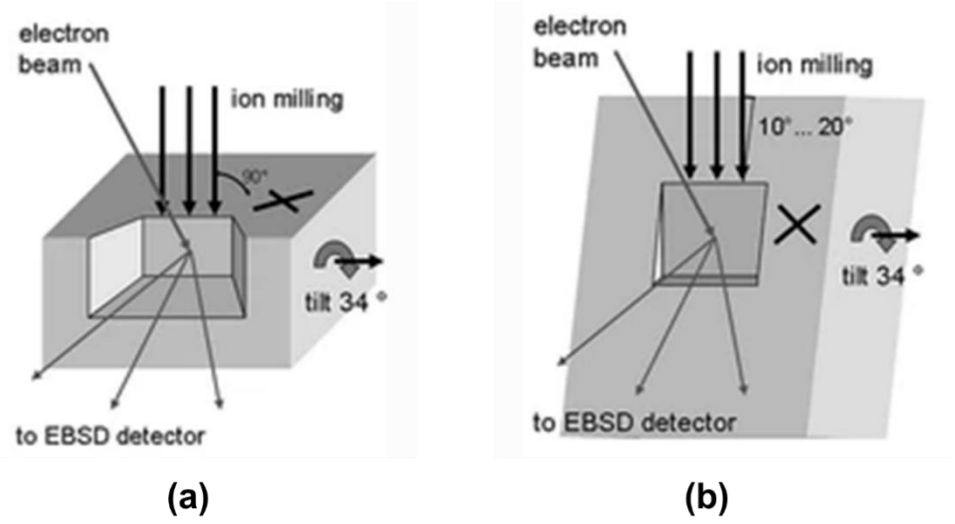


Figure 61: Schematic of Sectioning for 3D EBSD: (a) grazing incidence edge milling (GIEM) method; (b) low incidence surface milling (LISM) method [243].

In this thesis, GIEM method was used for sample preparation for acquiring 3D EBSD datasets in both the instruments as illustrated in *Figure 62b*.

The rotation setup approach of acquiring 3D EBSD data in Plasma FIB (PFIB) involves tilting of the sample in different ways. For EBSD scan, the sample is titled 70° from the horizontal position so that the surface is facing the EBSD detector. For FIB milling, the sample is titled 53.5° from the horizontal position so that ion beam is parallel to the milling edge of the sample. In order to minimise the displacements and inaccuracies in the sample position caused during the changing of positions from EBSD to FIB and vice versa, a pre tilt holder as shown in *Figure*

62 was used. The pre tilt of the holder is 53.5° and an additional stage tilt of 16.5° is performed so that the sample surface is ready for EBSD scan (53.5° + 16.5° = 70°), then the EBSD detector is inserted as shown in *Figure 62c*. Once the EBSD scan is completed, the EBSD detector is withdrawn to prevent any damage caused to the phosphor screen during the stage movement. Once the EBSD detector is retracted, a stage rotation of 180° is performed around the inclined axis, bringing the sample to the FIB position (*Figure 62d*) at 36.5° from the horizontal axis as shown in *Figure 62a*. The working distance of 4 mm is maintained for both the positions.

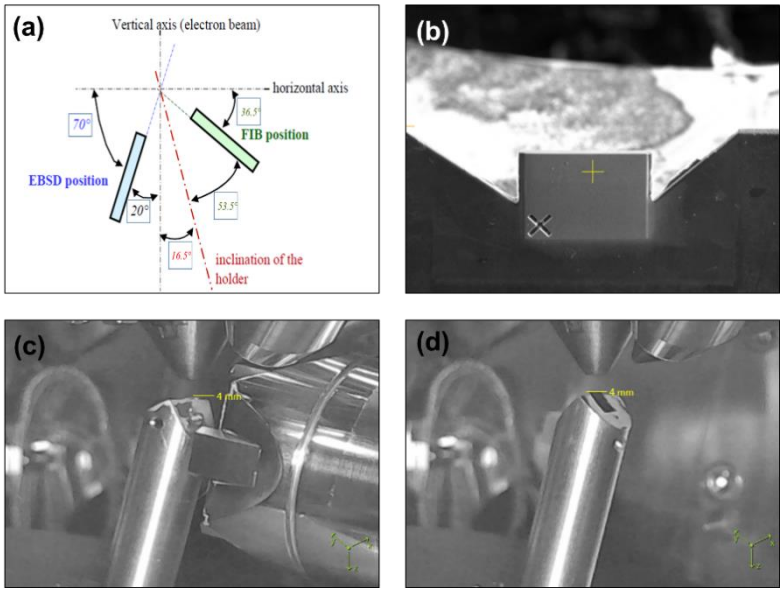


Figure 62: Rotation Setup 3D EBSD: (a) Geometrical setup with a rotation of 180° along the inclined axis allows changing position from EBSD to FIB. (b) Rectangular edge prepared on the sample for GIEM method sectioning (c) Chamber view of EBSD position (d) Chamber view of FIB position in Plasma FIB.

The tilt setup approach for acquiring 3D EBSD data in Zeiss Crossbeam 540 involves tilting of sample about an axis perpendicular to the electron beam and ion beam to change between EBSD and FIB positions respectively. Due to the sample proximity to the pole piece, insertion of EBSD camera and constraints in the angular movement of the stage, a y movement of the stage is necessary. The ideal working distance for the dual beam SEM-FIB is 5.1 mm (eccentric point). At this point, the usual FIB serial sectioning (described in *section 3.2.2*) is performed.

However, for 3D EBSD, repetitive FIB slicing and EBSD mapping is carried out at different working distances. This process can be automated by the on-going developments in Atlas 5 software developed by Oxford Instruments. Automating the process requires tremendous care in setting up the sample area and microscopic conditions. This step is not straight forward and quite tedious especially in preparing a region without any shadowing effects on the EBSD patterns and obtaining a better imaging quality. After setting the conditions, data acquisition can be run on automatic mode. The sample mounted on the pre-tilt holder is set for FIB mill position at the working distance of 5.1 mm, *Figure 63a*. Once the milling is finished the stage is brought down by moving in y and rotated 180° along the inclined axis to face the EBSD detector at 70°. The sample is now at the EBSD scan position at the working distance of 12 mm as illustrated in *Figure 63b*.

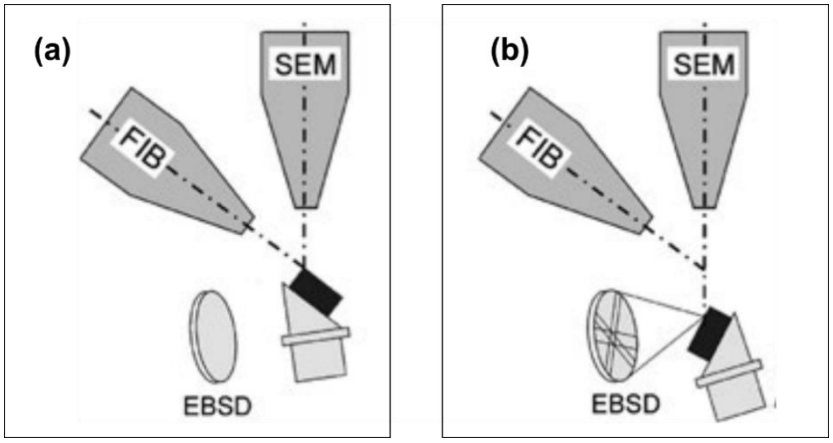


Figure 63: Geometry of Tilt Setup 3D EBSD: (a) FIB position at 5.1 mm working distance (b) EBSD position at 12 mm working distance.

3.5.1 3D EBSD Data Acquisition Conditions

The Xe^+ plasma in PFIB has the benefit of achieving significantly higher milling currents compared to the conventional Ga^+ ion FIB, thus enabling investigation of greater volumes [245,246]. The FEI Helios PFIB-SEM with Aztec 3D in University of Manchester has enabled us to collect large volume of 3D EBSD datasets. *Figure 64a* shows the region of interest to be

investigated which is of volume 300 x 200 x 60µm (where 300µm x 200µm is the size of the cross section and 60µm is the depth) represented in yellow box. The FIB slicing was carried out with ~250 nm thick slices using milling current of 22nA and accelerating voltage of 5 kV. The milling of each slice took around 2 minutes. EBSD maps were acquired at 20kV with a step size of 1 µm in x and y direction and each map acquisition takes around 5 minutes. An example is shown in *Figure 64b.* EBSD maps are recorded for every 4 FIB slices so that the resolution in z direction will also be 1 µm (to have a voxel size of 1µm). As, there is only one movement of the stage (180° rotation) for changing from FIB to EBSD position, a drift marker (cross hairs) is used for dynamic 3D tracking, auto focusing during each positional change (green box in *Figure 64a*).

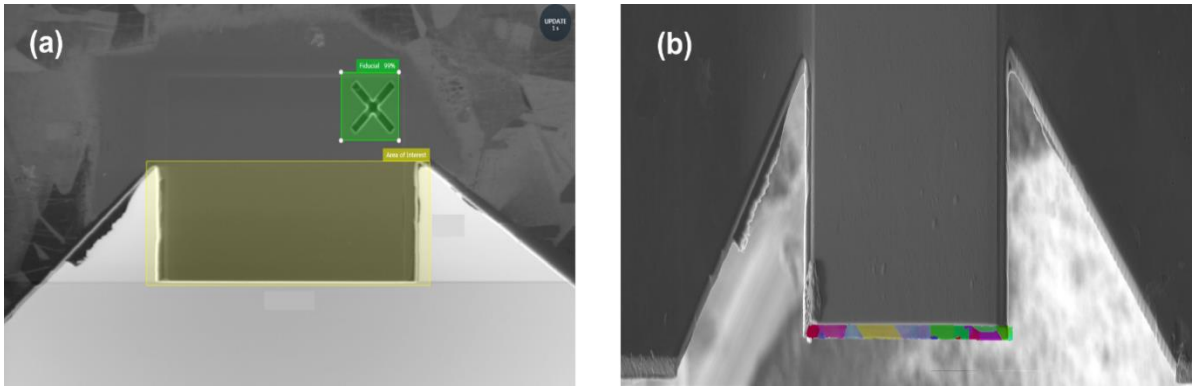


Figure 64: Data acquisition in PFIB: (a) Region of interest and 3D tracker; (b) Example of acquired EBSD map in Zeiss Crossbeam 540.

In the case of Ga^+ ion FIB, small volumes can be analysed but with higher resolution compared to the PFIB. The Zeiss Crossbeam 540 dual beam FIB-SEM with Atlas 5 and Aztec software in University of Oxford was used to collect the 3D EBSD datasets with higher image quality. The volume of the region investigated was 30 x 30 x 5 µm. Due to low milling currents, unlike PFIB, only 25 nm thick slices were sectioned using 1.5 nA milling current. EBSD maps were acquired for every 4 slices (i.e., for every 100 nm) and recorded at 20kV with step size of 100 nm (0.1 µm). In this setup, there are two movements of the stage for changing from FIB to

EBSD position and vice versa as shown in *Figure 65*. First, the stage is brought down in y direction and rotated 180°, hence an additional drift marker (cross hairs) along with the usual FIB sequential sectioning markers is used for auto focusing, auto stigmatism and dynamic 3D tracking during the whole 3D EBSD experiment at each positional change. The whole process is described in a flowchart in *Figure 66.*

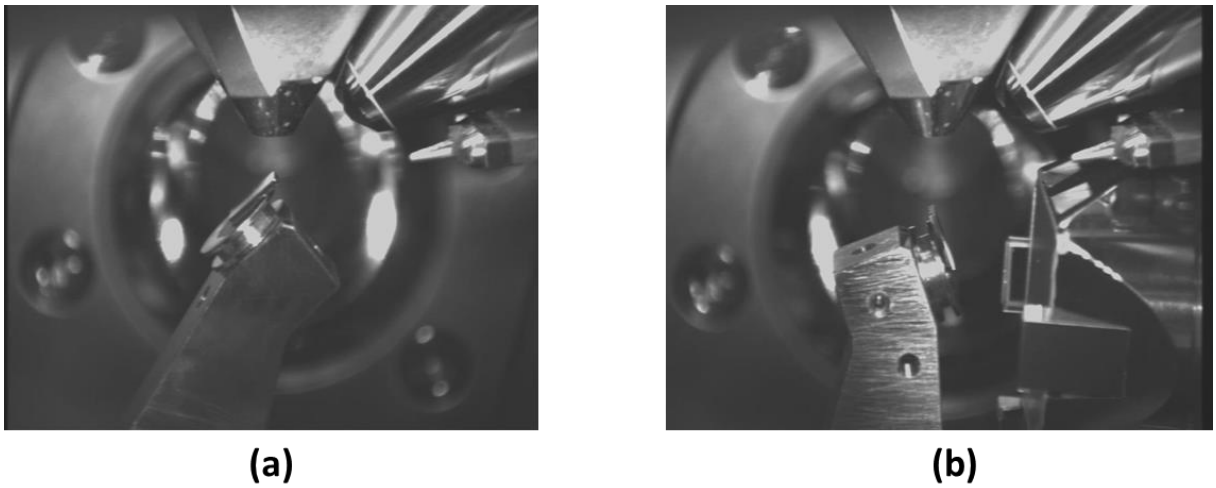


Figure 65: Chamber view of (a) FIB mode; (b) EBSD mode in Zeiss Crossbeam 540.

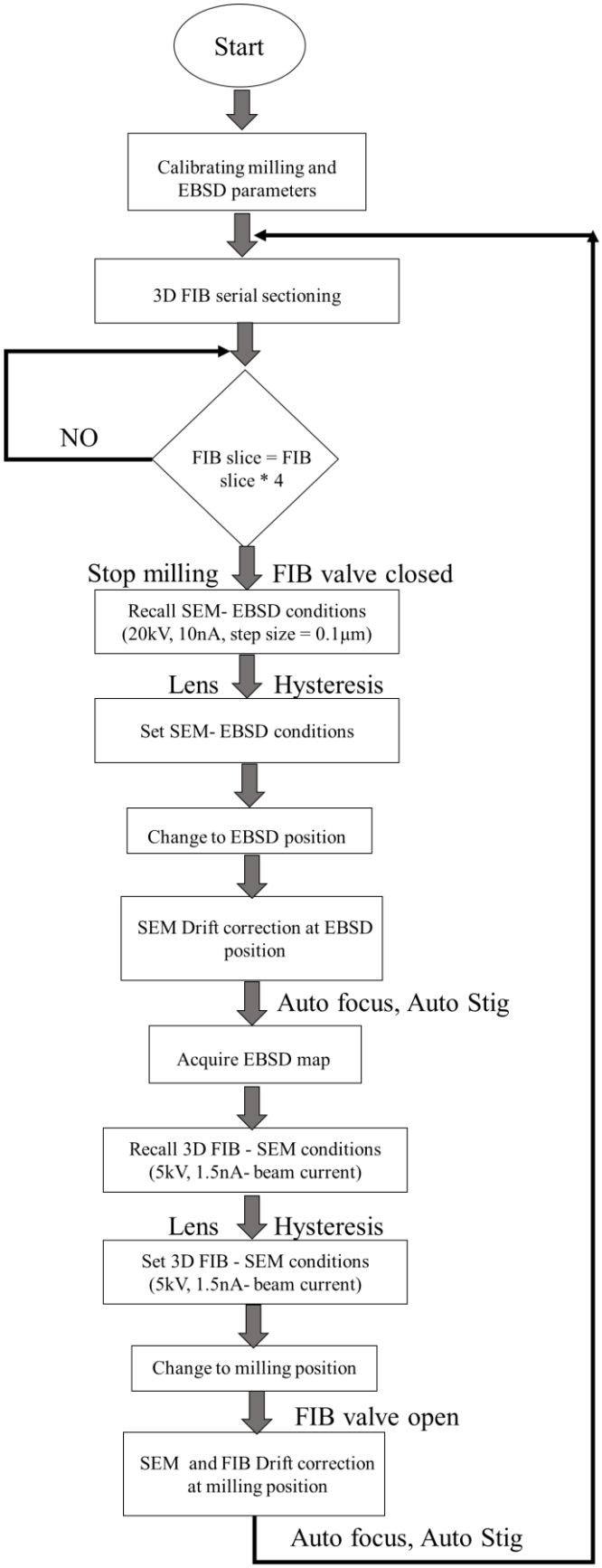


Figure 66: Flowchart explaining the sequential steps involved in 3D EBSD process.

Khorashadizadeh et. al [247] used 3D EBSD approach in Cu-Zr alloys to perform 3D grain boundary character distribution (GBCD) of a sample subjected to equal channel angular pressing (ECAP) after eight passes and successive annealing at 6508C for about 10 min is analysed. The experiments are conducted using a dual beam system of Zeiss XB1560 microscope to collect a series of electron backscatter diffraction (EBSD) maps using TSL/EDAX software, Hikari S/N 1040 camera of the microstructure (3D EBSD). The data set was aligned and reconstructed to a 3D microstructure. The crystallographic character of the grain boundary planes was determined using three different methods, namely, the line segment method, the stereological method, and the triangular surface mesh method. The line segment and triangular surface mesh methods produce consistent data sets, both yielding approximately a 7% area fraction of coherent twins. These results starkly contrast that of the statistical stereological method, which produced a 44% area fraction of coherent twins. This application of 3D EBSD is very important characterize grain boundaries and 3D grain deformation to IGSCC.

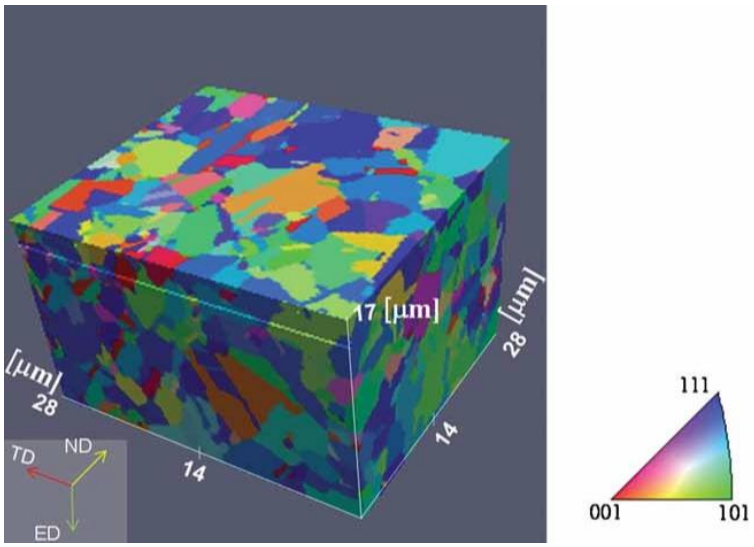


Figure 67: 3D microstructure of the Cu-0.17 wt% Zr sample after 8 ECAP passes and subsequent annealing at 650 °C for 10 min as obtained from 3D EBSD. The colour code indicates the crystal directions parallel to ED (extrusion direction). The alignment of the 2D slices is based on minimizing the disorientation between matching voxels in adjacent 2D EBSD layers [247] using Zeiss XB1560 microscope.

3.5.2 Limitations

There are quite a few limitations in performing the 3D EBSD experiment successfully. The first limitation mainly in the case of conventional FIB-EBSD set up is the duration of the experiment. The experimental setup is itself quite time consuming, especially the calibration procedures. Each cycle of 3D EBSD scan takes almost 14 minutes on average which involves stage movements, recognition of area of interest, drift correction, FIB slicing and EBSD map acquisition. Thus, acquiring a large volume of dataset takes longer and is unrealistic.

The recalling of microscope stage to milling and EBSD positions are difficult because the displacements of the stage during 3D EBSD need to be reproducible within nm. This is mainly caused because of the volume of the sample holder and insertion of the EBSD detector during the experiment. These displacements result in inaccurate repositioning of the reference drift markers and thus causing the experiment to fail/stop. This issue was encountered many times during the course of this thesis.

The EBSD pattern quality is largely compromised when lowering the accelerating voltage despite the increase in exposure time to balance the effect of the brightness and sensitivity of the phosphor screen. However, increasing the exposure time rapidly limits the feasibility of 3D EBSD experiment. Nevertheless, decreasing the accelerating voltage is very important for the EBSD analysis of the grain boundaries. Even for higher SEM voltages, the superposed crystal lattice structures at the grain boundaries causes more electrons channelling leading to poor contrasts in SEM and EBSD images.

3.5.3 Objectives of performing 3D EBSD experiments

The main objective of systematic recording of EBSD maps with a desired number of slices is to correlate the microstructural features obtained on the SEM imaging on a given slice with the

EBSD crystallographic information acquired on an adjacent or previous slice within the 3D sequence. In the context of this thesis, 3D EBSD is used to correlate the SCC cracked grain boundaries, grain boundary plane, misorientation, crack path and morphology.

The extracted crystallographic information such as grain orientation and morphology can be used to model representative 3D aggregates and perform simulation on them to evaluate the local stress on the grain boundaries (for SCC cracked and uncracked). The method of modelling and simulation is detailed in *Chapter 6*.

3.6 Summary

To have a better understanding of SCC, a thorough investigation of grain boundaries and crack area in the sample across different length scales – from millimetres to nanometres is required. For this multiscale approach, a range of complementary microscopy techniques have been used in this thesis have been discussed.

The main techniques used in this work are; Scanning electron microscopy (SEM), for preliminary examination of the surface, cracks and to calculate the grain boundary carbide coverage (GBC) using BSE imaging. Focused Ion Beam (FIB), used for TEM/TKD sample preparation, measuring the crack depth, making trenches for 3D EBSD. Electron Back Scattered Diffraction (EBSD), for preliminary measurement of grain size, grain boundary character, crack analysis with the grain boundaries. Transmission Kikuchi Diffraction (TKD), for local stress and GNDs around the cracked and uncracked grain boundaries. 3D Electron Back Scattered Diffraction (3D EBSD) for extracting the 3D polycrystalline aggregate to estimate the local stress using CPFEM simulation studies.

4 MATERIAL USED AND SCC TESTS

This chapter gives an overview of the materials used in this project, characterization of as-received alloy, SCC test, crack analysis, comparisons of cracks from different tests and types of grain boundaries cracked.

4.1 Specimen Orientation

The alloy used in this project is Alloy 600 solution annealed. The material reference is RND-M-T-265. This alloy is more representative of SG plates and tubes bottom mounted instrumentation nozzles. The different orientations of the specimen are presented in *Figure 68*.

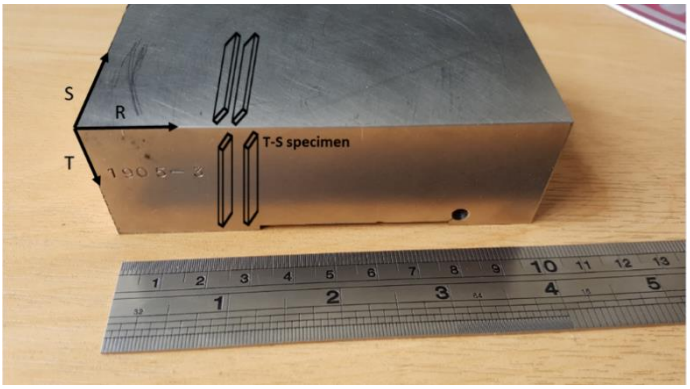


Figure 68: Specimen Orientations for T-265.

4.2 Metallurgical state

The material is solution annealed for 30 minutes at 1150°C and water quenched. The solution annealing treatment was conducted for the dissolution of intergranular carbides to increase the IGSCC sensitivity. The chemical composition of this alloy is presented in *Table 4*. The as-received state refers to the material after solution annealing.

Table 4: Chemical Composition of Alloy 600 (T-265)

Element	**Content (wt %)**
Carbon	0.07
Manganese	0.17
Silicon	0.29
Sulphur	<0.001
Phosphorous	0.007
Nickel	~73.5
Chromium	16.30
Copper	0.01
Aluminium	0.19
Titanium	0.19
Iron	9.20

To verify that the annealing treatment resulted in a desirable microstructure, the samples were studied using EBSD. EBSD maps are shown in *Figure 69* and *Figure 71*.

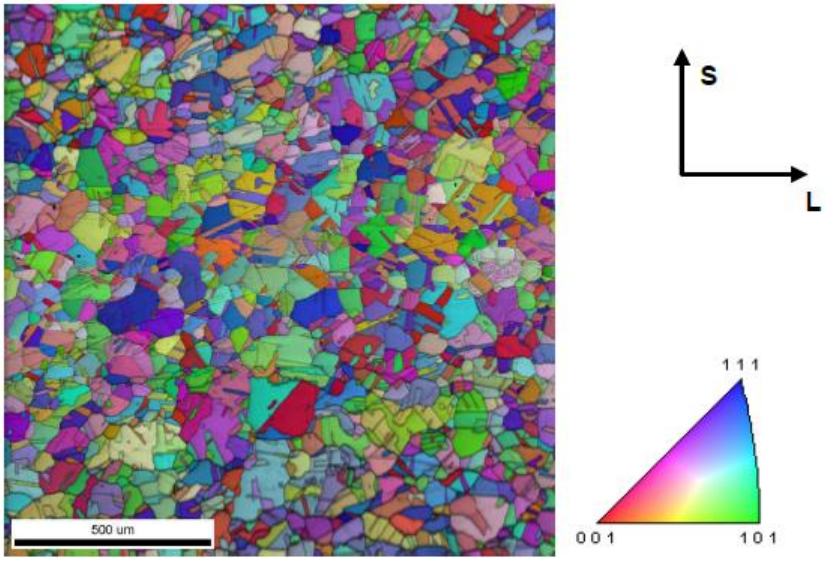


Figure 69: Inverse pole *Figure* (T direction) in T-265 material (LS), around the surface of plate in as-received state. Acquisition step: 1µm; working distance: 13 mm; acceleration voltage: 20kV.

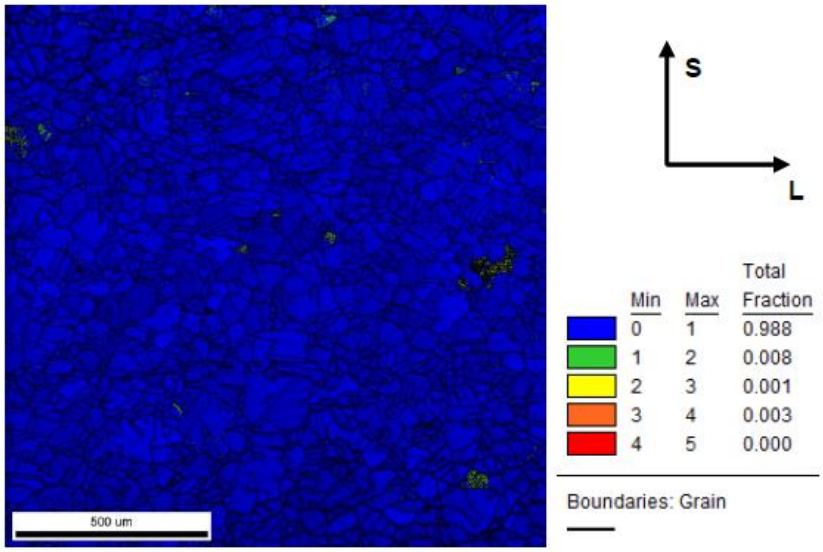


Figure 70: KAM mapping (4th neighbours) in T-265 material (LS), around the surface of plate in as-received state. Acquisition step: 1µm; working distance: 13 mm; acceleration tension: 20kV.

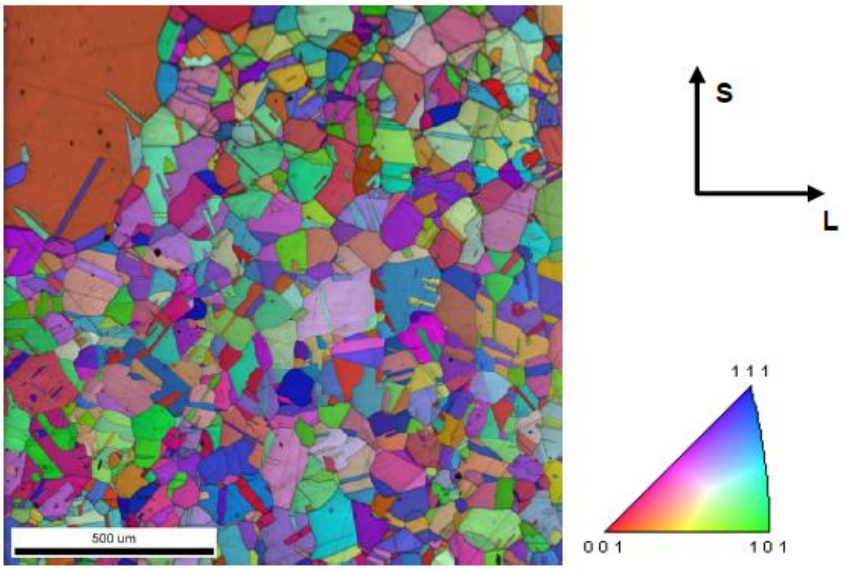


Figure 71: Inverse pole *Figure* (T direction) in T-265 material (LS), close to the centre of plate in as-received state. Acquisition step: 1µm; working distance: 13 mm; acceleration voltage: 20kV.

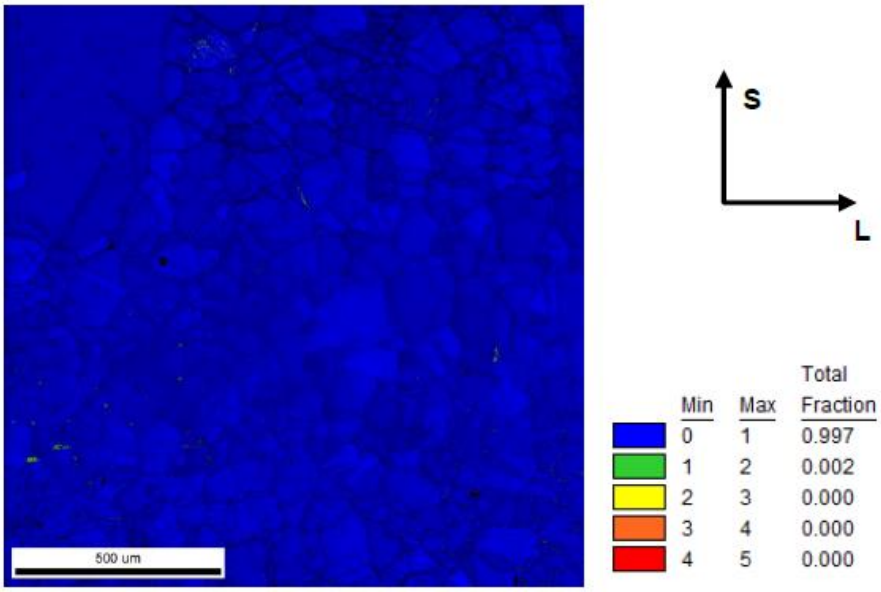


Figure 72: KAM mapping (4th neighbours) in T-265 material (LS), close to the centre of plate in as-received state. Acquisition step:1µm; working distance:13 mm; acceleration tension:20kV.

EBSD characterization revealed some poorly recrystallized grains close to the surface of the plate and better recrystallized grains close to the centre, respectively from the *Figure*s 61 and 63. The Kernel Average Misorientation (KAM) maps (*Figure 70* and *Figure 72*) revealed only

traces of residual strains, which testifies for a high quality of restoration of the alloy at as-received state (including in poorly recrystallized grains). In this thesis, as we are study about the crack initiation by IGSCC only the sample from the surface of the plate is of interest.

4.3 Mechanical Testing

Mechanical properties of the materials at 20° C and 360° C have been measured to plan the stress level to be applied during stress corrosion cracking testing. Mechanical testing has been performed according to EN 10002-5:1992 standards regarding tensile testing of metallic materials at high temperatures on an Instron tensile machine. The mechanical properties of this alloy are presented in *Table 5*.

Table 5: Mechanical Properties of Alloy 600 (T-265) data and sample provided by EDF.

	TT	**T° (°C)**	**Orientation**	**YS 0.2 (MPa)**	**UTS (MPa)**	**E (GPa)**
T-265	30min at 1150°C + water quench	20	T	241	607	172
		360		221	550	233

4.4 Pre-characterization

Prior to subjecting the sample for SCC tests, pre-characterization is necessary to obtain few important parameters such as the grain size, grain boundary characteristics, grain boundary coverage, type and size of carbides and misorientation. A small piece of sample was extracted from the bulk piece and the following steps were carried out.

4.4.1 Grinding and polishing procedure

It is important to have a clean, damage free surface before any optical or electron microscopy examinations. A considerable amount of time was spent on obtaining a mirror finish on the sample surface so as to obtain sharp good quality EBSD patterns and maps. The sample was

finely polished, and the surface was free from scratches. The routine was to first grind with silicon carbide paper grit 320, 600, 800, 1200, 2400 and 4000. This was followed by mechanically polishing the surface using diamond paste with various sizes of 9µm, 3µm and 1µm. Finally, the sample was polished using colloidal silica 0.06 µm to get a surface with no scratches. The systematic grinding and polishing procedure are presented in *Table 6*. After polishing, the sample was washed under running water then ultrasonically cleaned using acetone, propanol, and deionised water for 10 minutes to remove all the residues.

Table 6: Grinding and polishing procedure for Ni-based alloys.

Step	**Procedure**	**Time**	**Grit size**	**Pressure**	**Lubricant**
1	Grinding with SiC paper	5	320	applied by hand until flat	Water
2		3	600	applied by hand	
3		3	800		
4		3	1200		
5		5	2400		
6		5	4000		
7	Polishing with diamond paste	6	9µm	30 N	OS fluid
8		5	3µm	30 N	
9		5	1µm	30 N	
10	Polishing with colloidal Silica	3	0.06µm	20 N	Water for last 1 min

4.4.2 Grain size estimation

It is important to estimate the grain size because it has been shown to influence IGSCC behaviour (as discussed in *Chapter 2* *section 2.4.4*). The average grain size was estimated by obtaining EBSD maps of the sample at various magnifications using Zeiss Crossbeam 540 FEG-SEM equipped with Oxford Instrument (OI) EBSD NordlysMax detector and later processed using Tango maps in Channel 5 software. An EBSD map from one of the regions and overall grain size distribution plot is presented in *Figure 73* and *Figure 74*. While measuring the grain size, annealed twin boundaries were excluded from count. The average grain size was estimated to be 40 ± 16µm.

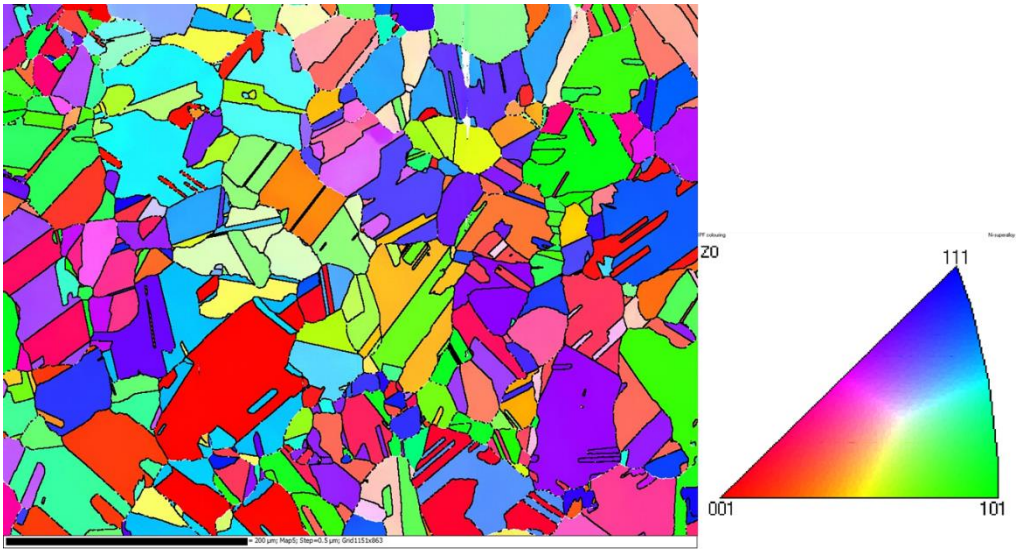


Figure 73: Inverse pole *Figure* (Z direction) in T-265 material in as-received state. Acquisition step: 0.5 µm; working distance: 13 mm; acceleration voltage: 20kV.

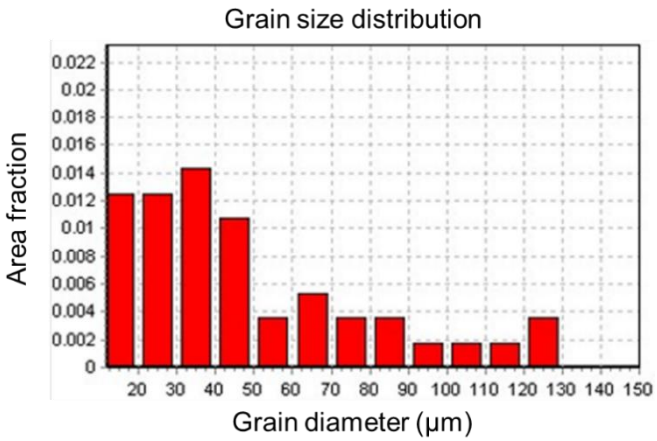


Figure 74: Grain size distribution of Solution Annealed alloy 600. The average grain size is approximately 40 µm.

4.4.3 Grain boundary characteristics

The grain boundary character was investigated using EBSD. This is mainly because in a variety of materials and environments, it has been reported that high angle grain boundaries (HAGBs) are less resistant to IGSCC than low angle grain boundaries (LAGBs). Added to this, annealed twin boundaries (∑3) have been reported to exhibit extreme resistance to degradation (as discussed in *Chapter 2 section 2.4.3*). The overall grain boundary character of alloy 600 has been estimated using the Bruker Software and presented in *Table 7*. It can be seen that almost 99% of the grain boundaries are HAGBs of which 72% constitute to ∑3 type grain boundary (annealed twin boundaries). The LAGBs corresponds to grain boundaries with a misorientation less than about 15° and HAGBs corresponds to grain boundaries with a misorientation angle greater than 15° with ∑3 boundaries with angle of 60° misorientation.

Table 7: Grain Boundary Character of Solution Annealed Alloy 600 (T-265).

Grain Boundary	Map 1	Map 2	Map 3	Average
LAB (%)	0.7	1.2	0.8	0.9
HAB (%)	99.3	98.8	99.2	99.1
∑ 3 (%)	73	68.5	72	71.2
∑ 9 (%)	7.8	8.3	8.6	8.23
∑ 27 (%)	3.5	2.8	2.9	2.4

4.4.4 Grain Boundary Coverage (Carbide Coverage)

The sample was examined using a Zeiss Crossbeam 540 FEG-SEM using backscattered electrons to differentiate between the carbides and the matrix. All images were captured at 1000-x magnification to ensure consistency in the results and representativeness of the area scanned. The processing of the captured images was carried out using ImageJ software, where for the intergranular carbides precipitated at the grain boundary, the grain boundary carbide coverage (GBC) was obtained manually by measuring the length of the carbides and the grain boundaries. To calculate this, a formula mentioned in equation (12) was employed. An example of the processed image is shown in *Figure 75*. It was calculated to be ~12 ± 3% and presented in *Table 8*.

$$Grain\ boundary\ coverage\ (GBC) = \frac{Total\ intergranular\ carbide\ lenght}{Total\ grain\ boundary\ length} \times 100 \quad \ldots\ldots\ldots\ldots (12)$$

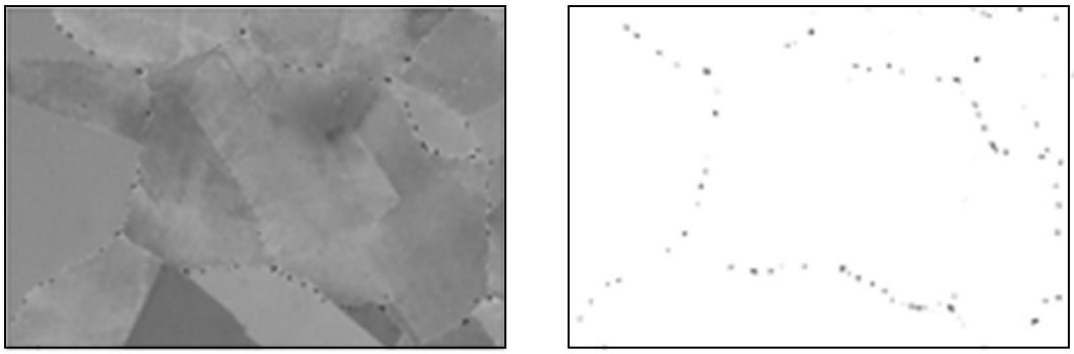


Figure 75: (a) Backscattered electron image (b) Binary image

Table 8: Grain boundary Coverage (GBC)

BSE Image	**Percentage of Grain Boundary Coverage (GBC)**
Image 1	10
Image 2	16
Image 3	9
Image 4	13
Image 5	15
Image 6	11
Image 7	9
Average	**11.85 ± 2.65**

4.4.5 Misorientation Analysis

The misorientation of the microstructure is a better way of understanding the interactions between the microstructure and intergranular stress corrosion cracking susceptibility. The EBSD maps were processed using Channel 5 software to obtain the misorientation in the microstructure. The main results regarding the material misorientation are shown in *Figure 76* and *Figure 77*. The misorientation maps are processed using grain reference orientation deviation (GROD) angle technique, which displays the angular deviation of the local orientation to the mean orientation of the grain. This is automatically processed and extracted

from the software. The reason for choosing GROD is to see whether there is any considerable orientation difference within the grain.

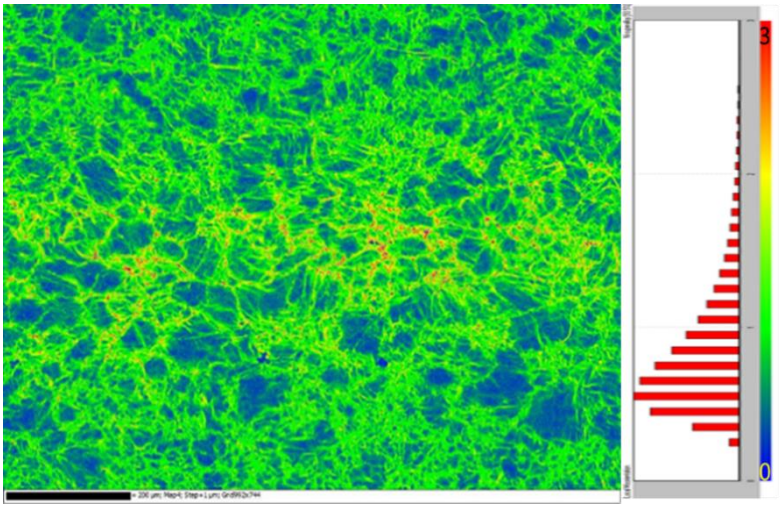


Figure 76: Misorientation map 1

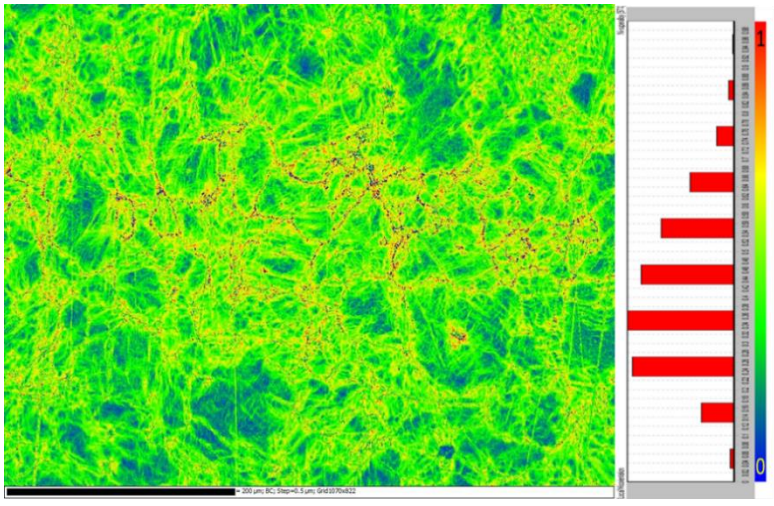


Figure 77: Misorientation map 2

It appears that the areas in the two misorientation maps are composed of homogeneous microstructure with relatively fine grains and a corresponding local misorientation that is very low (less than 1° for all values in map 2) with few values more than 1° in map 1. It is observed that there is a peak around 0.30°. It is seen from the misorientation maps that there is

preferential accumulation of dislocations along the grain boundaries, which will give rise to oxidation along them.

4.5 Stress corrosion cracking testing (SCC tests)

The SCC tests have been performed using constant load. The main aim of performing different SCC tests is to achieve deeper SCC cracks with different duration in order to correlate the function of time (crack growth rate in this case), follow the crack path and morphology of the crack tips for different testing duration. The constant load was applied using four-point bend test in an autoclave. The specimens and autoclave conditions are now detailed.

4.5.1 SCC test specimens

Three SCC specimens have been machined with orientation relative to the rolling direction. The specimens are cut in transverse orientation (T) meaning testing directions are perpendicular as shown in *Figure 78*. These specimens have been machined using electric discharge machining (EDM). The dimensions of each specimen are 60mm x 10mm x 7mm. The geometry of the specimen is shown in *Figure 79*.

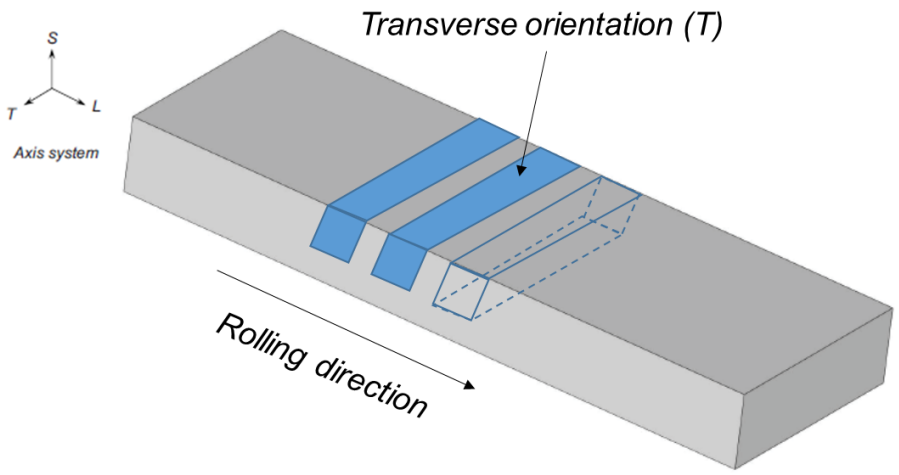


Figure 78: SCC specimen orientation

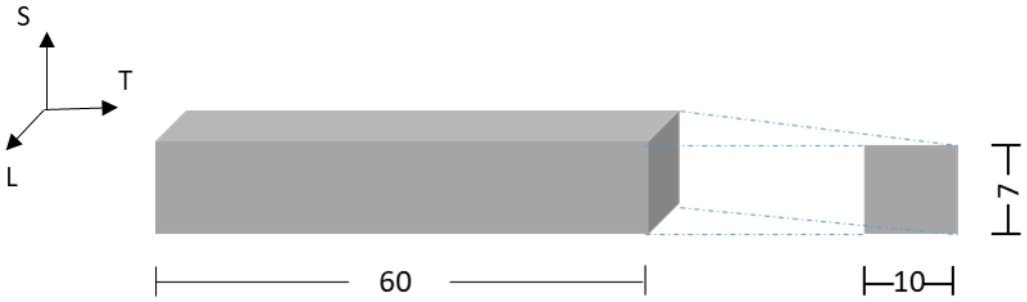


Figure 79: Geometry of SCC specimens (dimensions are in mm)

4.5.2 Autoclave conditions

The three specimens were tested in autoclave subjected to four-point bend test. The side exposed to the environment was polished in the similar way mentioned in *section 4.4.1*. The three tests were of durations 325, 800, and 2000 hours.

4.6 Experimental Set-up

The experimental setup to be modelled is the four-point bend test performed in autoclave as illustrated in Figure *80a* shows the entire autoclave and Figure *80b* presents the schematic illustration of the sample inside the autoclave along with the loading direction and contact with water. The four-point bend test has been adapted mainly to SCC testing as it provides a simple, compact, and easily operated device for applying loads. The load is applied using the push rod drive mechanism. The working principle of this set-up is straightforward; the specimen to be tested is placed in between the four cylindrical rods of 1 mm diameter. The set-up is placed into autoclave exposed to primary water conditions and actively loaded for several hundred hours. The load is applied by moving the lower cylindrical rods attached to the load cell, the gauges control the displacement of these rods. The upper cylindrical rods support the specimen and exert opposite reaction on the specimen for the load applied.

The main advantages of the four-point bend test over other conventional laboratory tests such as U-bends, reverse U-bends, C-rings are that the specimen is always flat, and the gauge length is maintained under a known uniform stress state. It is also easy to carry out post-autoclave characterization analysis on the flat specimens.

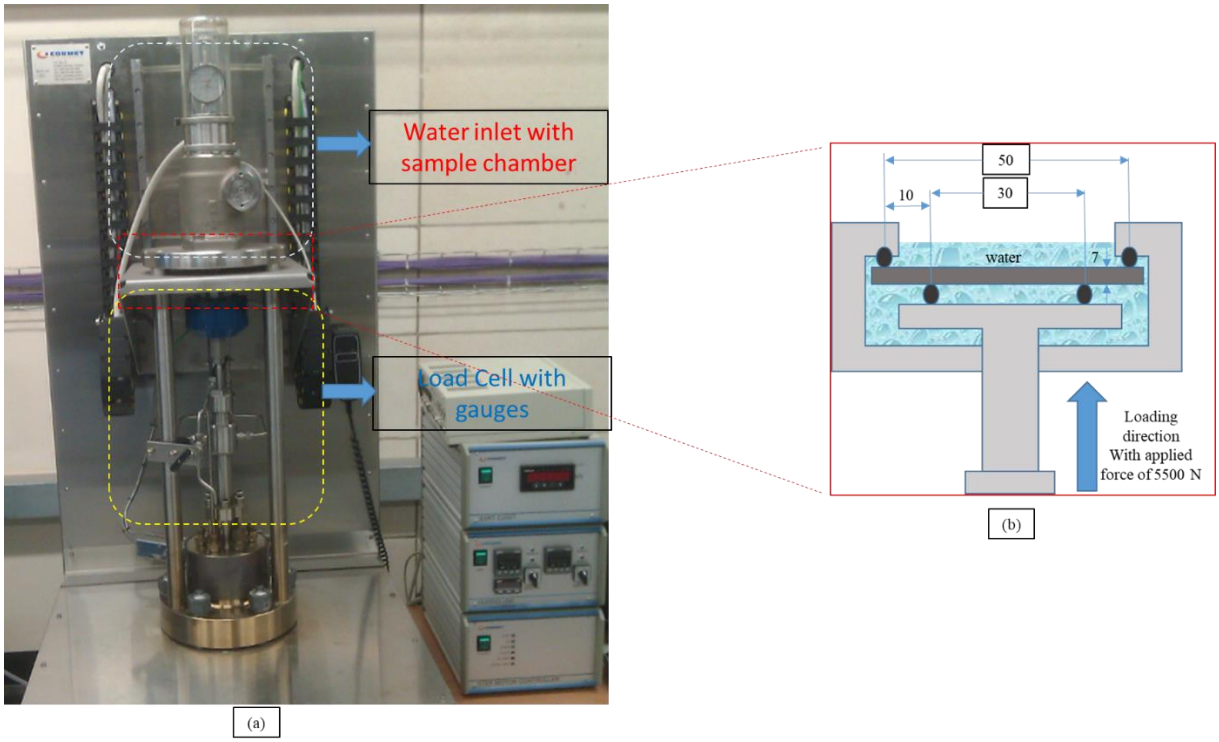


Figure 80: (a) Autoclave used in University of Manchester to perform SCC tests. (b) Schematic illustration of the sample inside the autoclave along with the loading direction and contact with water.

The main drawback of this set-up is that as the temperature raises, the mechanical strength of the material decreases and the specimen, which is plastically strained, has an extra strain imposed due to the drop in the mechanical properties. In other words, stress relaxation occurs as the temperature increases from room temperature to 345°C due to the displacement control. Licheron [248] studied the anisothermal relaxation behaviour in alloy 600 between 20°C and 350°C for C-ring test specimens. The author observed this phenomenon as the temperature was increased; an equilibrium was reached at high temperature with a stress level lower than that applied at 20°C. The author also demonstrated that for a stress applied at room temperature equal to the yield strength of the material at 20°C, the remaining stress at 350°C constitutes to only 80% of the actual applied stress and this decrease was consistent with the evolution of the yield strength.

Thus, only way to accurately evaluate the stress distribution on the specimen under constant load using four-point bend test is by performing finite element analysis.

4.6.1 Water chemistry and loading conditions

The three SCC tests were performed in simulated PWR primary water conditions at 345°C. The reason for choosing 345°C temperature is because the autoclave was unstable for any higher temperature, this was the maximum temperature we could use. However, this also came in to our advantage that, the pressurizer temperature in the reactor is maintained at this temperature. The primary water constituted of pure water with additions of boron as LiOH, H_2O, lithium as H_3BO_3 and hydrogen (as discussed in *Chapter 2 section 2.4.9*). The SCC test was conducted using a refreshed autoclave in simulated PWR water conditions with 2.7 ppm dissolved H_2 at 345^{o}C. With these conditions, the oxidizing potential of the samples was slightly in the reducing side of the Ni/NiO transition, thus corresponding to conditions where SCC initiation is most favourable [248,249]. The geometry of the samples used for this study was a bar 60 mm long and with a square cross section 10 mm × 7 mm that was actively stressed under 4-point bending at 310 MPa. The superficial stress on the sample was calculated using the ASTM G39-99 procedure. Throughout the test, the stress was maintained constant by ensuring active load. *Figure 81* shows the specimen after autoclave test.



Figure 81: Specimen after 4-point bend test in autoclave.

4.7 Crack Identification and length analysis

4.7.1 First autoclave test specimen

The first autoclave test was completed after 325 hours. The specimen was cut, and a sample was extracted from the region between the inner rollers (region where there is max. tensile stress). This sample was then mounted and examined under Merlin-SEM to properly identify the cracks and not to be mistaken with other features like dents and scratches. Six different cracks were chosen for measuring the crack length along the S direction (depth from the surface of exposure LT direction) along the cross section. FIB 200 was used to make trench and relieve the cracks cross section as shown in *Figure 82*. The crack length was measured at two different tilts and compensated using trigonometric functions to calculate the actual length. The crack length measurements for sample 1 is tabulated in *Table 9*. Measured. The average crack length is measured to be 2.70 ±1.15 µm.

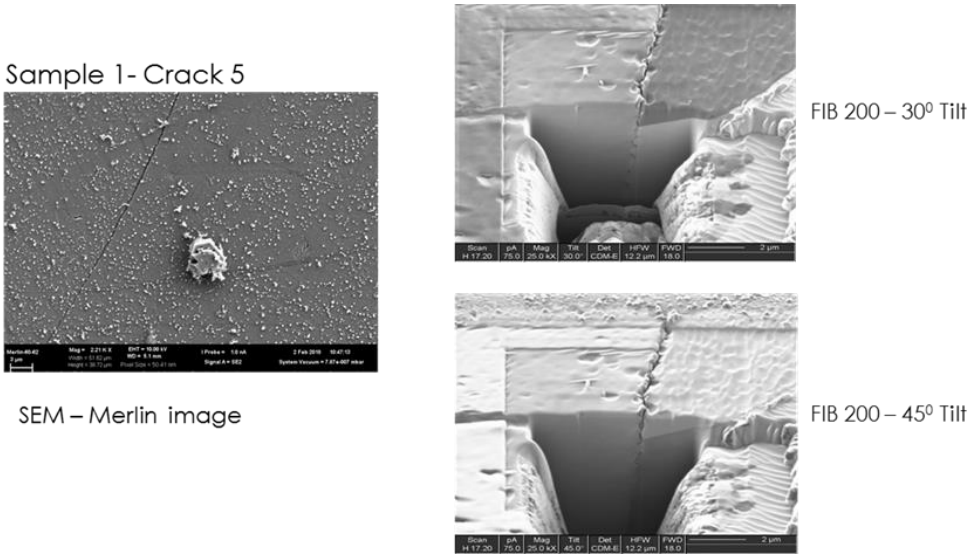


Figure 82: Crack length analysis of sample 1 (325 hours).

Table 9: Crack length measurement of sample 1 (325 hours) cross section.

Sample 1	**Length (µm)**	**Width to Depth Ratio**
Crack 1	3.2	0.005
Crack 2	1.2	0.006
Crack 3	3.65	0.006
Crack 4	2.4	0.007
Crack 5	3.51	0.01
Crack 6	2.2	0.012
Average	2.70 ± 1.15	

4.7.2 Second autoclave test specimen

The second autoclave test was completed after 800 hours. The specimen was cut, and a sample was extracted from the region between the inner rollers (region where there is max. tensile stress). This sample was then mounted and examined under Merlin-SEM to properly identify the cracks and not to be mistaken with other features like dents and scratches. Five different

cracks were chosen for measuring the crack length along the cross section similar to the first autoclave test specimen. It is shown in Figure *83*. The crack length measurements for sample 2 is tabulated in *Table 10*. The average crack length is measured to be 5.1 ±1.2 µm.

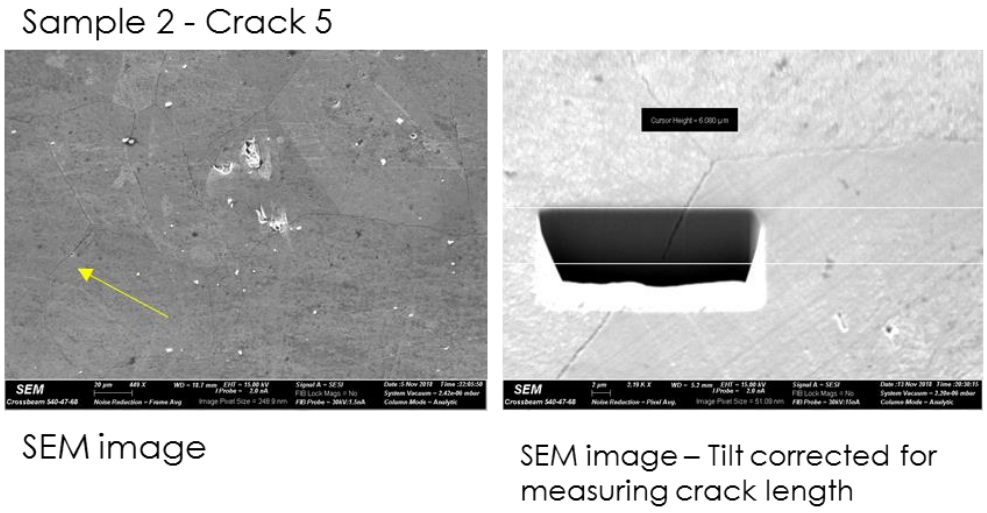


Figure 83: Crack length analysis of sample 2 (800 hours).

Table 10: Crack length measurement of sample 2 (800 hours) cross section.

Sample 2	**Length (µm)**
Crack 1	6.6
Crack 2	4.5
Crack 3	3.8
Crack 4	4.7
Crack 5	6.1
Average	5.15 ±1.2

4.7.3 Third autoclave test specimen

The third autoclave test was completed after 2000 hours. The specimen was cut, and a sample was extracted from the region between the inner rollers (region where there is max. tensile stress). Five different cracks were chosen for measuring the crack length along the cross section

similar to the first autoclave test specimen. It is shown in *Figure 84*. The crack length measurements for sample 3 is tabulated in *Table 11*. The average crack length is measured to be 5.5 ± 1.4 µm.

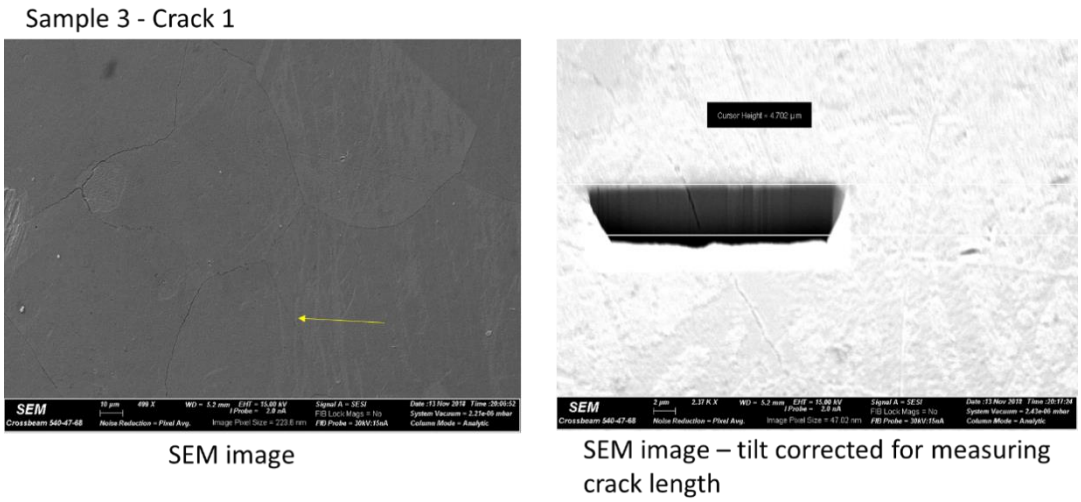


Figure 84: Crack length analysis of sample 3 (2000 hours).

Table 11: Crack length measurement of sample 3 (2000 hours) cross section.

Sample 3	**Length (µm)**
Crack 1	4.7
Crack 2	6.2
Crack 3	6.3
Crack 4	5.1
Crack 5	5.4
Average	5.54 ±1.36

4.7.4 Crack Analysis

In order to correlate the cracks with the nature of grain boundaries, EBSD analysis was carried out on the first autoclave sample after 325 hours of testing at 345°C. The surface analysed along the cross section by EBSD is 2000 µm x 5 µm with a step of 0.1 µm. In this region analysed, there were 86 grain boundaries of which 38 were ∑3 CSL boundaries, 26 were other

CSL boundaries and the rest were RHAGBs. From the observed boundaries, 2 of the other type CSL boundaries (one ∑17 and one ∑21 are the cracked other CSL boundaries) and 12 RHAGBs exhibited cracks. None of the ∑3 CSL boundaries had cracks and these boundaries have been excluded as the percentage evaluation of cracked grain boundaries do not include the twin boundaries. The percentage of the fractured grain boundaries are thus estimated to be ~30%. Figure *85* shows the nature of the grain boundary distribution and Figure *86* shows the fraction of cracked grain boundaries.

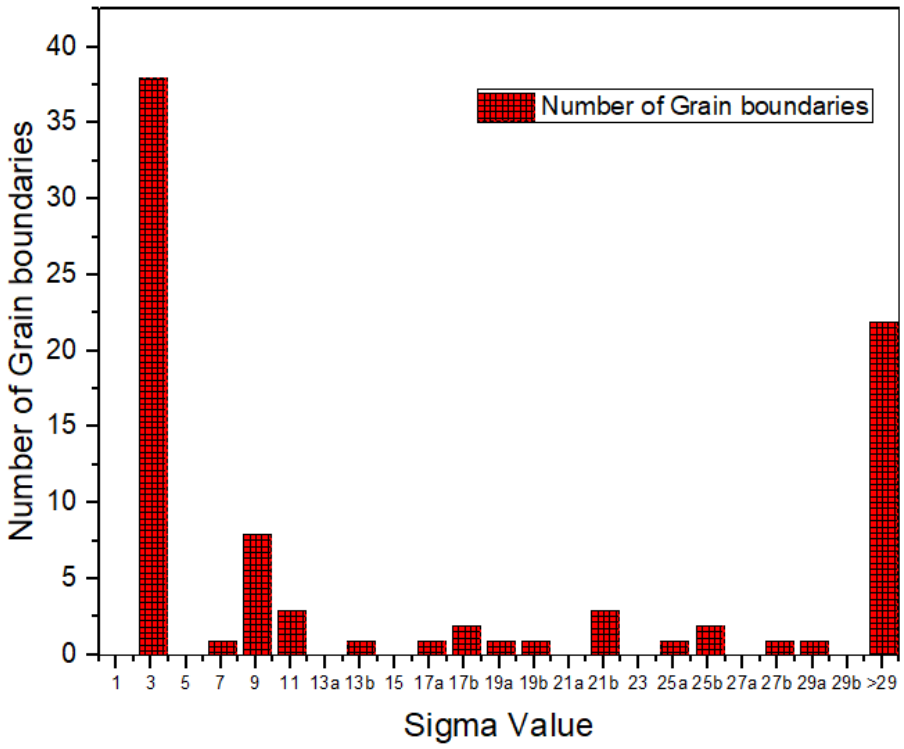


Figure 85: Grain boundary character distribution of the analysed Alloy 600.

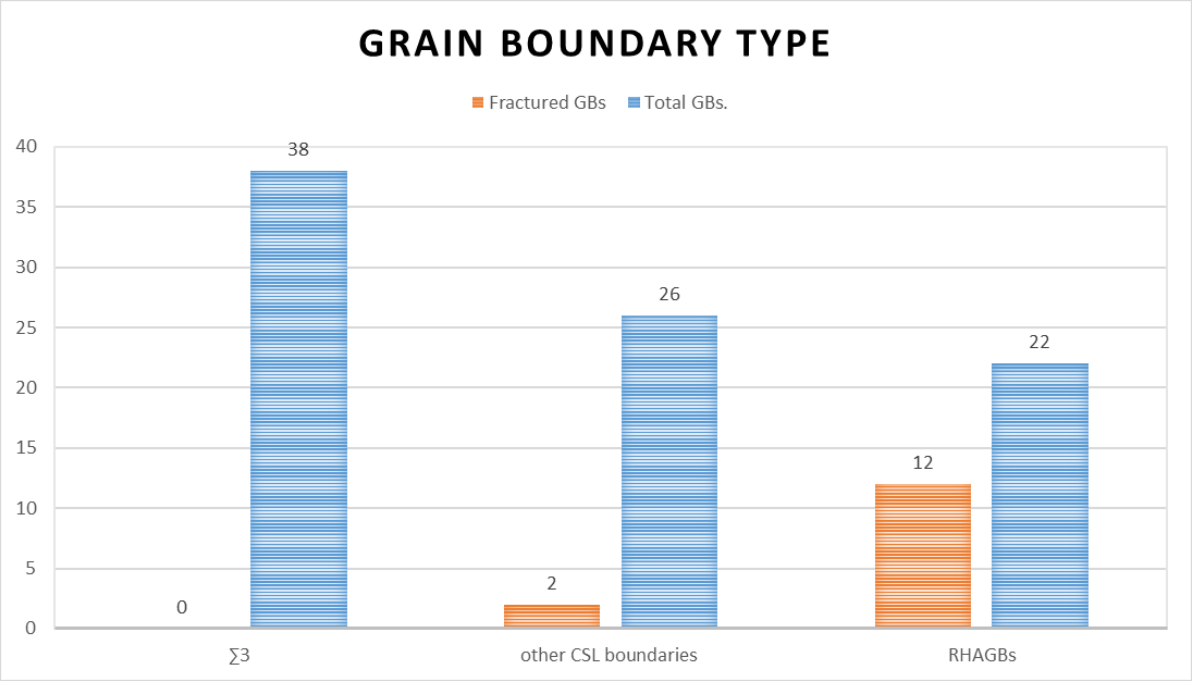


Figure 86: Grain boundary type along with the crack analysis.

4.7.5 Carbide Identification and Chromium Zone depletion

There is a possibility of two different types of carbides in alloy 600: (1) M_7C_3 and (2) $M_{23}C_6$ as discussed in section 2.2.2 and 2.2.3. For identifying the type of carbide, present TEM samples were extracted using the FIB system in Zeiss Crossbeam 540. TEM analysis were performed with JEOL 2100 for TEM imaging and selected area diffraction was done on carbides and is shown in *Figure 87*.

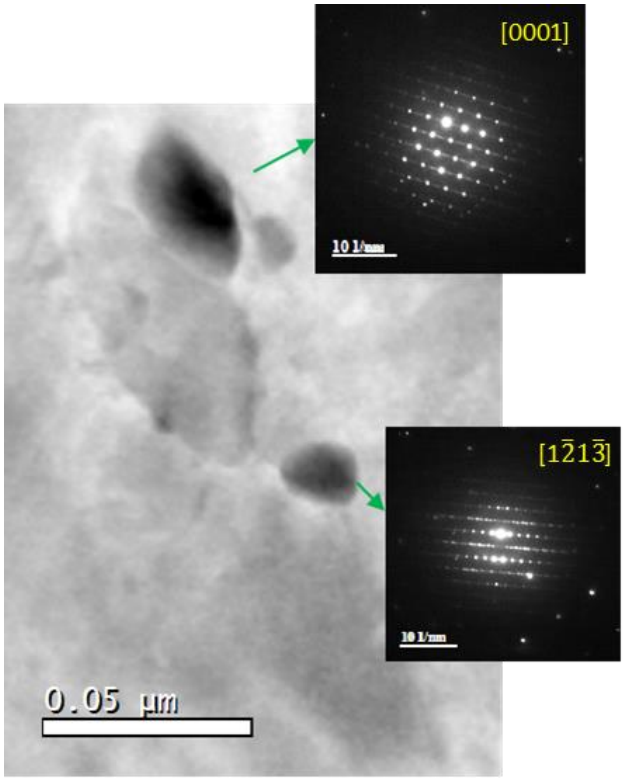


Figure 87: Selected Area Diffraction of M_3C_7 Carbides

It can be identified from the Selected Area Diffraction (SAD) patterns that the type of carbide is **M_3C_7** (M can be either Cr or Fe or combination of both). The size of the carbides is measured to be 90 ± 20 nm (radius ~ 45nm).

1. **STEM – HAADF imaging on the crack tip extracted in ARM**

The crack tips were extracted using Zeiss Crossbeam 540 for further analysis. High-resolution analysis such as STEM and EELS was done using JEOL ARM 200F (cold-FEG) operating at 200 kV with Quantum Gatan Image Filter (GIF) spectrometer. Both core and low loss spectra were acquired correcting spatial drift and recalibrated in energy using zero loss peak as the reference.

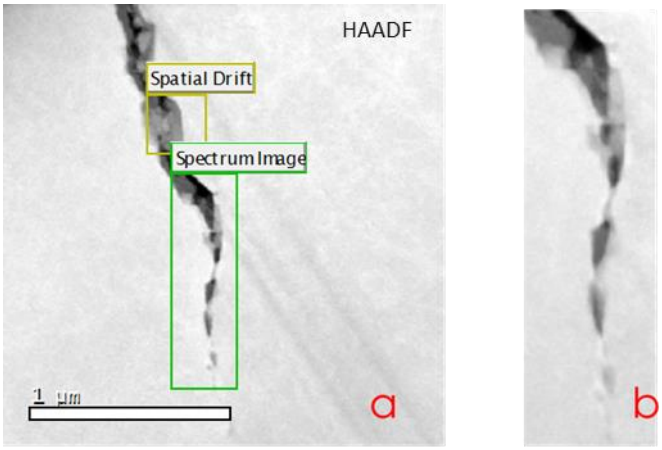


Figure 88: STEM-HAADF imaging on the crack tip from crack 3 (a) Survey image with spatial drift (b) actual spectrum image.

Principal Component Analysis (PCA) was performed using Hyperspy software to reduce the noise. The convergence and collection half angles are 31 and 41 mrad respectively.

2. EELS quantification

The EELS quantification was done using Digital Micrograph employing standard background subtraction method.

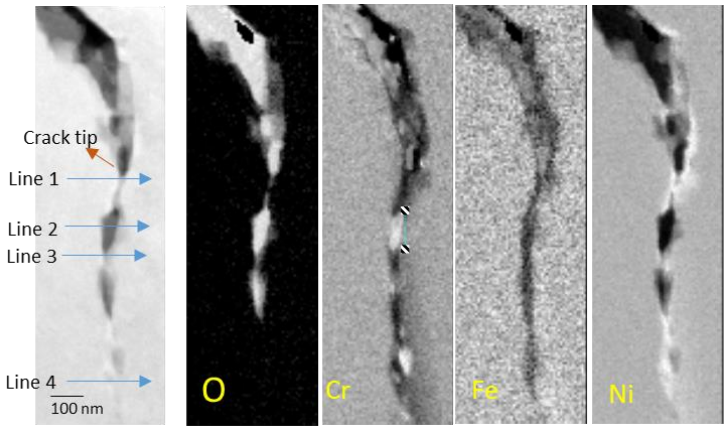


Figure 89: EELS line scanning locations on STEM-HAADF image and EELS Elemental composition of O K edge, Fe/Cr/Ni L edge maps.

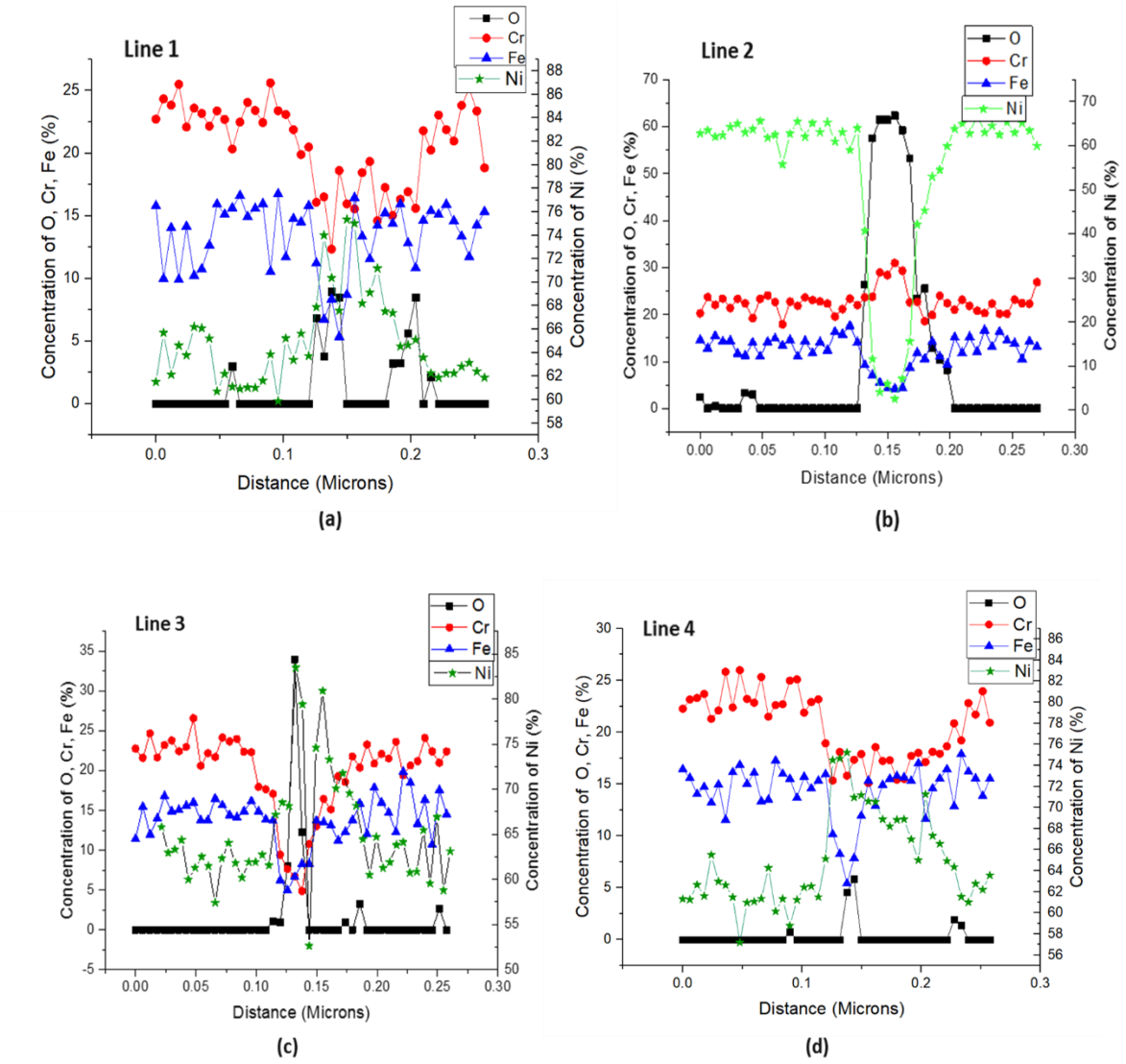


Figure 90: Composition line profiles obtained corresponds to lines in *Figure* 70 (a) Region just ahead of crack tip (b) On the carbide (c) Region ahead of carbide (d) far from crack tip.

The Line 1 represents the region ahead of crack tip. This region is Cr-Fe reduction associated with Ni- enrichment. The Ni-enrichment may also due to outward diffusion of Cr and Fe in the carbide ahead of it, which thermodynamically favours the formation of Ni- rich region. However, there is no clear case of Cr-depletion in this case. The Line 3 and Line 4 has similar composition as Line 1, but Line 3 was obtained between two carbides and Line 4 much ahead of the crack.

Across Line 2 (the region across Carbide), it can be seen that the Cr is rich due to the Cr_7C_3. This region also sees a large portion of O. This might be because Carbide is acting as oxygen reservoir. Thus, preventing further oxidation. This layer prevents the diffusion of oxygen to an extent because similar kind of O composition is not observed in the next carbide.

4.8 Summary

Initial pre-characterization of the as-received Alloy 600 solution annealed material had a grain size estimated to be 40 ± 16μm. The grain boundary characteristics revealed that almost 99% grain boundaries are HAGBs of which 72% constitutes to Σ3 type grain boundary (annealed twin boundaries) presented in *Table 7*. The grain boundary coverage (carbide coverage) was calculated to be 12 ± 3%. The specimen was then subjected to SCC tests in autoclave for three different time durations (325, 800 & 2000 hours) at 325°C. The post- characterization on the SCC tested samples revealed the average crack depth as 2.7, 5.15 and 5.5 μm for 325, 800 and 2000 hours respectively. The crack analysis of 86 boundaries excluding the ∑3 revealed that 30% of the grain boundaries are fractured with 2 other CSL boundaries and 12 of the RHAGBs. The type of carbide was found to be M_7C_3 type and the radius was measured to be ~45nm. All these preliminary results are the important input parameters which will be fed in to model for IGSCC initiation.

5 EFFECT OF LOCAL GND DENSITY TO STUDY SCC CRACK INITIATION IN ALLOY 600

5.1 Introduction

In the initial framework of the thesis, TKD analysis was not originally planned as a part of the model validation approach. Past research in the group on SCC crack propagation involved using conventional (off-axis) TKD and reported that local misorientation and dislocation density around SCC crack tips is an important factor in crack propagation [34,249]. I tried to further extend this to SCC initiation and observe the role of dislocation density here using on-axis TKD. This provided low sample drift and better estimation of misorientation and GND density. The details of this technique is discussed in detail in *section 3.4.1*. The results proved to be useful addition to the thesis, even though it does not directly relate to the model validation. The results about initiation through TKD demonstrated the shortcomings in the current Local model approach and pave a way for proposing new extension that could be relevant and useful in the future iterations of the model.

In this chapter, we consider the possibility of using geometrically necessary dislocations (GNDs) and strain maps calculated from high-resolution TKD patterns (details in next section) to characterize the build-up of dislocations around grain boundaries and its relation to intergranular crack initiation. The chapter is based on the findings presented in [226].

There is limited information on the relationship between strain and crystallographic features of different regions of the grain boundary. It is important to characterize the grain boundary because SCC is predominantly intergranular and to investigate the local changes that make a grain boundary susceptible. This study includes strain measurements and GNDs measurements.

After autoclave testing, the samples exhibited several intergranular cracks. Two cracked grain boundaries were selected for analysis. One of them (cracked grain boundary 1), contains a cracked and an uncracked portion (oxidized part, ahead of the crack). This grain boundary was at a very shallow angle (5°) with respect to the loading direction, which probably affected its SCC mode, and where the strain analysis might provide useful information. Lastly to have a comparison of the GNDs, a similar grain boundary (in terms of misorientation) in the as-received material prior to autoclave testing was selected. To improve the statistics another cracked grain boundary from a different region of the sample. These samples were chosen with the idea of obtaining the minimum amount (threshold value) of GNDs required for the crack to initiate and attempting to use the measured elastic strain and stress to elucidate the mode of cracking.

5.2 Materials and Experimental methodologies

5.2.1 Materials used

The material used for this study is Alloy 600, a Ni-based alloy. The chemical composition of this alloy, grain size, sample preparation, SCC tests and post autoclave test analyses done on the sample are presented in *Chapter 4*.

5.2.2 Site-specific sample preparation using FIB

Sample preparation is essential for the success of TKD analysis. A dual beam Zeiss Crossbeam 540 FIB-SEM was used for lifting-out the samples containing the regions of interest. Details on the procedure can be found on [230]. TEM samples were prepared from a grain boundary showing partial intergranular SCC along its length. This way, two samples could be extracted: one containing a portion of cracked grain boundary and another with a portion of the same

grain boundary but uncracked, as shown in *Figure* 91. Two different cracked grain boundaries were studied for increased statistical relevance. An extra sample was prepared from the as-received material (before autoclave testing) to characterize the dislocation densities around similar grain boundaries before deformation and cracking.

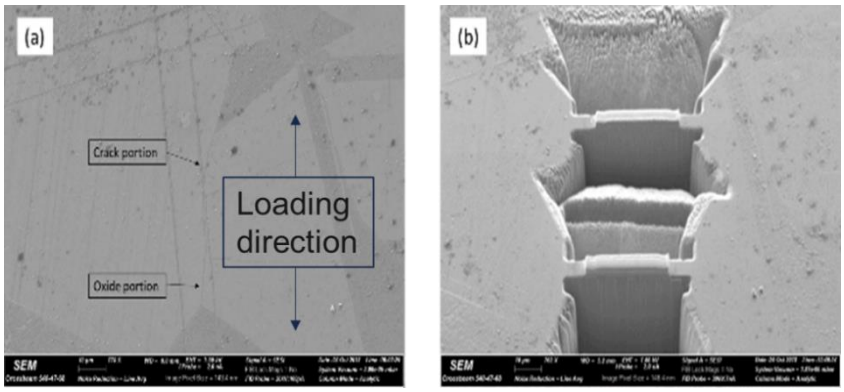


Figure 91: SEM SE images showing (a) the location of selected grain boundary with crack and oxidized portions (b) After making trench for TEM lift out

5.2.3 TKD analysis

In this study we have used a new TKD configuration developed recently called “on-axis” TKD as discussed in section 3.4.1 The OPTIMUS™ head also contains three forescattered electron diodes (FSD). When using the FSD imaging mode, the center of low-angle forescattered electron diode is aligned normal to the optic axis for generating bright-field images, and the two high-angle diodes for dark-field images [250].

Kernel Average Misorientation (KAM) maps, calculated from the TKD data, show the average misorientation angle of a given point with respect to all its nearest neighbors. The results are step size dependent and can sometimes be on the same order of magnitude as the measurement noise. The measurement noise is often linked to the quality of the Kikuchi patterns from which the orientation is usually determined. There are many studies in which the authors have made

use of KAM to measure the plastic zones around the crack tips/grain boundaries [230,240,251–253]. They were calculated for all the TKD datasets presented in this study.

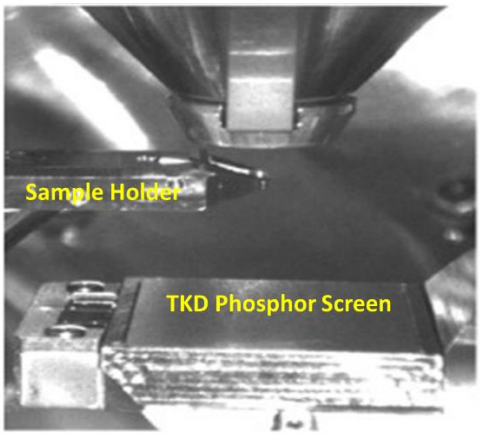


Figure 92: Chamber camera image showing the objective pole piece (top), the TKD sample holder (middle) and the "on-axis" TKD scintillator [231]

TKD maps were collected using a Zeiss Merlin FEG-SEM and eFlashHR camera with Bruker OPTIMUS^{TM} detector head system. An accelerating voltage of 30kV and a probe current of 2nA were used. All the other microscope and acquisition parameters are listed in Table *12*. After the TKD, the data file is processed using CrossCourt 4 software.

Table 12: Microscope and acquisition parameters

Microscope	Zeiss Merlin FEG-SEM
Configuration	On- axis TKD
Camera	Bruker eFlashHR camera
Detector	Bruker OPTIMUS^{TM} detector head
Accelerating Voltage	30 KeV
Probe current	2nA
Working distance	5.1 mm
Sample tilt	0°
Detector sample distance	19.6 mm
Acquisition/indexation software	Bruker Esprit 2.1

Pattern resolution	800 x 600 pixels
Step size	5 nm
Min. bands for indexation	10 bands

5.2.4 TKD patterns processing

Once the TKD map has been acquired, the diffraction patterns for each point on the map are saved and processed using CrossCourt 4 software. Pre-processing data filters help us to obtain the KAM maps and Image Quality (IQ) maps. The analysis essentially involves picking a reference pattern (to be chosen as a point with least deformation which is away from the grain boundary) and measuring pattern shifts with respect to this point for all the other points in that grain. The patterns are then subdivided into smaller regions of interest (ROIs). In case of on-axis TKD patterns, care has been taken to avoid using ROIs close to the center of the Kikuchi pattern, where there is influence of the bright transmitted beam. The measured shifts are used to estimate elastic strain distribution and lattice rotation (which can then be used to estimate GND density content). All CrossCourt 4 GND density calculations were performed based on L^1 optimization method developed by Wilkinson et al. [254], as it out of scope of the current project this method is not discussed in detail in this thesis, more details about the procedure are available in the literature [226,254] for reader's interest.

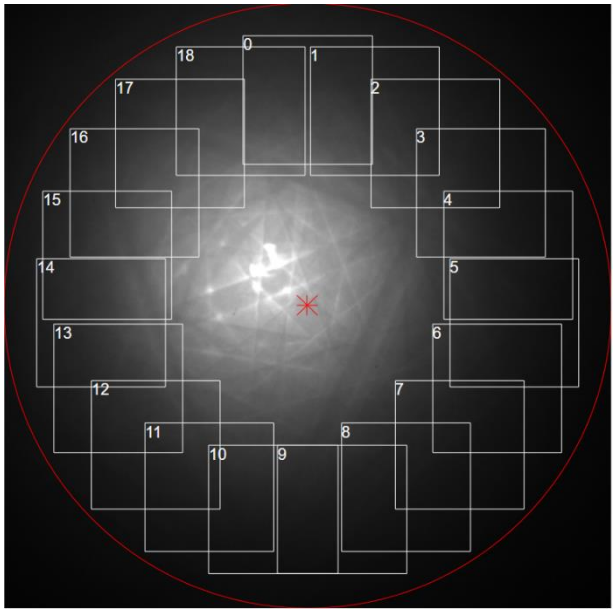


Figure 93: An example of TKD pattern with ROIs used for cross-correlation analysis marked.

5.2.5 Transmission Electron Microscopy (TEM) Characterization

TEM is the conventional tool for measuring and determining dislocation densities. TEM characterization of dislocations was performed on a JEOL 2100F LaB_6 microscope at 200 kV. In TEM observations, some defects may be invisible at certain sample depth or diffraction conditions. To improve the visibility of the defects, we had used the convergent weak beam dark-field imaging conditions [220], combined with electron beam precession method [255,256]. Precession of the electron beam was controlled by a script to capture 10 exposures with slightly varying deviation parameters ~0.01 nm^1, under weak beam conditions from 8g to 9g. The sequence of images were then aligned and stacked using ImageJ [257] to produce a single micrograph with reduced extinction distance-related absences of defects. The stacked micrographs were then shown in inverted contrast after background subtraction using the rolling-ball method (radius =40 pixels) in ImageJ [257]. More details about this technique and image acquisition procedure can be found in [258].

Direct determination of the average dislocation density in TEM images is carried out based on the line intersection method [259]:

$$\rho=(N_v/L_v+N_h/L_h)/t$$

where N_v is the number of intercepted dislocations by a length L_v along the vertical grid, and similarly N_h and L_h are the parameters obtained along the horizontal grid. The sample thickness, t, is around 80 nm. This sample thickness is also very important for TKD-GND analysis [231]. High levels of pattern background noise in too thick samples and obvious discrete diffraction spots in too thin samples limit the accuracy of GND measurements. The thicknesses of the region of interest was determined using Electron Energy Loss Spectroscopy (EELS) in a JEOL ARM 200F microscope operating at 200 kV with a pixel size of 10 nm, a convergence angle of 30 mrad and a collection angle of 40 mrad using the t/λ method suggested by Malis et al. [260], which after experimental calibration [261] can determine the absolute thickness to an accuracy better than 5%.

5.3 Results

Two cracked grain boundaries were selected for analysis. One of them (cracked grain boundary 1), contains a cracked and an uncracked portion. This grain boundary was at a very shallow angle (5°) with respect to the loading direction, as shown in *Figure 91*, which probably affected its SCC mode, and where the strain analysis might provide useful information.

5.3.1 Cracked grain boundary 1

The sample containing the cracked portion of the grain boundary was imaged using the forescatter diodes (Argus detectors) before TKD analysis (*Figure* 94*a*), providing an insight on how the dislocations are piled up along the crack flank, this was later confirmed by TEM imaging. After this initial screening, TKD maps were obtained as described previously. *Figure* 94*b* shows the Inverse Pole *Figure* map (out of the plane) of the cracked region. The misorientation between the grains is found to be approximately 18.8^{o}.

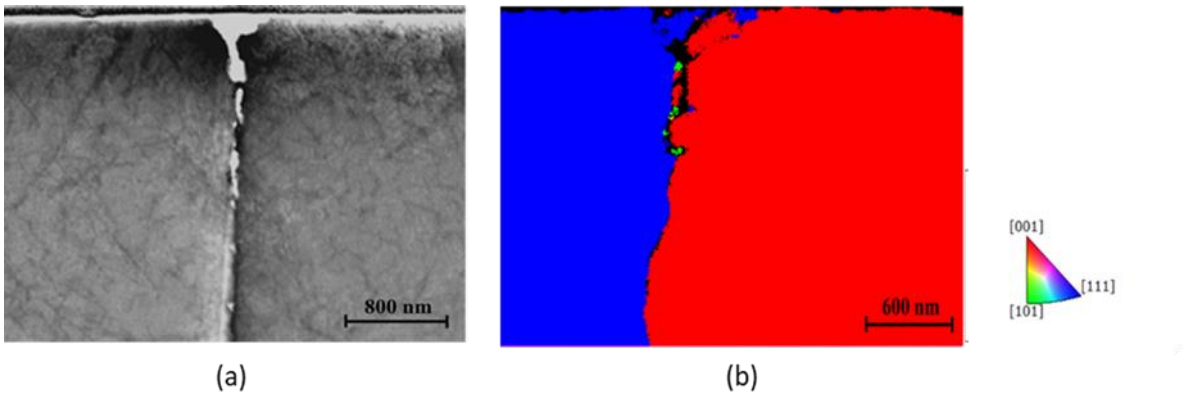


Figure 94: (a) Forescatter image and (b) Inverse Pole *Figure* (IPFZ) map of cracked grain boundary 1

Figure 95 shows the elastic strain distribution around the crack region with the strain distributions in ε_{22} suggesting that there is mostly tensile strain close to the crack flank. This is also in agreement with the sample lift out being in the tensile region of the 4-point bend test. With the chosen reference points, it is obvious that in the area above this point, the elastic strain distribution is tensile, while below it is compressive (with regards to the reference point, it gives relative stress meaning the regions of compression are less tensile the reference point itself). The strain in *Figure* 95 also seem to correspond to the dislocation pileups observed in the forescatter image in *Figure* 94*a*. It will be shown later that these pileups are also oriented along the slip directions in the corresponding grain.

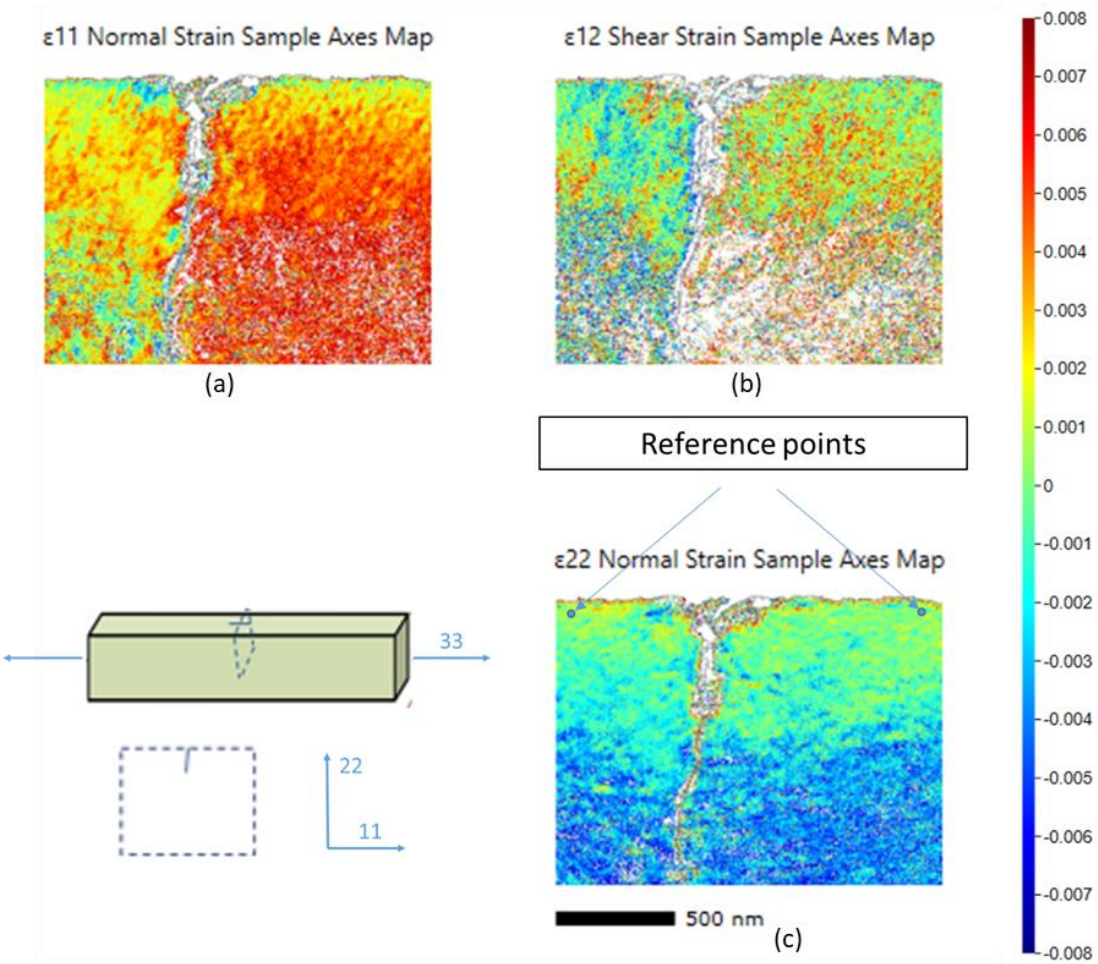


Figure 95: Elastic Strain maps around the cracked GB 1 region along (a) ε_{11} (b) ε_{12} (c) ε_{22}

The strains ε_{11} and ε_{22} refers to the normal strain along x and y directions respectively with respect to sample axis and ε_{12} refers to the shear strain along the xy of the sample axis.

5.3.2 Uncracked grain boundary 1

The sample containing the uncracked part of the grain boundary exhibited intergranular oxidation with a depth of 3 µm. It was imaged using the forescatter diodes before TKD analysis and this provided insights on how the dislocations are piled up along the grain boundary as a result of deformation. *Figure* 96 shows the forescatter image and IPF-Z maps around the oxidized grain boundary region. Note that, due to detector saturation, the oxidized portion of the grain boundary appears white and similar to an open crack, but a careful examination

confirmed that it was only oxidized down to 3 μm and uncracked. After this, a TKD map was obtained in a similar way as the cracked grain boundary and analyzed using Crosscourt 4 software.

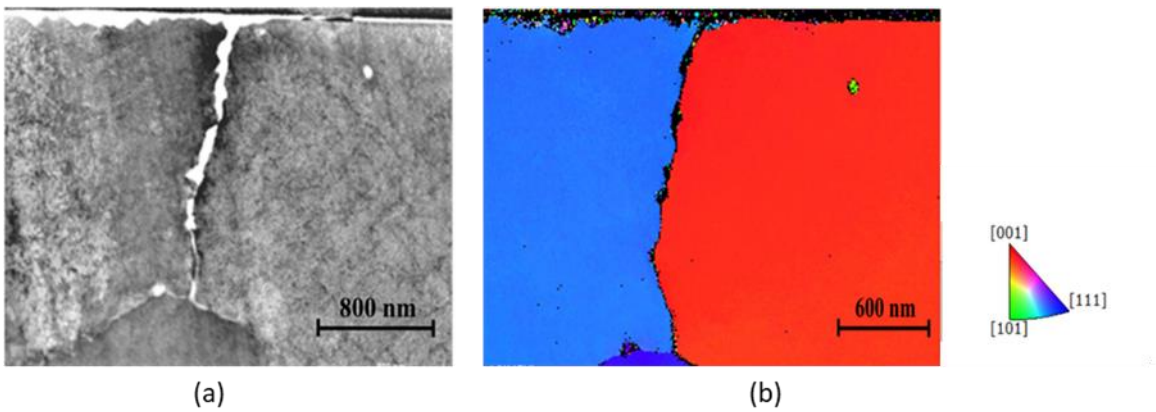


Figure 96: (a) Bright field forescattered electron image and (b) Inverse Pole *Figure* (IPFZ) map of the uncracked portion of GB 1

Figure 97 shows the elastic strains around the oxide grain boundary. It is seen that in the strain ε_{22} one grain has higher compressive strain and the other grain has higher tensile strain with reference to the grain boundary plane in the center.

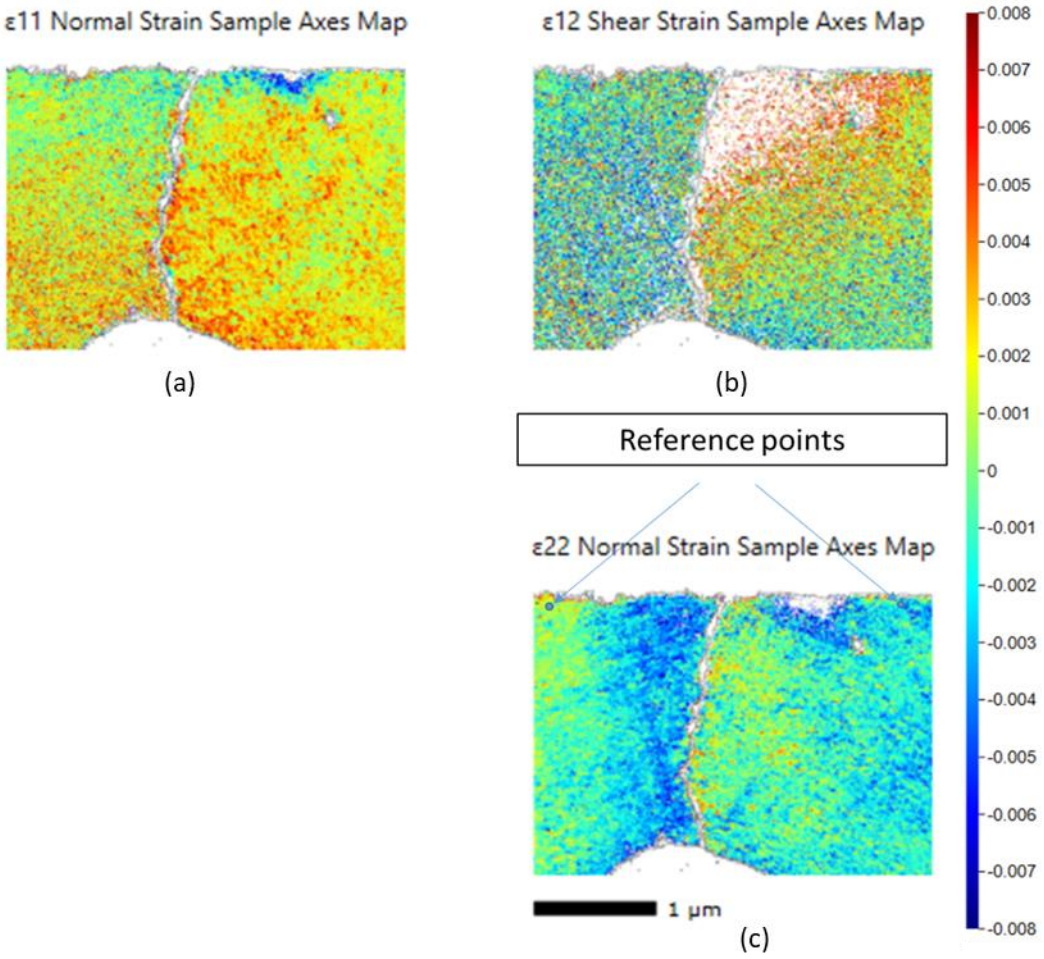


Figure 97: Elastic Strain maps around the uncracked portion of GB 1 along (a) ε_{11} (b) ε_{12} (c) ε_{22}

5.3.3 As-Received grain boundary

An EBSD scan was run on the as-received sample before autoclave testing in order to find a similar grain boundary to the cracked grain boundary 1 (with a misorientation close to 18.8°). *Figure* 98 shows the selected grain boundary which was extracted in cross-sectional orientation as a TEM lift-out for analysis.

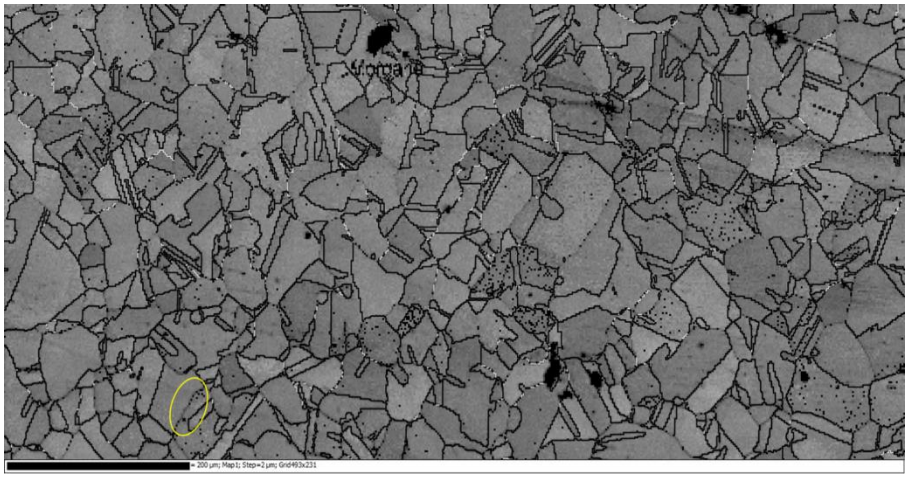


Figure 98: EBSD grain boundary map from the as-received sample showing the selected GB (circled) with a misorientation of 19°

Using a similar routine as in the above cases, the as-received sample was analyzed using Argus forescatter detector before TKD analysis. The forescatter image in *Figure* 99 showed no pile up of dislocations as seen in the two samples extracted from the cracked grain boundary. The elastic strain map in *Figure* 100 only shows regions with much lower strain, likely due to prior thermal treatment.

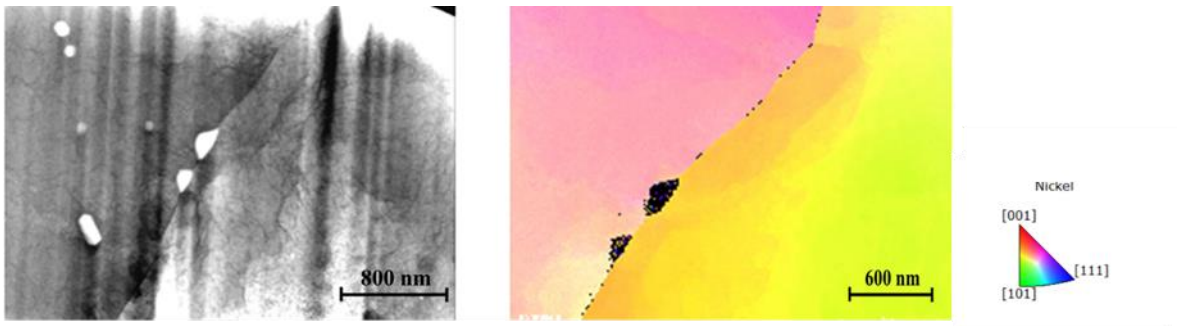


Figure 99: (a) Bright field forescattered electron image and (b) Inverse Pole *Figure* (IPFZ) map of as-received grain boundary region

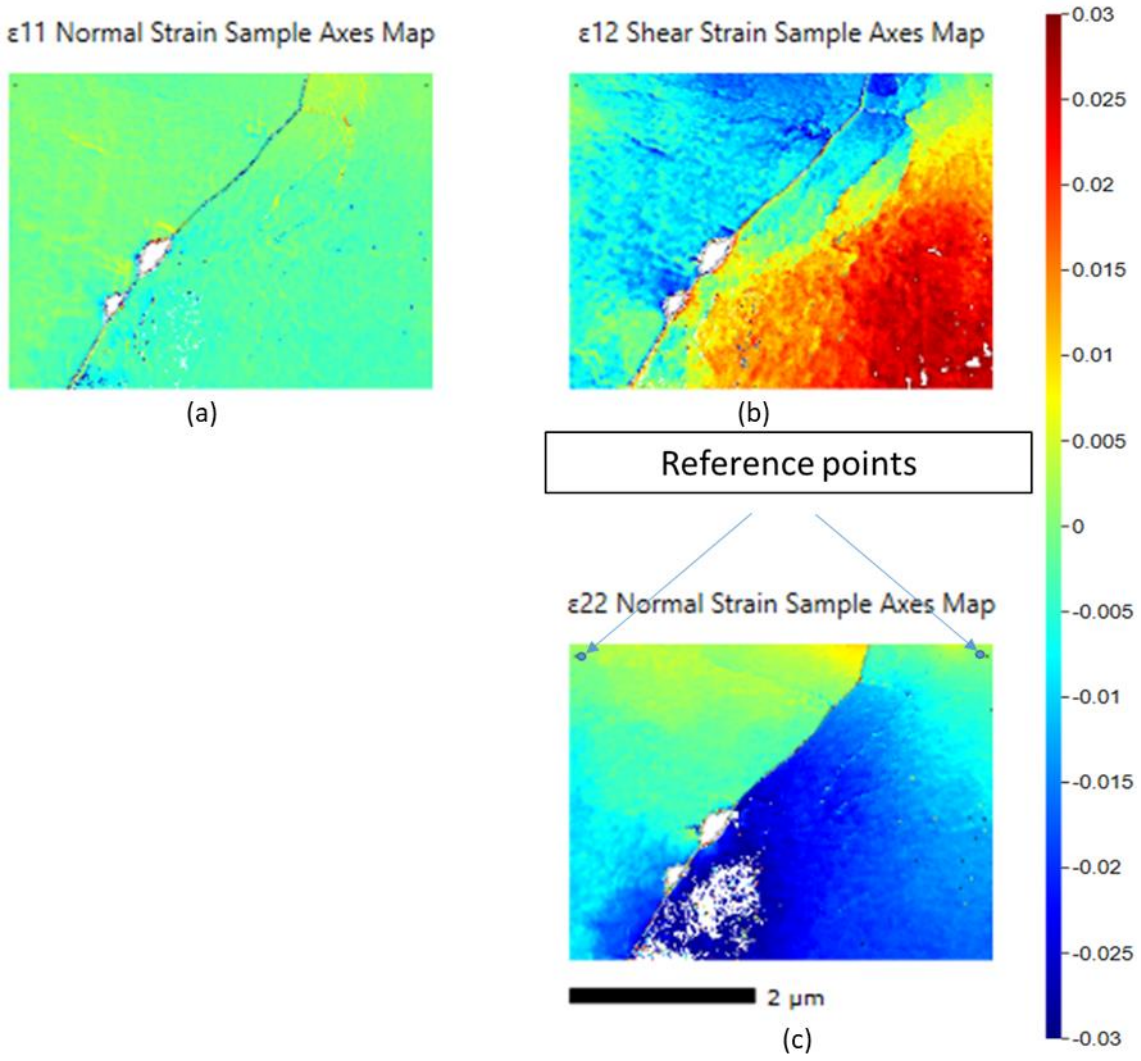


Figure 100: Elastic Strain maps around the as-received grain boundary region along (a) ε_{11} (b) ε_{12} (c) ε_{22}

5.3.4 Cracked grain boundary 2

In order to improve the significance of the measurements around cracked grain boundaries, a sample containing a different cracked grain boundary was lifted out and analyzed. *Figure* 101 shows the location of the crack grain boundary 2 with respect to the loading direction. The cracked grain boundary 2 was imaged using the forescatter diodes (Argus detectors) before TKD analysis (*Figure* 102*a*), providing insights on how the dislocations are piled up along the

crack flank. After this initial screening, TKD maps were obtained as described previously. *Figure* 102*b* shows the Inverse Pole *Figure* map (out of the plane) of the cracked region. The misorientation between the grains is found to be approximately 17^{o}.

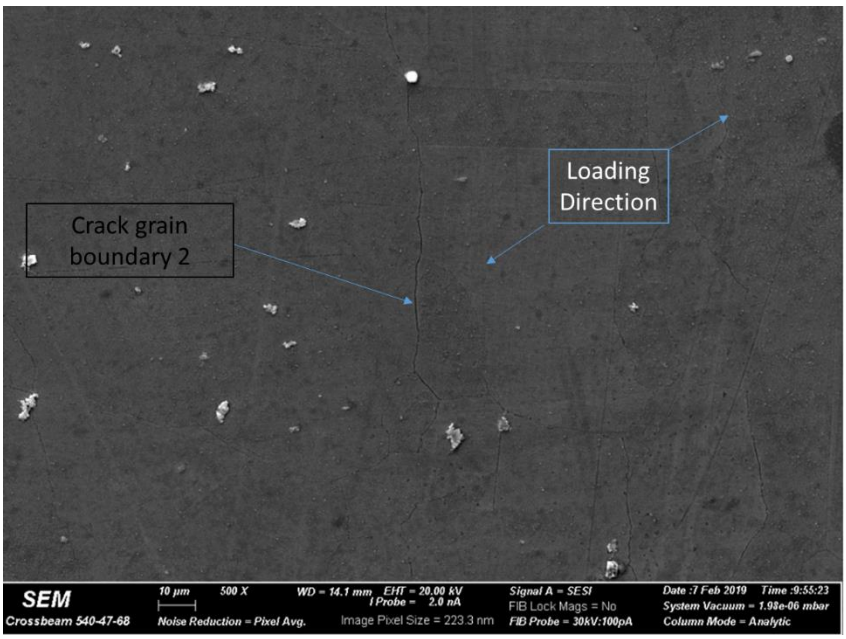


Figure 101: SEM (SE) image of the location of crack grain boundary 2 with respect to loading direction

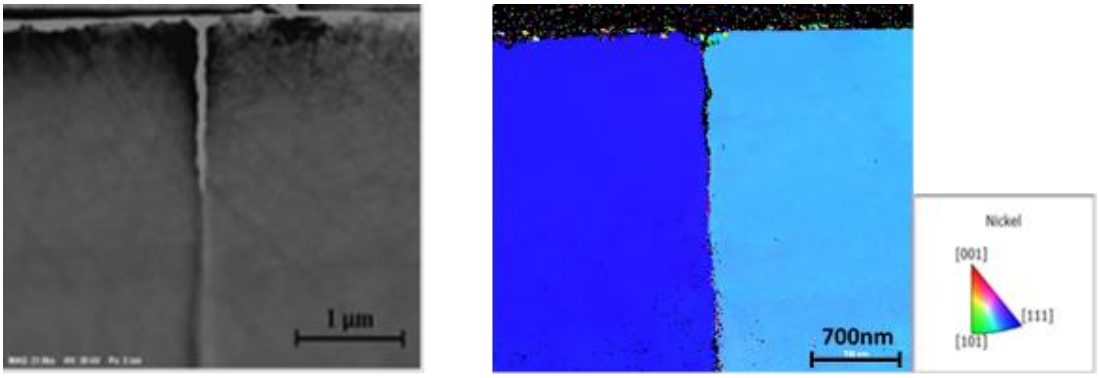


Figure 102: (a) Bright field forescattered electron image and (b) Inverse Pole *Figure* (IPFZ) map of crack grain boundary 2 region

Figure 103 shows the elastic strain distribution around the crack 2 region with the strain distributions in ε11 suggesting that there is mostly tensile strain close to the crack flank. This is also in agreement with the sample lift out being in the tensile region of the 4-point bend test

as seen in cracked grain boundary 1. With the chosen reference points, it is obvious that in the area above this point, the elastic strain distribution is tensile, while below it is compressive. The strain in *Figure* 103 also seem to correspond to the dislocation pileups observed in the forescatter image in *Figure* 102*a*. It will be shown later than these pileups are also oriented along the slip directions in the corresponding grain.

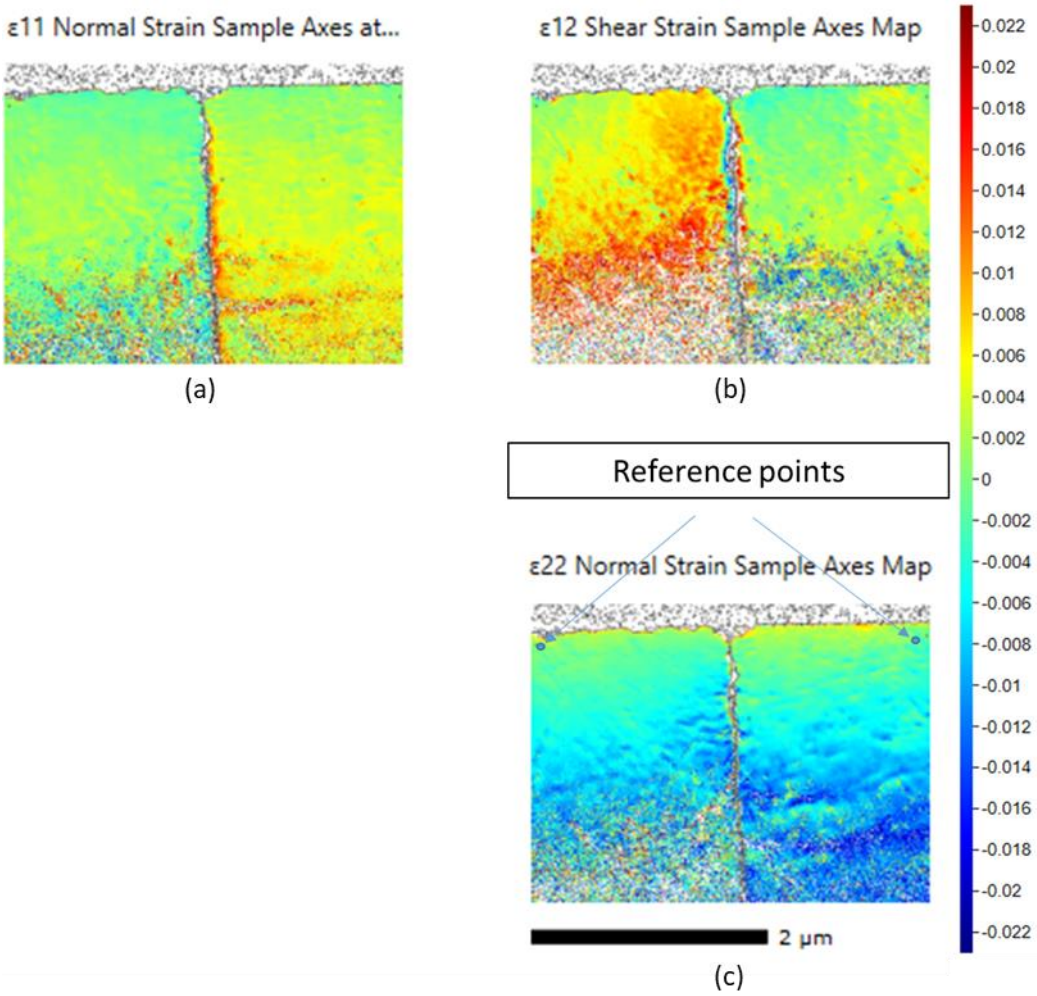


Figure 103: Elastic Strain maps around the cracked grain boundary 2 region along (a) ε11 (b) ε12 (c) ε22

5.3.5 *Kernel Average Misorientation (KAM) characterization*

Figure 104 shows the kernel average misorientation (KAM) maps of the three samples analyzed as part of the grain boundary 1 study. Each pixel represents the misorientation average value (in degrees) with regards to all the neighboring pixels. A color temperature scale (dark blue to red) is used for easy visualization. The regions with high misorientation average appear brighter (green, yellow) than those with less misorientation average.

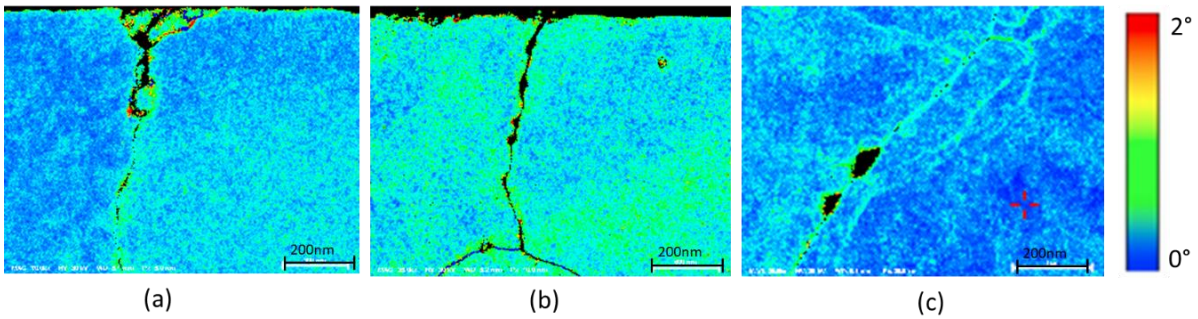
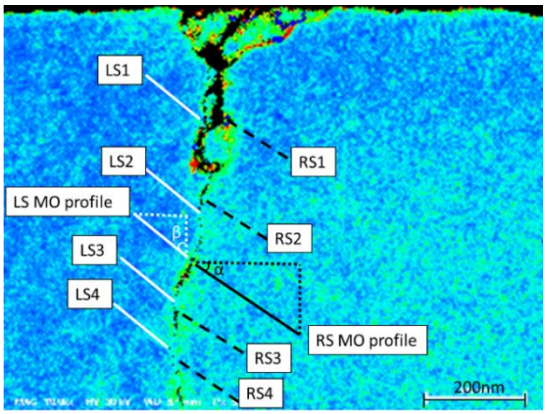


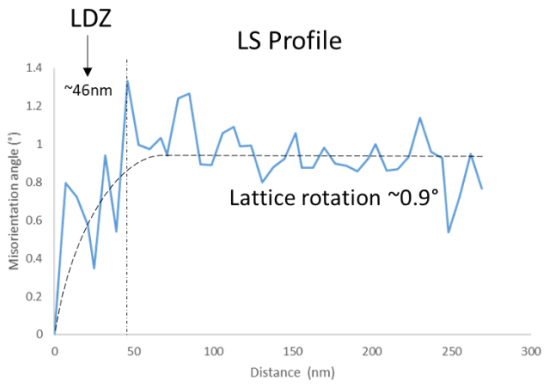
Figure 104: Kernel Average Misorientation (KAM) (a) cracked grain boundary 1 (b) oxidized grain boundary (c) as-received grain boundary

Misorientation line profiles for left and right side grain (LS and RS respectively) similar to those used in [237,249] as shown in *Figure* 105 have been acquired at the crack tip region in the cracked grain boundary sample. It can be seen that only at distances of ~50nm from the crack tip, there is a misorientation gradient before a plateau is reached.

a. KAM profile of cracked GB 1



b. Left side grain (LS) profile



c. Right side grain (RS) profile

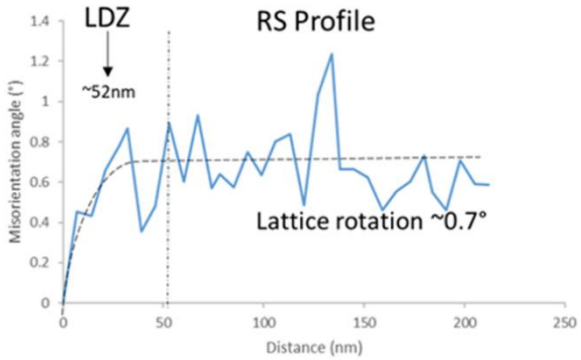


Figure 105: KAM profiles for cracked sample: (a) KAM map, location of LS profile (white line), LS1-LS4 (white dashed lines), RS profile (black line), RS1-RS4 (black dashed lines); (b) LS profile (solid blue line: raw data, dashed line: fitted data): misorientation reaches plateau at lattice rotation of 0.9°±0.3° at ~46 nm; (c) RS profile (solid blue line: raw data, dashed line: fitted data): misorientation reaches plateau at lattice rotation of 0.7°±0.3° at ~52 nm from the grain boundary.

The gradient in the misorientation suggests a higher lattice deformation in the region. This is called lattice deformation zone (LDZ). From this, we obtain two parameters – distance from the grain boundary at which the misorientation value reaches the maximum and lattice rotation which is caused by the localized deformation. In both the grains, misorientation reaches a plateau value at a similar distance, with slight difference in the lattice rotation value (where misorientation reaches a plateau). The length of the local deformation zone – left grain: 46nm, right grain: 52nm and the lattice rotation at which the plateau is reached – left grain: 0.9°±0.3°,

right grain: 0.7°±0.3°. The profiles are obtained at a different angle from the grain boundary orientation (horizontal) in order to avoid the intersection with the deformation bands. Therefore, using basic trigonometry, actual comparable distances from the grain boundary, open crack and crack tip have been calculated and are shown in Table *13*. These results suggest a higher dislocation density localized around the crack tip/cracked grain boundary [253].

Table 13: Misorientation profiles: the LDZ refers to the distance from the grain boundary within which there is a misorientation gradient is present. The actual LDZ refers to the LDZ perpendicular to the grain boundary.

Profile no.	**Grain**	**LDZ (nm)**	**Angle (°)**	**Actual LDZ (nm)**	**Lattice rotation (°)**
LS	Left	46	50	35.23	0.9°±0.3°
LS1	Left	48	50	36.77	1°±0.3°
LS2	Left	30	50	22.9	0.6°±0.3°
LS3	Left	36	50	27.57	0.7°±0.3°
LS4	Left	32	50	24.51	0.8°±0.3°
RS	Right	52	45	36.7	0.7°±0.3°
RS1	Right	48	45	33.94	1.2°±0.4°
RS2	Right	35	45	24.7	0.7°±0.3°
RS3	Right	40	45	28.28	0.6°±0.3°
RS4	Right	38	45	26.87	0.8°±0.3°

5.3.6 Geometrically Necessary Dislocation (GND) Density calculation

As a result of cross correlation analysis, we also obtain lattice rotations as an output. With knowledge of dislocation types in the system, we fit the dislocation type to the measured curvatures supporting these rotations and can thus obtain an estimate of geometrically necessary dislocation density (GND density). After deformation, the residual stresses remain due to the inhomogeneity of the plastic deformation throughout the grains [253]. GNDs maps

and the quantification of local dislocation densities could contribute to better understanding SCC initiation, since they could highlight some form of density threshold that would allow stress localization to reach the minimum required to fracture an oxidized grain boundary [262,263]. For this reason, after cross-correlation, dislocation density maps were calculated for all samples analyzed as part of the grain boundary 1 study as shown in *Figure* 106. GND density calculations were performed based on L^1 optimisation method developed by Wilkinson et al. [254] using CrossCourt 4 software. An average value was extracted from the region close to the grain boundary (first 50nm). The cracked grain boundary had the highest value with ~ 3 x 10^{16} lines/m^2. The oxidized grain boundary comes second with a value ~ 5 x 10^{15} lines/m^2 whereas the as-received grain boundary has value ~5 x 10^{14} lines/m^2. This is expected as both cracked and uncracked oxidized grain boundary should have experienced deformation during testing under 4-point bending.

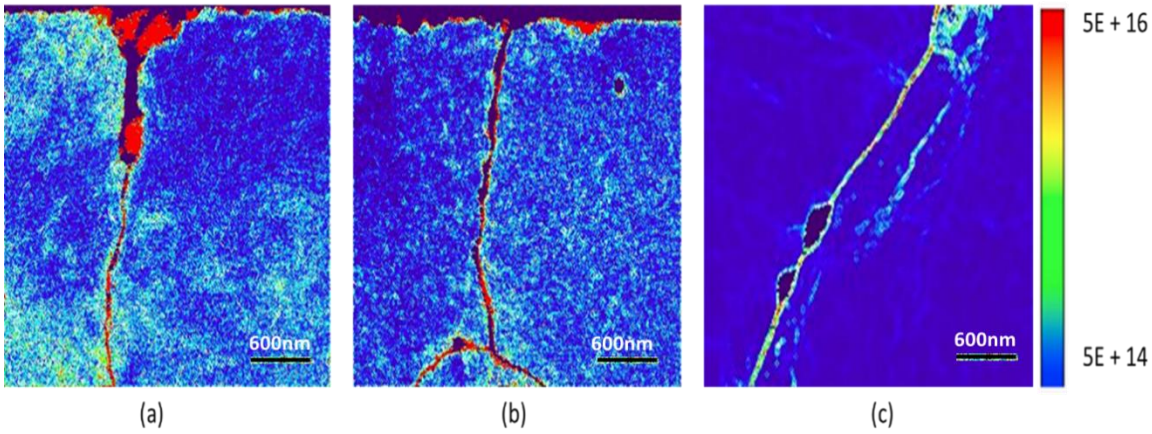


Figure 106: GNDs map (lines/m^2) (a) cracked grain boundary 1 (b) uncracked grain boundary 1 (c) as-received grain boundary (similar to 1)

Figure 107 shows GND density maps of the second crack. In case of the second crack, a GND density of ~1 x 10^{16} lines/m^2 was measured. Thus, from GNDs of both the cracked regions, the minimum observed GNDs around the grain boundaries that failed (initiating cracking) was found to be more than 5 x 10^{15} lines/m^2.

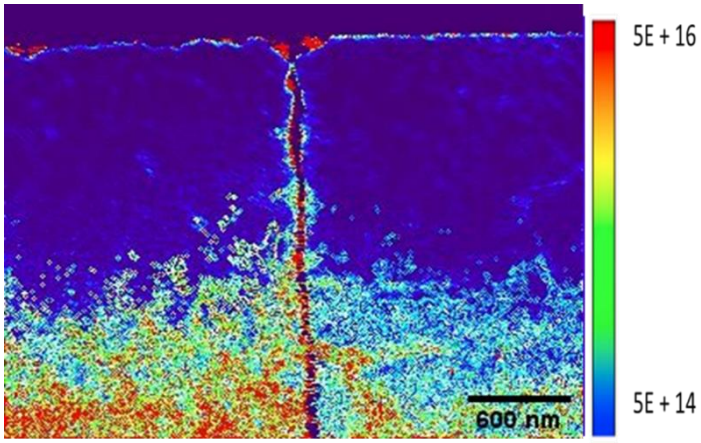


Figure 107: GND density maps of crack grain boundary 2 (lines/m^2)

GND line profiles similar to the KAM analysis ones (*Figure* 105) were extracted from the GND map of the cracked grain boundary 1, as shown in *Figure* 108. The line profiles start at the grain boundary (crack) and are averaged over a width of 50 nm perpendicular to the profile (see *Figure* 108*a*), in order to reduce the influence of local noise. The GND profiles from each of the flanks of the cracked grain boundary (*Figure* 108*b and 95c*) show that there is a higher GND density in the first 20-40nm after the crack before reaching a plateau. This is within the region of the localized deformation zone (LDZ). According to Ashby [262], the lattice rotation gradient can be directly related to the dislocation densities. Using this, we can quantitatively estimate the maximum GNDs in the LDZ and these two parameters are very much correlated.

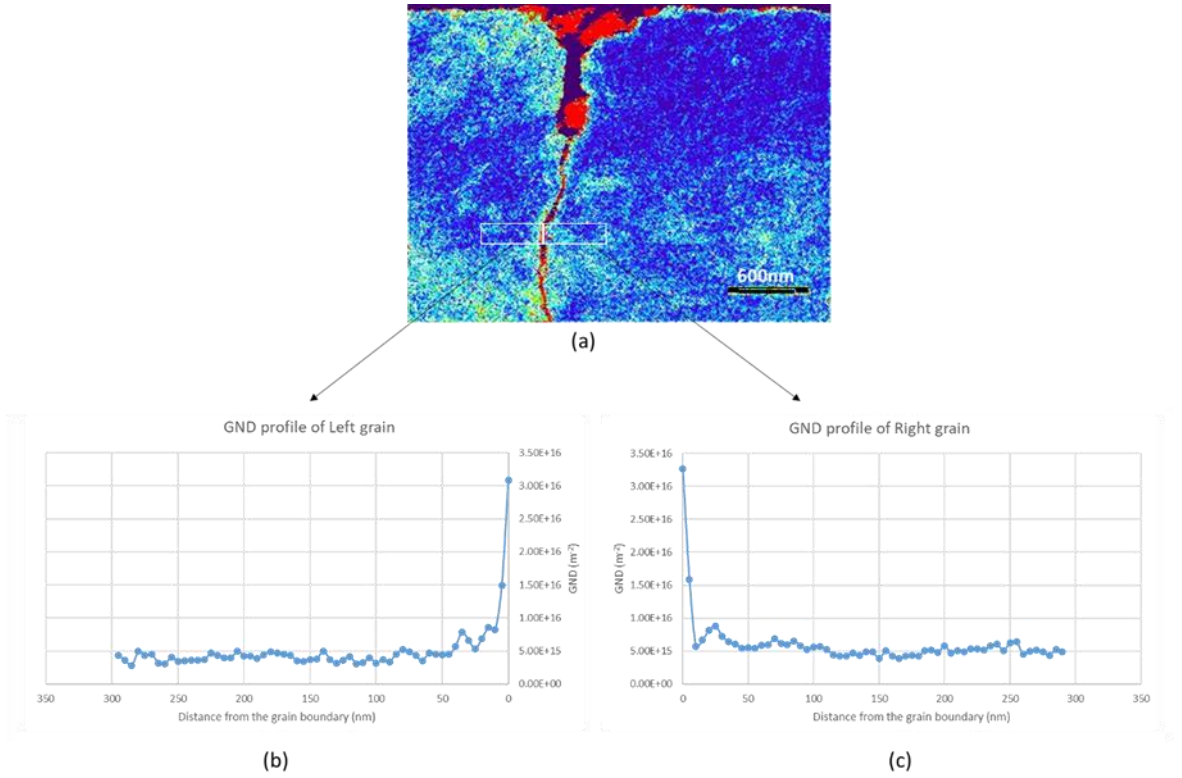


Figure 108: GND map containing the cracked grain boundary (a) GND map with indication of the line profile positions. (b) GND line profile left grain (c) GND line profile right grain

5.3.7 Dislocations and Schmidt factor calculation

Dislocation accumulation and pileups around microstructural features play a crucial role in crack initiation and propagation. Microstructural investigation at this scale gives an insight into the complex nature of the local deformation. TKD investigation at this scale offers knowledge about the dislocation and strain accumulation around the microstructural features of interest.

In case of cracked grain boundary, there is significant amount of strain along the crack flank on the right grain. The components of elastic strains are of the order 10^{-3} which is relatively large. This is evident from the GND density maps as a region of elevated GND content. This was proved by TEM analysis of dislocations in this region. TEM analysis along this region (*Figure* 109) showed that the dislocations were straight and along the same plane as shown in *Figure* 94.

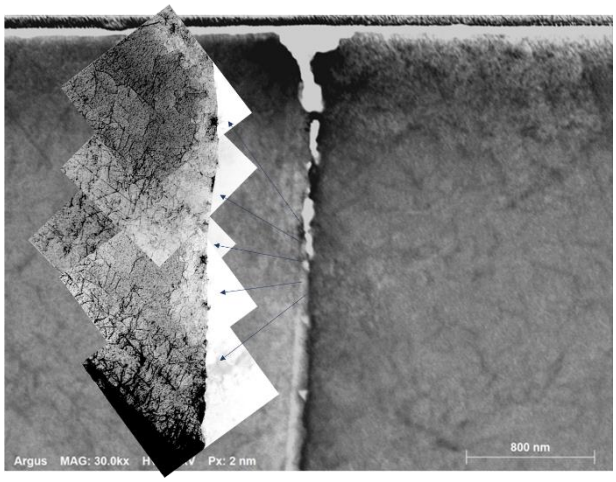


Figure 109: Montage of dislocations using TEM close to the cracked grain boundary 1

A series of TEM micrographs, *Figure* 110*a*, were acquired under convergent weak beam dark-field imaging conditions controlled by a beam precession script similar to that demonstrated by Prokhodtseva et al.[255]. Each micrograph was taken using a slightly different deviation parameter (g, 8**g**-9**g**) to change the phase of the extinction-bands. These micrographs were then converted into a stack using ImageJ [257]. Before being summed together, the images were aligned using a Correct 3D Drift [264] plugin in ImageJ. The final summed image, *Figure* 110d, is shown with inverted contrast, and after background subtraction using the rolling-ball method (radius = 40 pixels) in ImageJ. With the application of this imaging method, defects at all sample depths are supposed to be made visible.

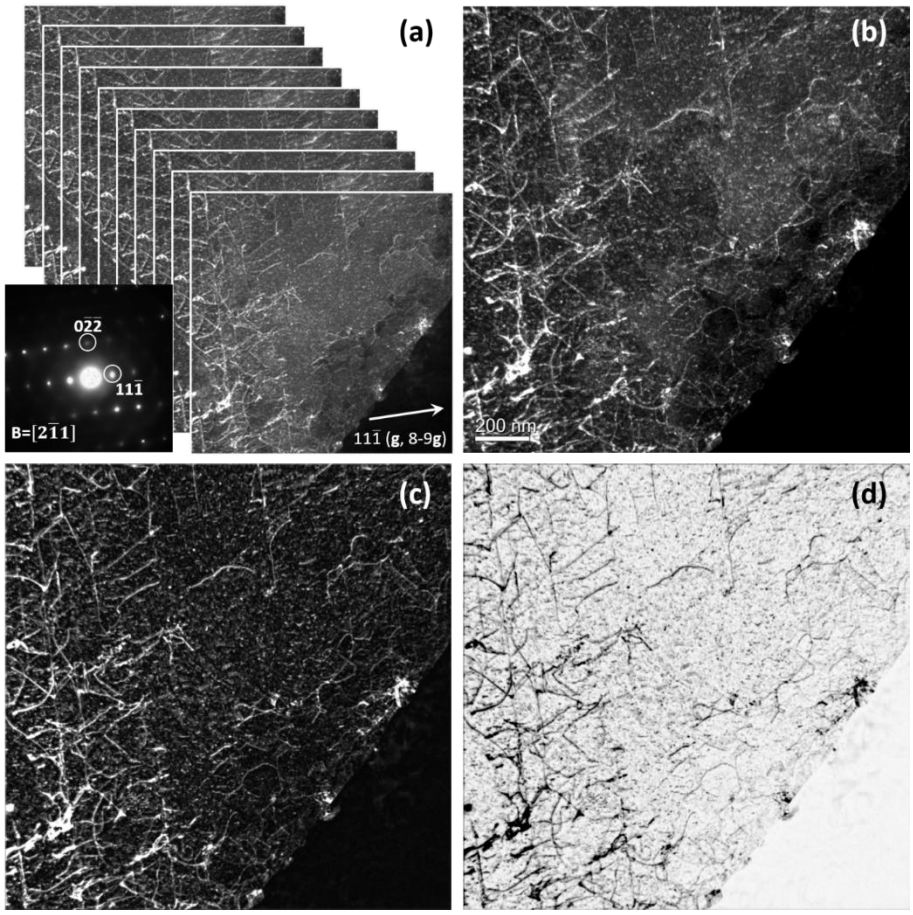


Figure 110: (a) A series of TEM micrographs (each with a slightly different deviation parameter) taken under weak beam dark-field conditions close to a zone axis of $[21\bar{1}]$, (b) a single dark-field TEM micrograph, (c) summed micrographs after background subtraction using the rolling-ball method (radius = 40 pixels) in ImageJ, (d) the final image is shown with inverted contrast.

Processed TEM micrographs from five regions were used for dislocation counting. A 6 x 6 grid was created in each image as shown in *Figure* 111. The average density of line dislocations and dot-like defects were counted respectively and the counting results are summarized in Table 14 and Table 15.

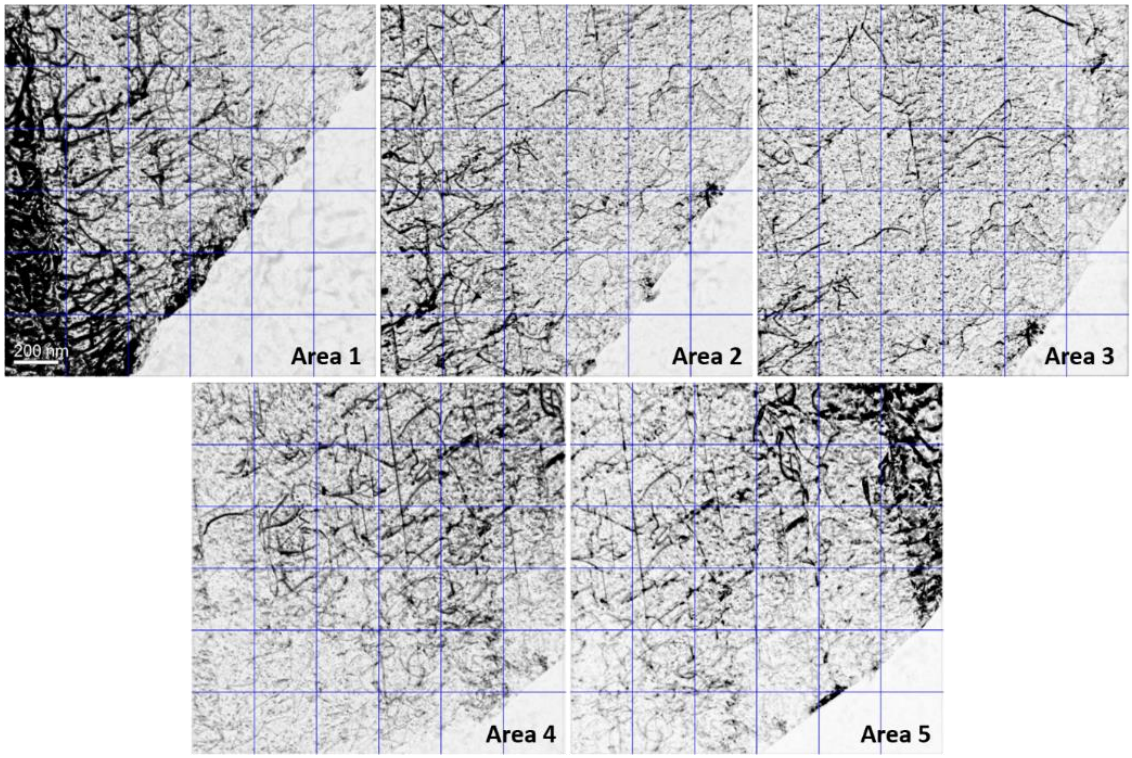


Figure 111: Processed micrographs for the dislocation counting by the line intersection method [4].

Table 14: Counting results of Line dislocations

		Horizontal lines					Vertical lines				
Area 1	Line number	1	2	3	4		1	2	3	4	5
	Line length (Lh), nm	1372	1098	895	704		1098	1098	1098	930	549
	Intercepted defects (Nh)	11	11	12	9		9	17	17	9	4
Area 2	Line number	1	2	3	4	5	1	2	3	4	5
	Line length (Lh), nm	1647	1647	1522	1316	1098	1647	1647	1647	1372	1098
	Intercepted defects (Nh)	8	12	16	16	13	27	18	16	13	11
Area 3	Line number	1	2	3	4	5	1	2	3	4	5
	Line length (Lh), nm	1647	1647	1647	1495	1310	1647	1647	1647	1647	1310
	Intercepted defects (Nh)	12	22	7	8	8	13	8	5	11	10
Area 4	Line number	1	2	3	4	5	1	2	3	4	
	Line length (Lh), nm	1098	1098	1098	1098	823	1647	1647	1647	1372	
	Intercepted defects (Nh)	16	14	8	14	15	14	19	12	12	
Area 5	Line number	1	2	3	4	5	1	2	3	4	5
	Line length (Lh), nm	1647	1647	1647	1647	1372	1647	1647	1647	1098	1098
	Intercepted defects (Nh)	20	18	21	17	8	12	11	16	14	10
Summary	Average spacing (nm)	105									
	Average density (lines.m-2)	2.4E+15									

Table 15: Counting results of dot-like dislocations

		Horizontal lines					Vertical lines				
Area 1	Line number	1	2	3	4		1	2	3	4	5
	Line length (Lh), nm	1372	1098	895	704		1098	1098	1098	930	549
	Intercepted defects (Nh)	48	34	30	29		34	40	47	26	17
Area 2	Line number	1	2	3	4	5	1	2	3	4	5
	Line length (Lh), nm	1647	1647	1522	1316	1098	1647	1647	1647	1372	1098
	Intercepted defects (Nh)	54	56	59	40	31	69	56	54	37	38
Area 3	Line number	1	2	3	4	5	1	2	3	4	5
	Line length (Lh), nm	1647	1647	1647	1495	1310	1647	1647	1647	1647	1310
	Intercepted defects (Nh)	46	57	49	51	44	50	58	54	49	35
Area 4	Line number	1	2	3	4	5	1	2	3	4	
	Line length (Lh), nm	1098	1098	1098	1098	823	1647	1647	1647	1372	
	Intercepted defects (Nh)	42	43	39	42	30	46	33	45	36	
Area 5	Line number	1	2	3	4	5	1	2	3	4	5
	Line length (Lh), nm	1647	1647	1647	1647	1372	1647	1647	1647	1098	1098
	Intercepted defects (Nh)	46	42	49	51	37	47	57	52	37	37
Summary	Average spacing (nm)	31									
	Average density (lines.m^{-2})	8.0E+15									

The slip pileups are seen to occur in the {111} direction in the crystal. Traces of <011> planes are shown in *Figure* 112 and they correspond to the pileup directions. This is in good agreement with the fcc slip system [252,265].

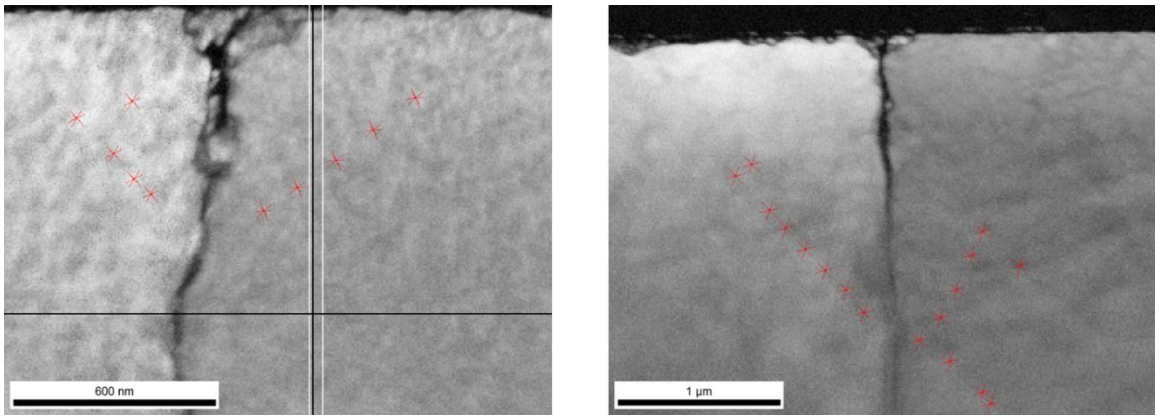


Figure 112: Slip plane tracing using TSL OIM software on Image quality map (the red markers point the direction of the slip planes in crack GB 1 & 2)

Schmid factor [266] is taken into account once the critical resolved shear stress has been reached as the dislocations tend to move along the slip plane. The Schmid factor does not directly describe slip within a grain; however, it does examine the resolved shear stress acting on a single slip system, which is important when considering the critical resolved shear stress (CRSS) needed to initiate slip on that slip system. The Schmid factor was found to be 0.45 for the grains adjacent to the two cracked grain boundaries in this study. Clear evidence of slip lines can be observed in *Figure* 112, indicating that the applied stress is past the CRSS value. This is similar to what was previously reported (although for IASCC) [267–269].

Example of GND density maps of two specific types of dislocations are shown in *Figure* 113. These results are important for understanding how the different grains accommodated to the applied stress and deformed differently. It will also help to better visualize slip transfer (or the lack of) between grains.

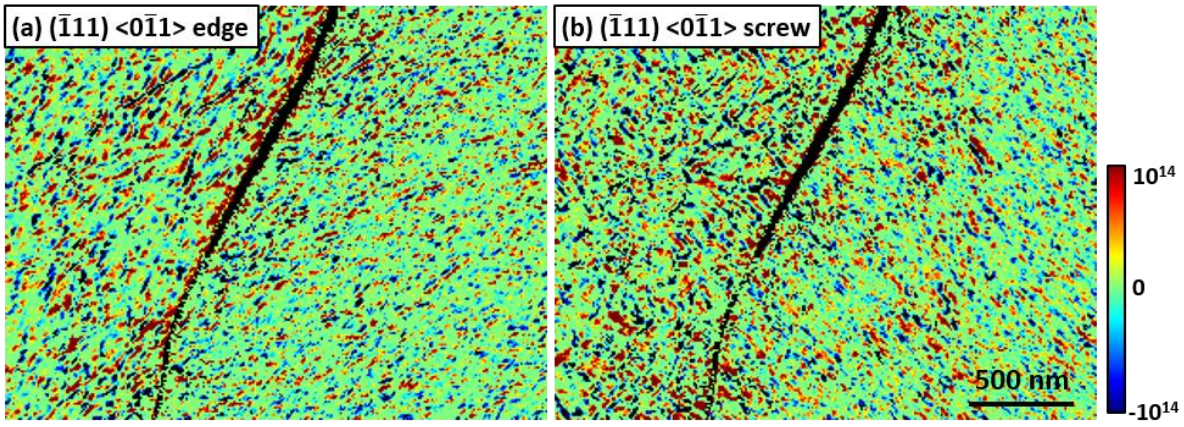


Figure 113: An example of GND density maps of specific types resolved using the minimal line energy strategy in the cracked grain boundary 2, (a) (1̄11) <01̄1> edge dislocations and (b) (1̄11) <01̄1> screw dislocations (unit: lines.m-2). Step size for these maps is 5 nm and pattern resolution is 800 x 600. Negative density values indicate dislocations of opposite sign.

5.3.8 Effect of step size on the measurements of GNDs using TKD

TEM is a powerful and conventional tool in determining dislocation densities. TEM was used here to provide a comparison with regards to the measurements of dislocation distribution and density. The same specimen for TKD-GND analysis has been characterised through TEM. A high-density of dislocations were created during processes of corrosion test, *Figure* 114 (a). *Figure* 114 (b) shows a higher magnification micrograph of the dislocation structures and a high density of dot-like defects can be seen. These could be short segments of line dislocations or FIB induced damage [270]. The average density of line dislocations and dot-like defects were counted respectively using the line intersection method [259] as described above. To achieve a statistically-significant estimation of dislocation densities, 5 micrographs of similar area to *Figure* 114 (a) were selected for dislocation counting. The counting results are summarized in Table 14. More details about TEM image processing and dislocation counting can be found in the supplementary files.

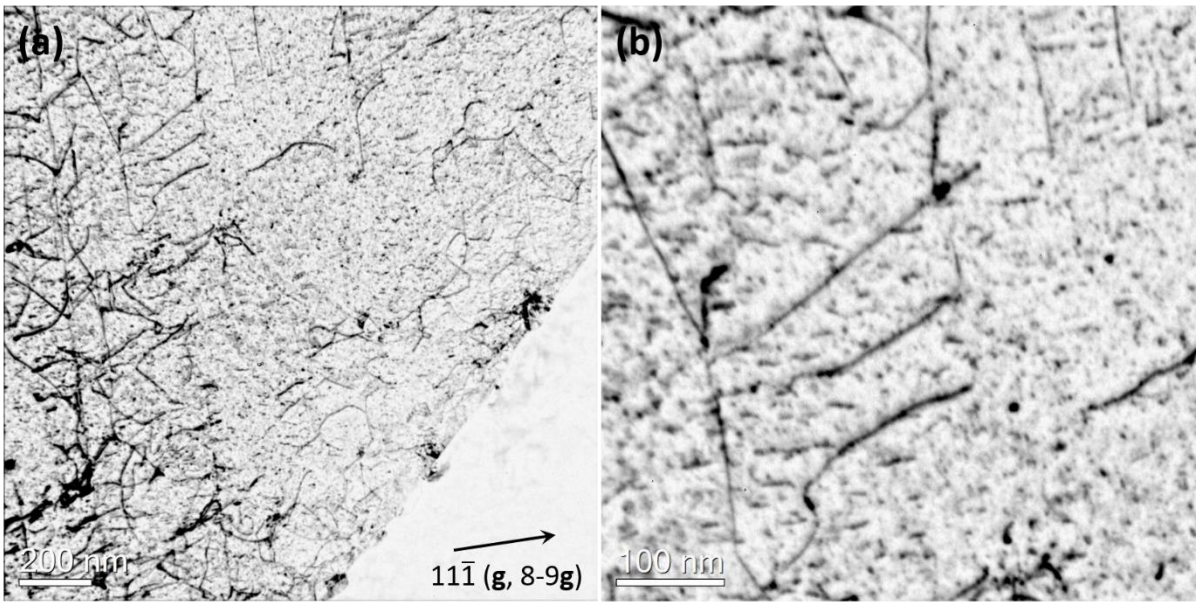


Figure 114: TEM micrographs (inverted contrast) showing dislocations in the Alloy 600 sample nearby a stress corrosion crack, captured in weak-beam dark-field conditions close to a [21$\bar{1}$] zone axis.

The bright-field FSD imaging provides an overview of the region for TKD-GND analysis, *Figure* 115 (a), and similar to that in a TEM image in *Figure* 114 high density of line dislocations can be seen. However, owing to limits of the SEM-based imaging technique in spatial resolution and sensitivity to strain field [250], some small features, e.g. the dot-like defects in *Figure* 114, are not resolved in *Figure* 115 (a). Variation of GND density as a function of scanning step size is shown in *Figure* 115 (b-f). All these GND density maps have revealed the expected accumulation of GND features adjacent to the stress corrosion crack. At 5 nm and 10 nm step sizes, the line dislocation structure is apparent and shows strong correlations with the location and morphology of dislocation network seen in the bright field image, *Figure* 115 (b and c). As step size is increased, the dislocation network becomes difficult to resolve. When step size is increased to 80 nm, the observed GND based dislocation structure is significantly different from the initial one and only the GND features nearby the stress corrosion crack can be revealed, *Figure* 115 (f). The reason for lower values of GND densities at larger TKD step sizes is that increasing the step size would increase the likelihood of combinations of dislocations between the measurements points that have the opposite burger vectors and make no contribution to the lattice curvature, and thus will not be counted as GNDs. In other words, using smaller step sizes, more dislocations will be counted as GNDs to maintain local lattice curvature, until every single dislocation is considered as GND when the step size is close to (or slightly smaller than) the average spacing of dislocations. If the step size is too small, the measured GND density will be dominated by noise [271]. In principle, a suitable step size for TKD-GND analysis would be slightly smaller than the average spacing of discrete dislocations, with the added advantage that a larger fraction of the dislocations can be detectable as GNDs. However, the presence of localized deformation or high dislocation density regions might require the use of a smaller step size to observe the key microstructural

features, such as dislocation cell walls and accumulation of dislocations near the SCC tip in *Figure* 115 (b and c).

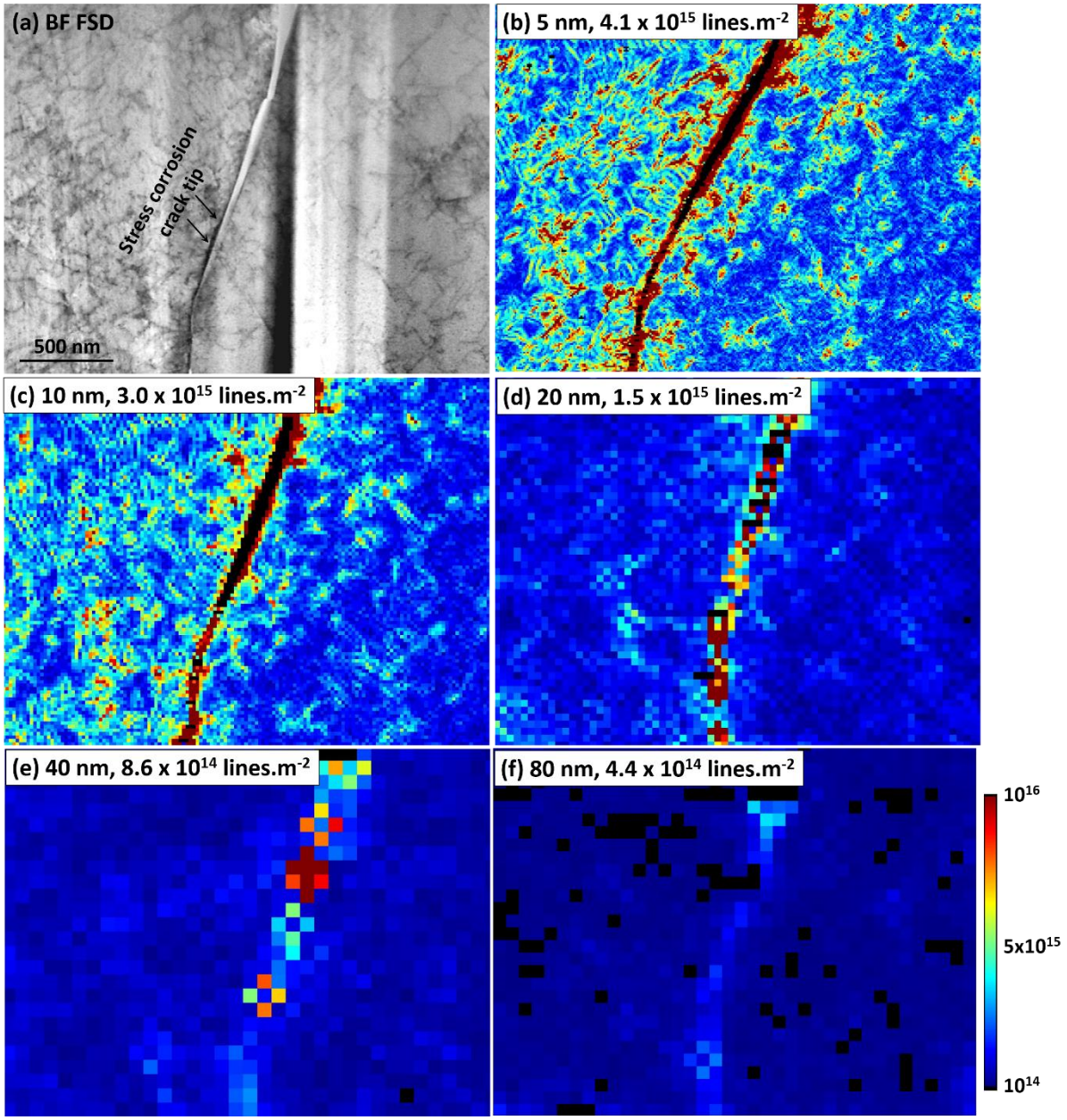


Figure 115 : (a) Bright-field FSD image showing the TKD-GND analysis region and (b-f) GND density maps with 800 × 600 pattern resolution of using different step size (unit: lines.m-2) on Alloy 600 sample.

The dislocation densities determined by TKD-GND analysis are then compared with that measured from the TEM images, where line dislocations average spacing of ~105 nm and

average densities of 2.4 x 10^{14} lines.m^{-2} were found, as shown in *Table 14* and *Table 15*. They are both close to the mean GND density determined in TKD-GND measurements at a step size of 80 nm, 4.4 × 10^{14} lines.m^{-2}, *Figure* 115 (f). And when the TEM counting includes the small dot-like defects, the average spacing turns into ~30 nm and a density of 8.0 × 10^{14} lines.m^{-2}, again in good agreement with the mean GND density determined by TKD-GND measurements, which is 8.6 × 10^{14} lines.m^{-2} at a step size of 40 nm, *Figure* 115 (e). In addition, depending on the TEM imaging conditions and sample thickness, some defects cannot be resolved, which can lead to lower measurements of dislocations densities using the TEM images compared to the TKD-GND analysis using step size close to the average spacing of dislocations.

Comparing the two GND density curves calculated from both sides of the thin foil (e.g. in two separate experiments, after flipping the TEM sample in the SEM holder), *Figure* 116 (a) shows that the variation of GND density as a function of step size follows a similar trend, but the top-surface scanning shows slightly higher values than the bottom-surface scanning. The depth resolution in Alloy 600 for the applied imaging conditions is ~24 nm according to our recent study [272], which means that the detectable TKD signals mainly originate from a sample volume of 24 nm above the bottom foil surface. Since the TEM sample has a thickness ~ 80 nm, more small GND features (e.g. dislocations, FIB-induced defects) may lie closer to one surface than the other, and lead to measurements of different GND densities. However, it should be pointed out that these differences are small and of the same order of the noise (blue plot in *Figure* 116 (a)), so not significant.

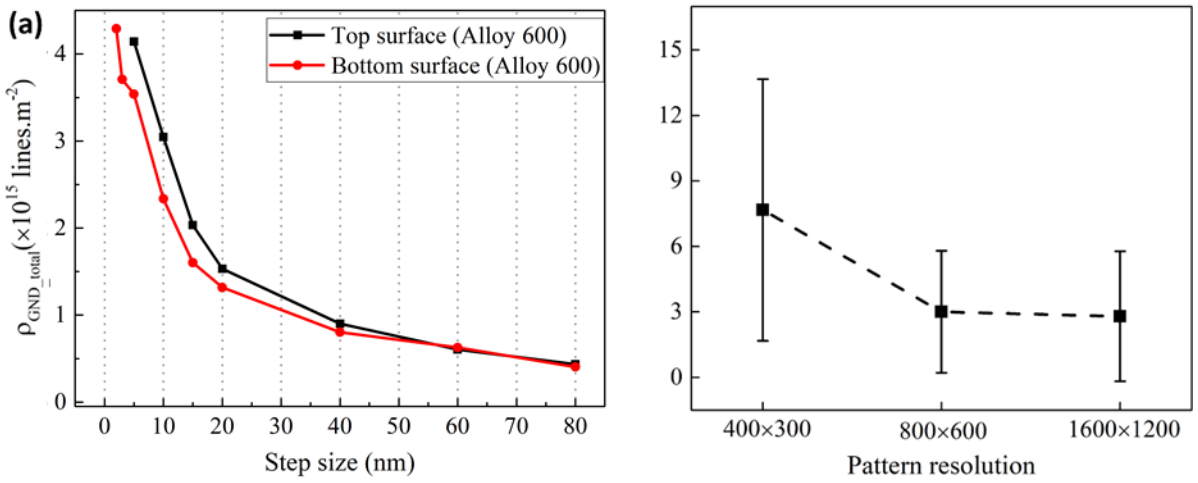


Figure 116 (a) GND density of 20% cold-worked Alloy 600 sample varies as a function of step size using TKD pattern resolution of 800 x 600. (b) GND density variations in Alloy 600 as a function of TKD pattern resolution. The step size used to capture TKD maps for (b) is 10 nm.

The pattern background noise will induce scatters in the pattern shift measurement. In practice, at the full unbinned resolution of the camera, just the pattern background noise can contribute to a measured GND density of 1.4×10^{13} lines.m^{-2}, using a step size of 50 nm with EBSD measurements [271]. To study the noise contribution when step size is reduced, TKD-GND analysis was performed on 20% cold worked alloy 600 as shown in *Figure* 116 (a), and the decrease in GND density with the increase of step size is believed to be a consequence of length-scale dependent of distinguishing SSDs and GNDs rather than from noise contribution [271,273].

The correlation between mean GND density and TKD pattern resolution is shown in *Figure* 116 (b). Similar to that reported in [227,271] for EBSD-GND analysis, the decrease in TKD pattern resolution (or increases in binning size) also leads to an increase in feature shift, and the measured GND densities noise, *Figure* 116 (b). As TKD pattern resolution decreases, smaller ROIs were utilised for the cross-correlation analysis which results in higher scatter values in shift measurements and angular resolution [227]. However, the plot, *Figure* 116 (b),

shows a relatively small variation in the mean GND density values when the pattern resolution decreased from 1600 × 1200 (full CCD resolution, no binning) to 800 × 600 (2 × 2 binning). A scanning scheme of using 800 × 600 pattern resolution for TKD-GND analysis is thus suggested to achieve faster acquisition speed. This is especially important in the TKD-GND analysis at the nanoscale where sample drift can be a serious problem.

Owing to the number of operative slip systems and complex dislocation distributions [273], determining which specific slip plane each dislocation was travelling on was not straightforward from the TEM analysis, but is feasible by applying the TKD-GND method. The total GND density is comprised of individual dislocation densities from each dislocation slip systems. At each point in the GND density map, a set of possible combination of dislocation types that satisfies the measured lattice curvatures can be found. The Crosscourt 4 software calculates the least energy solution [254], in which the arrangement of GNDs produces the observed lattice rotation gradients with the least energy.

5.4 Discussion

In this study, three grain boundaries and four different regions are analyzed using a novel on-axis TKD technique. This technique provides a remarkable spatial resolution allowing orientation mapping and lattice deformation in a better way.

The forescatter images (*Figure* 94, *Figure* 96, *Figure* 102) are an effective way of identifying the defects in the material. The regions of higher dislocation density or deformation zone appear darker, whereas crack and oxides appear brighter due to the contrast settings. Hence, with these forescatter images it is possible to locate the SCC crack, grain boundary, deformation bands, slip planes and dislocation pile ups with higher resolution.

Figure 100 shows the strain distributions in a grain boundary similar to GB 1, in the as-received sample before it was tested. It is worth mentioning that the already existent strains around

boundaries or inclusions are non-homogenously distributed as a result of cooling after annealing. A similar situation is observed in the uncracked portion of GB 1 (*Figure* 97). The strain components parallel to the GB (ε_{22}) exhibit a gradient towards the grain boundary. Using a reference point about 1 micron from the GB, one grain appears to be under compression and the other under tension the region close to the GB. Once the grain boundary has failed (*Figure* 95), a strain gradient is observed in the direction parallel to the grain boundary, where the upper part of the grain (next to the free surface) appears to have relaxed due to the crack. This behavior is observed in the crack grain boundary 2 (*Figure* 103) as well, where the upper part appears to be relaxed.

The alloy is deformed plastically and unloaded after the 4-point bend test in autoclave, bringing in the geometrically necessary dislocations (GNDs) to maintain the lattice continuity [252][265]. After such deformation, the residual stresses remain due to the inhomogeneity of the plastic deformation throughout the grains [253]. In order to have a realistic GND density reference to compare to, GND densities in the as-received sample (*Figure* 99 *and Figure* 106*c*) were measured, with an average value of 5 $x10^{14}$ m^{-2}.

By studying the GBs that failed (including their oxidized uncracked portion), local GND density values could be obtained, revealing any potential threshold above which an oxidized GB would fail. Cracked GB 1 was found to have the highest local GND density, in the order of 3 x 10^{16} m^{-2}, crack GB 2 has a value of 1 x $10^{16}$$m^{-2}$ and the oxidized uncracked portion of GB 1 exhibited values in the order of 5 x 10^{15} m^{-2}. The GND density measurements have been used to compare the dislocation densities determined by TEM analysis, and the results show good agreements. TKD-GND analysis, on comparison with TEM analysis, can not only give information on dislocation densities but also reveal the dislocation nature in a complex dislocation network.This is expected as both cracked GBs have experienced deformation

during testing. The amount of GND observed in all these cases could be a combination of both the intergranular oxidation and mechanical deformation.

The cross-correlation analysis of TKD patterns provides us the means of investigating the dislocation arrangements at a microscopic scale. At this scale, many important phenomena occur during plastic deformation as a result of complex interactions between dislocations and microstructural features. In the case of the cracked grain boundaries, there is significant amount of strain gradient in the normal direction to the free surface. The correlation between local misorientation and strain carried out previously by Sasaki et.al. [240] and Ilevbare et. al. [241] using DIC already showed that the measured local strains (elastic and plastic) are higher around cracked GBs, although with much lower spatial resolution. In addition, DIC can only measure the strain on the surface of the sample. Since SCC initiation and propagation are local phenomena, they are likely to be influenced by changes in the microstructure or strain distribution around the crack tip and, therefore, at a much smaller scale. Using TKD, we can accurately calculate the elastic strain and GND densities with nm resolution, resulting in more realistic values of strain than the previously reported [241]. GND analysis has the potential of becoming a more reliable technique than DIC and KAM analysis for SCC initiation studies, since it is sensitive to small strain changes and, more importantly, happening in volumes of just a few nanometers. The effect of sample thinning on strain and GND measurements is still under investigation, although preliminary results suggest that both measurements are still fully representative of the bulk sample [274]. These observations support the conclusion that SCC initiation is controlled by local deformation.

5.5 Summary

A significant amount of microstructural and micromechanical features related to SCC have been analyzed successfully using on-axis TKD, a novel high-resolution orientation mapping method. Several grain boundaries have been analyzed and their cracked and uncracked portions compared. All cracked boundaries analyzed had local GND densities higher than 1 x $10^{16}m^{-2}$. Similar grain boundaries, from as-received samples had GNDs of 5 x 10^{14} m^{-2}, while an intermediate level was found in the oxidized but uncracked portion of the same GB. This suggests that a threshold value for local GND density is required to generate the stress required for an oxidized grain boundary to fail (SCC initiation) and can be implemented into local model as one of the criterion for initiation. Strain maps were used to better understand the evolution of local strain distributions around grain boundaries before and after cracking, which might prove useful when validating finite element modelling results. High-resolution strain and GND maps have the potential to contribute to a better understanding of crack initiation and propagation.

In this study, we have studied the effects of step size and pattern resolution on the GND density measurements using TKD at the nanoscale. The GND density measurements have been used to compare the dislocation densities determined by TEM analysis, and the results show good agreements. While comparing to the TEM analysis, the TKD-GND analysis not only give information on dislocation densities but also reveal the dislocation nature in a complex dislocation network. The GND measurements have length scale dependence. Determining the appropriate step size for GND density analysis using TKD-GND method is very important. Suitable step size can be selected depending on the spacing of GNDs features using the FSD imaging system before scanning a TKD map. To analyze nanoscale GND features, the step size should be smaller than their spacing distance. Using a smaller step size allows us to obtain

more detail on dislocation structure and may provide more information about the mechanisms involved. To reduce the scanning time, and the potential of sample drift, a scanning scheme of using 800 × 600 pattern resolution (2 x 2 camera binning) for TKD-GND analysis is suggested.

6 EVALUATION OF GLOBAL STRESS, STRAIN FIELDS AND LOCAL STRESS ALONG THE GRAIN BOUNDARIES

In this chapter, the finite element (FE) model that has been used to design, mesh and evaluate the global stress and strain fields of the four-point bend test and crystal plasticity finite element (CPFE) model will be described in detail.

6.1 Finite Element Model of four-point bend test

In this section the various parameters incorporated into the finite element analysis of the four-point bend test are described. The FEM analysis was performed using Code_Aster, an in-house FEM tool developed by EDF [209]. The design and meshing of the specimen are performed using Salome Meca, a numerical platform developed by EDF researchers.

6.1.1 Components

The components to be modelled are the cylindrical rods and the specimen. They are designed using the geometry module (GEOM) in Salome Meca. The geometrical design of the four-point test is presented in *Figure* 117.

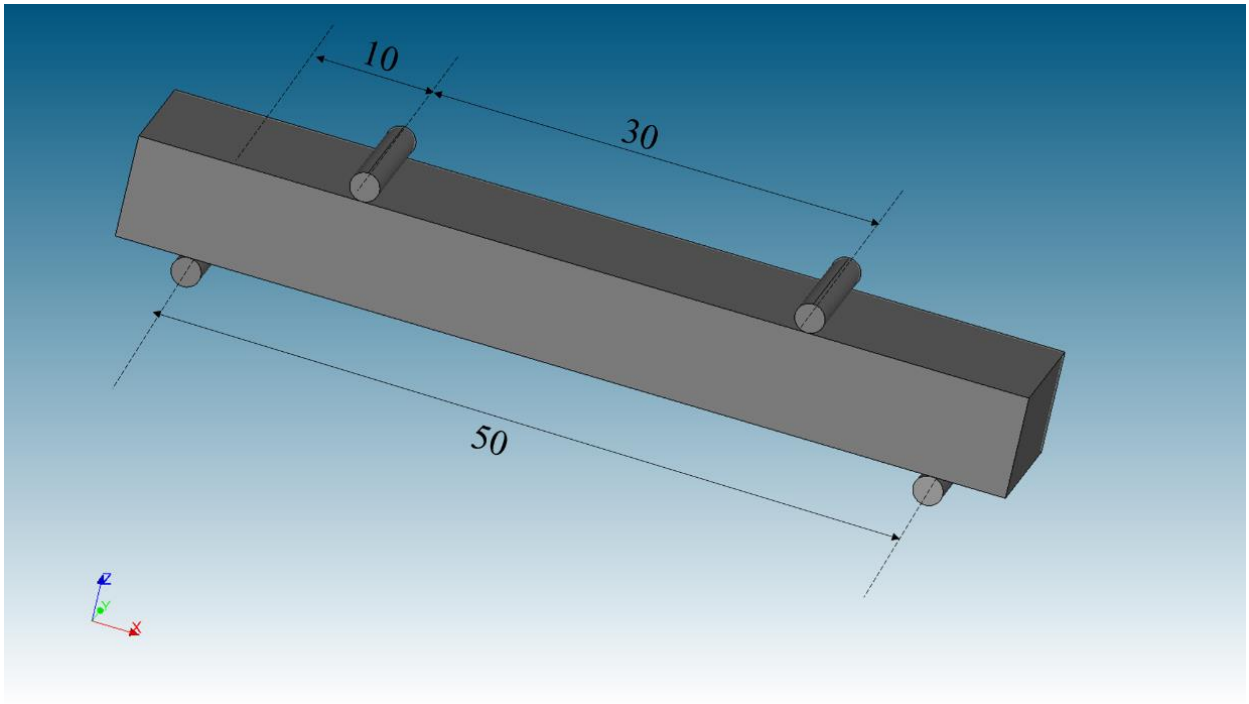


Figure 117: Geometry of the specimen for four-point test designed using GEOM module in Salome Meca (all dimensions are in mm).

6.1.2 Mesh

The specimen is meshed using the Mesh module in Salome Meca. The mesh is programmed to contain the material and the mechanical properties that define how the specimen will react to the loading conditions. Elements and nodes are assigned at certain density throughout the specimen depending on the anticipated stress levels especially in the region supposed to be in contact with water and the cylindrical rods. Tetrahedral elements were used in this model to mesh as it is more suitable for complex stress states. However, by using tetrahedral elements as shown in *Figure* 118, the number of elements is much higher than when using hexahedral elements and hence, the computation time is drastically increased. There are 40000 elements with 7131 nodes in this initial mesh.

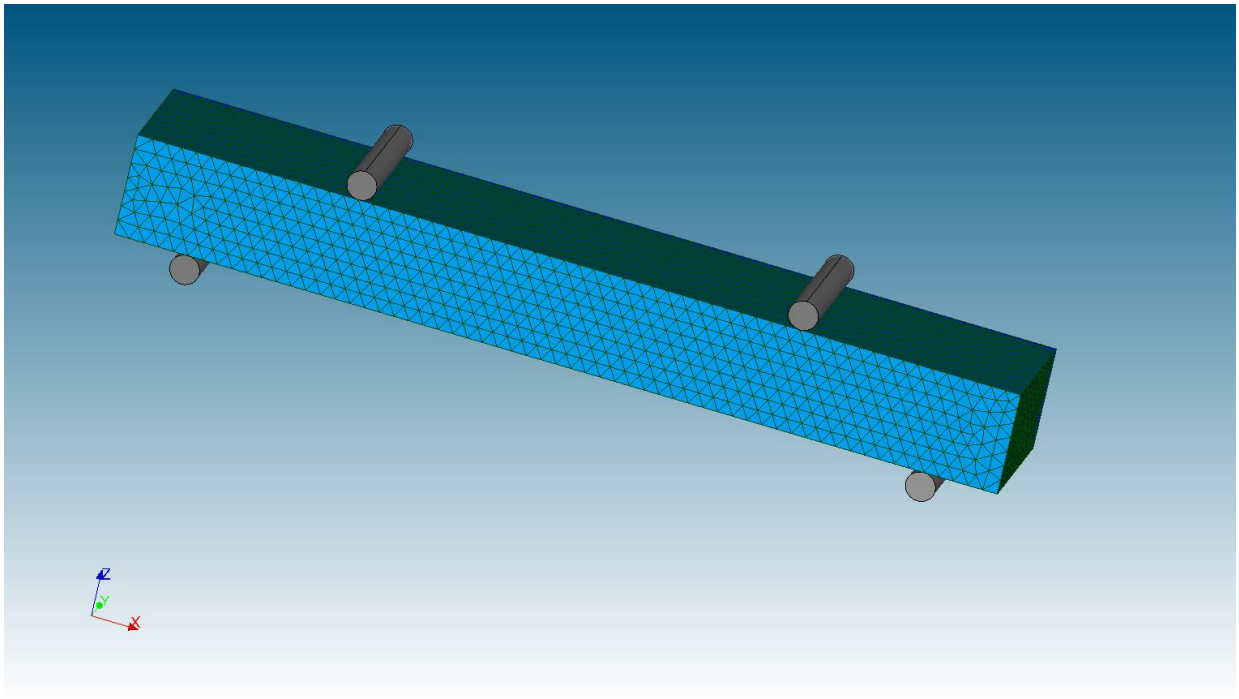


Figure 118: Meshing done using MESH module in Salome Meca.

To reduce the computation time and complexity, the model was simplified by assigning symmetry function. Also, due to the complex interaction between the cylindrical rods and the specimen, the volume of the anticipated interaction region is replaced by a box as shown in *Figure* 119. These boxes are assigned with higher Young's modulus so that their effect on the specimen volume is negligible.

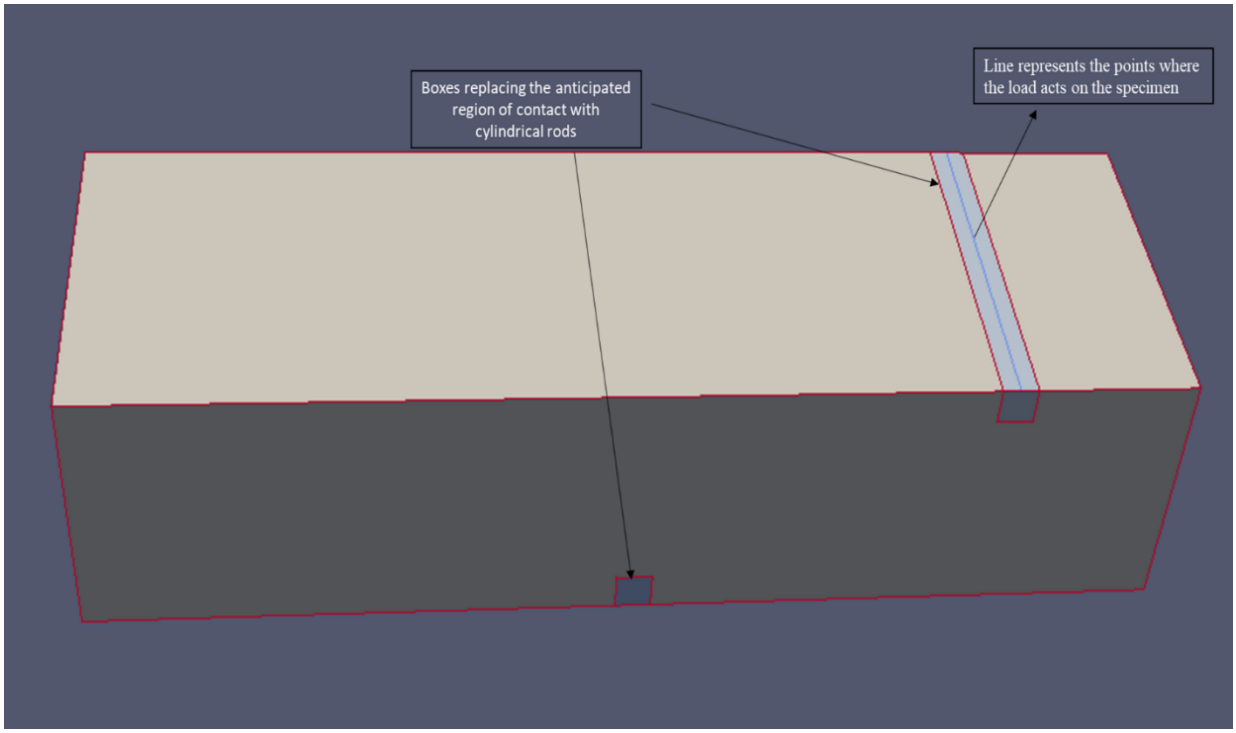


Figure 119: Geometry of the simplified specimen and the boxes denoting the anticipated regions of interaction with the cylindrical rods in the four-point test and points were the load acts on the specimen during the simulation.

The regions close to the boxes, symmetry and contact with water are finely meshed. The nodes and elements in contact with water are properly defined with much care as the displacements and stresses are mainly calculated from the nodes of the elements. *Figure* 120 shows the nodes and elements where symmetry (highlighted in yellow) is introduced and *Figure* 121 shows the nodes and elements which come in contact with the water. *Figure* 122 shows the mesh elements of the model along with the overall quality. The mesh after finely refined has total of 25621 elements and 31133 nodes.

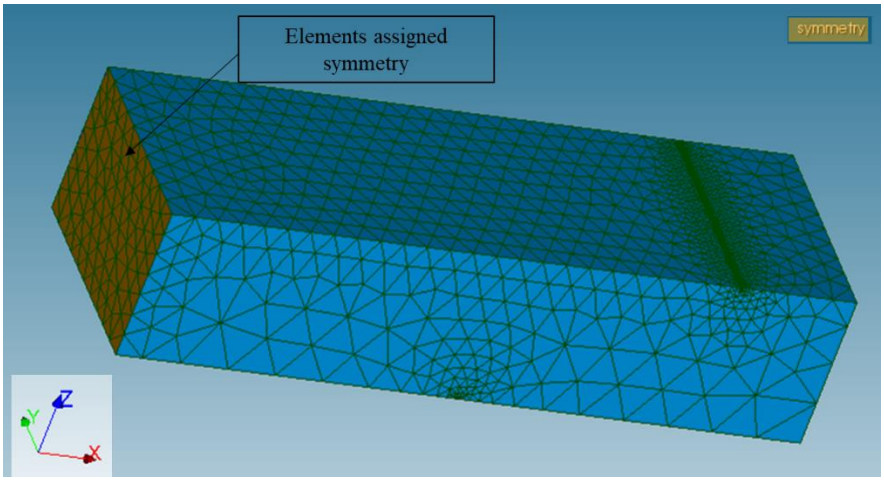


Figure 120: Mesh elements symmetry where symmetry imposed (highlighted in yellow).

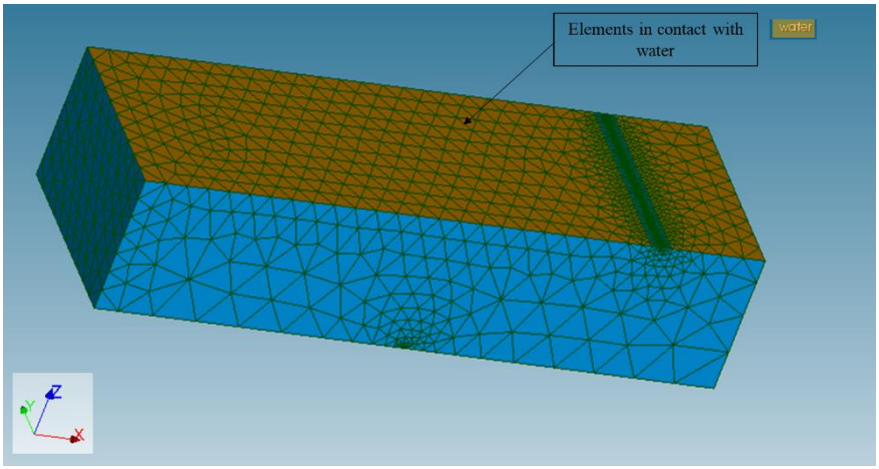


Figure 121: Mesh elements in contact with water (highlighted in yellow).

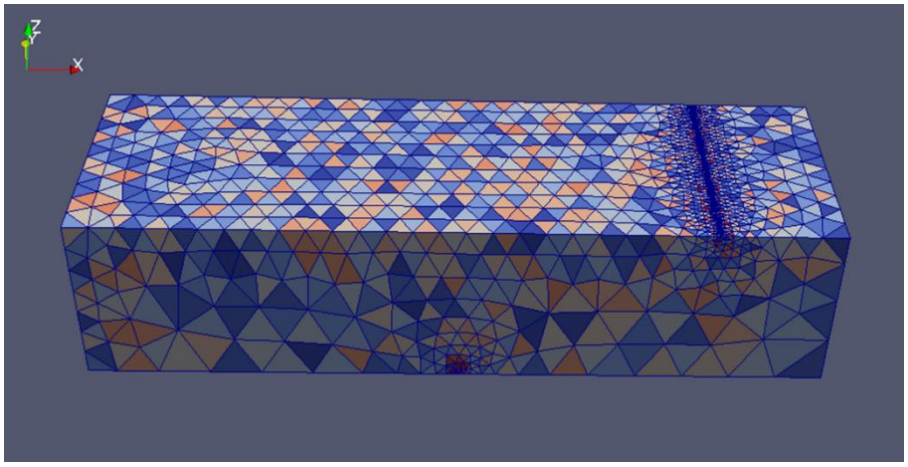


Figure 122: Overall model with refined mesh elements.

6.1.3 Material Properties

The mechanical properties of alloy 600 are defined using the Ramberg-Osgood relation-based deformation plasticity model. This relation is given by the equation (32) and represents a non-linear relationship between stress and strain near the yield point. In other words, for all stress levels there is presence of plastic strain due to the power-law relationship and this non-linearity becomes significant for stress values much greater than yield stress.

$$\varepsilon = \frac{\sigma}{E} + K\left(\frac{\sigma}{E}\right)^{n} \dots\dots\dots\dots (32)$$

where, ε is the strain, σ is the stress, E is the Young's modulus, and K and n are constants depending on the material. This one-dimensional model is generalised to multiaxial stress states and is in built in Code_Aster. Further details of this model can be found in [209]. The main reason for choosing this model is because it evaluates the mechanical response in both elastic and plastic regions. The main input parameters are Young's Modulus (E), yield stress (σ_0) and Poisson's ratio (ν).

6.1.4 Boundary conditions and Loading

The boundary conditions or constraints are applied to the mesh to avoid any free displacement of the model in space and to reach convergence during calculation. For this, displacements in various selected nodes in the model is limited. The nodes in the symmetry face were assigned with zero displacement in x and y direction. The nodes corresponding to the upper cylindrical support rod were assigned with zero displacement in y and z direction. The nodes corresponding to the loading cylindrical rod were assigned with zero displacement in x and y direction with the degree of freedom only in z direction corresponding to the applied displacement. *Figure* 123 illustrates the boundary conditions applied to the model.

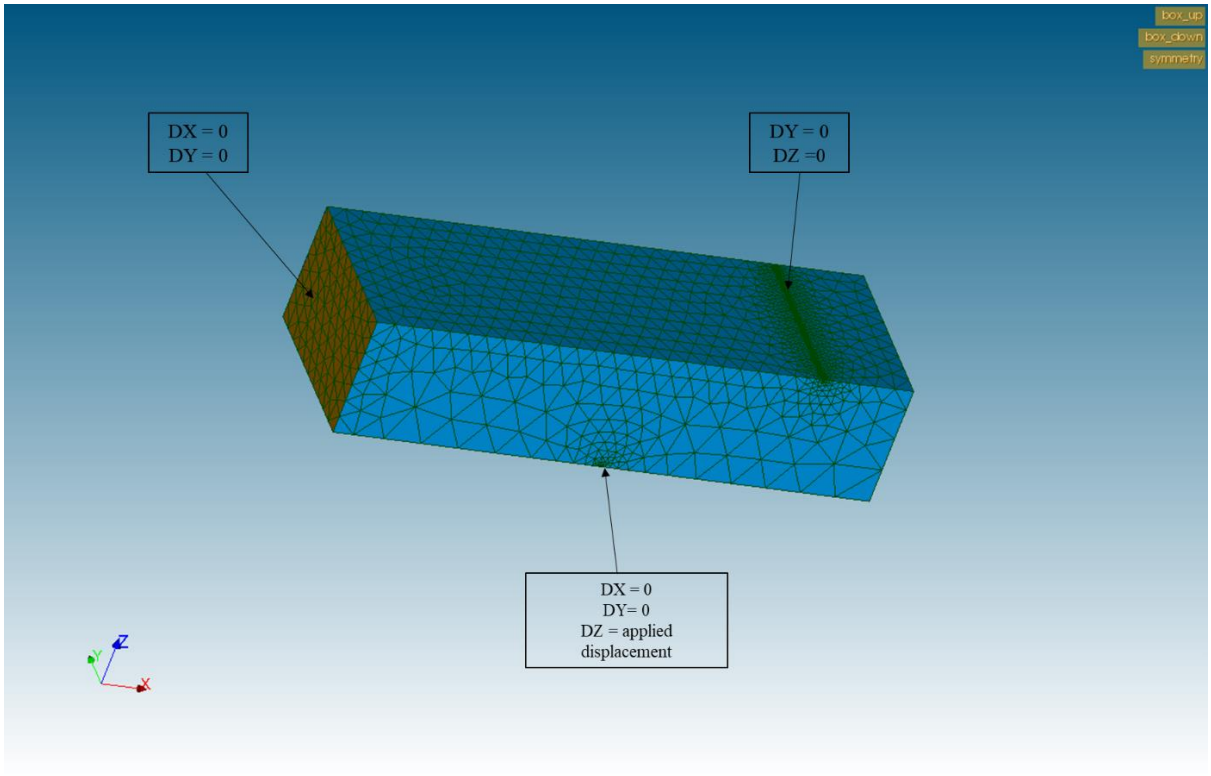


Figure 123: Boundary conditions applied to the model.

6.1.5 FEM calculation

The material properties, boundary conditions and applied displacement are fed into Code_Aster using a script written in FORTRAN language. An example of this code is presented in Appendix A. For the FEM calculation to finish properly, the model should reach convergence, if not the obtained result will not be accurate to proceed further.

6.1.6 Convergence of the model

Convergence is an excellent indication of the quality of the model due to the influence of mesh and element number on the results. For any FEM simulation, it is necessary to reach convergence to have a better solution. To obtain accurate solution for stress output, Newton Raphson equilibrium iteration method is used. Convergence is achieved by incrementally or iteratively changing the stress within the current time increment until the residual stress

becomes close to zero within the defined tolerance level (in this case it was $<10^{-5}$ MPa). If convergence is not reached for the current time increment, the time step is further reduced by increasing the number of supplementary iterations. Hence, the error is reduced at each time step. For example, at the start of the calculation, the elastic stress at t +δt is changed incrementally hence, the stress obtained at the end of t +δt is updated in the equation to calculate the strain for the next time step. This solution is then passed to Code_Aster and recorded.

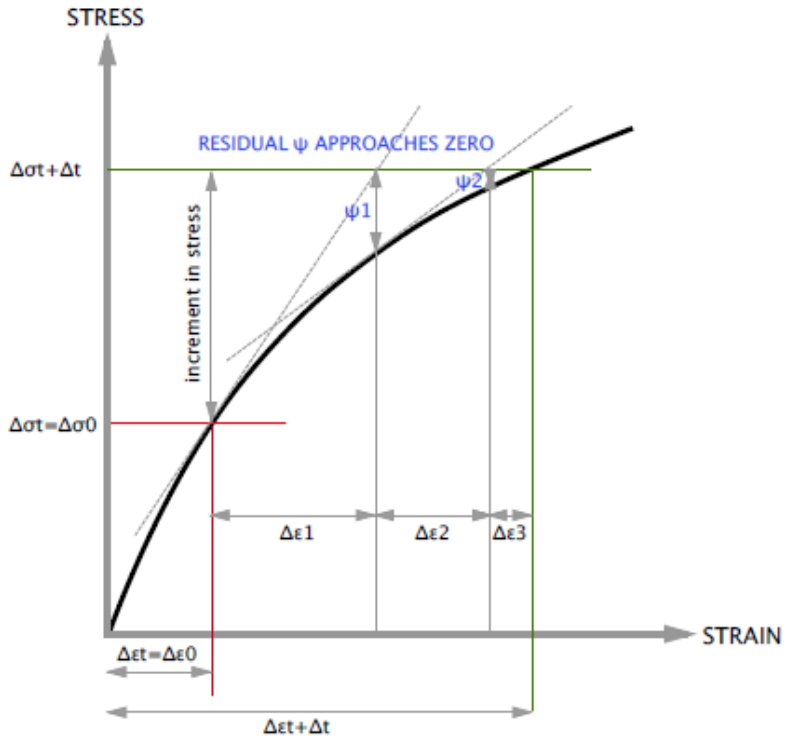


Figure 124: Schematic of the Newton Raphson equilibrium iteration, carried out within one time increment to bring the stress residual close to zero, within a specified tolerance, to find a more accurate solution. Once the equilibrium solution is found the loop is terminated and the solution is used to calculate the next increment in time adapted from [275].

6.2 Results

The material properties were defined using the deformation plasticity model in Code_Aster, the boundary conditions were assigned, and simulation was carried out for different

displacements applied to the cylindrical rod and corresponding stress and strain fields were extracted. This was then compared with the experimental results.

6.2.1 Experimental results

The mechanical properties of the as-received sample have been measured at 20°C and 360°C and provided by EDF (*section 4.3*). However, the mechanical properties of the alloy at 345°C are measured from the SCC tests carried out applying constant load of 5500N (20% above the yield stress) by gradually pushing the central rods up to 1 mm displacement and recording the load to displacement. The summary of the mechanical properties is tabulated in Table 16. The Stress-Strain curve is plotted from the experimental results in *Figure* 125.

Table 16: Mechanical Properties of Alloy 600 (T-265).

Temperature (°C)	**Yield Stress (MPa)**	**UTS (MPa)**	**E (GPa)**
20	241	607	172
360	221	550	233
345	238	No fracture	204

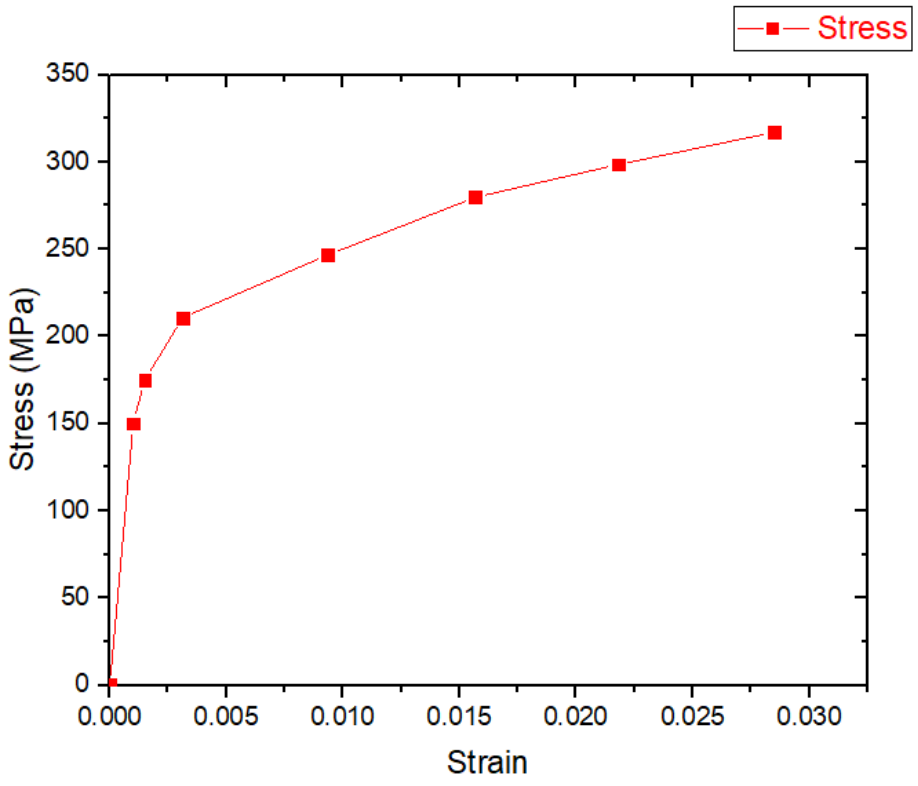


Figure 125: Stress-strain curve of Alloy 600 tested in autoclave at 345°C.

6.3 FEM Modelling results

As mentioned in section 7.1.3, the mechanical properties of the materials were defined using the deformation plasticity model and the data to be used in the finite element analysis were extracted from the true stress-strain curve of the experimental results. The constant load on the loading points in the mesh were applied by varying the displacement of the push rod and corresponding stress and strain values along with the overall deflection was recorded by using Code_Aster. The stress and strain fields from each node was saved in a file called *RESU*. The resulting mesh file saved in *.med* format. *resu.med* format was visualized using the ParaView module in Salome Meca. The outputs from 0.5 mm and 1 mm displacements are presented in the following section and outputs from other results are presented in Appendix B. A

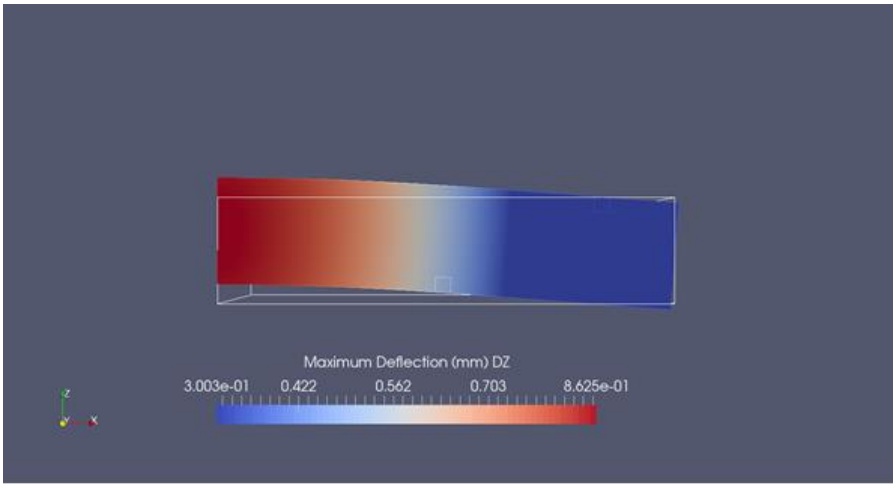
preliminary matrix for each FEM analysis along with results has been created as shown in Table 17.

6.3.1 FEM analysis result for 0.5 mm displacement

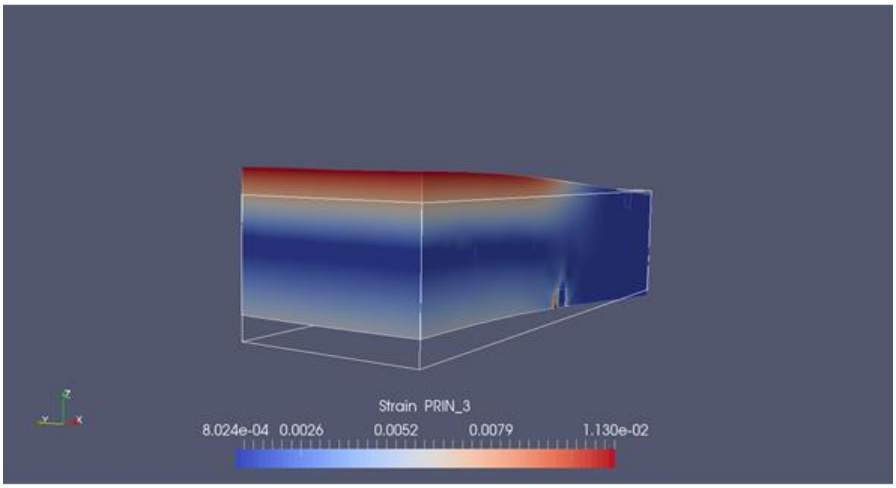
The FEM calculation was performed as mentioned in section 7.1.5 with an applied displacement of 0.5mm on the push rods. For the calculation to reach convergence, the parameters such as total number of time steps, number of increments in each time step, minimum tolerance stress value to be reached for the calculation to proceed to the next time step and maximum number of supplementary iterations for the time increments were properly defined in the FORTRAN script used as input to Code_Aster tool. A uniform value of each of these parameters was maintained for all the simulations and they are mentioned under the column Code_Aster parameters in the Table 17. At the end of the computation, on visualizing the resulting mesh file in ParaView, the predicted maximum principle stress, strain and maximum deflection were 263.3 MPa, 0.0114 and 0.8625 mm respectively. The results from the calculation is presented in *Figure* 126.

6.3.2 FEM analysis result for 1 mm displacement

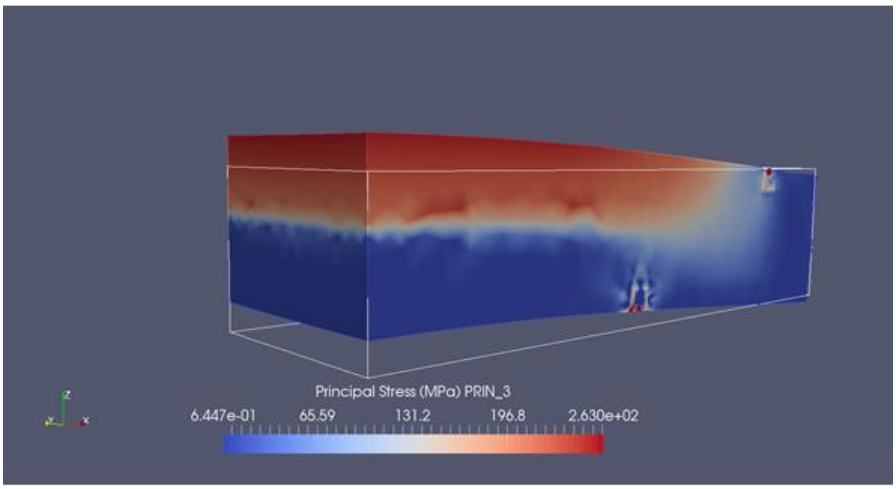
The FEM calculation was carried out with an applied displacement of 1 mm with similar conditions of previous case and the stress and strain fields were recorded by Code_Aster. The predicted maximum principle stress, strain and maximum deflection were 304.1 MPa, 0.0233 and 1.743 mm respectively. The results from the calculation are presented in *Figure* 127.



(a) Deflection of the beam (mm)

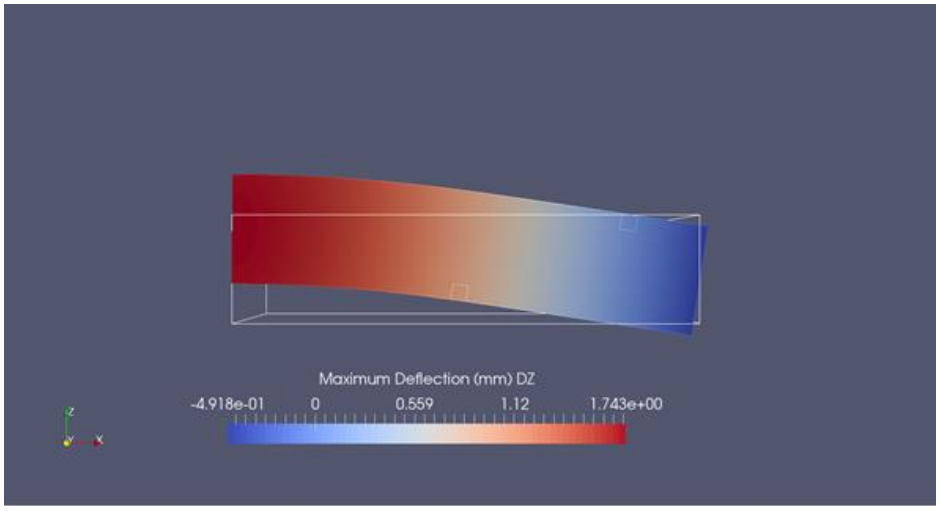


(b) Strain

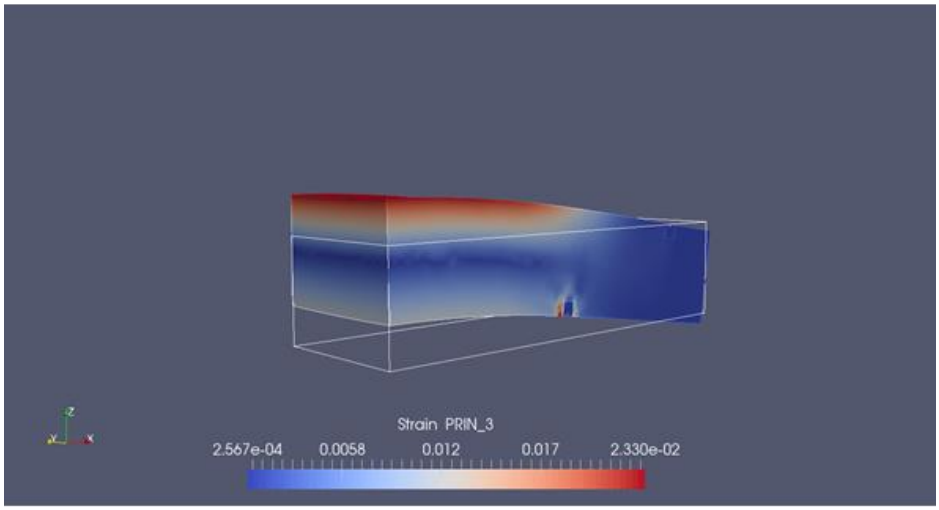


(c) Principle Stress (MPa)

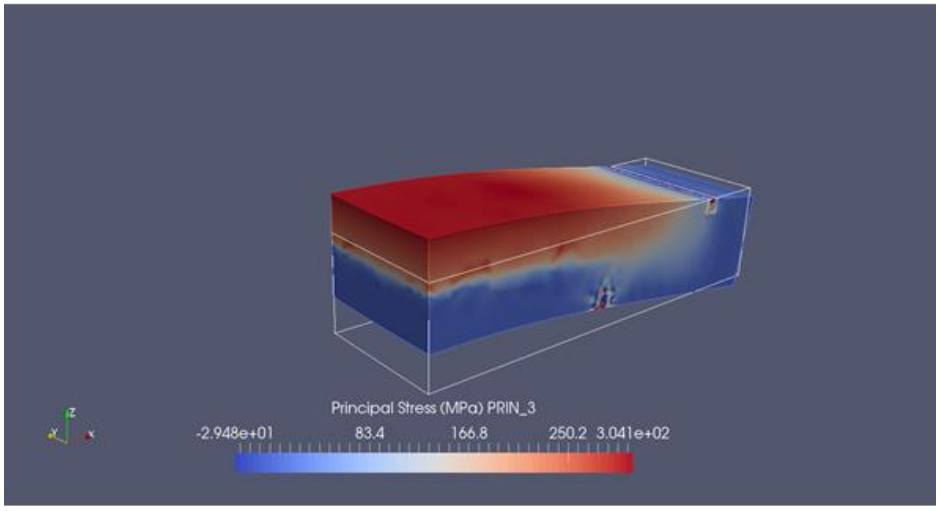
Figure 126: FEM results for 0.5 mm displacement of push rods.



(a) Deflection of the beam (mm)



(b) Strain



(c) Principle Stress (MPa)

Figure 127: FEM results for 1 mm displacement of push rods.

Table 17: Preliminary matrix for each FEM analysis

GLOBAL SAMPLE – FEM analysis									
Mesh Dimensions									
Length : 30 mm Width : 10 mm Height : 7 mm									
FEM_ID	Displacement Applied (mm)	Code Aster Parameters				Maximum deflection in the centre (mm)	Max Principal Stress (MPa)	Max. Strain	
	(.comm file)	Number of Time steps	Number of Increments in each time step	Tolerance level (MPa)	Number of Supplementary Iterations	(output)	(output)	(output)	
1	0.01	10	10	5 e-5	12	0.01594	27.6	1.82×10^{-4}	
2	0.1	10	10	5 e-5	12	0.1581	192.1	1.89×10^{-3}	
3	0.2	10	10	5 e-5	12	0.3236	225.1	4.16×10^{-3}	
4	0.5	10	10	5 e-5	12	0.8625	263	1.13×10^{-2}	
5	0.8	10	10	5 e-5	12	1.394	288.3	1.84×10^{-2}	
6	1	10	10	5 e-5	12	1.743	304.1	2.33×10^{-2}	
7	1.5	10	10	5 e-5	12	2.613	335.7	3.44×10^{-2}	
8	2	10	10	5 e-5	12	4.35	406.8	5.80×10^{-2}	
9	3	10	10	5 e-5	12	6.23	462.4	8.3×10^{-2}	
10	5	10	10	5 e-5	12	8.471	520.5	1.073×10^{-1}	
11	8	10	10	5 e-5	12	13.42	640	1.66×10^{-1}	
12	10	10	10	5 e-5	12	16.70	718.8	2.056×10^{-1}	

6.4 Discussion

Finite element modelling has been used to design and evaluate the four-point bend set-up used for constant load stress corrosion cracking testing in autoclave. The geometry and complex interactions between the cylindrical push rods and the specimen have been simplified based on two approximations.

The first approximation was to not model each and every component of the four-point bend test and use symmetry in order to simplify the mesh and reduce the computation time. The elimination of the cylindrical rods was necessary as it becomes too complex to design and model the interaction between the contact points. However, the geometry differences will have an effect on the modelling results. FEM analysis should be performed with high level of care in these regions; hence the anticipated contact region was assigned with higher Young's modulus so that the effect of the approximation would be negligible. Despite the approximation, the results from the experimental and FEM analysis showed high level of agreement as shown in *Figure* 128, especially in the region of stresses experienced during the experiment. The constant load of 20% above yield stress that is 285 MPa was achieved by applying a displacement of 1 mm to the cylindrical push rods. The FEM results predicted a maximum value of 304.1 MPa for 1 mm displacement. This shows that the model correctly used the input properties.

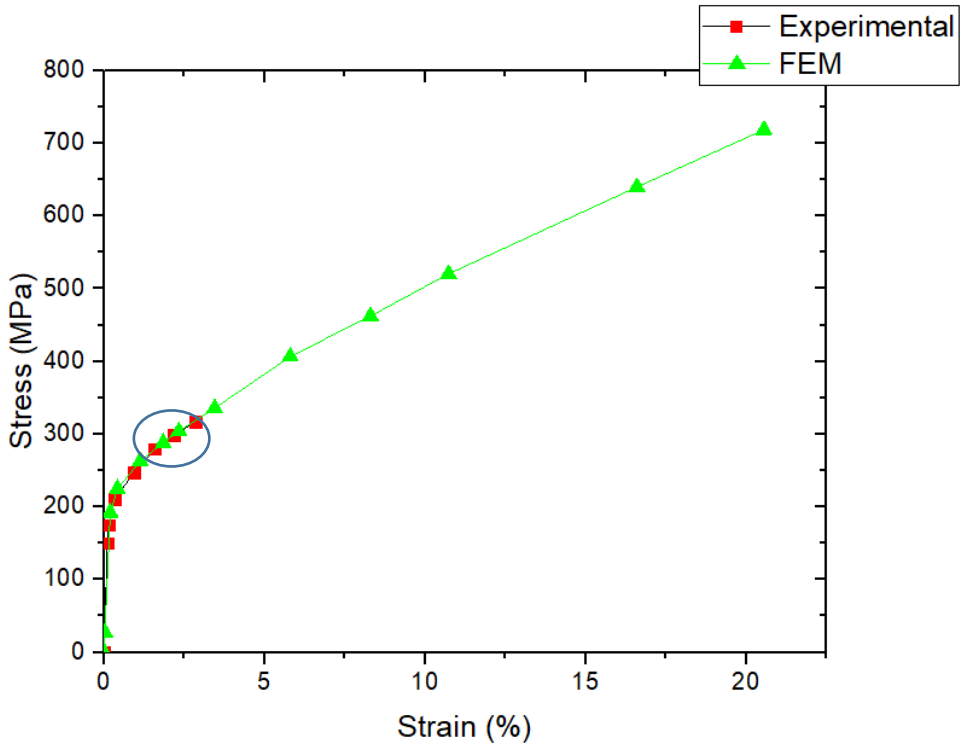


Figure 128: Stress-strain curve for Experimental and FEM results. The encircled region denotes the stress levels experienced when the constant load of 20% above yield stress was maintained during the experiment.

The second approximation affects the description of the mechanical properties and behaviour of the specimen. The equation governing the mechanical behaviour used in this model implies nonlinearity even for stress levels lower than yield stress due to the power law relationship. This nonlinearity becomes significant for the stress levels higher than the yield stress. The experimental data input and the model fully describes the mechanical response of the specimen in both the elastic and plastic regions. The agreement between the experimental and predicted stress levels emphasises the validity of the model. Nonetheless, a better fit would have been possible if the experimental data were available for higher stress levels.

The results from FEM modelling have demonstrated a good level of reproducibility especially for the experimental conditions for 1 mm displacement (around 2.5% strain). Therefore, this model is used as the input mesh and corresponding stress and strain fields recorded using

Code_Aster simulation for 1 mm displacement are used as the input stress and strain fields for SCC computation using Local Model in Code_Coriolis.

6.4.1 Summary

The methodology of using FEM tools to model the four-point bend test performed in autoclave has been described. The four-point bend test has been adapted mainly to SCC testing as it provides a simple, compact, and easily operated device for applying loads. The load is applied using the push rod drive mechanism and the specimen is in tension along the specimen axis.. The main advantages of the four-point bend test are that the specimen is always flat, the gauge length is maintained under a known uniform stress state and it is easy to carry out post-autoclave characterization analysis on the flat specimens.

The mesh is programmed to contain the material and the mechanical properties that define how the specimen will react to the loading conditions. The boundary conditions or constraints are applied to the mesh in order to avoid any free displacement of the model in space and to reach convergence during calculation. These material properties, boundary conditions and applied displacement are fed into Code_Aster using a script written in FORTRAN language. The FEM calculation was performed with various applied displacement on the push rods. The predicted maximum principle stress, strain and maximum deflection for various applied displacements are compared with the experimental observations.

The key observation is that results from FEM modelling have demonstrated a good level of accuracy especially for the experimental conditions for 1 mm displacement (around 2.5% strain). Therefore, this model can be used as the input mesh and corresponding stress and strain fields (applied strain of 2.5%) recorded using Code_Aster simulation for 1 mm displacement can be used as the input stress and strain fields for SCC computation using Local Model in Code_Coriolis.

6.5 Evaluation of Local Stress along the grain boundaries

As discussed in the previous chapters, SCC degradation is a local phenomenon, and it is important to evaluate the local stresses acting on the grain boundaries to better validate the Local Model. A novel methodology of obtaining the local stress from the SCC tested samples using 3D EBSD is described in detail in the following sections. This involves a series of steps starting with obtaining datasets from 3D EBSD, converting them into suitable model aggregate meshes and performing simulation analysis on them to extract the local stresses acting on the grain boundaries. It is important to note that for crack initiation studies, the local stress concentration on the surface and along the grain boundaries to the depth of initial 10 µm is necessary. Due to the delicate equipment set-up of 3D EBSD, as mentioned in *section 3.5*, out of 20 trials only 4 successful datasets were obtained.

6.6 Conversion of 3D EBSD data into aggregate mesh

It is necessary to obtain the local stresses acting on the grain boundaries to better evaluate the local stress (critical stress) required for crack initiation in the local model. To do this, a 3D representative aggregate model and CPFEM simulation was performed to obtain the stress concentration at the grain boundaries. 3D EBSD technique was used to extract information on the orientation, grain morphology and boundary plane in 3D. The routine of converting the 3D EBSD data into a mesh is novel in SCC research and it involves a series of steps. In the following sections, the steps involved in this routine are described for one 3D EBSD dataset (3D EBSD dataset 1 – this denotes first dataset and same term is used in the following sections) and the same procedure was carried out on the other datasets.

6.7 3D EBSD dataset 1

As mentioned in *section 3.5.2*, a FEI Helios PFIB-SEM with Aztec 3D in the University of Manchester was used to collect the 3D EBSD dataset 1. The region of interest to be investigated is of volume 300 x 200 x 60µm (where 300µm x 200µm is the size of the cross section and 60µm is the depth) represented by the yellow box in *Figure 57* (in Chapter 2). *Figure* 129 shows the SE image of investigate area. FIB slicing was carried out using milling current of 22nA and accelerating voltage of 5 kV with each slice being 250 nm thick. EBSD maps were acquired at 20kV, with a step size of 1 µm in x and y direction and were recorded for every 4 FIB slices so that the resolution in z direction was also 1 µm (to have a voxel size of 1µm). Due to the delicate 3D EBSD set-up, the EBSD scan failed after 87 slices. The EBSD slices were saved using Aztec software as shown in *Figure* 130. The EBSD maps were saved on *.oip* file format (Oxford Instruments EBSD file format). Using the HKL EBSD software, these files were converted into *.ctf* files.

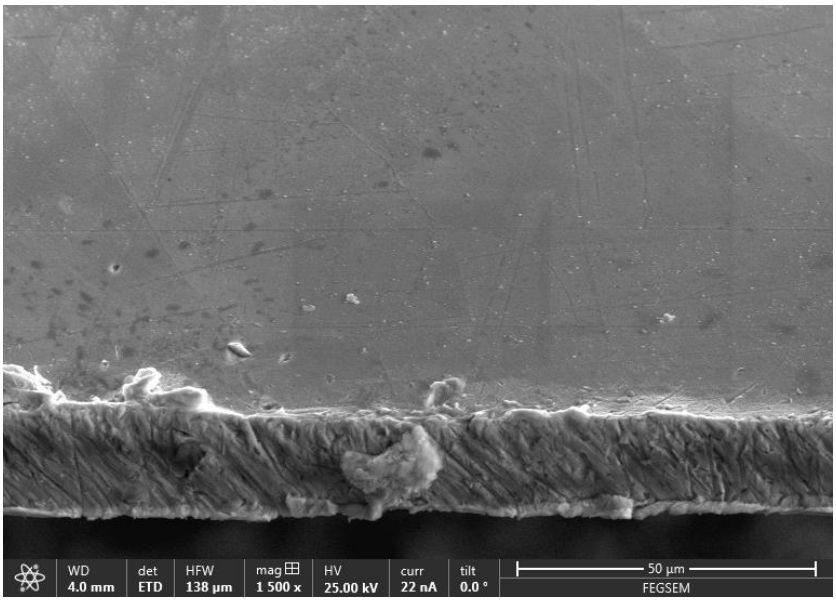


Figure 129: SE image of area of interest for 3D EBSD dataset.

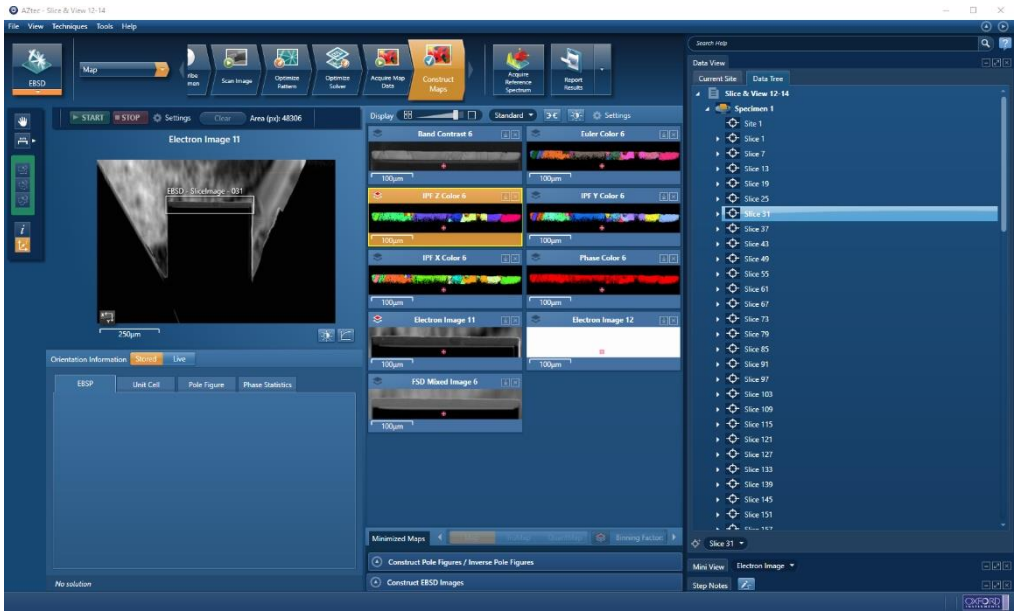


Figure 130: Oxford Instruments Software (Aztec) to save EBSD maps.

DREAM3D, an open source software, was used for data treatment of 3D EBSD. This software works on serial 2D EBSD data providing alignment of sliced sections, cropping the area of interest, allowing segmentation of the grains, and providing noise reduction with different computer algorithms in the form of various pipelines. The saved *.ctf* files were treated with the DREAM3D algorithm *'Import Orientation Files to H5EBSD'* to perform stitching (aligning) of individual slices and then they were converted into the DREAM3D readable format *'.h5ebsd'*.

6.7.1 3D Reconstruction of 3D EBSD dataset 1

Following the conversion of the file format, the alignment and segmentation of the grains was performed. This was achieved by using the DREAM3D pipeline illustrated in *Figure* 131 which was developed by the author of this thesis. Each step in the pipeline has been described in the following sections.

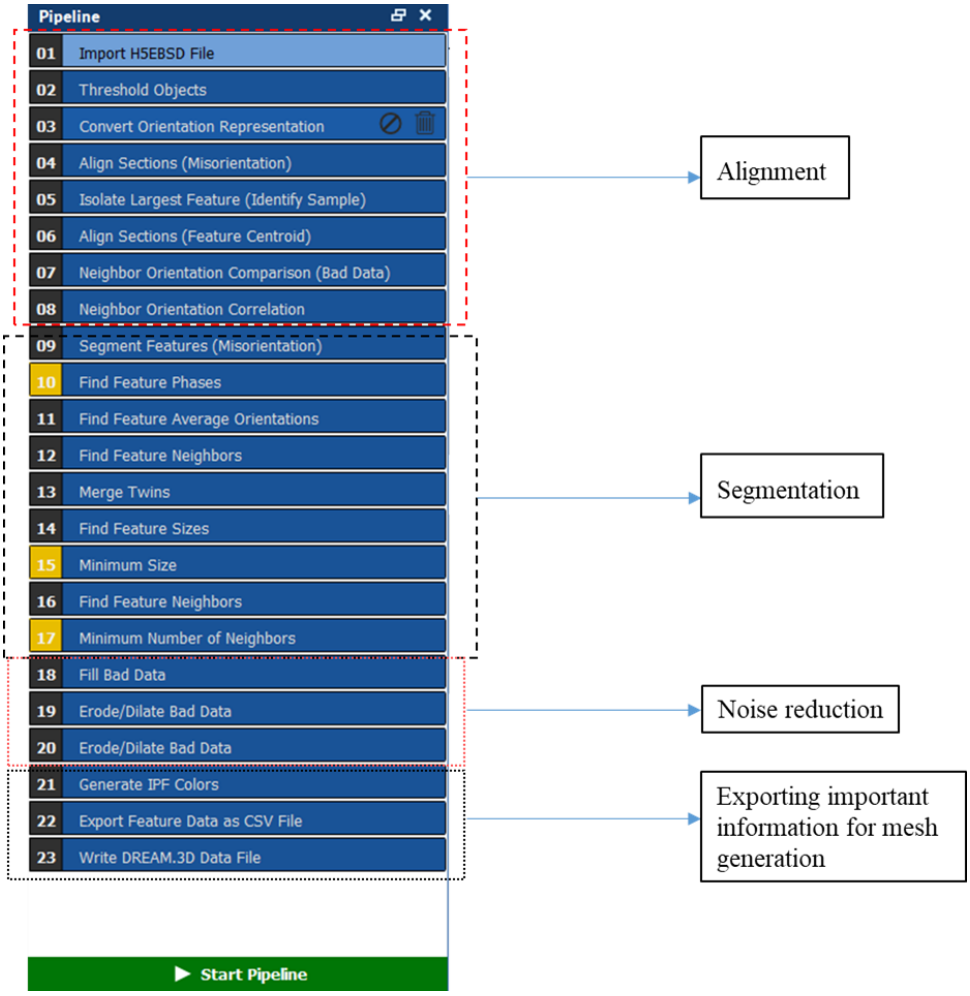


Figure 131: DREAM3D pipeline used for 3D reconstruction of EBSD dataset.

6.7.1.1 Alignment

The alignment of the dataset consists of the first eight steps (1-8) in the DREAM3D pipeline presented in *Figure* 131. Firstly, the saved *.h5ebsd* file was imported into the pipeline and the dimensions were defined. Secondly, a mask was created for the objects with the band contrast threshold value less than 65. The reason for creating this mask was to remove any existing regions other than the sample. In the third step, the orientation representation is converted from Euler into quaternion format. The quaternion format contains x, y, and z components, which represent the axis about which a rotation will occur, and a w component, which represents the amount of rotation which will occur about this axis. Compared to Euler angles, they are simpler

to compose and avoid the problem of gimbal lock [276]. In the fourth step, the sections are aligned based on the misorientation where the maximum tolerance degree is set to 10. This was followed by aligning the sections based on the centroid of the features (grains). Once this was completed, the neighbour orientation comparison was performed by defining the number of required neighbours (4) and the misorientation tolerance angle. Finally, the neighbour orientation correlation was performed by assigning the minimum confidence index of 0.5, as misorientation tolerance. At the end of this step, all the crystal structures were properly aligned.

6.7.1.2 Segmentation

The steps 9-17 in the DREAM3D pipeline, presented in *Figure* 131, carried out the segmentation of the dataset. In step 9 of the pipeline, the segmentation of the features (grains) were performed and individual grain IDs were recorded. This step was followed by collecting the phase, grain size (equivalent diameter and volume), average orientation and neighbour information of the each of the grains. In this step, the quaternions were converted back to Euler representation and recorded. The minimum size of the grain volume was assigned to a threshold value to remove any inclusions in the data. Using the filter, *'Find Feature Neighbours'* the shared surface area list between the grains were obtained. Thus, by the end of the segmentation process, grain size (equivalent diameter and volume), average orientation and position of the centroids of each grain was gathered.

6.7.1.3 Noise reduction

Segmentation was followed by noise reduction steps. During this process, the dataset was subjected to a series of erode/dilate bad data function so that all the non-indexed data points were extrapolated with the orientations of the neighbouring grain. This was carried out for 4 iterations to obtain a dataset representative of the real aggregate.

6.7.1.4 Exporting data

The data was exported into two parts: the geometry and the orientation file. The orientation file contains all the necessary information obtained such as centroids, average Euler angles, phases and volume of the grains. The geometry was saved in *'.inp'* and *'.dream3d'* format. The *'.dream3d'* format can be opened using ParaView module in Salome Meca as shown in *Figure* 132. Even though, the dataset looks like a thin sheet, the interactions of the grain on the surface and to the level of 10 µm is sufficient to estimate the local stress for crack initiation as the maximum crack depth has reached only 5.5 µm in this case.

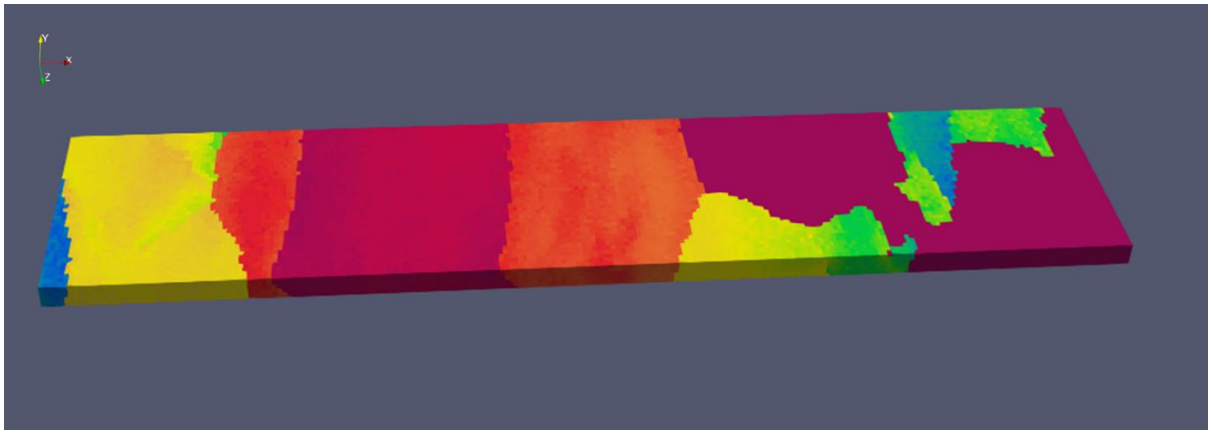


Figure 132: Geometry of 3D-reconstructed aggregate from 3D EBSD dataset 1 (16 grains).

6.8 Polycrystalline aggregate mesh generation

To perform the CPFEM calculation on the aggregate mesh to evaluate the stress concentration on the grain boundaries, it was necessary to couple the orientation information obtained with the right grains in the geometry. This was a crucial step to make sure the conditions were correct for the computation to work properly. The assignment of proper orientation to the grains was accomplished in a series of operations on the geometry. The python scripts used for this are presented in Appendix C for reader's interest. The mesh generation can be automated, and each step involved in the process is explained in this section.

6.8.1 Assigning nodes and elements to the geometry

The first step of aggregate mesh generation was to convert the *'.dream3d'* file to *'.mesh'* file. In this step, the nodes and elements were assigned to the features (grains) in the triangulation geometry and a surface mesh was created using the script *'inp2mesh.py'*. This file contains all the information needed to entirely describe the surface mesh and its underlying geometry. It is organized as a series of fields identified by keywords. In addition to the vertex coordinates and the list of faces, it allows one to specify additional information such as corners, edges, ridges, required entities, etc. This was then visualized using gmsh [277] tool in Meshgems software and is presented in *Figure* 133.

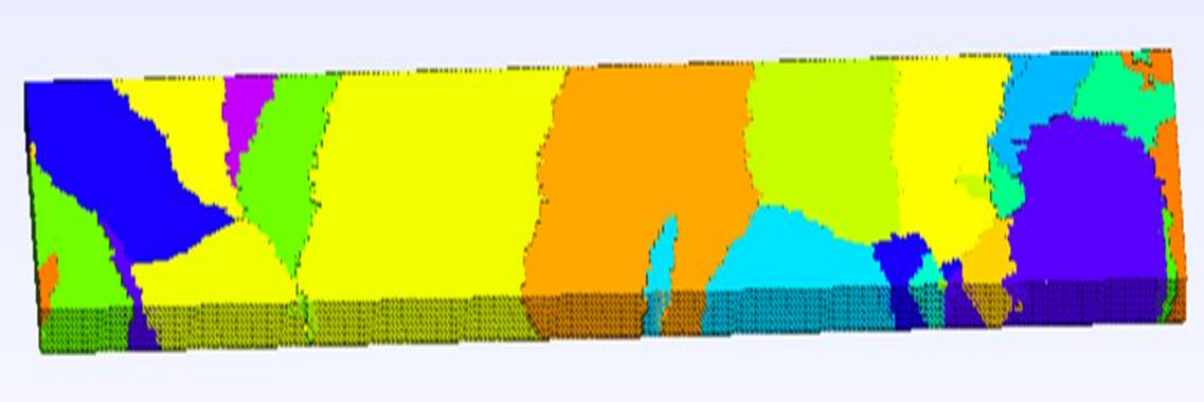


Figure 133: Surface mesh obtained from geometry of 3D EBSD dataset 1

6.8.2 Smoothening of grain boundaries

When the reconstructed grain boundaries were closely observed, step like artefacts (ridges) with high curvature variations to the given surface were formed as shown in *Figure* 134 . These artefacts would reduce the quality of the mesh when refined close to the grain boundaries and might affect the results of the computation.

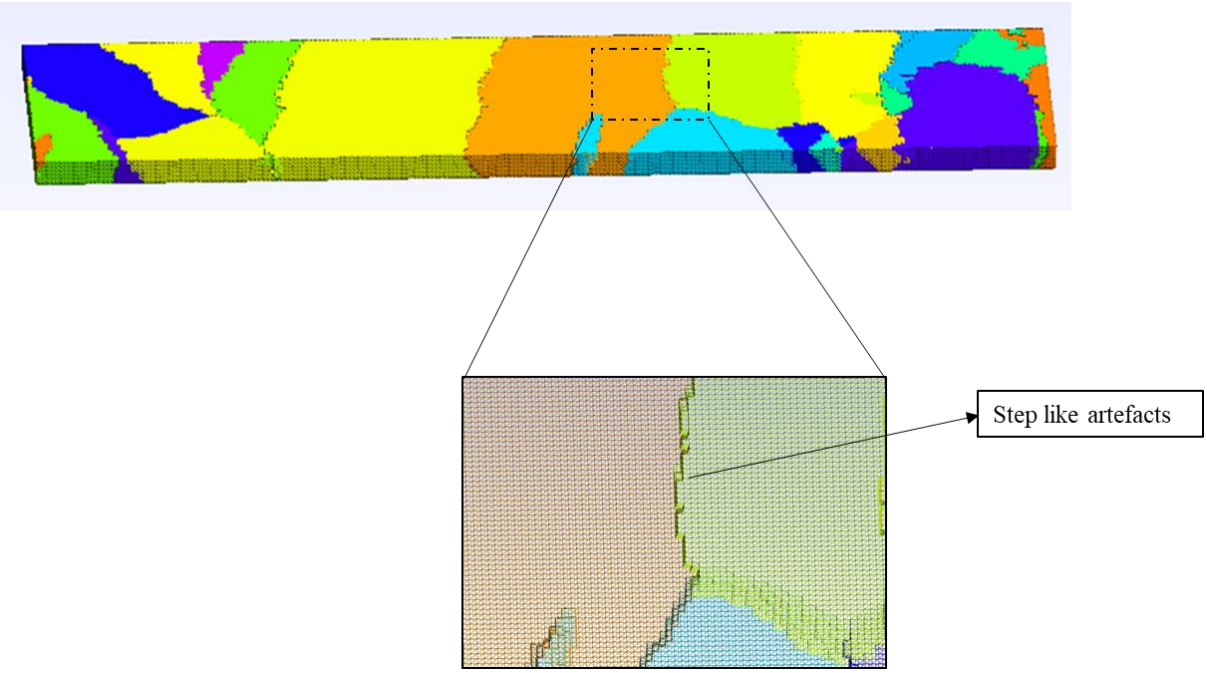


Figure 134: Surface Mesh with irregularities close to the grain boundaries

In order to overcome this discrepancy in the microstructure from the experimental data, an optimization strategy generating Vornoi tessellations on synthetic polycrystal, as proposed by Renversade [278] in his PhD work, was used. Thus, the Euclidean distance between each voxel near the grain boundary was minimized by an iterative process as shown in *Figure* 135.

With respect to optimization procedure, the ridges were orderly given numbers and computed to differentiate the grain boundaries with the edges of the samples using the script *'compute ridges.py'*. The output mesh file has all the ridges and corners properly defined.

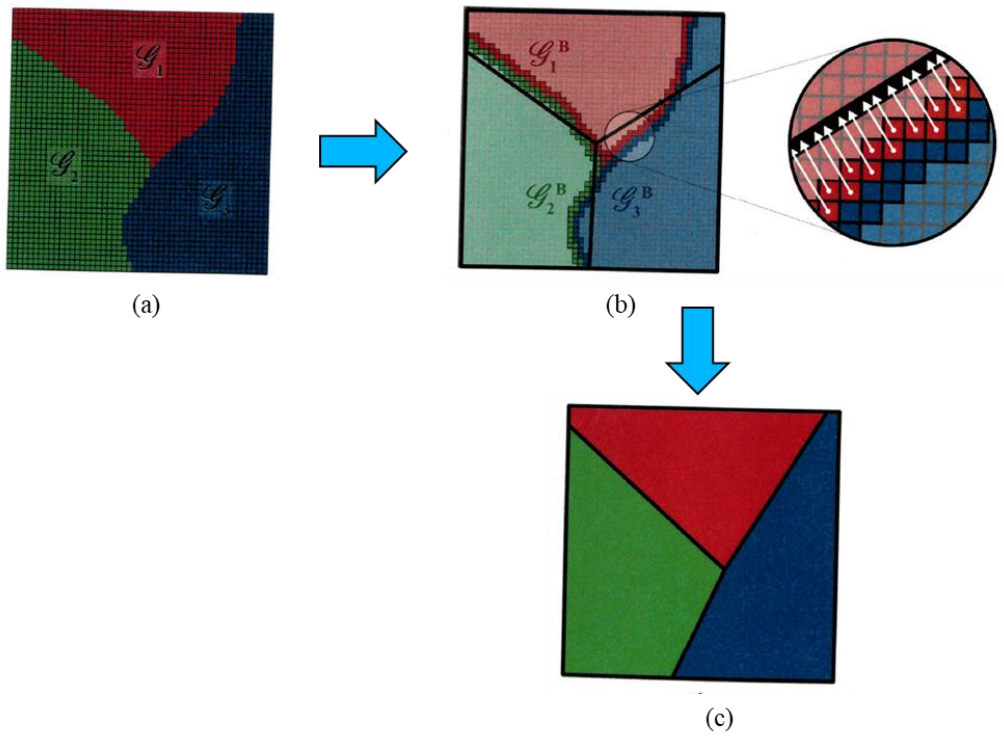


Figure 135: Optimization procedure exemplified for a 2D microstructure. (a) Experimental microstructure containing three grains (voxel sets G1, G2 and G3). (b) Comparison between the experimental grain boundaries (GB1, GB2 and GB3) and tessellation boundaries. (c) Optimized Laguerre tessellation after minimization of Euclidean distance adapted from [278]

The surface sandpapering was carried out using the MeshGems-SurfOpt function in the Salome Meca environment [279], which provides automatic adaptive surface remeshing. The aim of this step was to avoid shrinkage of the given surface triangulation, i.e., the high curvature variations of the given surface will be smoothed out without shrinking the volume. The surface remeshing algorithm provides another surface mesh as the output but with improved element density and mesh quality. It also includes additional geometric surface properties and information that will be used to control and drive the surface remeshing (such as constrained entities, corners, ridges, normal, etc.). At the end of this step, the grain boundaries were smoothened in such a way that the texture of the actual grain morphology was retained and at the same time the Euclidean distance was reduced.

To correct any defects or faults in the surface mesh before performing volumetric meshing, it was treated with MeshGems-Cleaner function in the Salome Meca environment [280]. The aim of this step was to scan the input surface mesh, detect several types of mis-features such as overlaps, intersections, holes or gaps and apply several corrective strategies in sequence as described in [280]. *Figure* 136 shows the surface mesh after treating with MeshGems-Cleaner function that is ready for volumetric meshing. Thus, MeshGems-Cleaner function acts as a pre-processor to make surface meshes suitable for volumetric meshing (using MeshGems-Tetra), that is watertight and not self-intersecting.

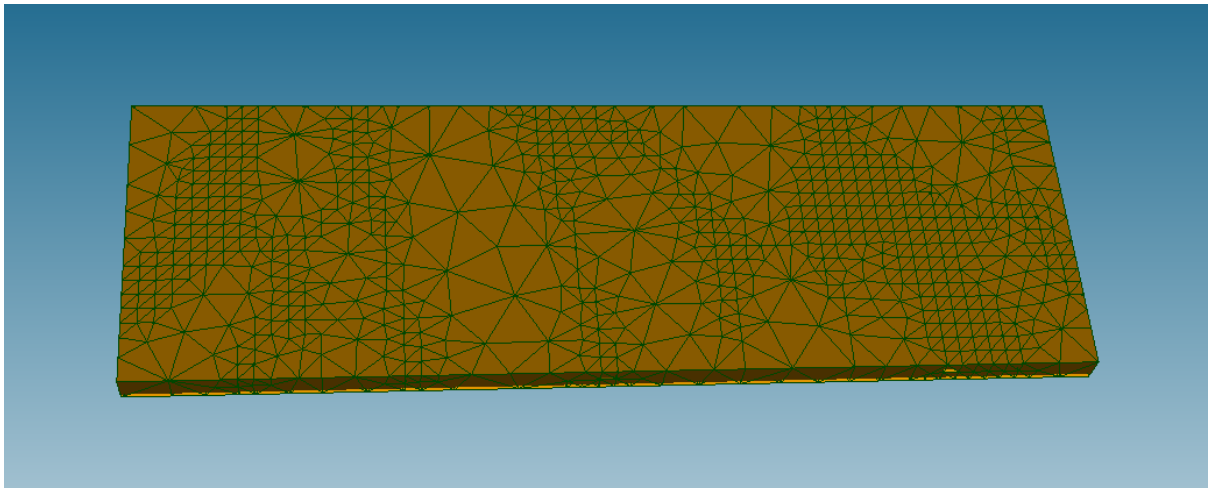


Figure 136: Surface mesh with mis-features corrected and ready for volumetric meshing.

Finally, the volumetric meshing was done using the MeshGems-Tetra function, which is a fully automatic tetrahedral mesh generator [281]. This creates a volume tetrahedral mesh defined by a watertight input triangular surface mesh. At this point, the grains were given a random grain number and changed to assign the correct orientation to the grain. The grains were renumbered by correlating the centroid position and volumes using the script *'grainrenumbering.py'*. Thus, at the end of this step, a tetrahedral volumetric polycrystalline aggregate was modelled, and it was ready for evaluating the stress concentration at the grain boundaries. The polycrystalline aggregate mesh along with the grain representation in standard triangle for the four 3D EBSD

datasets is presented in *Figure* 137 - *Figure* 140. The 3D EBSD dataset 1 was acquired from PFIB on a larger volume with 16 grains. The dimension of the geometry is 185 µm x 60 µm x 18 µm. To reduce the computation time, moderate level of meshing was done. The final 3D EBSD dataset 1 mesh is composed of 7811 elements and 2063 nodes as shown in *Figure* 137*a*. The grain representation of the mesh for 16 grains is reported for z-axis in a standard triangle and is given in *Figure* 137*b*.

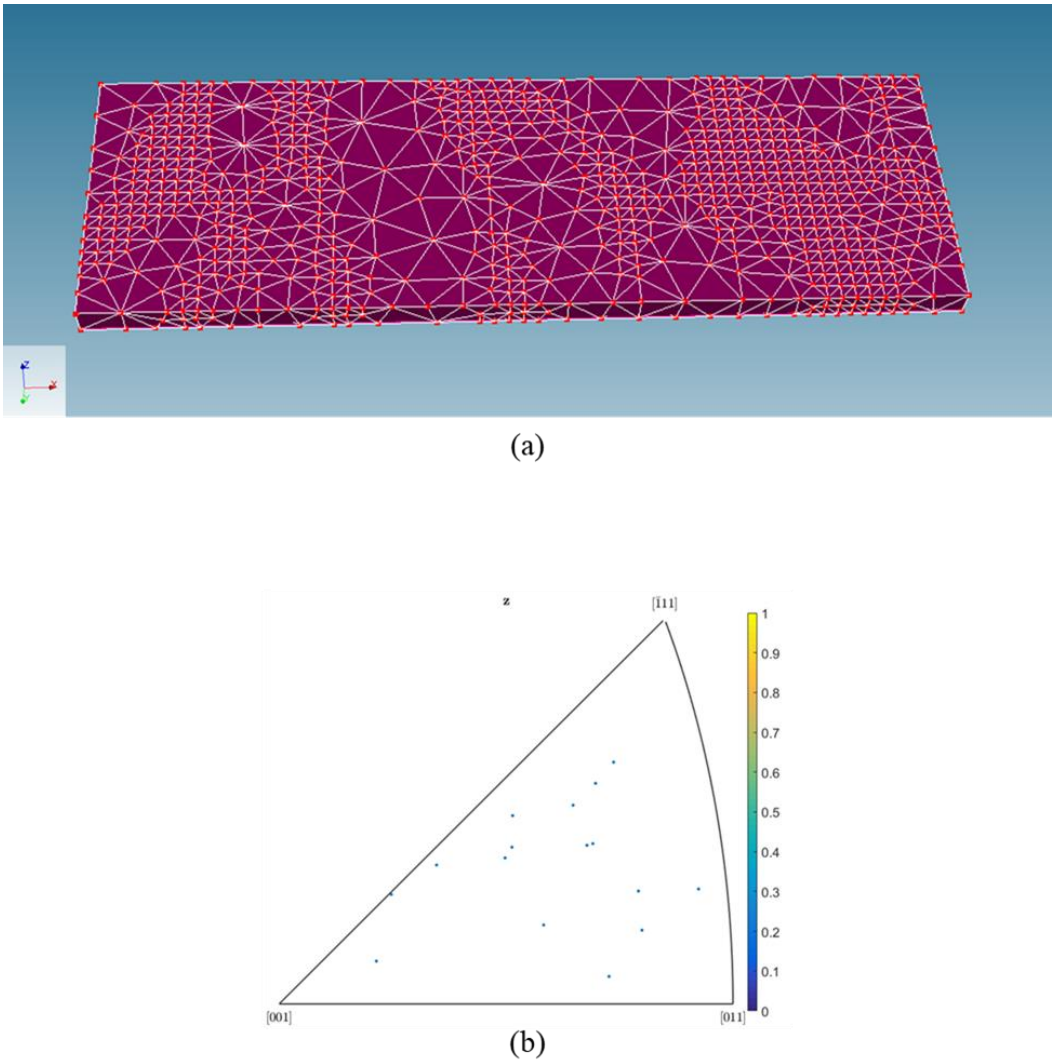


Figure 137: (a) 3D Finite element mesh for dataset 1 with 16 grains, 7811 elements and 2063 nodes (Dimension is 185 µm x 60 µm x 18 µm). (b) Grain representation of the mesh for 16 grains reported for z-axis in a standard triangle.

The 3D EBSD dataset 2 was similarly acquired from PFIB on a larger volume with 22 grains. The dimension of the geometry is 200µm x 138µm x 30µm. To reduce the computation time, moderate level of meshing was done. The final 3D EBSD dataset 2 mesh is composed of 16931 elements and 6871 nodes as shown in *Figure* 138*a*. The grain representation of the mesh for 22 grains is reported for z-axis in a standard triangle and is given in *Figure* 138*b*.

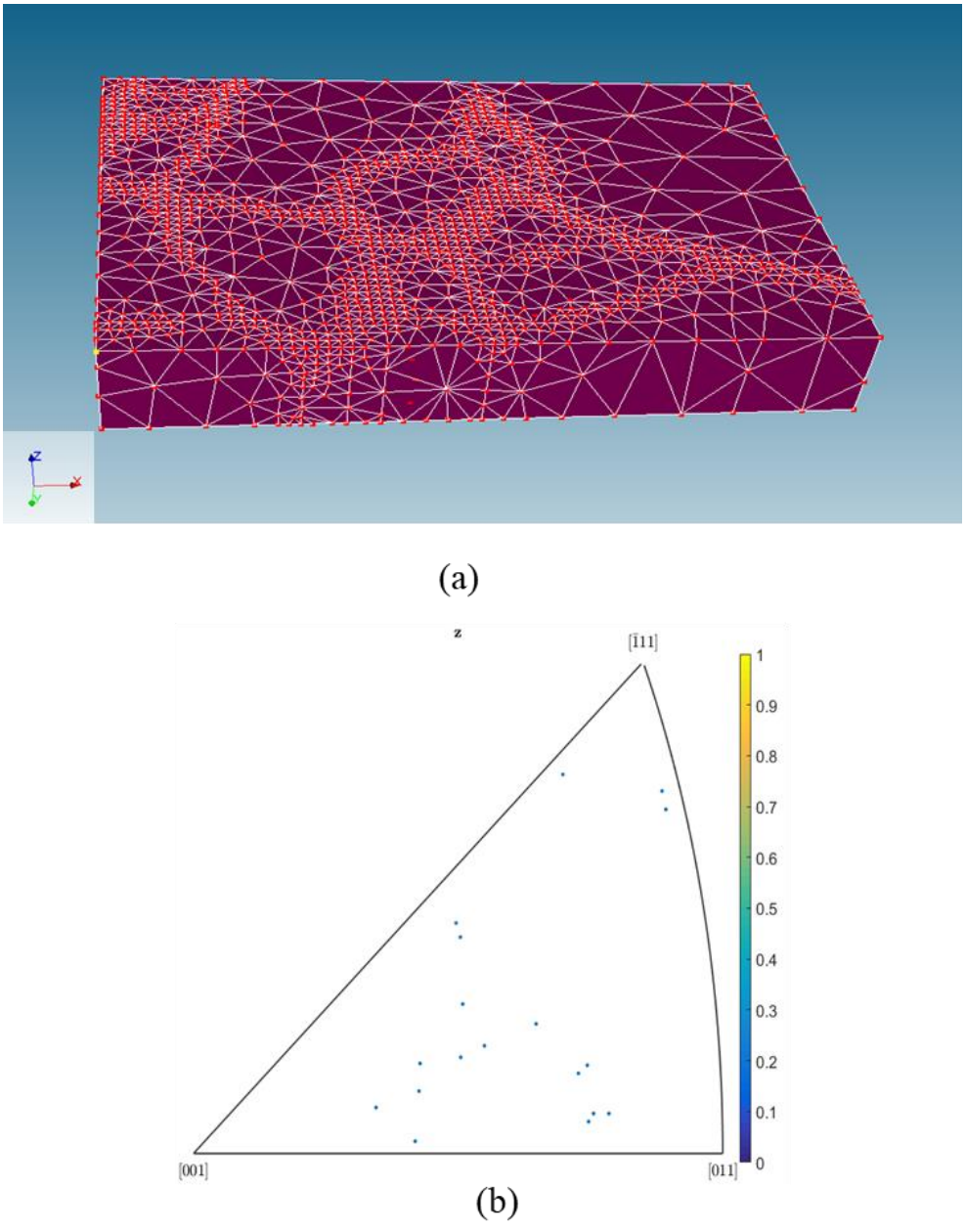
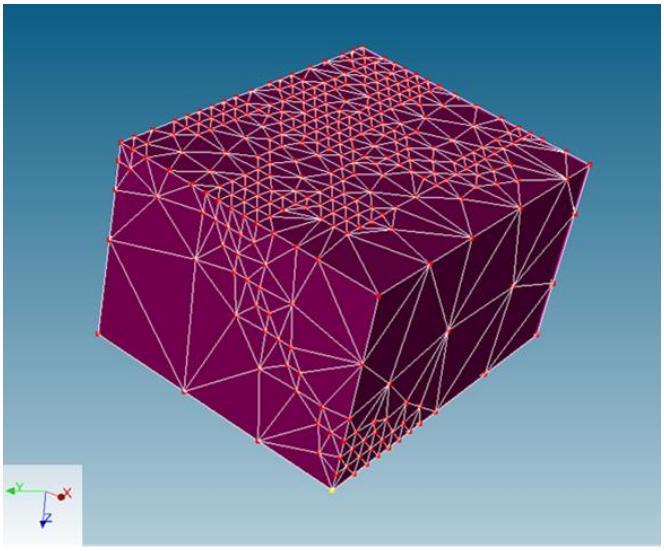
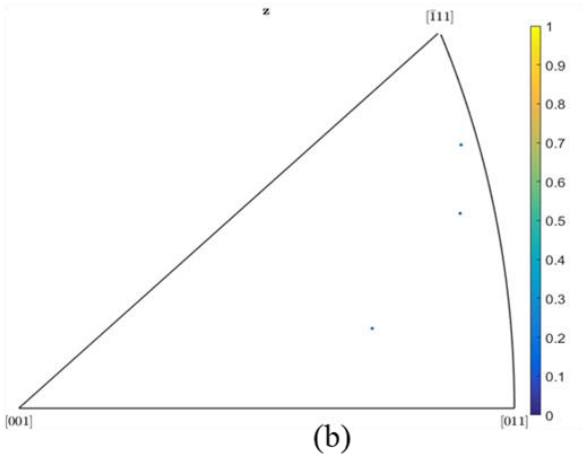


Figure 138: (a) 3D Finite element mesh for dataset 2 with 22 grains, 16931 elements and 6871 nodes (Dimension is 200 µm x 138µm x 30 µm). (b) Grain representation of the mesh for 22 grains reported for z-axis in a standard triangle.

The 3D EBSD dataset 3 was acquired in a Zeiss Crossbeam 540 Ga^+ ion FIB on a smaller volume, but with better resolution, with 4 grains. The dimension of the geometry is 8µm x 16µm x 12µm. As the mesh size is small, finer level of meshing was done on this dataset. The final 3D EBSD dataset 3 is composed of 9628 elements and 1918 nodes as shown in *Figure* 139*a*. The grain representation of the mesh for 4 grains is reported for z-axis in a standard triangle and is given in *Figure* 139*b*.



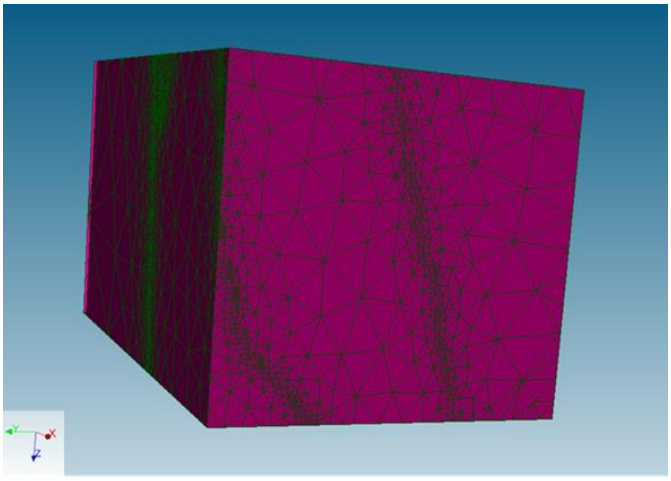
(a)



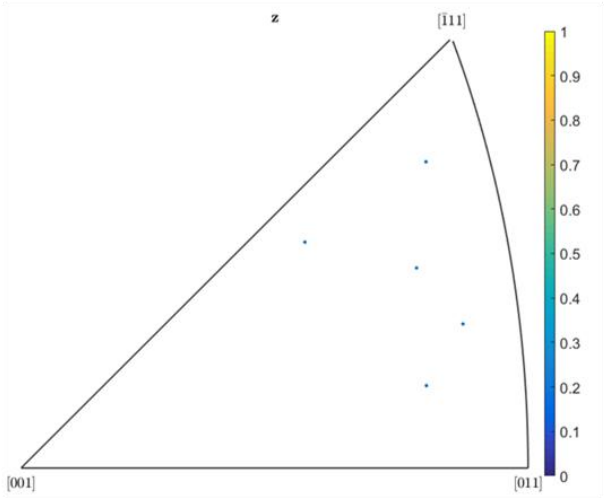
(b)

Figure 139: (a) 3D Finite element mesh for dataset 3 with 4 grains, 9628 elements and 1918 nodes (Dimension is 8µm x 16µm x 12µm). (b) Grain representation of the mesh for 4 grains reported for z-axis in a standard triangle.

The 3D EBSD dataset 4 was acquired in a Zeiss Crossbeam 540 Ga^+ ion FIB on a small volume with better resolution with 7 grains. The dimension of the geometry is 35µm x 25µm x 20µm. As the mesh size is small, finer level of meshing was done on this dataset. The final 3D EBSD dataset 4 is composed of 87370 elements and 15518 nodes as shown in *Figure* 140*a*. The grain representation of the mesh for 7 grains is reported for z-axis in a standard triangle and is given in *Figure* 140*b*.



(a)



(b)

Figure 140: (a) 3D Finite element mesh for dataset 4 with 7 grains, 87370 elements and 15518 nodes (Dimension is 35µm x 25µm x 20µm). (b) Grain representation of the mesh for 7 grains reported for z-axis in a standard triangle.

6.9 Stress concentration at the grain boundaries

Once the microstructure was simulated from the 3D EBSD datasets and the aggregates were meshed with tetrahedral elements, it was ready for crystal plasticity finite element modelling (CPFEM) calculations. The local stress concentration at the grain boundaries were evaluated on the generated polycrystalline aggregate. By using CPFEM, the activation of slip systems are taken in account in the frame of small deformation assumption and the strain rate can be decomposed into elastic and plastic strain rates [113,205].

$$\tilde{\dot{\varepsilon}} = \tilde{\dot{\varepsilon}}e + \tilde{\dot{\varepsilon}}p \ldots\ldots\ldots\ldots\ldots\ldots (32)$$

Considering that intragranular deformation is the main contribution, the plastic strain in the grain is the sum of elementary shear rates extending over all the active slip systems s:

$$\tilde{\dot{\varepsilon}}p = \sum_{s} \dot{\gamma}^{s} \tilde{m}^{s} \ldots\ldots\ldots\ldots\ldots\ldots (33)$$

where $\tilde{m}^{s}$ is the orientation tensor.

$$\tilde{m}^{s} = \frac{1}{2}\left(\tilde{l}^{s} \otimes \tilde{n}^{s} + \tilde{n}^{s} \otimes \tilde{l}^{s}\right) \ldots\ldots\ldots\ldots\ldots\ldots (34)$$

and where is $\tilde{n}^{s}$ the normal vector to the slip plane and $\tilde{l}^{s}$ is a vector corresponding to slip direction and $\otimes$ is the tensor product. CPFEM relies on the assumption that plastic deformation between room temperature and 345°C occurs by crystallographic slip following Schmidt's law. The shear rate $\dot{\gamma}^{s}$ is linked to the motion of dislocations in active slip systems. The resolved shear stress τ^{s} on the given slip system s is the projection of the local stress tensor on $\tilde{m}^{s}$.

$$\tau^{s} = \tilde{\sigma} : \tilde{m}^{s} \ldots\ldots\ldots\ldots\ldots\ldots (35)$$

Thus, after the computation on polycrystalline aggregate, the standard deviation of the local stresses can be correlated to the mean stress (σ) assuming a Gaussian distribution of the local stresses.

$$SD(\sigma) = S \times mean(\sigma) \dots\dots\dots\dots\dots\dots (36)$$

The parameter S is the stress linear coefficient and can be obtained from the finite element computations on the polycrystalline aggregate. The stress levels are usually observed to be higher in the grain boundaries, hence in local model the tail of the Gaussian stress distribution is assumed to be responsible for initiation.

Hardening behaviour was calibrated on the stress-strain curves and cyclic tension-compression curves were calibrated by EDF [203,205] for a reference alloy 600 (RND-M-B-369 material) assuming the Norton-like viscoplastic relation and is given by the equation (37):

$$\dot{\gamma}^s = \left\langle \frac{|\tau^s - x^s| - \tau_c^s}{K_s} \right\rangle^{n_s} \cdot \frac{(\tau^s - x^s)}{|\tau^s - x^s|} \dots\dots\dots\dots\dots\dots (37)$$

where, K_s is the viscosity constant, n_s is the stress sensitivity and x^s is the kinematic hardening proportional to α^s which is given by the equations (38) & (39):

$$x^s = c \cdot \alpha^s \dots\dots\dots\dots\dots\dots (38)$$

$$\dot{\alpha}^s = \dot{\gamma}^s - d\alpha^s |\dot{\gamma}^s| \dots\dots\dots\dots\dots (39)$$

where, c is a constant. τ_c^s is the isotropic hardening and it depends on the cumulated strain γ_{cum}^r given by equations (40) & (41):

$$\tau_c^s = \tau_0 + Q \sum_r h_{rs}(1 - \exp(-b\gamma_{cum}^r)) \dots\dots\dots\dots\dots (40)$$

$$\gamma_{cum}^r = \int_t |\dot{\gamma}^r| \, dt \dots\dots\dots\dots\dots (41)$$

where h is the interaction matrix, describing the self-hardening (diagonal components) and the latent hardening (non-diagonal components) of the crystal slip systems. All components h_{rs} of h were normalized by the self-hardening components. Only five-interaction coefficients h_{rs} exist in face cubic centred structures such as austenitic materials. When strain hardening is isotropic, h is independent of the active slip system. Therefore, in this situation $h_{rs} = 1$. Usually, self-hardening components are lower than latent components. Both isotropic and kinematic hardenings were considered to model the behaviour of the material. The orientations were included in the CPFEM code on Code_Aster and the calculations were performed. The lattice rotations were considered to update the orientation of the normal to the slip planes at each step of the computation. The mean stress, along with the Gaussian distribution of the principal stresses were obtained from the CPFEM calculations and correlated with the fraction of crack grain boundaries to estimate the critical stress to fail the oxidized grain boundaries.

6.10 Results

The material properties, grain orientations, percentage of elongation (2.5%) in the loading direction on the aggregate models with respective to the loading direction on the four-point bend test were defined in Code_Aster and simulations were carried out. The strain on the loading direction was applied using periodic boundary condition and on the other directions, strains were negligible; hence, the movement in those directions were constrained for the aggregate computations. The parameters used for Code_Aster simulation of polycrystalline aggregate is presented in Table 18. At the end of the computation, the corresponding six stress components were extracted, and principal stresses were calculated from them. This was correlated with the experimental observation of fraction of crack grain boundaries and critical stress to fail the oxidized grain boundaries was estimated.

Table 18: Parameters of crystalline behaviours (elasticity and plastic hardening defined by equations 24 -28) for Code_Aster CPFEM computation of Polycrystalline aggregate mesh.

Material Registration	**E (GPa)**	**ν**	**n_s**	**K_s**	**c**	**τ_0 (MPa)**	**b**	**Q (MPa)**	**h_{rs}**
Alloy 600 (T-265)	204	0.33	7	65	600	247.5	3	45	1

6.10.13D EBSD Dataset 1

CPFEM computations were performed on the polycrystalline aggregate mesh of Dataset 1 to estimate the maximum principal stress distribution on the surface of the mesh. The strain of 2.5% was applied as displacement along the y-axis that corresponds to the loading direction on the macroscopic specimen. The maximum principal stress was calculated from the six stress tensors recorded by Code_Aster. *Figure* 141 shows the CPFEM calculation result of maximum principal stress for 3D EBSD Dataset 1 along with the loading direction. The histogram of the corresponding stress after 2.5% elongation of the aggregate along y-axis is plotted as shown in *Figure* 142. The mean maximum principal stress for 3D EBSD Dataset 1 was found to be 382.4 MPa with a standard deviation of 283.41 MPa.

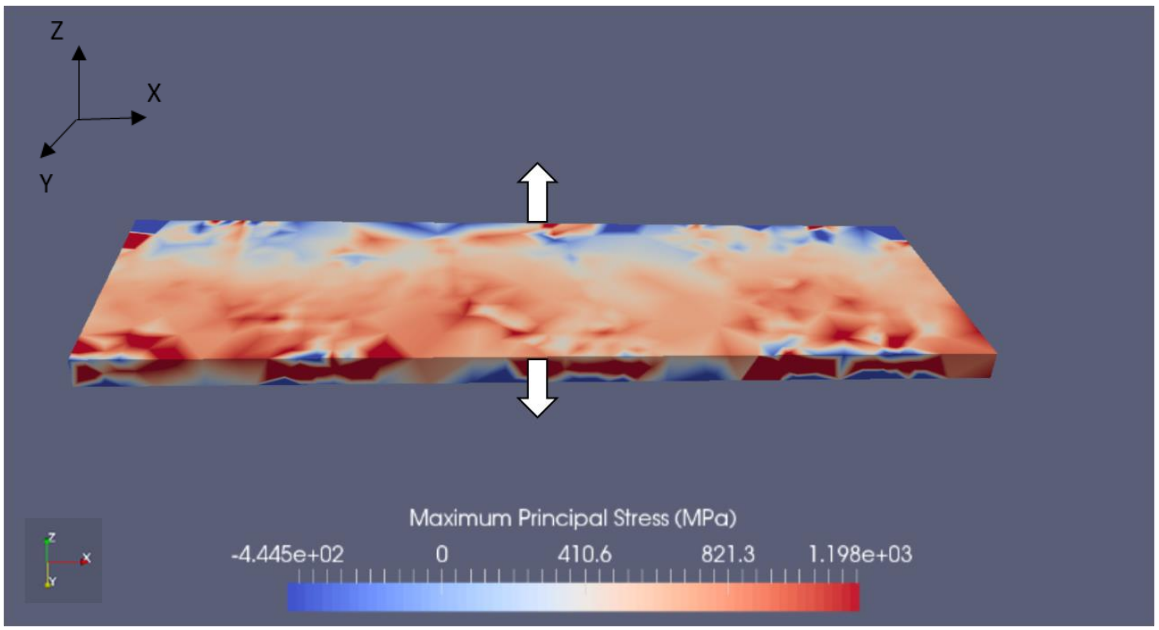


Figure 141: CPFEM calculated Principal Stress in 3D EBSD dataset 1 with 2.5% strain applied along y-axis corresponding to the loading direction of the macroscopic specimen loading direction.

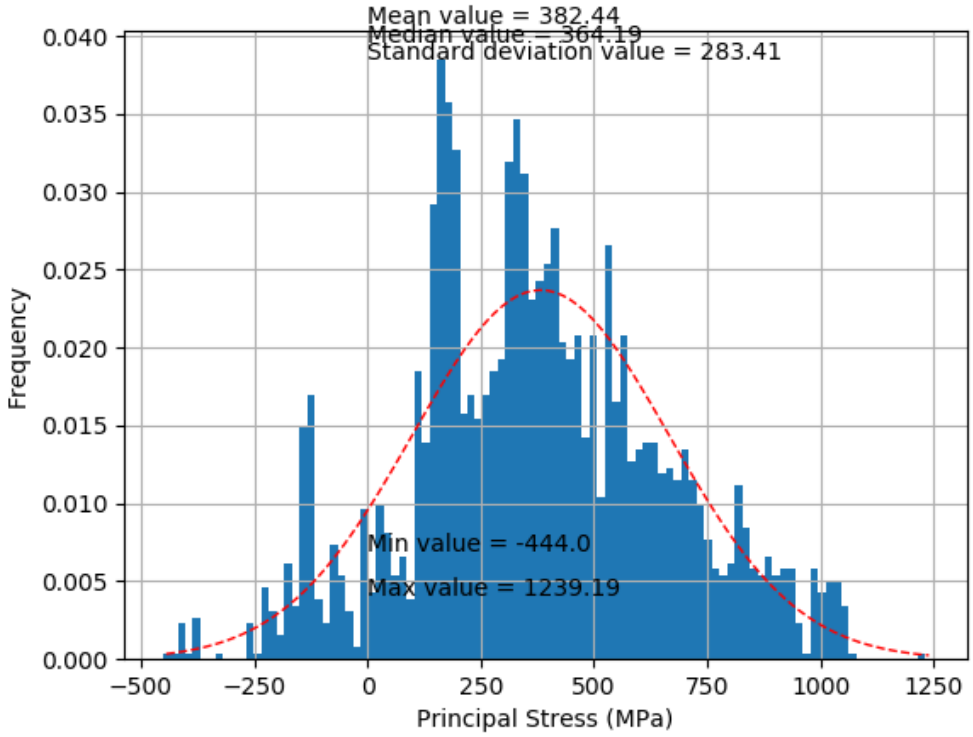


Figure 142: Histogram of the corresponding Principal stresses for 3D EBSD dataset 1 after 2.5% elongation of the aggregate along y-axis. The mean maximum principal stress is 382.4 MPa with a standard deviation of 283.41 MPa.

6.10.23D EBSD Dataset 2

Similar to the Dataset 1, CPFEM computations were performed on the polycrystalline aggregate mesh of Dataset 2 to estimate the maximum principal stress distribution on the surface of the mesh. The strain of 2.5% was applied as displacement along the y-axis that corresponds to the loading direction on the macroscopic specimen. The maximum principal stress was calculated from the six stress tensors recorded by Code_Aster. *Figure* 143 shows the CPFEM calculation result of maximum principal stress for 3D EBSD Dataset 2 along with the loading direction. The histogram of the corresponding stress after 2.5% elongation of the aggregate along y-axis is plotted as shown in *Figure* 144. The mean maximum principal stress for 3D EBSD Dataset 2 was found to be 375.05 MPa with a standard deviation of 201.83 MPa.

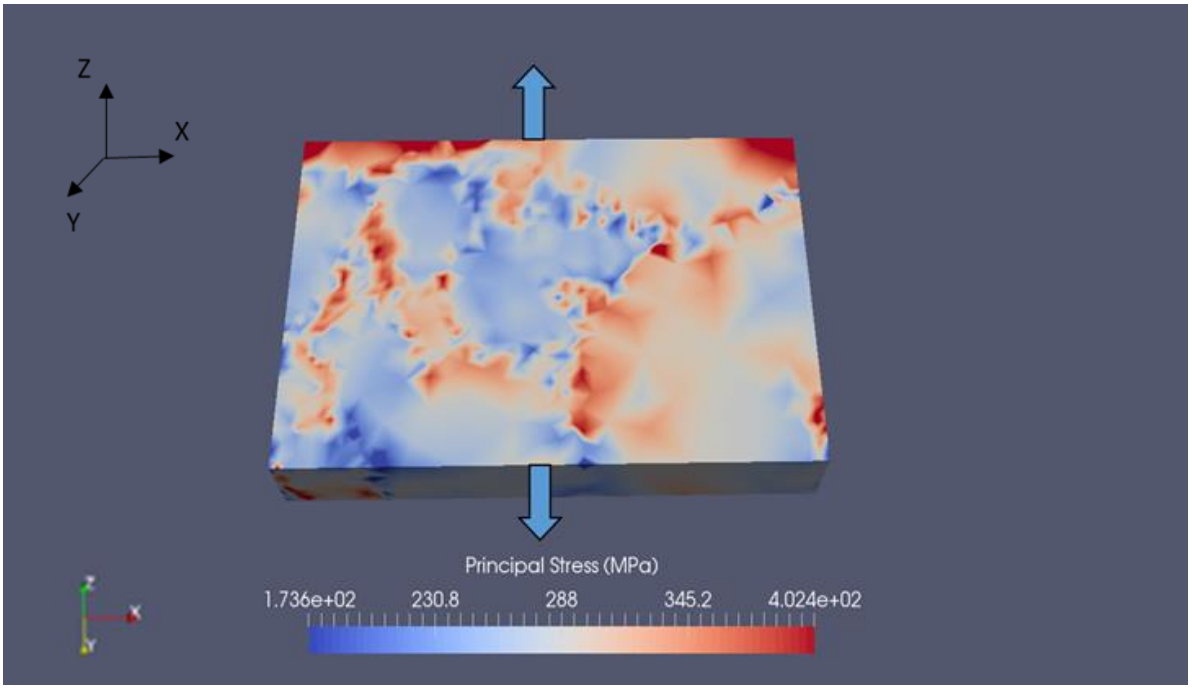


Figure 143: CPFEM calculated Principal Stress in 3D EBSD dataset 2 with 2.5% strain applied along y-axis corresponding to the loading direction of the macroscopic specimen loading direction.

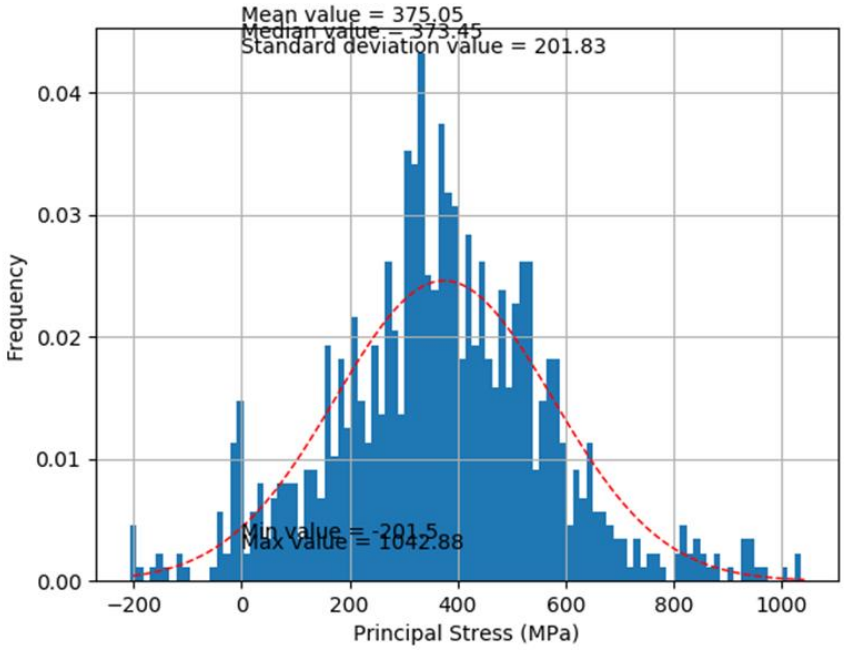


Figure 144: Histogram of the corresponding Principal stresses for 3D EBSD dataset 2 after 2.5% elongation of the aggregate along y-axis. The mean maximum principal stress is 375.05 MPa with standard deviation of 201.83 MPa.

6.10.33D EBSD Dataset 3

CPFEM computations were performed on the polycrystalline aggregate mesh of Dataset 3 to estimate the maximum principal stress distribution on the surface of the mesh. The strain of 2.5% was applied as displacement along the x-axis that corresponds to the loading direction on the macroscopic specimen. The maximum principal stress was calculated from the six stress tensors recorded by Code_Aster. *Figure* 145 shows the CPFEM calculation result of maximum principal stress for 3D EBSD Dataset 3 along with the loading direction. The histogram of the corresponding stress after 2.5% elongation of the aggregate along y-axis is plotted as shown in *Figure* 146. The mean maximum principal stress for 3D EBSD Dataset 3 was found to be 401 MPa with a standard deviation of 295.27 MPa.

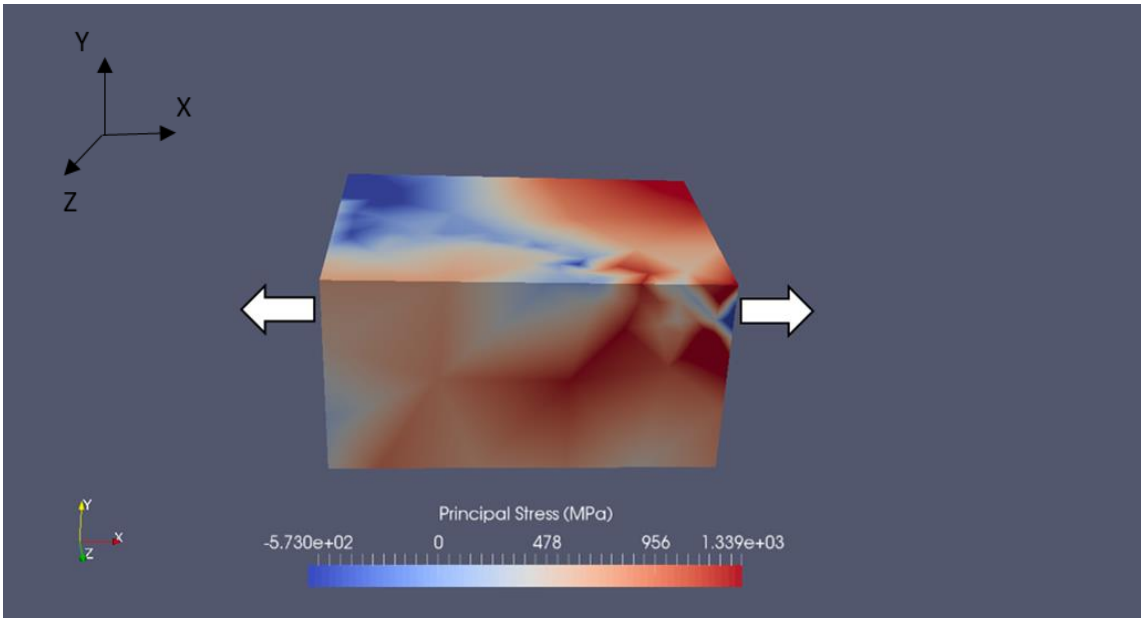


Figure 145: CPFEM calculated Principal Stress in 3D EBSD dataset 3 with 2.5% strain applied along x-axis corresponding to the loading direction of the macroscopic specimen loading direction.

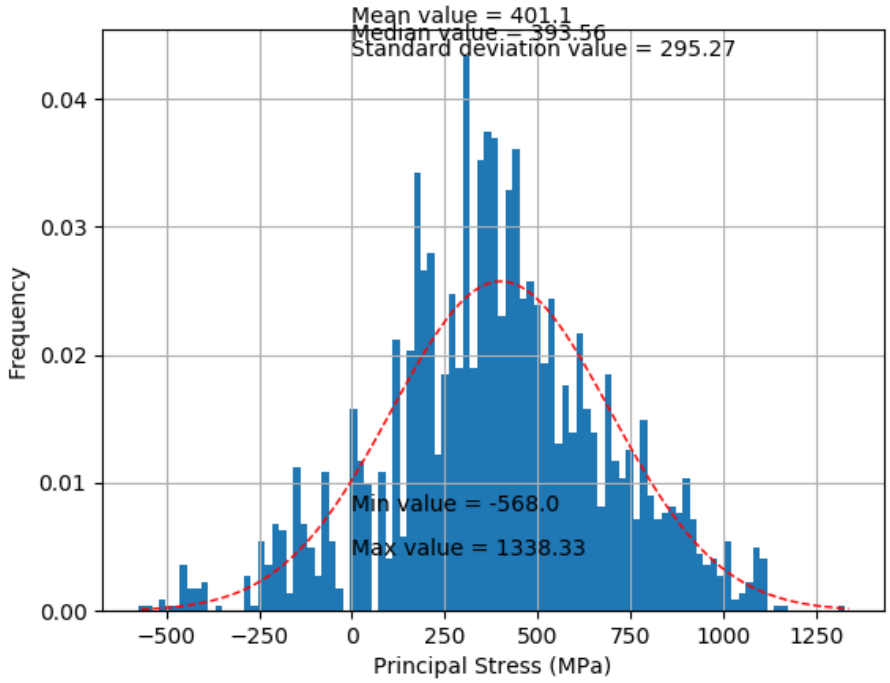


Figure 146: Histogram of the corresponding Principal stresses for 3D EBSD dataset 3 after 2.5% elongation of the aggregate along x-axis. The mean maximum principal stress is 401 MPa with standard deviation of 295.27 MPa.

6.10.43D EBSD Dataset 4

CPFEM computations were performed on the polycrystalline aggregate mesh of Dataset 4 to estimate the maximum principal stress distribution on the surface of the mesh similar to previous cases. The strain of 2.5% was applied as displacement along the x-axis that corresponds to the loading direction on the macroscopic specimen. The maximum principal stress was calculated from the six stress tensors recorded by Code_Aster. *Figure* 147 shows the CPFEM calculation result of maximum principal stress for 3D EBSD Dataset 4 along with the loading direction. The histogram of the corresponding stress after 2.5% elongation of the aggregate along y-axis is plotted as shown in *Figure* 148. The mean maximum principal stress for 3D EBSD Dataset 4 was found to be 410.24 MPa with a standard deviation of 289.6 MPa.

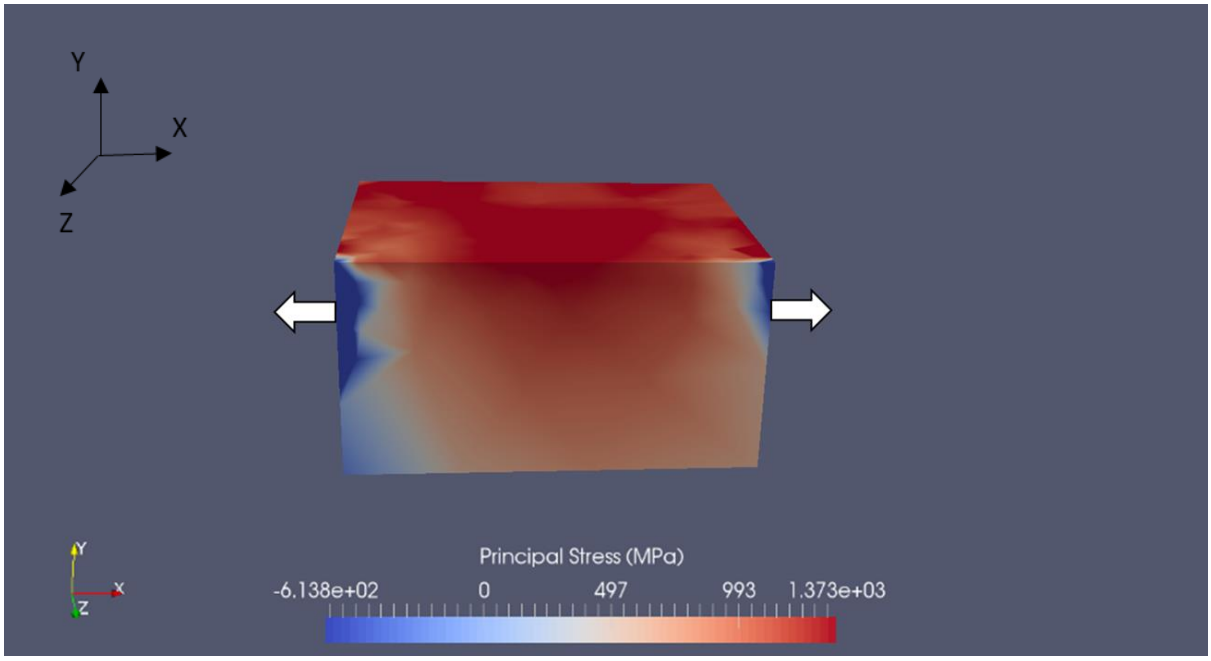


Figure 147: CPFEM calculated Principal Stress in 3D EBSD dataset 4 with 2.5% strain applied along x-axis corresponding to the loading direction of the macroscopic specimen loading direction.

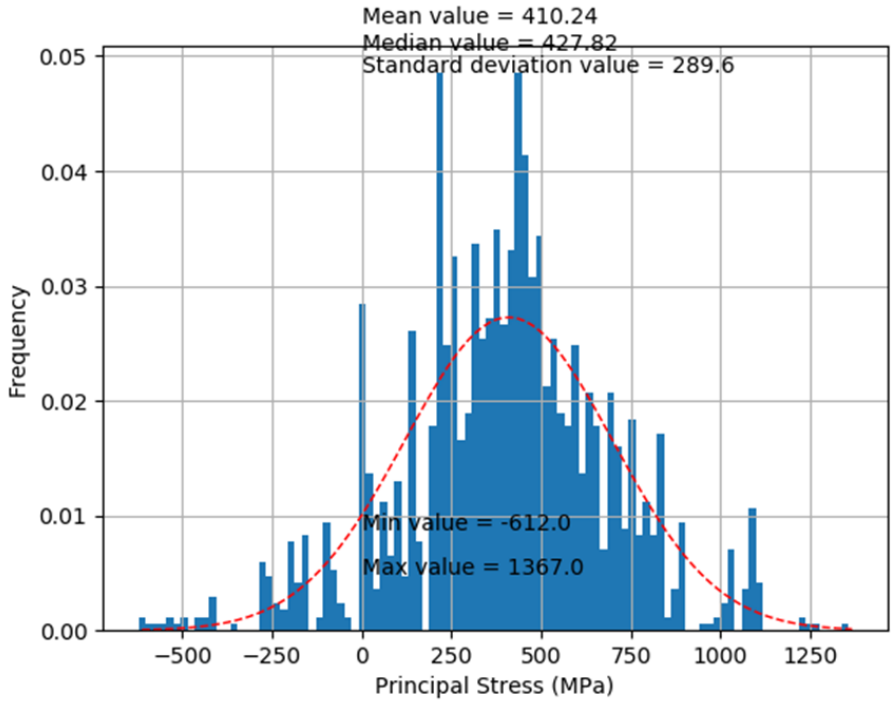


Figure 148: Histogram of the corresponding Principal stresses for 3D EBSD dataset 4 after 2.5% elongation of the aggregate along x-axis. The mean maximum principal stress is 410.24 MPa with standard deviation of 289.6 MPa.

6.10.5 Cracking criteria for oxidized grain boundaries

As discussed in Chapter 4, after the autoclave tests, the fraction of cracked grain boundaries (F_{CGB}) was estimated by cross sectional EBSD analysis and was 30%. From the CPFEM computations, the stresses usually present wider distributions close to the grain boundaries. The local stresses σ in the microstructure were fitted by Gaussian distributions for the polycrystalline aggregate meshes and their mean stress along with standard deviation was estimated.

The critical stress for cracking of oxidized grain boundaries were correlated using the quantile functions on the Gaussian distribution of local stresses representing 30% of highest loaded grain boundaries. This would statistically correspond to the critical stress to crack oxidized grain boundaries. By using this approach, the critical stresses were estimated for the four

datasets and results are presented in Table 19. *Figure* 149 - *Figure* 152 illustrate the assumed Gaussian stress distribution at the surface of the tested specimen and stress to fail oxidized grain boundaries at 345°C for a corresponding mean stress and standard deviation for each case with observed failure happened on 30% of most highly stressed grain boundaries.

Table 19: Calculated stress to fail oxidized grain boundaries at 345°C for 30% FCGB.

CPFEM_ID (3D EBSD)	**No. of grains**	**Mean principal stress (MPa)**	**Standard Deviation (MPa)**	**Estimated stress to fail oxidized grain boundaries (MPa)**
Dataset 1	16	382.4	283.41	497
Dataset 2	22	375.05	201.83	486
Dataset 3	4	401.1	295.27	549
Dataset 4	7	410.24	289.6	554

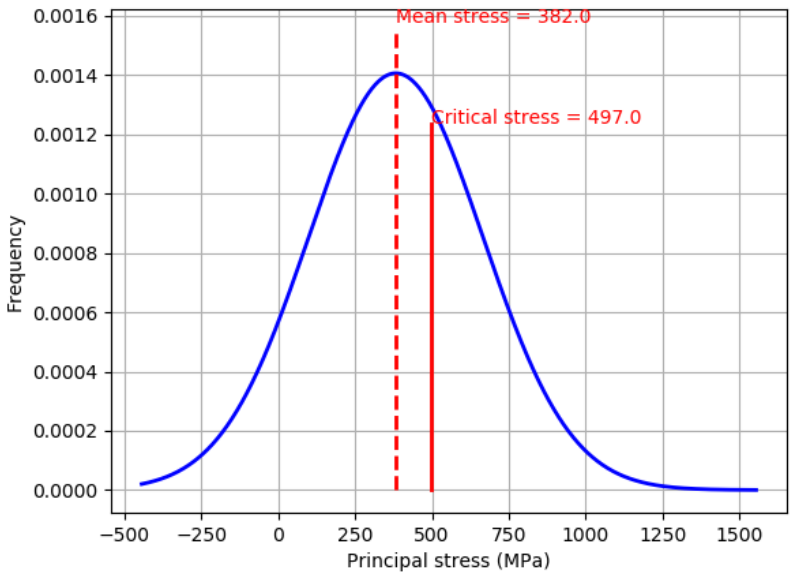


Figure 149: Assumed Gaussian stress distribution and critical stress to fail oxidized grain boundaries at 345°C for a mean applied stress of 366 MPa from 3D EBSD dataset 1. The critical stress threshold was estimated to be 497 MPa considering the failure observed on 30% of the most highly stressed grain boundaries.

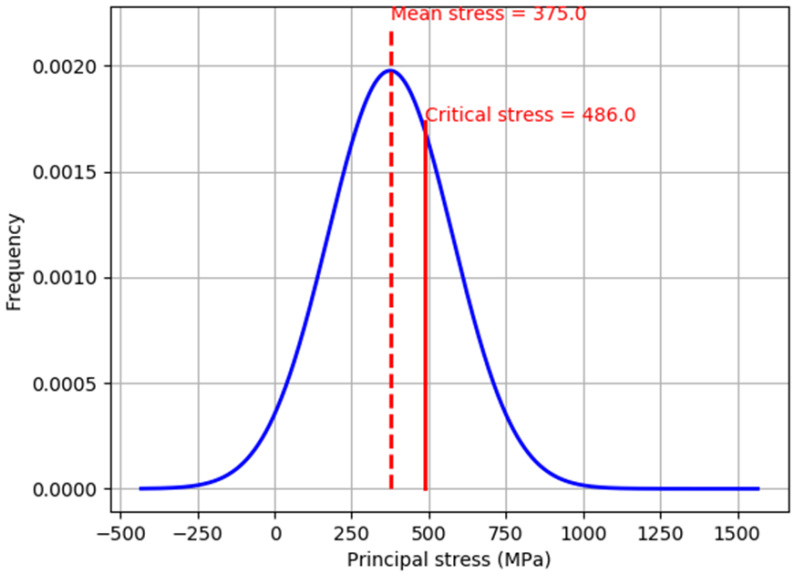


Figure 150: Assumed Gaussian stress distribution and critical stress to fail oxidized grain boundaries at 345°C for a mean applied stress of 375 MPa from 3D EBSD dataset 2. The critical stress threshold was estimated to be 486 MPa considering the failure observed on 30% of the most highly stressed grain boundaries.

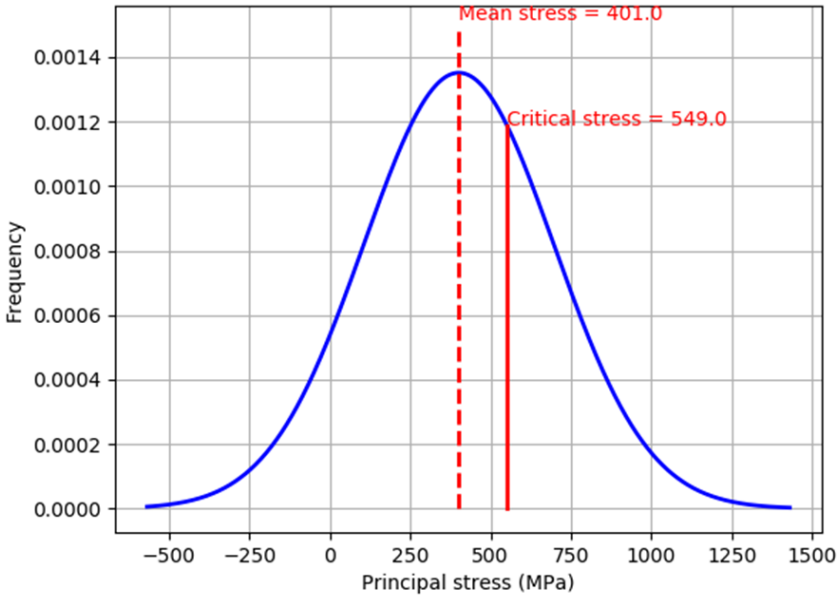


Figure 151: Assumed Gaussian stress distribution and critical stress to fail oxidized grain boundaries at 345°C for a mean applied stress of 401 MPa from 3D EBSD dataset 3. The critical stress threshold was estimated to be 549 MPa considering the failure observed on 30% of the most highly stressed grain boundaries.

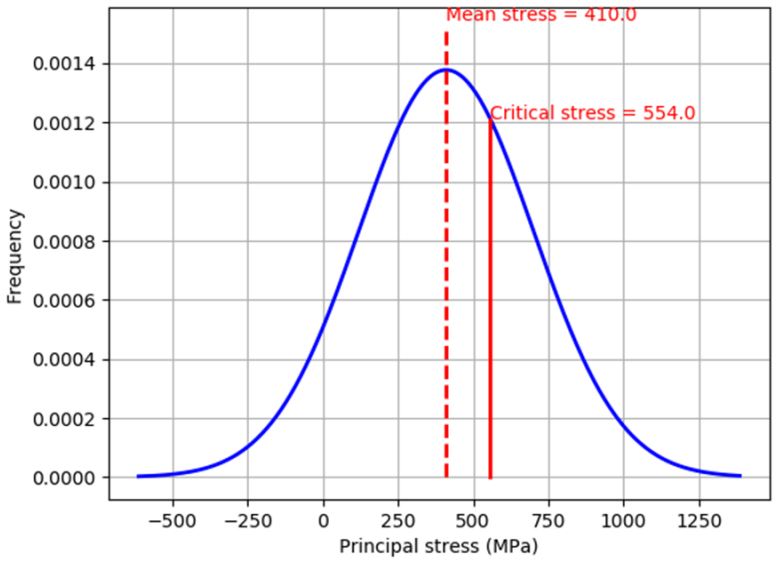


Figure 152: Assumed Gaussian stress distribution and critical stress to fail oxidized grain boundaries at 345°C for a mean applied stress of 410 MPa from 3D EBSD dataset 4. The critical stress threshold was estimated to be 554 MPa considering the failure observed on 30% of the most highly stressed grain boundaries.

6.11 Misorientation analysis of the cracked grain boundaries

The 3D EBSD datasets 1 & 4 had cracked grain boundaries as shown in *Figure*s 152 & 153 and they were compared with the 3D EBSD data and misorientation between them were calculated using the MATLAB script in Appendix C. The EBSD maps that were used to determine whether a correlation between the crystallography of the grain boundary and IGSCC failure could be established. The grain orientations of the cracked grain boundaries were compared with the position and their orientations were extracted from the 3D EBSD data.

For the 3D EBSD dataset 1, the cracks were observed between grains G1 & G2 and G2 & G3 as shown in *Figure* 153. The Euler angles ($\phi 1$, Φ, $\phi 2$) obtained from the EBSD data for the corresponding grains G1, G2 & G3 are (196, 29,141), (44, 10, 293) and (224, 27, 146) respectively. The misorientation between G1 & G2 was calculated to be 38° and between G2 & G3 was calculated to be 49° using the MATLAB script. The local stresses were extracted

from the CPFEM computation for the grain boundary between G1 & G2 and the mean local stress was found to be 673 MPa with a standard deviation of 481 MPa and for the grain boundary between G2 & G3, the local mean stress was found to be 550 MPa with a standard deviation of 385 MPa. The mean local stress were extracted for the grain boundary G1 & G4, it was found to be 387 MPa with a standard deviation of 216 MPa and for the grain boundary G1 & G5, it was found to be 438 MPa with the standard deviation of 315 MPa. In both the cases, the grain boundary does not exhibit any cracks and the local mean stress was found to be below the estimated stress to fail oxidized grain boundary.

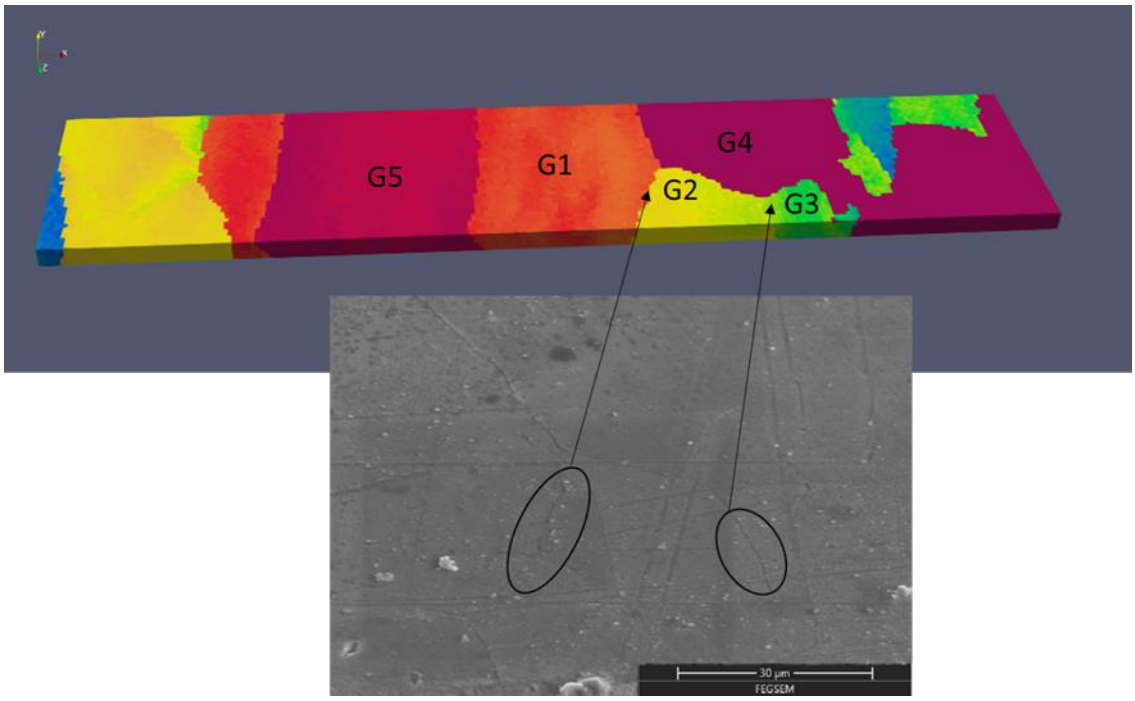


Figure 153: Correlation between crack grain boundaries and misorientation for observed cracks in 3D EBSD dataset 1 with SE image. The grain boundary misorientation between G1 & G2 and G2 & G3 is 38° and 49° respectively.

For the 3D EBSD dataset 4, a crack observed between grains G1 & G2 on 3D FIB-SEM slice (cross section) is shown in *Figure* 154. The Euler angles ($\phi 1$, Φ, $\phi 2$) obtained from the EBSD data for the corresponding grains G1 & G3 are (165, 22,230), and (44, 35, 270) respectively. The misorientation between G1 & G2 was calculated to be 46° using the MATLAB script. The

local stresses were extracted from the CPFEM calculation for these grains and the mean local stress was found to be 620 MPa with a standard deviation of 432 MPa.

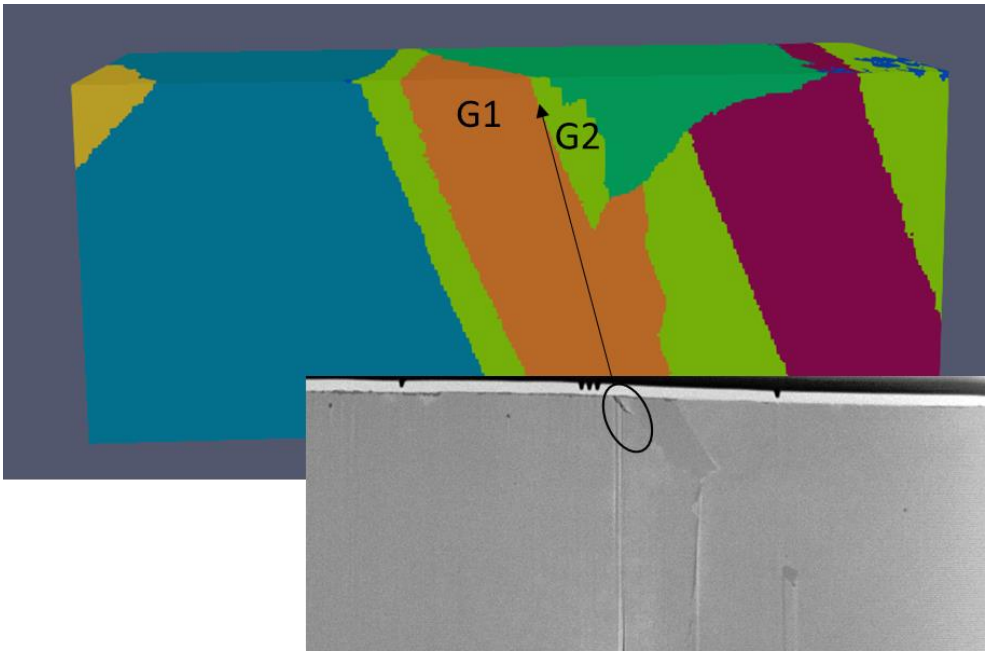


Figure 154: Correlation between crack grain boundaries and misorientation for observed cracks in 3D EBSD dataset 4 with cross sectional slice of SE image. The grain boundary misorientation between G1 & G2 is 46°.

6.12 Discussion

To better understand the mechanical response, local microstructure and a possible link between the local stress concentration on the grain boundaries with critical stress to failure of oxidized grain boundaries, CPFEM computations on polycrystalline aggregate mesh were performed as presented in sections *6.7*, *6.8* and *6.9*. The misorientation analysis was carried out between the observed cracked grain boundaries as presented in *section 6.10*. The findings will be discussed in this section starting with misorientation analysis.

6.12.1 Misorientation analysis

The effect of grain boundary characteristics has been widely investigated as discussed in Literature review *section 2.4.3.* It is widely agreed by the SCC community that in Alloy 600 grain boundaries with $\sum > 29$ also referred as random high angle grain boundaries (RHGBs) tend to show more susceptibility to IGSCC. While the grain boundaries with $\sum \leq 29$ show increased resistance to IGSCC, it is also believed that CSL boundaries and boundaries with misorientation angles less than 10° show higher resistance to cracking with twin boundaries ($\sum$ 3) exhibiting more resistance. The results of observed cracked grain boundary's misorientation are consistent with it. In spite of the statistical limitations, with very limited misorientation data available from the cracked grain boundaries, the observations in this study seems in good agreement with the previous findings [35,83,282].

6.12.2 Stress to fail oxidised grain boundary

Dugdale et al. [53] performed micromechanical tests on alloy 600 coupons and did finite element modelling to reproduce the observed fracture behaviour on the oxidised grain boundary using cohesive zone elements. The authors reported only a single value of 1.35 GPa as stress to fail the oxidised grain boundary. The high value reported can be attributed to not considering the presence of brittle oxide phase on the exposed surface in their FEM modelling. In the PhD work of Dohr [275], she performed micromechanical cantilever tests on similar alloy 600 from EDF on 9 different oxidized grain boundaries and used cohesive zone modelling to estimate the failure stress to crack the oxidised grain boundaries. However, she included the presence of brittle oxide phase in her FEM model. She estimated that stress to fail the oxidized grain boundaries are in the range 330 MPa to 770 MPa. In both these studies, the authors estimated the stress to failure of oxidised grain boundary by performing FEM simulations on single grain boundaries. The CPFEM simulations performed in sections 8.4, is carried out on

not just one grain boundary hence, it produces a statistically significant data. The critical stress to failure estimated from the local stresses in *section 6.10* for the observed 30% fraction of cracked grain boundaries (F_{CGB}) is in the range of 550-750 MPa. This estimate is from the correlation between the fractured grain boundaries and stress distribution without the effect of introducing oxidation or cohesive zone elements in the model. The grain boundaries exhibited stress level below the estimated stress to fail in the cases of uncracked grain boundaries. However, the estimated critical stress to failure seems to be more than the failure stress values of 180 – 300 MPa reported for microtensile analysis on alloy 600 by Fuji et al. [283] and less than the reported value of 825 MPa for the exposure time of 1000h in the macro-scale study performed during the PhD work of Hinostroza [284].

6.12.3 Statistical approach of estimating critical stress to failure and stress linear coefficient 'S' parameter for Local model

Couvant et al. performed experiments on different heat-treated alloy 600 to study the critical stress to failure. The reported results were based on simulations and a statistical approach in determining the critical stress based on the Gaussian distribution of stress. Assuming an average stress of 774 MPa, 467 MPa and 767 MPa for three different alloy 600 with imposed elongation of 15%, 2.5% and 10% respectively, the author estimated the stress linear coefficient 'S' value to be 1.27 , 0.67 and 1.11 respectively using the equation (36) . As discussed earlier, this parameter is responsible for assigning the standard deviation to the Gaussian distribution of stress on the particular node during Local model SCC computation. If the value is more than 1, it means that the standard deviation is very high compared to the mean principal stress. This discrepancy of observing the S value more than 1 in this case could be attributed to random sampling of the grain orientations to the polycrystalline aggregate used for extracting the principal stresses. Using this approach with the results obtained on *section 6.9*, the stress representing 30% of the highest loaded grain boundaries would statistically

correspond to 518 MPa with the final mean principal stress of 392 MPa and the stress linear coefficient (S) value of 0.64 for assumed Gaussian stress distribution as shown in *Figure* 155. In a first approach for the Local model SCC computation, the initiation criterion to produce crack in alloy 600 at 345°C was assumed to be 518 MPa applied on grain boundary oxidized to or deeper than the critical oxidization depth of 300 nm.

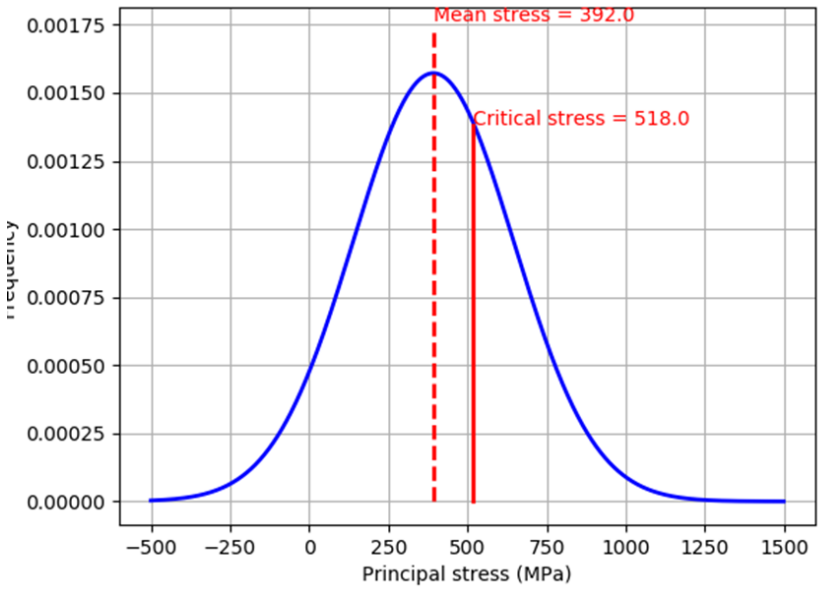


Figure 155: Assumed Gaussian stress distribution and critical stress to fail oxidized grain boundaries at 345°C for final mean applied stress of 392 MPa from all 3D EBSD datasets. The critical stress threshold was estimated to be 518 MPa considering the failure observed on 30% of the most highly stressed grain boundaries. The S parameter is calculated to be 0.64.

6.13 Summary

The methodology of creating polycrystalline aggregate mesh from the 3D EBSD data is described sequentially. The mesh generated is representative of the real sample and is provided with material properties and corresponding grain orientations. CPFEM computation is performed on the polycrystalline meshes using Code_Aster to extract the stress concentration on the grain boundaries. The maximum principal stress is calculated from the stress tensors and Gaussian distribution of the stresses is plotted for each case. The critical stress to failure of

oxidized grain boundary is determined statistically by comparing with the observed fraction of cracked grain boundaries (30%). From CPFEM computations, the Gaussian stress distribution and critical stress to fail oxidized grain boundaries at 345°C for final mean principal stress of 392 MPa from all 3D EBSD datasets is obtained. From this, the critical stress threshold is estimated to be 518 MPa considering the failure observed on 30% of the highly stress grain boundaries. The stress linear coefficient 'S' parameter is calculated to be 0.64 using the equation (36). These calculated values for critical stress to failure (Local stress σ_c) and S parameter will be used as the input for SCC computation in Local model and this will be discussed in *Chapter 7*.

7 VALIDATION AND OPTIMISATION OF LOCAL MODEL

In this chapter, the performance of the simulations using EDF's Local model is discussed along with the cross correlations between the predicted and observed behaviour to identify the model's strength and limitations. The goal is to identify the major parameters whose accurate quantification would have the potential to significantly improve the quality of the modelling, rank the driving parameters and optimize it in order to provide better calibration for the model.

7.1 Validation of Initiation

Initiation in the Local model refers to the failure of an oxidized grain boundary. Initiation occurs when 1) a grain boundary is sufficiently oxidized so that the oxidation depth is deeper than the critical oxidation depth (p_c) based on the evaluation from intergranular oxidation kinetics and 2) local stress experienced by the grain boundary is higher than the critical stress (σ_c) to fail the grain boundary. The critical oxidation depth (p_c) was found to be 300 nm for alloy 600 from previous studies [284] and using the intergranular oxidation kinetics the parameters such as b_{nom}, b_{depl} and b_{carb} values for alloy 600 are calibrated as 3.14 $x10^{-15}$ nm^{-1}, 2.42 $x10^{-15}$ nm^{-1} and 4 $x10^{-14}$ nm^{-1} respectively. The C_{nom}, C_{depl} and C_{carb} values are calibrated as 3.35 h^{-1}, 2 h^{-1} and 0.01 h^{-1} respectively.

7.1.1 Testing of Local Model Initiation

Using the Code_Coriolis platform, the global mesh of the four point bend test generated as discussed in *section 6.1* is imported in *.med* format in the mesh module of the platform as

shown in *Figure* 156. After importing the required mesh, it is necessary to define the material and the conditions for the SCC computation.

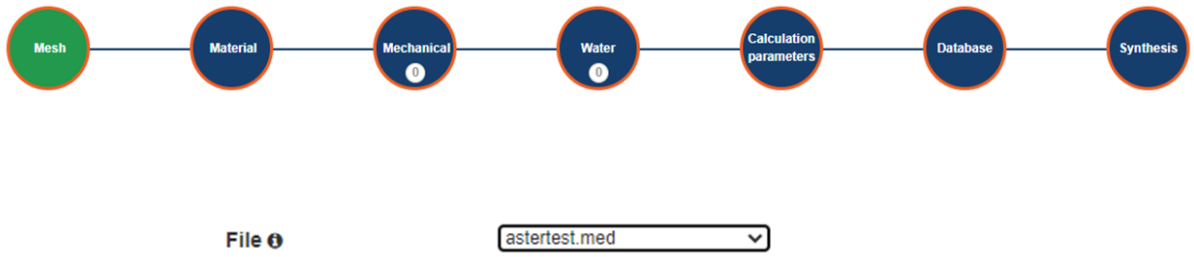


Figure 156: Mesh Module in Code_Coriolis platform

The material for testing using Code_Coriolis platform is defined by four steps as shown in *Figure* 157. The first step is to define the group of nodes by specifying the right name when saving the mesh file. Following this, the initiation model should be selected from the drop-down and all the necessary parameters required for the selected initiation model should be defined. The third step is to set a crack growth model from the drop-down list and define all the necessary parameters for the selected crack growth model. Finally, an analytical function to calculate the stress intensity factor K is set.

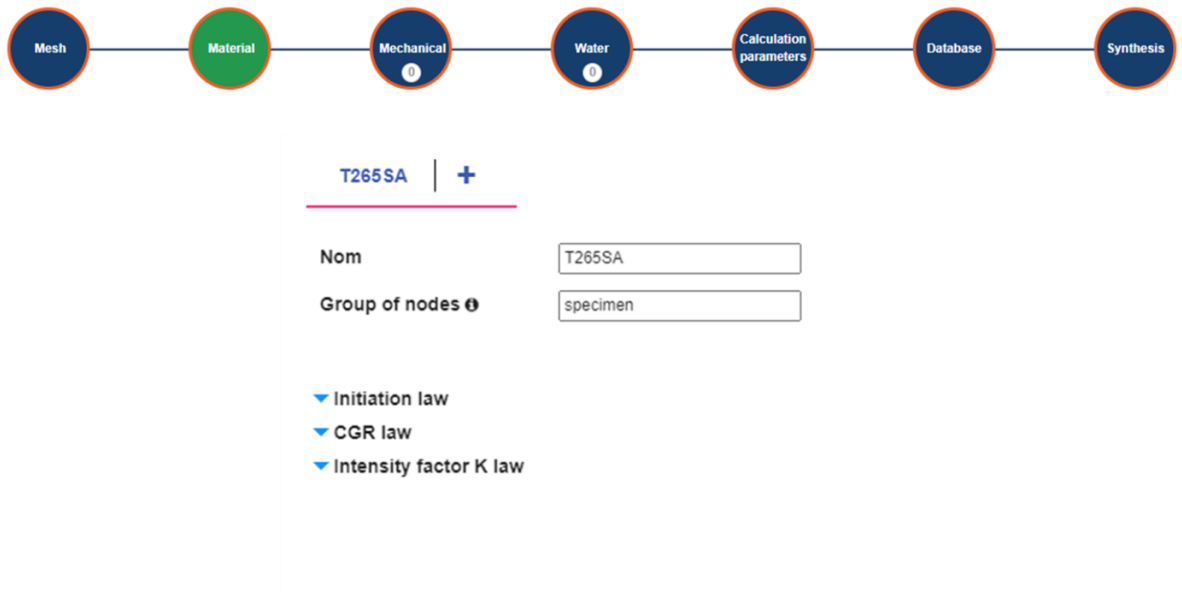


Figure 157: Material Module in Code_Coriolis platform with four steps.

The group of nodes which has to be assigned with the properties for the SCC initiation is the entire global mesh and the name assigned to it in the mesh generation is *'specimen'*. As the modeling is to evaluate the 'Local model', under initiation law *'local_initiation_model'* is selected and the parameters in this model are defined as shown in *Figure* 158.

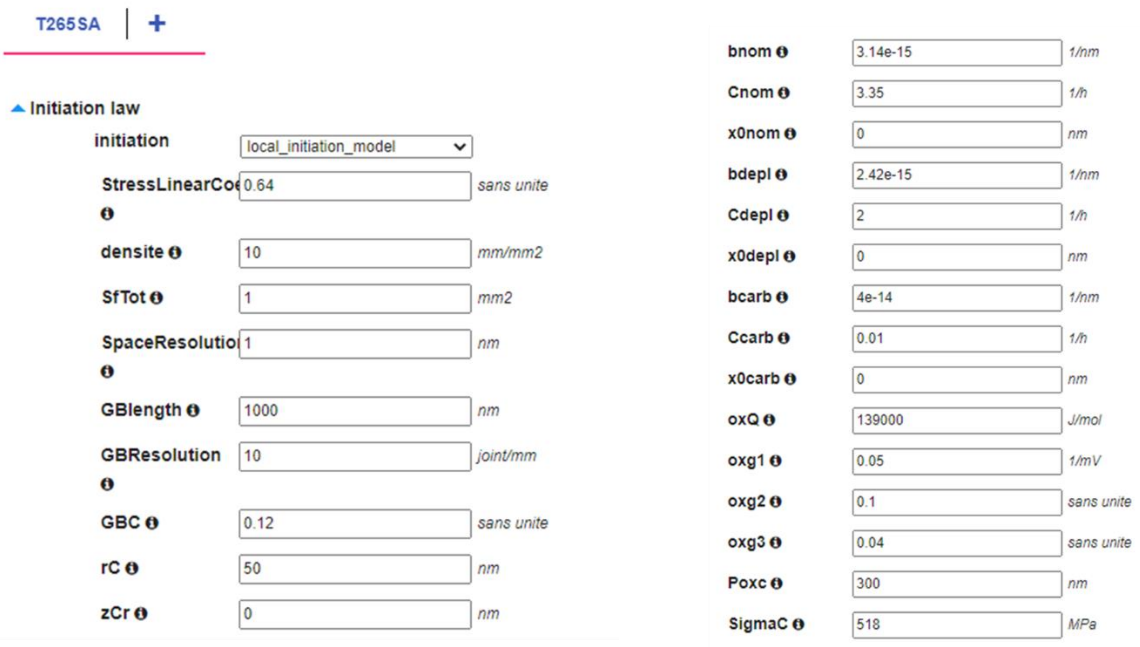


Figure 158: Parameters in *'local_initiation_model'*.

Once the Local model is selected, the various parameters necessary for the SCC initation computation of the model required have to be filled. The Stress Linear Coefficient is the 'S' parameter calculated from the statistical approach of estimating the critical stress to failure as discussed in *section 6.10.5*. The calculated value of 0.64 was used as the input. The parameters density, SfTot, space resolution, and GB resolution are responsible for assigning the number of grain boundaries to oxidize to each node at the surface exposed to water. It is given by the expression:

Number of GBs in a node = density x SfTot x GB resolution.

With this expression and the given set of values, the number of grain boundaries assigned to each of the nodes is 100. The GB length, GBC (grain boundary coverage) and rC (radius of carbides) are the parameters responsible for assigning the number of carbides present on a grain boundary. The only condition for choosing the GB length is that, it must be greater than the critical oxidation depth for the computation to run. It is given by the expression:

$$\text{Number of carbides assigned to each grain boundary} = \frac{GB\ length\ x\ GBC}{2\ x\ rC}$$

Using this expression and the given set of values for GBC and rC, the number of carbides asigned to the grain boundary is calculated to be 1.2. The critical oxidation depth (p_c) was found to be 300 nm for alloy 600 from previous studies [284] and using the intergranular oxidation kinetics the parameters such as b_{nom}, b_{depl} and b_{carb} values for alloy 600 are calibrated as 3.14 $x10^{-15}$ nm^{-1}, 2.42 $x10^{-15}$ nm^{-1} and 4 $x10^{-14}$ nm^{-1} respectively. The C_{nom}, C_{depl} and C_{carb} values are calibrated as 3.35 h^{-1}, 2 h^{-1} and 0.01 h^{-1} respectively as discussed *section 2.4.1* and these values were used. The parameters oxg_1, oxg_2 and oxg_3 are responsible for evaluating $g(\Delta EcP)$ as given by the equation 1 and 2 in *section 2.4*. The critical stress (local stress, σ_c) to failure of oxidized grain boundary calculated (518 MPa) from the CPFEM simulation of

aggregates is used as input in SigmaC. The stress assigned to each grain boundary during the computation is randomly sampled in a Gaussian distribution where the centre is the maximum principal stress at the node and the standard deviation is given by maximum principal stress assigned times the stress linear coefficient. All chosen values for the local initiation model are summarized in Table 20.

Table 20: Summary of chosen values for the local initiation model in Code_Coriolis.

Steps	**Input Parameters**	**How are they obtained**
Specimen loading	Size and Shape	Direct observation
	Temperature	Autoclave conditions
	Density, GB length, SfTot, GB resolution	Arbitrary
Intergranular Oxidation Kinetics	GBC, r_c	Experimental observations
	bnom, cnom, bcarb, ccarb, bdepl, cdepl	Taken from [205]
	Dissolved hydrogen	Autoclave conditions
Code_Coriolis (Local Model Initiation)	P_{oxc}	Taken from [205]
	SigmaC	CPFEM model calculation

For the first step in validating the initiation part of the Local Model, the propagation rate given by the crack growth law is chosen to be constant by selecting *'cgr_constant'* under propagation and the crack growth rate is set to zero so that only initiation happens. For the stress intensity factor (K) law, K_function is selected for simple case and α constant is defined as 1.22 as shown in *Figure* 159.

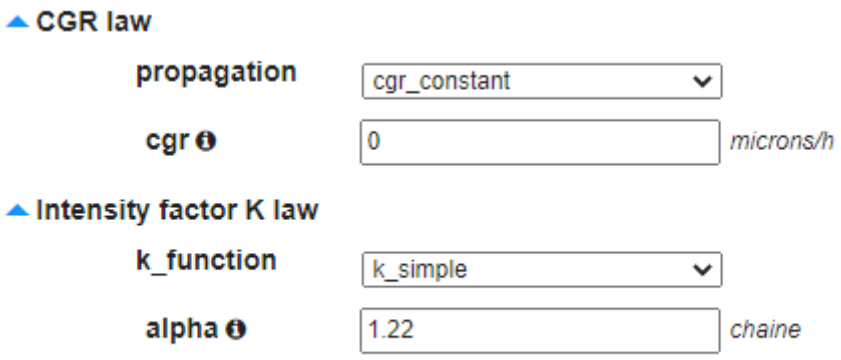


Figure 159: Propagation Law in Code_Coriolis platform.

Once the material properties for initiation and crack growth are defined, the next module in the Code_Coriolis platform is the mechanical. In this module, the results from the finite element simulations with nodal stresses and strain calculated on the global specimen are imported. The Code_Aster simulation results obtained for 1 mm displacement in *.resu* format has been used as input for the mechanical aspect of the model as shown in *Figure* 160.



Figure 160: Mechanical module in Code_Coriolis platform with .resu file from Code_Aster test imported.

The next step is to assign the environmental parameters. In Code_Coriolis platform, the Water module is used to assign the environmental parameters. The environmental parameters are defined by the group of nodes at the surface which is contact with the water, zinc concentration, dissolved hydrogen content in the water, pH of the water and temperature as shown in *Figure* 161. The group of nodes that has to be defined with the environmental parameters is water group, which is assigned during the mesh generation. The number of nodes in water group in

contact with water is 2144 nodes. The other parameters are the same as the experimental conditions used in Autoclave testing.

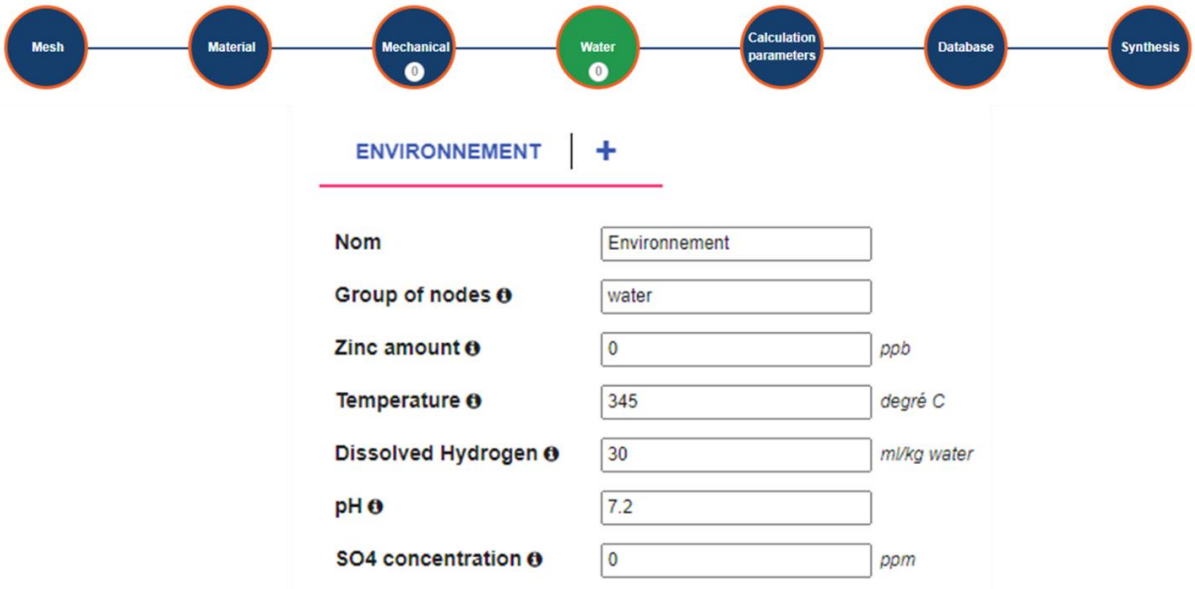


Figure 161: Environment parameters imported in the Code_Coriolis platform from the autoclave conditions.

The next step is to define the set of computational parameters for the study. This is done in the Calculation parameters module of Code_Coriolis. The set of computational parameters are defined by providing a stopping criteria in time, a stopping criteria in crack length, number of cracks to be followed during the study and submeshing parameters for CGR accuracy. In this first case of validating the local model initiation, the maximum time to stop the computation if there is no crack is set to be 100000 hours, the maximum crack depth to stop the computation is 1 mm and number of cracks to be followed is always set to 1 as shown in *Figure* 162. At the end of this step, the study is submitted for computation.

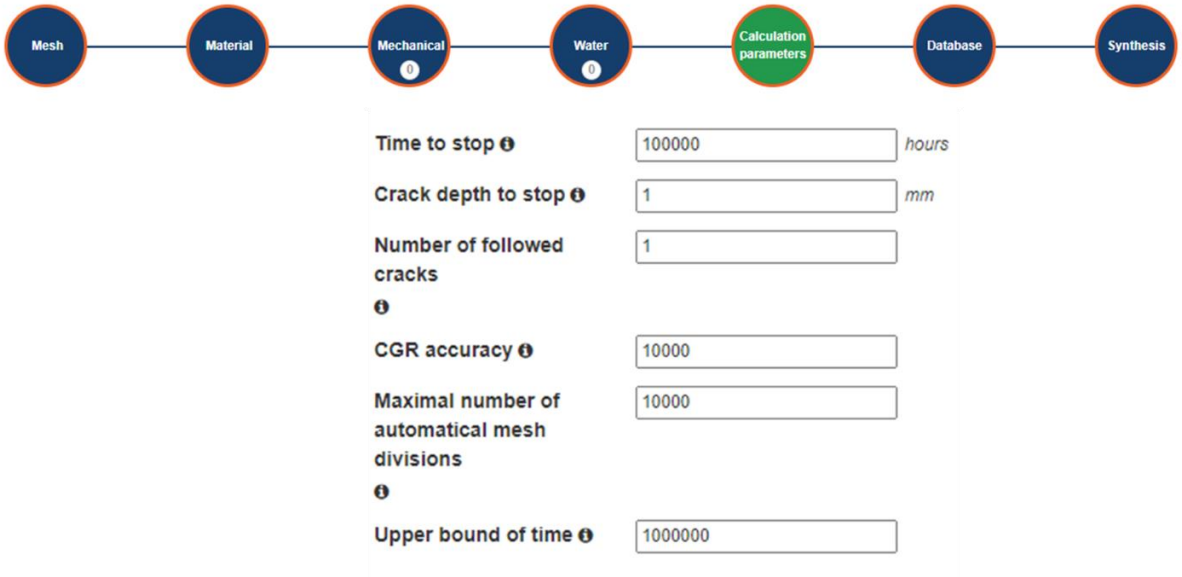


Figure 162: SCC computational parameters

7.1.2 Results of Local Model Initiation

Once the study is submitted for computation, all the necessary conditions and parameters are applied to the desired nodes and the calculation will run until at least one of the stopping criteria defined in the calculation parameters module of the platform is reached. On completion of the computation, Code_Coriolis provides various results in the form of plots and data file. Along with this, it provides two *'.med'* files for 3D visualization of the results. These files are saved as *SCC_initiation.med* and *SCC_propagation.med* to separately visualize the initiation and propagation. These files can be exported from the Code_Coriolis platform and viewed using Paraview software. It is observed that the crack has been initiated at 150 hours. On 3D visualization of the initiation, the node of the crack initiation site's stress distribution is given by the model as shown in *Figure* 163. The stress at the node of crack initiation was predicted to be 297 MPa.

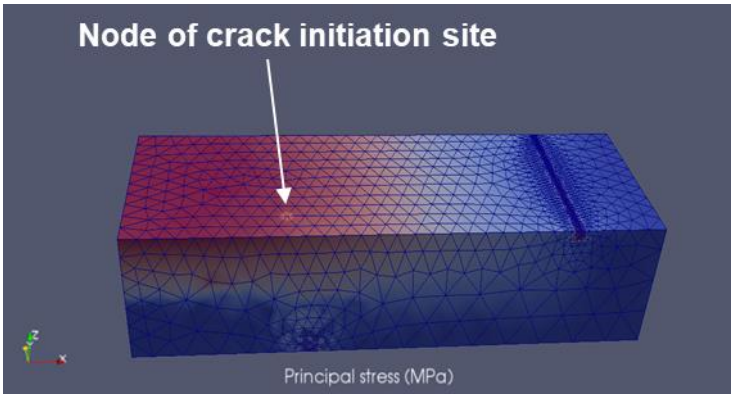


Figure 163: Node of Crack Initiation site with stress distribution.

7.2 Validation of Propagation

To establish a link between initiation and propagation, the crack propagation governed by the crack growth rate law is assumed to have a sigmoidal dependence to stress intensity factor (K). This dependency mainly allows the model to provide a link between initiation and propagation as well as for the slow and fast crack growth regimes. The Code_Coriolis platform allows choosing between the three sigmoidal crack extension laws as discussed in *section 2.4.5*. However, for validation, only *'cgr_sigmoid_cw2_h'* crack growth law is selected.

7.2.1 Testing of Propagation

The crack growth rate (CGR) is selected as *'cgr_sigmoid_cw2_h'* in the Code_Coriolis platform and the model parameters cgr1 to cgr11 are given to calculate the rapid crack propagation rate at a node as shown in *Figure* 164. To test the propagation part of the model, the values cgr1 to cgr4 were used from the test case analysis of EDF [208], the values cgr5 to cgr 7 defines the prior cold work on the global specimen, cgr 8, cgr 9 and cgr 10 are the values from the pourbaix diagram for the corresponding Ni/NiO equilibrium and cgr 11 is the activation energy after cracking used by EDF. The input values of the parameters, cgr1 to cgr 4 needs to be validated and calibrated.

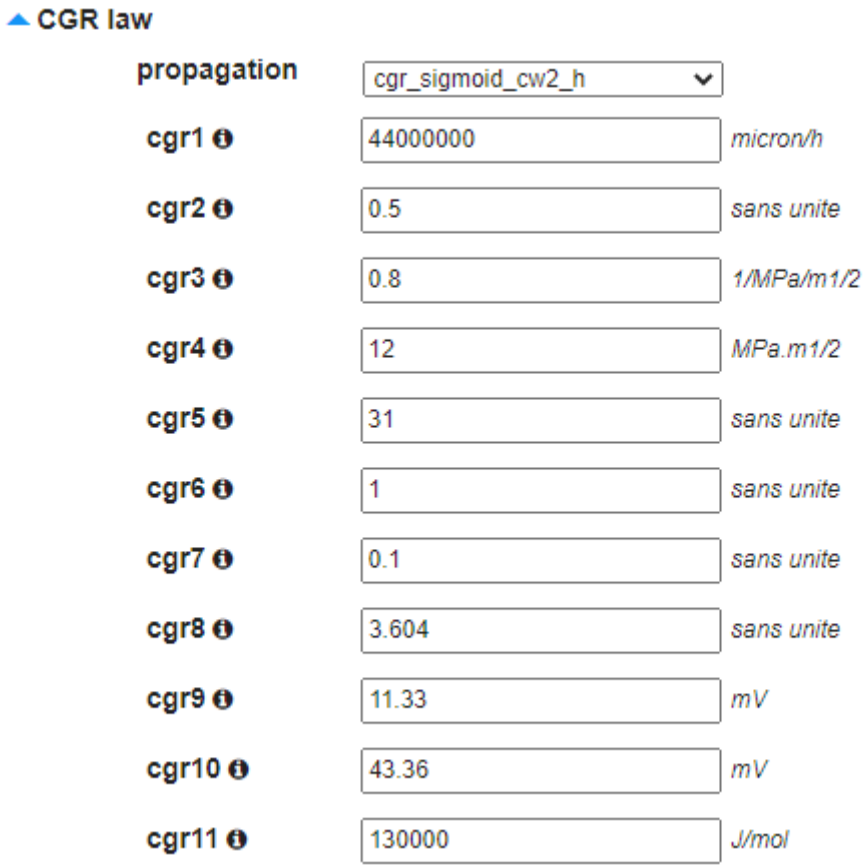


Figure 164: Parameters for crack propagation in *'cgr_sigmoid_cw2_h'* law.

The study is submitted then for SCC computation and the results are obtained.

7.2.2 Results of Local Model Propagation

SCC computation is performed by the evaluation of stress intensity factor for assigned maximum crack depth. This is followed by computation of crack extension length, evaluation of K for maximum crack depth + crack extension length (total crack depth), evaluation of mean crack growth rate (CGR) along the crack extension length and time to crack along crack extension. The SCC computation ends when the computation reaches either the maximum final time or maximum crack depth during the pre-processing step.

Once the SCC computation is completed, it is possible to visualize sites of SCC initiation on the component and the crack path followed by the main crack tip within the model as shown in

Figure 165. Thus, kinetics and crack growth paths are predicted along with statistics on initiation time and cracking location. This gives evolution of crack depth with time as shown in *Figure* 166.

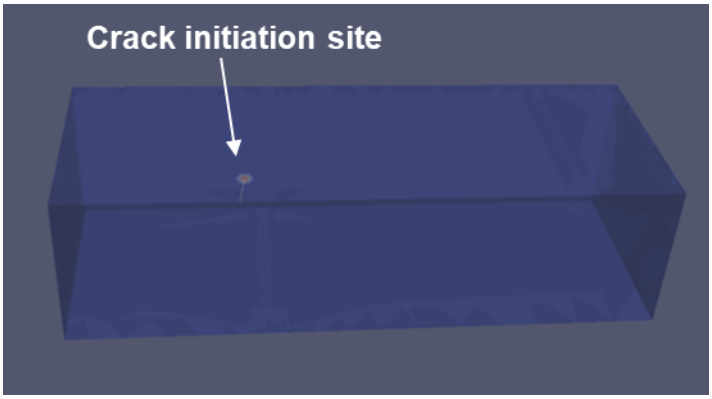


Figure 165: Crack Initiation site along with crack propagation path.

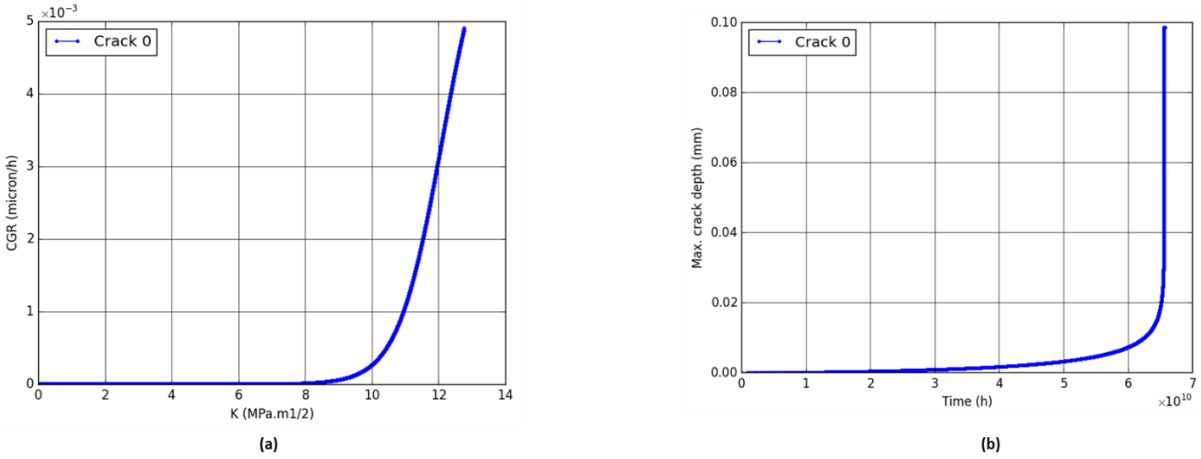


Figure 166: Results obtained after SCC computation (a) CGR vs Stress intensity factor K; (b) Crack depth vs Time.

7.2.3 Comparison of predicted crack propagation and observed crack depths

The observed crack depths from the experimental results from autoclave testing for 325, 800 and 2000 hours are compared with the predicted crack depths. *Figure* 167 shows the comparison of Crack depth (µm) vs time (h) in log scale for the observed and predicted crack depths. It is seen that after initation at 150 hours the crack propagation predicted is very slow for the slow crack propagation regime. Hence, the parameters used in the crack propagation law have to be calibrated in order to have a better prediction of crack depths to the observed experimental results. As there are four parameters cgr1 to cgr 4 to be calibrated, the strategy used in calibrating each of the values involve the understanding of the influence of the each of the parameters in the cracking kinetics.

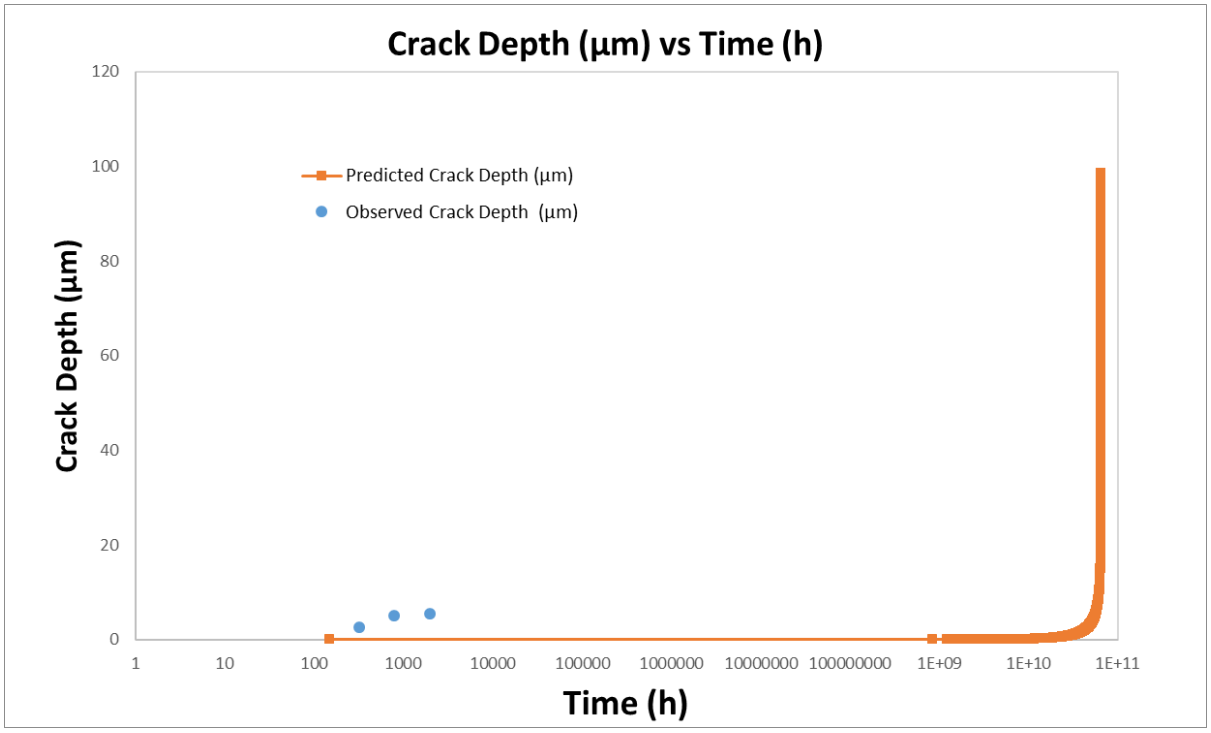


Figure 167: Comparison of predicted and observed Crack Depth vs Time

7.3 Validation of Propagation Calibration of ‘cgr1,cgr2,cgr3 & cgr4’ parameters

In order to calibrate the four parameters, it is necessary to understand the influence of each of the parameters separately on crack growth rate (CGR) and check the effect on the crack depth vs time plot.

7.3.1 Effect of ‘cgr3’ parameter

The values of parameters cgr1, cgr 2 and cgr 4 were kept constant (from *Figure* 164) and the effect of cgr3 parameter was studied by changing the values from 0.005 to 5. The influence of cgr3 parameter on crack depth vs time is plotted as shown in *Figure* 168. As seen in the *Figure* 168, cgr3 has a huge influence on the slope of the slow crack growth regime. When the cgr3 parameter is increased the slope of the curve in the slow crack regime decreases drastically.

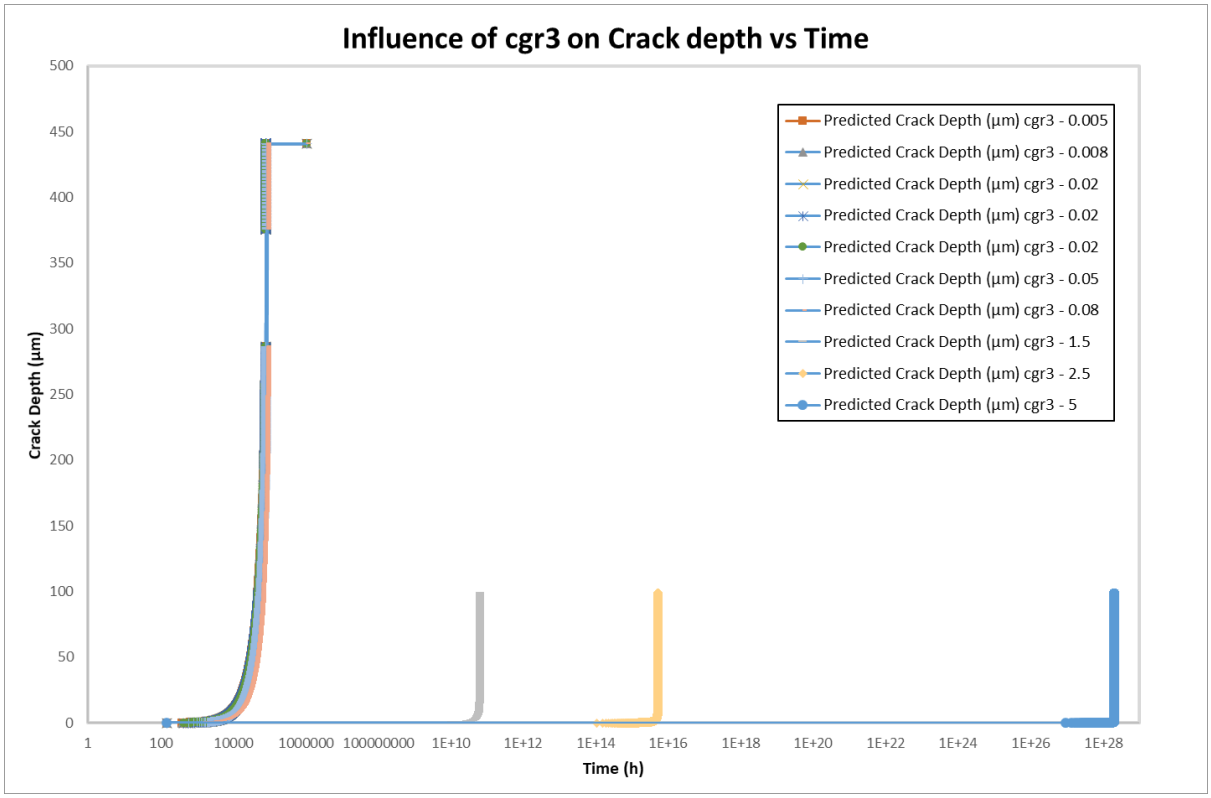


Figure 168: Overall influence of cgr3 parameter on Crack depth vs Time.

However to compare with the observed crack depth vs time, only the lower cgr3 value results were used and comparison was made upto 6 microns as shown in *Figure* 169. It is obseverd that by reducing the cgr3 parameter, the slope of the slow crack growth regime increases rapidly and shows no change or remains constant for values 0.008 and 0.005. For further calibration of other cgr parameters, the cgr3 value is chosen to be 0.005.

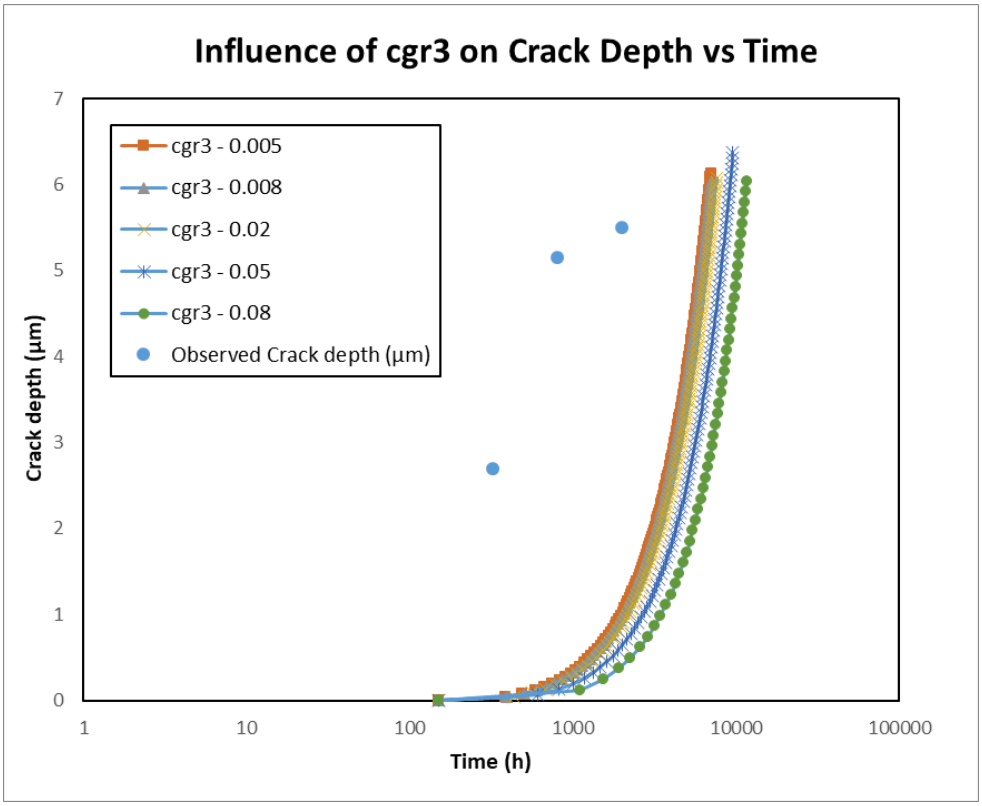


Figure 169: Influence of cgr3 on Crack depth vs Time up to 6µm.

7.3.2 Effect of 'cgr2' parameter

The values of parameters cgr1 and cgr 4 were kept constant (from *Figure* 164), cgr3 is 0.005 and the effect of cgr2 parameter was studied by changing the values from 0.1 to 1.5. The influence of cgr2 parameter on crack depth vs time is plotted as shown in *Figure* 170 As seen in the *Figure* 170, cgr2 does not show any drastic change in the CGR or slope in the slow crack regime. But it does influence the slope in the transition from slow crack regime to fast crack growth regime. When the cgr2 parameter is increased correspondingly the slope of the transition from slow crack to fast crack regime increases, hence the transition happens at a faster rate.

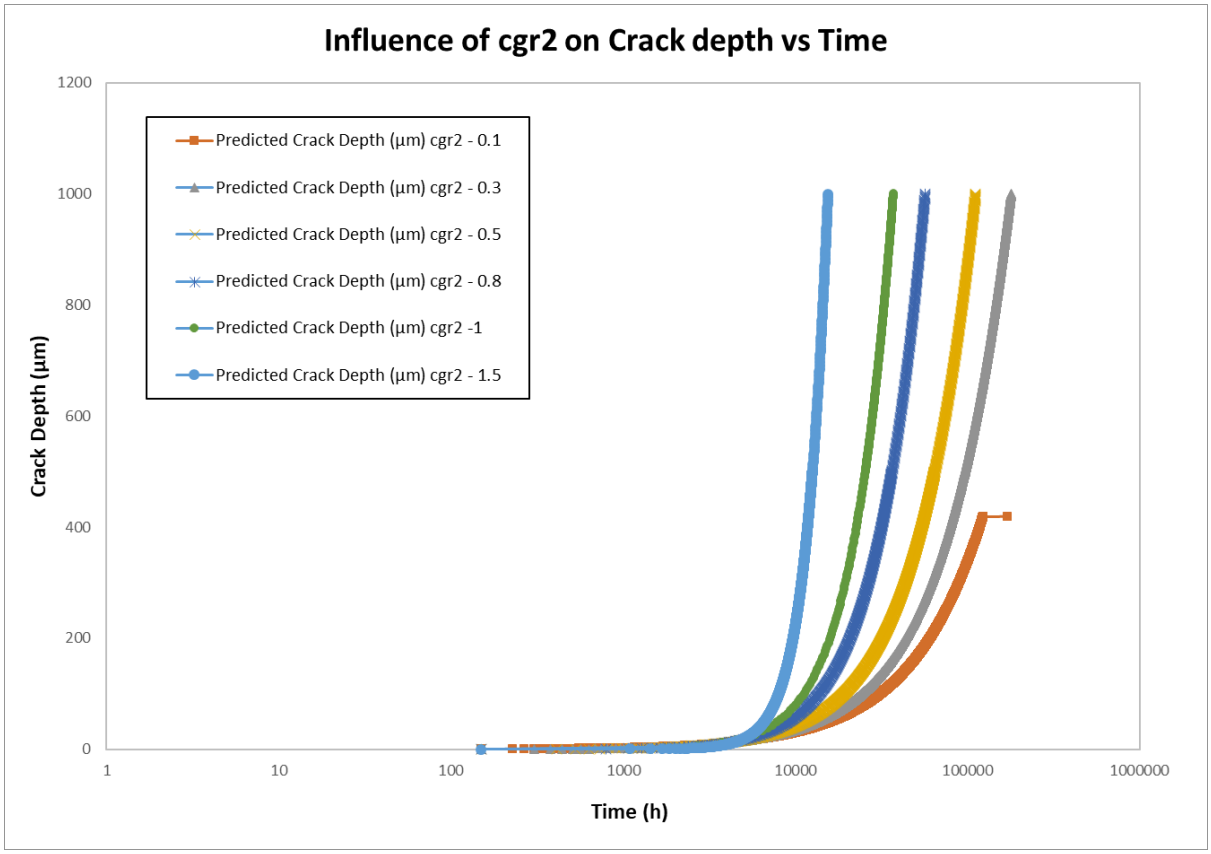


Figure 170: Overall influence of cgr2 parameter on Crack depth vs Time.

To compare for the observed crack depths, comparison was made upto 3000 hours of predicted crack depths as shown in *Figure* 171. It is observed that in the region of slow crack growth rate especially in the initial duration after the crack initation, faster crack gowth rate is shown by the lower cgr2 values. However, for the compromise between the sigmoidal dependancy and faster crack propagation rate in the slow crack regime and fast crack regime, cgr2 values are set to 0.8 for further calibration of the parameters.

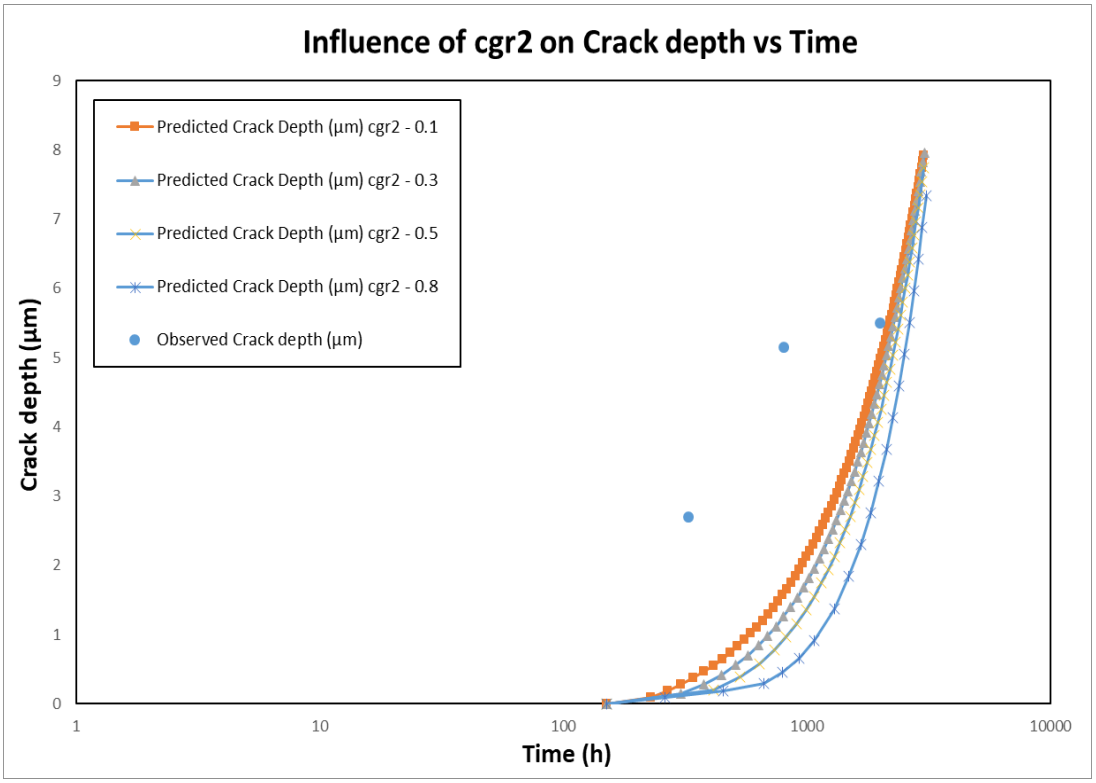


Figure 171: Influence of cgr2 parameter on Crack depth vs Time up to 3000 hours.

7.3.3 Effect of 'cgr4' parameter

The effect of cgr4 parameter was studied by changing the values from 8 – 20 with cgr2 and cgr3 kept at 0.005 and 0.8 respectively. The influence of cgr4 parameter on crack depth vs time was plotted as shown in *Figure* 172. As seen in the *Figure* 172, cgr4 does not have any effect on the crack growth rate.

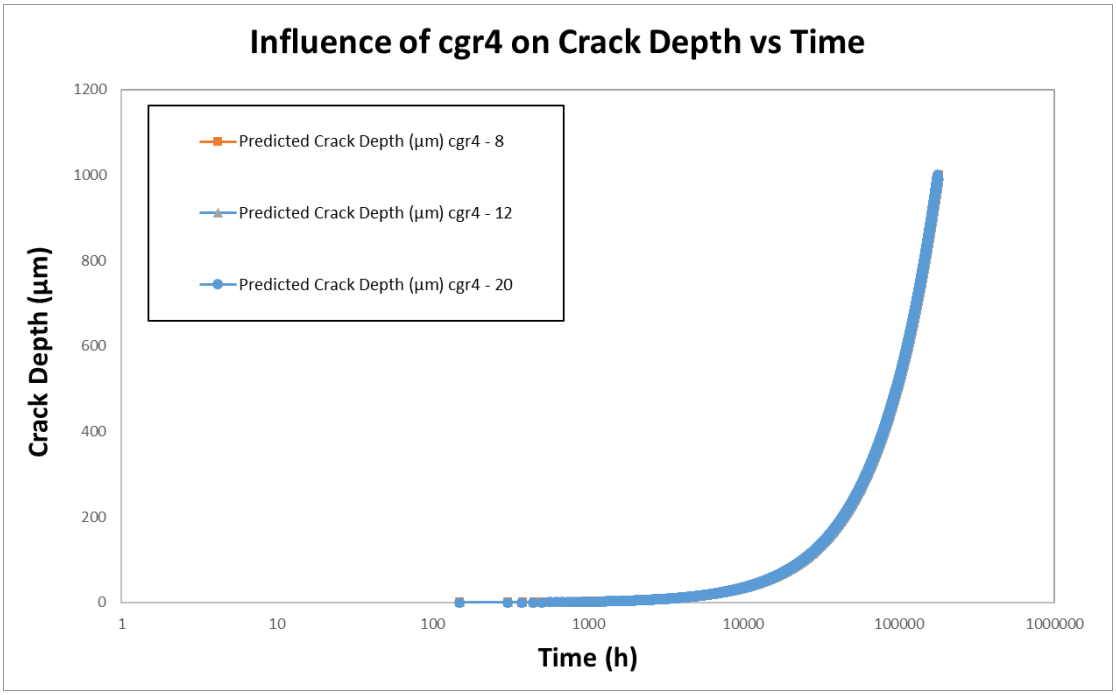


Figure 172: Overall influence of cgr4 parameter on Crack depth vs Time.

Comparisons with the observed crack depths were made upto 3000 hours of predicted crack depths as shown in *Figure* 173. It is observed that in the region of slow crack growth regime, for values of cgr4 from 8 – 20 there is no effect on the crack growth rate and it remains constant for all the values. Hence, for further calibration of cgr1, cgr4 value is chosen to be 12.

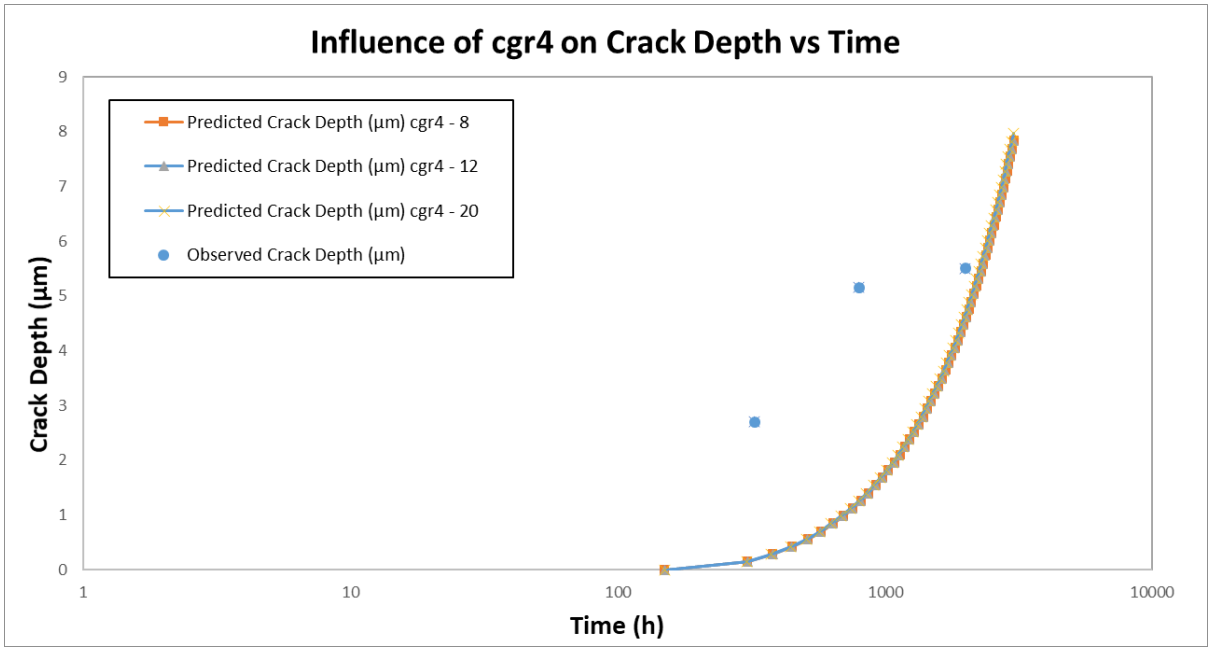


Figure 173: Influence of cgr4 parameter on Crack depth vs Time up to 3000 hours.

7.3.4 *Effect of 'cgr1' parameter*

The effect of cgr1 parameter was studied by changing the values from $4.4x10^{7}$ to $4.4x10^{8}$ with cgr2, cgr3 and cgr4 kept at 0.005, 0.8 and 12 respectively. The influence of cgr1 parameter on crack depth vs time is plotted as shown in *Figure* 174. It can be seen that cgr1 does affect the crack growth rate in all the regimes uniformly. But it does not influence the slope in the slow crack regime or in the transition from slow crack regime to fast crack growth regime.

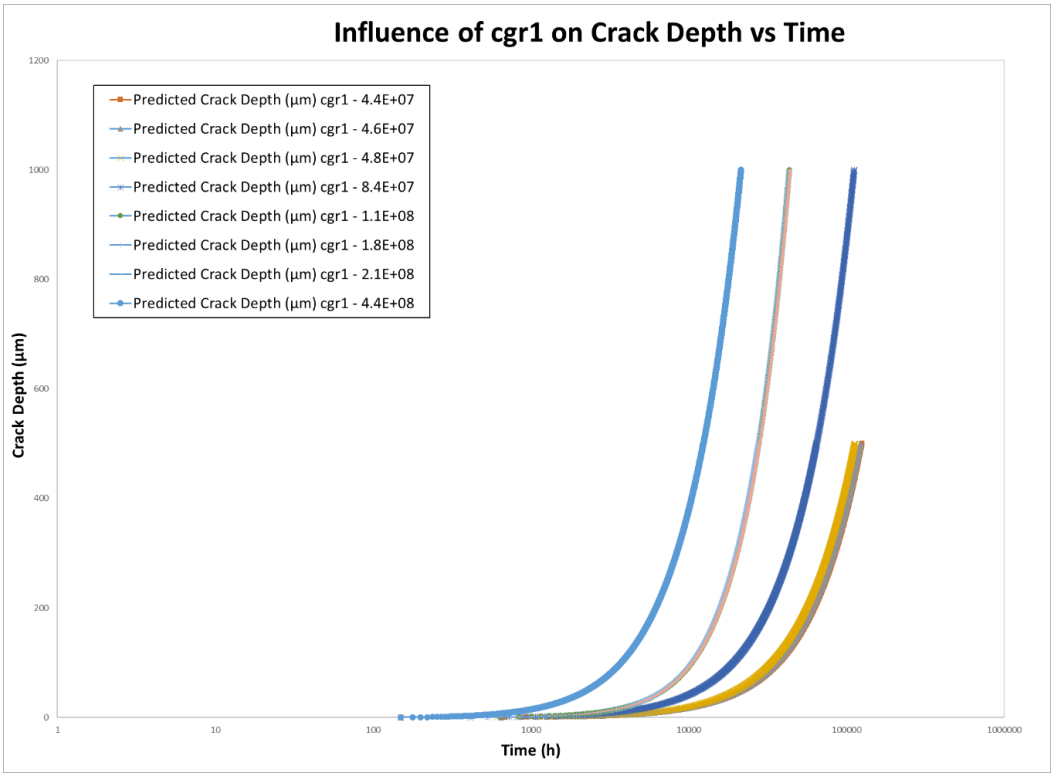


Figure 174: Overall influence of cgr1 parameter on Crack depth vs Time.

Comparisons with the observed crack depths were made upto 3000 hours of predicted crack depths as shown in *Figure* 175. It is observed that in the region of slow crack growth regime, for values of cgr1 from $4.4x10^{7}$ to $1.1x10^{8}$ the observed crack depths have reached much faster than the prediction. However, cgr1 value of $4.4x10^{8}$ seems to have a good comparison to the observed crack depths. It is seen that the predicted values of crack depth have occurred in time scale compared to the observed ones. *Figure* 176 shows the comparison of cracke depth vs time for alloy 600 solution annealed tested in similar conditions. Couvant et. al. [205] observed crack depth of 63µm at 1000 hours with the much higher stress and strain level (350 MPa and 31% strain) used in this thesis. Zhai et al. [285] observed initiation of crack with depth of 1 µm at 1250 hrs for alloy 600 plate with applied stress of 435 MPa, 3808 hrs for in service piece of CRDM with applied stress of 240-255 MPa and 4967 hrs for CRDM plate with applied stress of 290 MPa. These are only data registered with Alloy 600 T-265 heat, making a comparison

with other heats of alloy 600 is not direct in this case as several parameters needs to adjusted to consider the manufacturing effects.

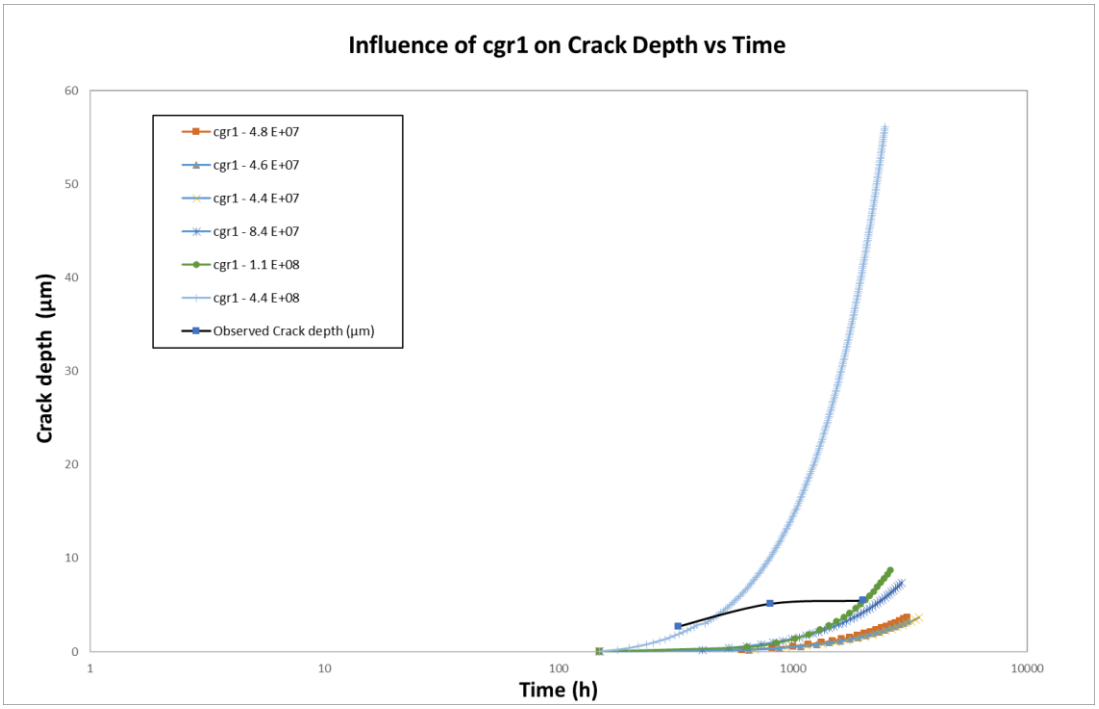


Figure 175: Influence of cgr1 parameter on Crack depth vs Time up to 3000 hours.

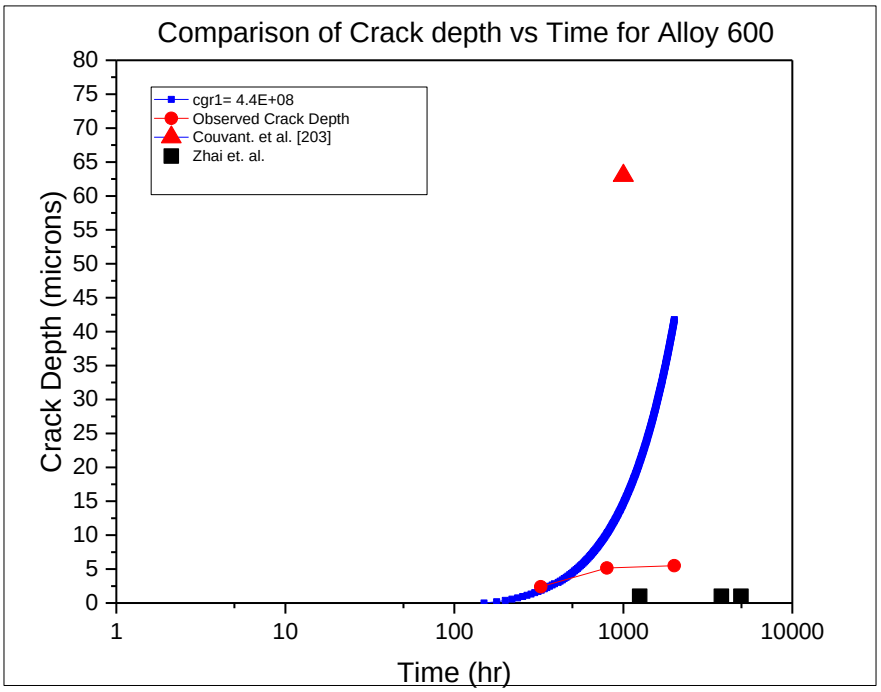


Figure 176: Comparison of Crack Depth vs Time for Alloy 600.

7.4 Comparison of Crack Growth Laws

After the initial calibration of the parameters, the effect of other crack growth laws was discussed in *section 2.4.5* used in Code_Coriolis platform was tested and compared. *Figure* 177 shows the influence of cgr_sigmoid, cgr_sigmoid_cw1 and cgr_sigmoid_cw2_h crack growth law on the predicted depth vs time. It is observed that introducing the function of plastic deformation and potential difference to the sigmoidal equation has a huge effect in increasing the crack propagation rate and bringing it close to the observed experimental results.

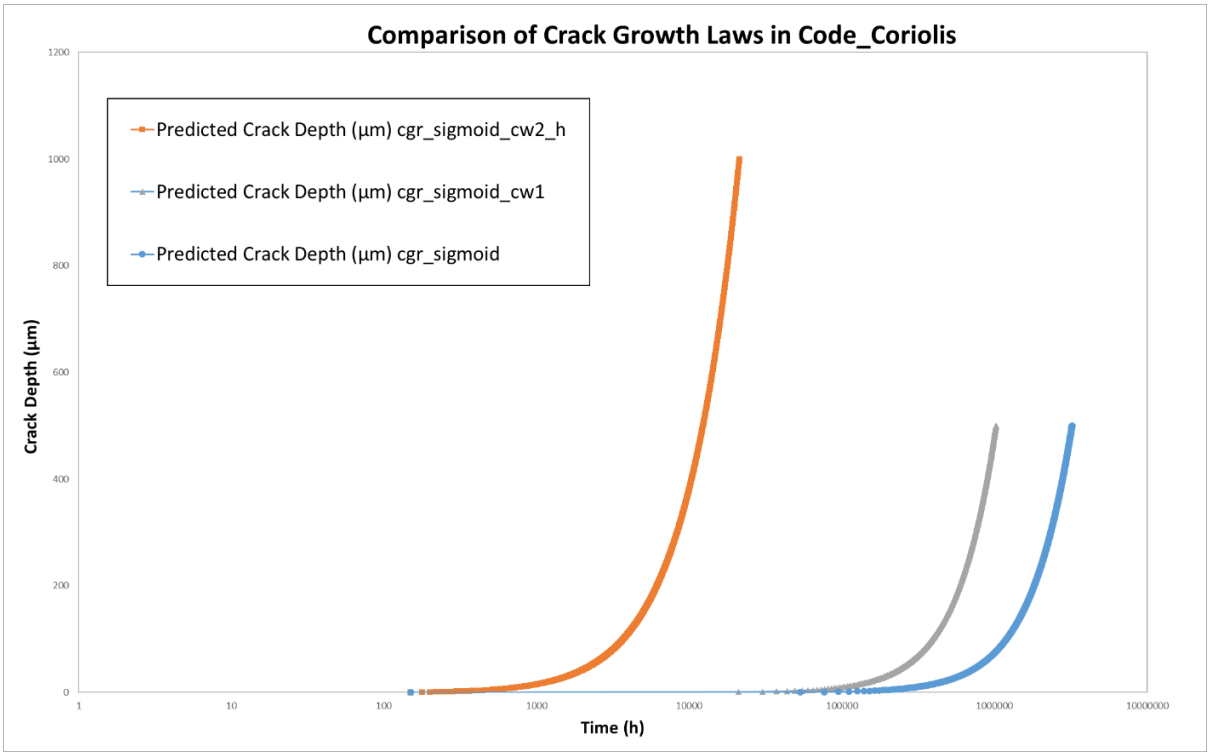


Figure 177: Comparison of Crack Growth Laws in Code_Coriolis.

7.5 Effect of Temperature

As Code_Coriolis platform allows to change the temperature of the water environment, the effect of temperature on crack initiation and propagation was studied. The effect was studied at 295°C, 330°C, 345°C and 360°C. It is observed that for the crack to initiate it took 150

hours in all cases. *Figure* 178 shows the effect of temperature on crack depth vs time. However, the crack propagation rate shows considerable amount of change for the temperatures. The crack propagation is faster in the case of 360°C and slower for the temperature of 295°C. It is also worth mentioning that if the oxidation rate was couple to stress, we would observe faster initiation times and you would move your simulated plot to the left (with a similar effect the T does).

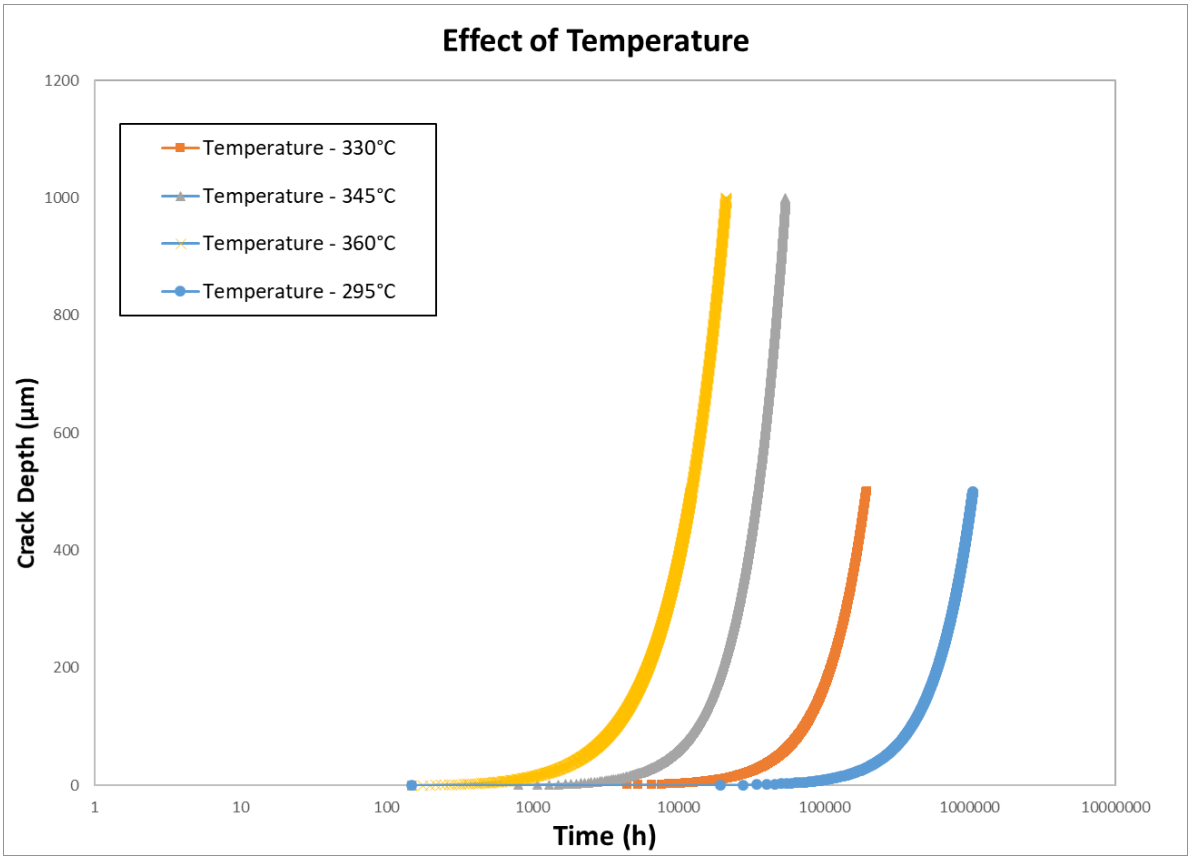


Figure 178: Effect of Temperature on Crack Depth vs Time.

7.6 Discussion

The development of Local model consists of proposing a degradation scenario that allows following the different stages of the cracking process from (1) the incubation of the crack by identification of intergranular oxidation kinetics, (2) the initiation of cracks by establishing the

two necessary criteria – reaching of critical oxidation depth and critical stress required to fail the oxidized grain boundary and (3) the propagation of cracks in two regimes (slow crack and fast crack), therefore following a dependence on K of the sigmoidal type. This model is capable of covering easily a wide range of crack sizes ranging from few hundred nanometers to a few millimeter depth.

The SCC mechanism taken into account in this model is based on the selective oxidation of the grain boundaries as an essential condition for SCC to occur. From the previous studies [203], scenario postulates that when the alloy 600 is subjected to a simulated PWR primary water environment, oxygen diffuses preferentially along the grain boundaries giving rise to intergranular oxide formation. The depth of these penetrations will depend on the test conditions, type of the grain boundaries and intergranular precipitation. This gives rise to mechanical weakening of the grain boundaries.

Based on these postulates, the initiation of microcracks is intergranular, so the testing and calibration of the Local model was done. The testing of initiation in Local model was performed by assigning the group of nodes in the global mesh with the SCC initiation properties. The stress assigned in each grain boundary is randomly sampled in a Gaussian distribution where the centre is the maximum principal stress at that node to initiate cracking. With the test for initiation stress was found that 297 MPa. It means that the stress assigned to a node can be lower than the average stress within the aggregate supposed to be located on the node. The stress reported in the result (section 9.1.2) is the mean stress, not the intergranular/local stress in the aggregate that lead to cracking. The initiation time reported after the test is 150 hours, it is the minimum time to rupture of a population of grain boundaries whose phase distribution (nominal and chromium carbides) is drawn randomly and whose normal stress at the grain boundary is also drawn randomly from a Gaussian distribution centered on the mean stress.

The observation of the initiation using DIC technique would give a better correlation between the observed time to initiation and predicted time.

In the study by Couvant et. al [203], the grain boundary stresses (local stress/critical stress to failure) from the CPFEM calculations on the polycrystalline aggregate was predicted to be 820 MPa, correspondingly the macroscopic stress were higher. This is because the CPFEM calculations were performed on the synthetic aggregate with random grain boundaries. In our case, the CPFEM calculations to estimate the local stress to failure of the oxidized grain boundaries were performed on the actual 3D-polycrystal aggregate extracted using 3D-EBSD technique. Thus, the local stress to failure of the oxidized grain boundaries is estimated to be 518 MPa.

Previous studies of the intergranular oxidation kinetics along with crack initiation [284] observed that the first grain boundary opening takes place at the start of the plastic deformation and found that the linear fraction of the cracked grain boundaries depend on the applied stress and the type of grain boundaries. Also, the oxidized grain boundary crack initiation was observed after 2.5% deformation with the macroscopic applied stress of 520 MPa. In our case, the first oxidized grain boundary crack initiation was observed at a similar deformation but with a lesser macroscopic applied stress of 310 MPa. The cross-sectional observations of the oxidized grain boundaries show a range of intergranular oxidation penetration depths for which a grain boundary is most likely to crack. The areas of cracking are determined by associating the level of grain boundary stresses (local stress/critical stress to failure) from the CPFEM calculations performed on the polycrystalline aggregate and the depth of intergranular oxidation.

Once the initiation occurs, the term local refers to the crack and the crack propagation is governed by the sigmoidal dependence of stress intensity factor. The crack growth or

propagation in the local model is controlled by one of the CGR laws. Foct et. al [186] stated that the critical stress intensity factor (K_{ISCC}) would be defined by the minimum values for which the crack can itself generate enough stress state necessary for its propagation. By this, the SCC computation for propagation was carried out with *'cgr_sigmoid_cw2_h'* law and it was found that after the initiation, the rate of crack growth by the main crack tip was very slow in comparison to the observed experimental results. In other words, K_{ISCC} was reached after a longer duration for the current model parameters. The model parameters were calibrated and ranked based on their effect on crack growth rate.

7.6.1 Ranking of model parameters

The effect of four paramaters on crack growth rate (CGR) were studied separately. It has been observed that each of the parameters have an influence in different regions of the crack depth vs time plot.

Based on the comparison studies with cgr1, cgr2, cgr3 and cgr4, it has been found that cgr1 has a huge influence in the propagation regime. As the value of cgr1 is increased from $4.4x10^7$ to $4.4x10^8$, crack growth rate increases massively in all the regimes of the curve. With the interdepencies of other parameters, for lower values of cgr3 (<0.005) it shows faster crack propagation rates and there is a slight increase for the changes in cgr2 values (0.2-0.8). However, it remains predominantly constant for all the changes in cgr4 values.

The second most influencing parameter in the crack growth rate is cgr3. As the values of cgr3 is increased from 0.005 to 5, there is a massive drop in the crack growth rate. This drop is most evident in the slope of the slow crack regime. When the cgr3 parameter is increased, the slope of the curve in the slow crack regime decreases drastically. With the interdepencies of other parameters, for higher values of cgr3, there is a negative effect on crack growth rate.

The parameter cgr2 is ranked third in influencing the crack growth rate. As the values of cgr2 is increased from 0.1 to 1.5, the transition of the slow crack regime to fast crack happens in lesser time. However, there is no change in the slow crack regime. With the interdepencies of other parameters, cgr2 increases the crack growth rate for higher values of cgr1 and lower values of cgr3. No change in the rate is observed for changes in cgr4 parameter.

The cgr4 parameter does not show any change in the crack growth rate for any change in values from 8-20. With the interdepencies of other parameters, for higher values of cgr3 there is a redution in the crack growth rate and slight increase in the rate for higher values of cgr1. *Figure* 179 shows the interdependency matrix of the four parameters *Figure* 180 shows the effect of the model parameters on specific region of crack depth vs time plot.

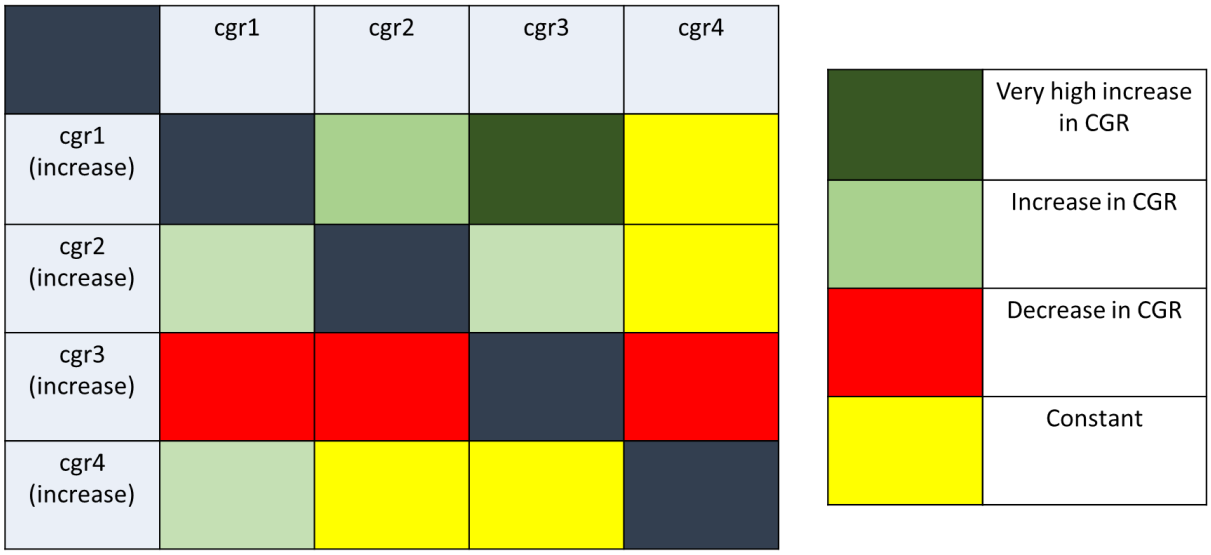


Figure 179: Interdependency Matrix showing the influence of the four parameters.

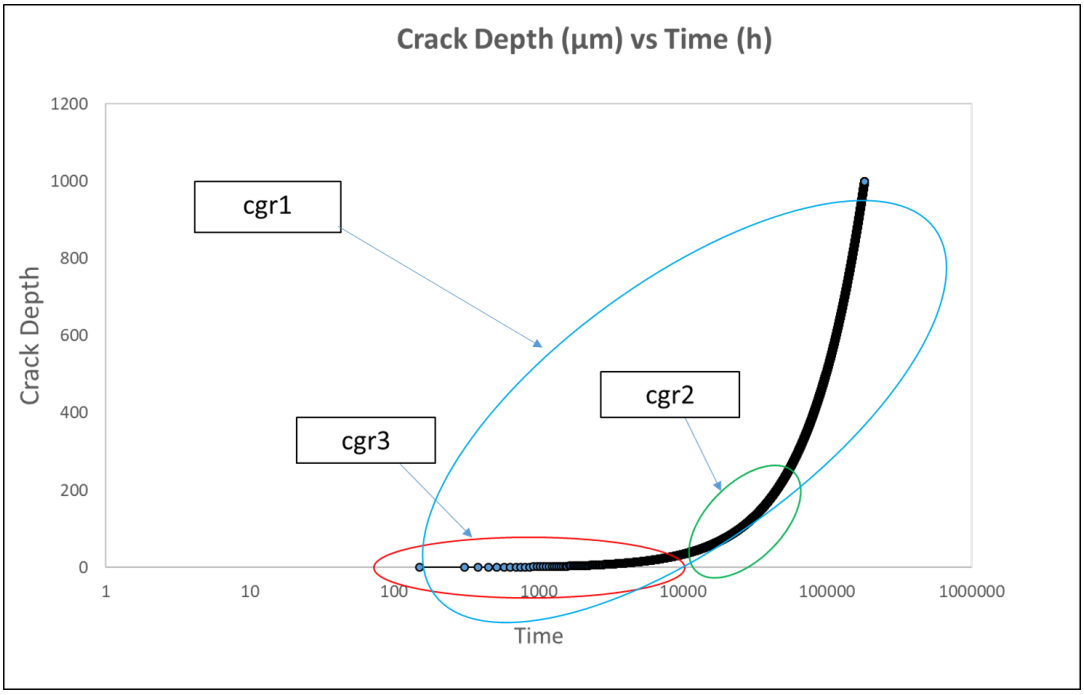


Figure 180: Influence of model parameters on the specific regions in the crack evolution plot.

In comparison with other CGR laws for SCC computation of propagation, *'cgr_sigmoid_cw2_h'* proved to be better in predicting the crack depths closer to the observed depths. This law depends on the strain, intensity factor of constraints but also temperature by means of activation energy and dissolved hydrogen content. Hence, the change of regime from slow to fast crack has a sigmoid shape. All calibrated and validated values for cgr2_sigmoid_cw2_h law for SCC computation are summarized in Table 21.

Table 21: Summary of Calibrated and validated parameters for cgr2_sigmoid_cw2_h law for SCC computation

Input Parameters	Value	How are they obtained
Cgr1	4.4×10^{8}	Fitted
Cgr2	0.8	
Cgr3	0.005	
Cgr4	12	
Cgr5	31	Obtained from Code_Aster calculation on Global specimen from prior to deformation [207]
Cgr6	1	
Cgr7	0.1	
Cgr8	3.604	Extracted from Pourbaix diagram for Ni/NiO equilibrium
Cgr9	11.33	
Cgr10	43.36	
Cgr11	130000	Activation energy used once the crack initiated from EDF studies [207]

7.6.2 Limitations of the model

The Local model evaluated in this thesis makes it possible to link incubation, initiation and crack propagation in SCC. The steps involved in this model are purely based on the phenomenonological mechanisms observed at the grain boundary scale. The model is good in capturing both the initiation and propagation at a local scale. The stress to fail an oxidized grain boundary has been studied by various authors. Studies carried out by Dugdale [53] show that the critical stress to fail oxidized grain boundary by FEM is 1.35 GPa. For the similar alloy 600, Dohr [275] estimated it to be in the range 330-770 MPa. In both these studies, the authors estimated the stress to failure of oxidised grain boundary by performing FEM simulations on

single grain boundaries. The studies carried out by EDF show that the failure to stress determined using the tensile tests in SEM at 20°C remain close for materials with different sensitivities towards SCC. For instance, for a material with GBC of 15%, the breaking stress of the oxidized grain boundaries is 980 MPa and for a material with GBC of 60%, the stress at rupture is 924 MPa. This suggests that the breakdown of the oxide is independent of the microstructure of the material. The effect of the microstructure (precipitation) will therefore be important in predicting the oxidation kinetics but not the failure criterion. This can also be seen from the studies of Fuji [191], where in situ tensile tests on oxidized samples in primary environment was carried out in a FIB. He found that the grain boundary stress to break an oxidized grain boundary is about 180 MPa for 1500 hours and 300 MPa for 2700 hours. In addition, the failure of the grains occurs at the metal/oxide interface.

The failure of oxidized grain boundaries in this thesis is determined to be 518 MPa. From mechanical tests performed on micro-samples prepared at FIB and finite element calculations, Dohr determined that the stress at rupture of grain boundaries (without the influence of the thick oxide layer formed on the surface) is between 300 and 500 MPa for a similar material. Even though Dohr identified the stress to crack for the material with preserved oxidized surface, the tests were carried out at room temperature. The difference between the limitations of failure evaluated may be caused due to the stress mode used. The limitation/constraint determined in this thesis was evaluated from the constant load four-point bend test in an autoclave and based on the observation of the extracted polycrystalline aggregate using 3D-EBSD. Contrary to this, Dohr used cantilever technique to produce crack on the single oxidized grain boundary on which the tensile stress has been evaluated using numerical simulation. The failure criteria of stress estimated in this thesis has a statistical approach whereas that estimated by Dohr is from a single grain boundary. The failure criterion established in this thesis can be

questioned because it only considers one single oxidation depth associated with one single local stress.

The crack initiation sites predicted by the model could not compared or correlated with the observed experimental samples as the autoclave experiments were conducted without using DIC. The model captures that for the longest autoclave test (2000 hours) the crack propagation to be still in the slow crack growth regime. The curvature of the experimental crack growth plot as shown in *Figure* 175 is the opposite of what is predicted. The experimental points have a negative 2nd derivative (concave downward shape) and the model have a positive 2nd derivative (concave upward shape). By fitting all the cgr1-4 parameters, there is no change the curvature of the plot, just the location to match the results closer to the observed one. Even though the predicted crack growth rate is conservative than observed, the trend can be further optimised by calibrating the stress intensity factor function in the model. The difference in the predicted and observed crack depths is large because there are lot of parameters to be tuned and calibrated other than the cgr parameters. The plateau in the curve of experimental data can be because of one of the two reasons, the compressive stresses in depth during the four point bend test can cause the crack propagation slow and the data is properly aligned in the slow CGR regime. In this case, it would be better if there is few more data points for larger test duration will help to tune the cgr1 and cgr3. This is again area which needs to be explored more.

With respect to temperature, it is seen that initiation occurs at 150 hours for 345°C. The study was carried out for other temperatures and corresponding time to initation was predicted by the model and it is presented in *Figure 181*. The model predicts that for increase in temperature the time to initiation is reduced. However, this can be validated only by performing the autoclave tests with DIC to capture the exact time to crack initaiton. This will help to

understand the model better in terms of the major criteria for initiation is either predominantly relies on local stress or on the intergranular oxidation kinetics.

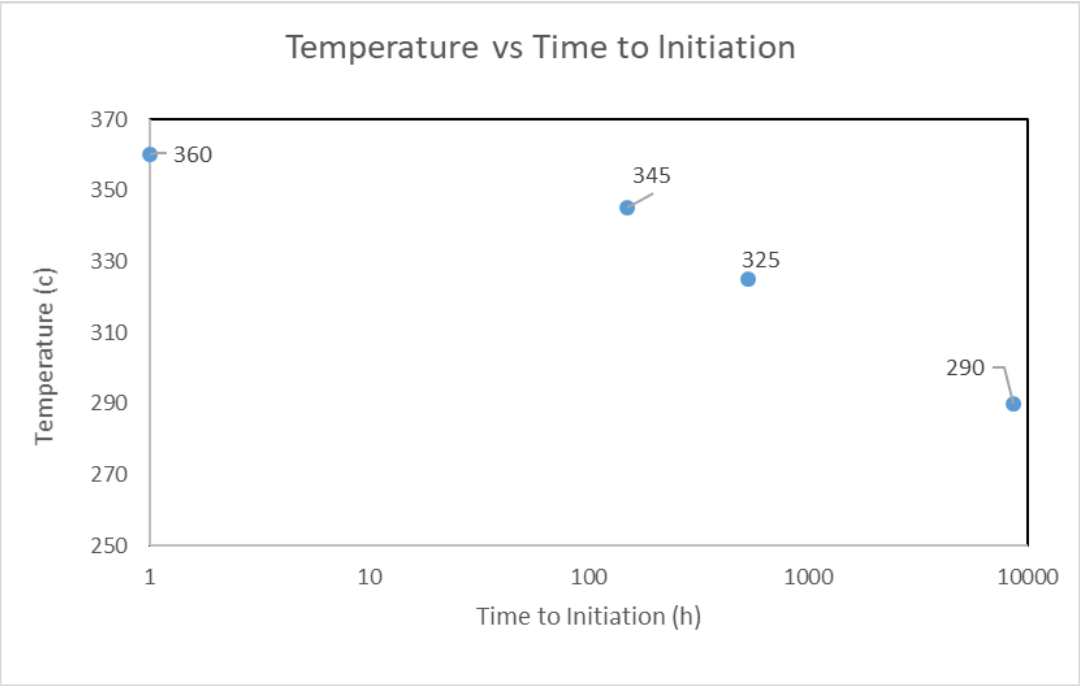


Figure 181: Intergranular Oxidation Kinetics for 295°C.

In place of the local stress state, a better estimate for plasticity around the grain boundary or a short crack is the dislocation density as described in *Chapter 5*. The accumulation of the dislocations along with the stress state provides a path for crack initiation and propagation. This aspect is not included in the current model and hence an addition of this would possibly make this model more predictive of the accurate local condition describing crack initiation and propagation.

7.7 Summary

The performance of the simulations of EDF's local model with the predicted and observed behaviour was studied. For the crack initiation part, the various input parameters such as grain size, grain boundary coverage, autoclave conditions (such as temperature, water chemistry, load etc.) along with the key inputs parameters from this thesis work such as the global stress, strain parameters on the four point bend test specimen, local stress concentration on the 3D polycrystalline aggregate, critical local stress to fail (SigmaC) were all fed in to the GUI interface of Code_Coriolis. The simulation results predicted the time required for crack initiation as 150 hours and crack initiation site. For the crack propagation part, of various crack growth extension laws, *'cgr_sigmoid_cw2_h'* was selected and used. The effect of various parameters such as cgr1, cgr2, cgr3 and cgr 4 were studied, calibrated and ranked depending on their influence in crack growth rate. The cgr1 parameter showed maximum dependency on crack growth rate followed by cgr3, cgr2 and cgr4 respectively. After calibration, the correlation between observed crack depth and predicted ones showed a better conservative fit. However, the experimental data points were not sufficient enough to explain the slope of the observed curve fit. The model predicts that for increase in temperature the time to initiation is reduced. However, this can be validated only by performing the autoclave tests with DIC to capture the exact time to crack initaiton. This will help to understand the model better in terms of the major criteria for initiation is either predominantly relies on local stress or on the intergranular oxidation kinetics.

8 CONCLUSIONS

The aim of this thesis is to experimentally evaluate the predictive model developed by EDF for investigating IGSCC in Alloy 600. Within the framework of this thesis, a systematic methodology to study the grain boundaries and the stresses along them was developed and investigated with the expectation that the analysis would contribute to our understanding of SCC mechanisms. A new strategy was developed in order to estimate the local stresses and validate the model.

8.1 New experimental approaches

The following are the new experimental techniques that have been developed and utilised successfully in model validation:

1. 3D EBSD

A new technique of extracting the actual grain morphology and orientation of the tested sample proved to be very useful. The 3D FIB-SEM sequencing along with EBSD enabled a more complete examination of the cracking behaviour and the path along the grain boundaries. This allows using more realistic aggregate for performing CPFEM computations.

2. On-axis Transmission Kikuchi Diffraction

As the interaction volume of the electron beam with the sample has been reduced, the spatial resolution of the orientation and strain mapping was significantly increased by the use of electron transparent TEM foil with on-axis TKD. In the framework of the thesis, TKD was used to determine the grain orientations and misorientations, and for the plasticity estimate with the dislocation density along the grain boundaries.

3. CPFEM computation on 3D-aggregate

The conversion of the realistic 3D-aggregate into a simulation mesh has always been a challenge. With the help of 3D-EBSD and other tools, this novel technique of extracting a 3D polycrystalline aggregate from the sample and performing CPFEM computations to determine the local stresses along on the grain boundaries was successfully achieved.

8.2 Summary of Results

1. SCC cracks

In this thesis, during the post analysis of autoclave tested samples from the observation of 86 grain boundaries, it is inferred that 30% of the grain boundaries have exhibited SCC cracks. The predominant number of cracks observed are on the random high angle grain boundaries (RHAGBs).

2. FEM stress evaluation on global specimen

FEM modelling used in evaluating the four-point bend test for constant load displayed high level agreement especially in the region of high stresses experienced during the experiment. The FEM results predicted a value of 304 MPa for 1 mm displacement.

3. CPFEM local stress evaluation on 3D-aggregate

CPFEM calculation was performed on the 3D-polycrystalline aggregate extracted using 3D-EBSD. The initiation criterion to produce a crack in alloy 600 at 345°C was predicted to be 518 MPa. This was applied on grain boundaries oxidized to or deeper than the critical oxidization depth of 300 nm. The stress representing 30% of the highest loaded grain boundaries would statistically correspond to 518 MPa, with a final mean principal stress of 392 MPa and the stress linear coefficient (S) value of 0.64 for assumed Gaussian stress distribution.

The critical stress calculated in this thesis is in accordance with some of the previous studies and deviates from others. However, this may be due to the different sample history, autoclave time, conditions and other possible explanations. This includes a possible influence from H_2, which was not studied in this thesis.

4. GND analysis

The most reliable way of estimating the plasticity around the grain boundary or crack tip region is the dislocation density. The cracked boundaries analyzed had local GND densities higher than 1 x $10^{16}m^{-2}$. Similar grain boundaries, from as-received samples had GNDs of 5 x 10^{14} m^{-2}, while an intermediate level was found in the oxidized but uncracked portion of the same GB. This suggests that a threshold value for local GND density is required to generate the stress required for an oxidized grain boundary to fail.

5. Local Model Initiation and Propagation

The testing of initiation in Local model was performed in Code_Coriolis and the initiation stress was predicted to 297 MPa at 150 hours. The SCC computation for propagation was carried out with *'cgr_sigmoid_cw2_h'* law and it was found that after the initiation, the rate of crack growth by the main crack tip was very slow in comparison to the observed experimental results. The four important paramaters on crack growth rate (CGR) were optimized to match with the observed experimental results as good as possible. The parameter cgr1 was found to have the biggest influence on the overall CGR in the model developed.

8.3 Suggestions for future research

Although a systematic strategy was used and presented in this thesis for the experimental validation of the IGSCC predictive model, SCC remains a highly complex and broad field of

research. Some questions remain unresolved and new techniques can be developed to further improve the model utility. By doing this, the model can perform at higher standard.

1. Use of in-situ DIC during autoclave experiments

Using in-situ DIC during autoclave experiments mainly in the region of high stress levels will be helpful in knowing the exact time of crack initiation and initiation sites on the global specimen. By doing so, the time of crack initiation can be compared to the observed duration and observed initiation site. Stratulat et. al. [286] studied the grain boundary structure and observed IGSCC crack intiation in austenitic stainless steels (SS 304) and compared the schmid factor for the fractured and intact grain boundaries as shown in *Figure 182*.

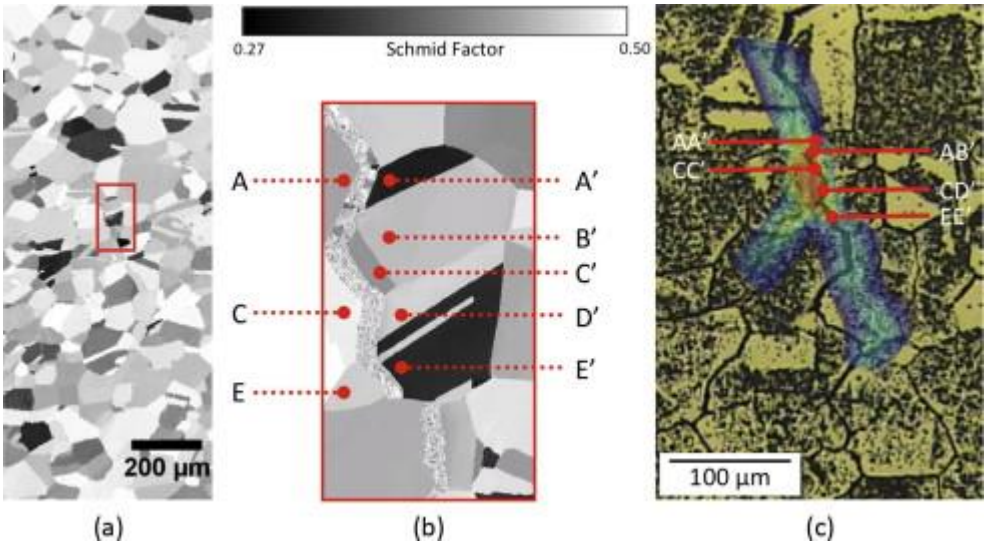


Figure 182: (a) Schmid factor map of the region of the crack initiation site of hot –rolled type 304 austenitic stainless steel; the observed values range from ~0.27 to 0.5, (b) five grain boundaries (AA′, AB′, CC′, CD′ and EE′) are identified and (c) their positions relative to the strain map indicated [286].

In this way the model can be further optimised for better predictability of initiation time and initiation sites. This approach was not feasible in this project due to degradation of the sapphire autoclave window used in Manchester with hydrogenated water.

2. Extended study on the temperature dependence of the CGR

The previous studies show the temperature dependence on the CGR (for higher temperature, faster CGRs). In this thesis, only one temperature was chosen and microstructural studies were used to validate the model. However, this data is not enough to explain the reasons for the discrepancies of initiation time predicted for other temperatures. In order to elucidate this shortcoming in the model, it is recommended to test samples at different temperatures. Shen et.al. [35] studied the mechanistic understanding of the temperature dependence of crack growth rate in alloy 600 and 316 stainless steel using high-resolution characterization where the samples were tested at 320°C, 340°C and 360°C.

3. Inclusion of GNDs in the assumption of initiation

At present the Local Model initiation criteria is based only on two assumptions. In place of the local stress state, a better estimate for plasticity around the grain boundary or a short crack is the dislocation density as described in *Chapter 5*. The accumulation of the dislocations along with the stress state provide a path for crack initiation and propagation. This aspect is not included in the current model and hence an addition of this would possibly make this model more predictive of the accurate local condition describing crack initiation and propagation.

Das et.al. [287,288] studied the hardening and strain localisation in Helium- Ion- implanted Tungsten, where the author created a CPFE model where hardening was implemented in the CPFE formaulation as a function of evolving GND density. The explicit incorporation of GNDs in the formulation is key for introducing length-scale effects. Further, the GND distribution provided insights into the plastic zone size, which was used directly compare experiments. GND densities were computed from both HR-EBSD and Laue measurements and compared with the CPFE predictions as shown in Figure *183*. This would be a starting point for introducing GNDs in the assumption of initiation into the Local Model for the case of IGSCC.

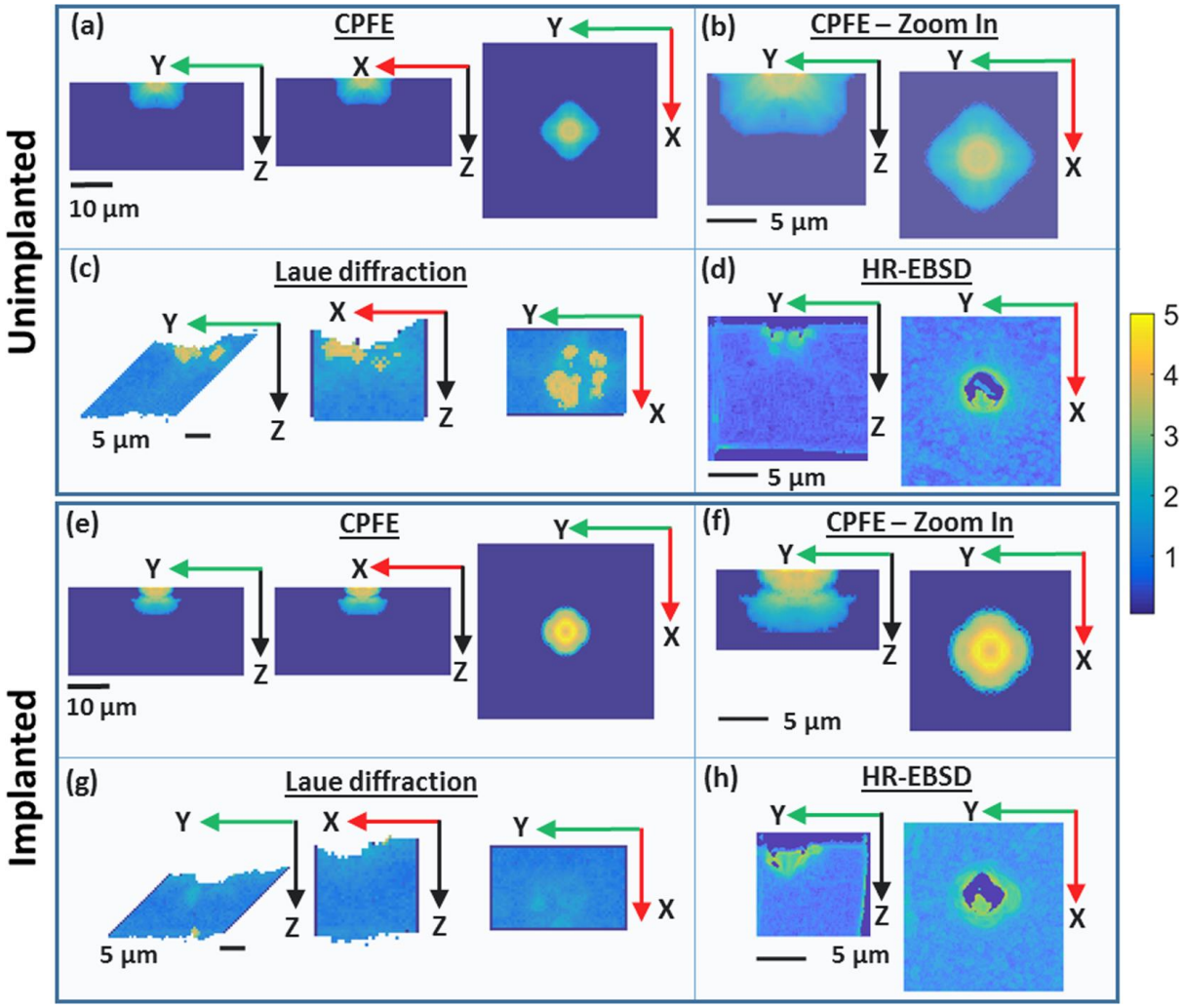


Figure 183: Total GND density plotted on YZ, XZ and the XY cross-sections through the indent centre. GND density was calculated using L2 optimisation. Predictions from CPFE calculations are shown in (a) and (b) for the unimplanted sample, and (e) and (f) for the helium-implanted sample. GND density computed from Laue diffraction measurements for the unimplanted and implanted samples are shown in (**c**) and (**g**) respectively. GND density determined by HR-EBSD for the unimplanted and the implanted sample is shown in (**d**) and (**h**) respectively. The same colour scale is used for all plots showing $\log_{10}(\rho)$ with ρ in $1/\mu m^2$. (**a**), (**c**), (**e**) and (**g**) are plotted on the same length scale. (**b**), (**d**), (**f**) and (**h**) show magnified plots of GND density and are also all shown on the same length scale [287].

4. Combining Cohesive Zone Model into the CPFEM calculation of 3D-aggregate

Couvant et.al. [113] performed simulation studies on IGSCC of austenitic stainless steels (annealed 304L) exposed to primary water. In this work, the author created a synthetic polycrystalline aggregate with 172 grains and modelled the initiation and the extension of the

crack along the grain boundaries, cohesive elements were inserted between grains. The model was then tested under constant simulated elongation rate tensile test till the initiation occurred as shown in Figure *184*. Coupling cohesive zone model and intergranular oxidation kinetics into the CPFEM computation of 3D-aggregate modelling will help in even better prediction and quantification of local stresses at the grain boundaries and correlation of the cracking behaviour with observed experimental results.

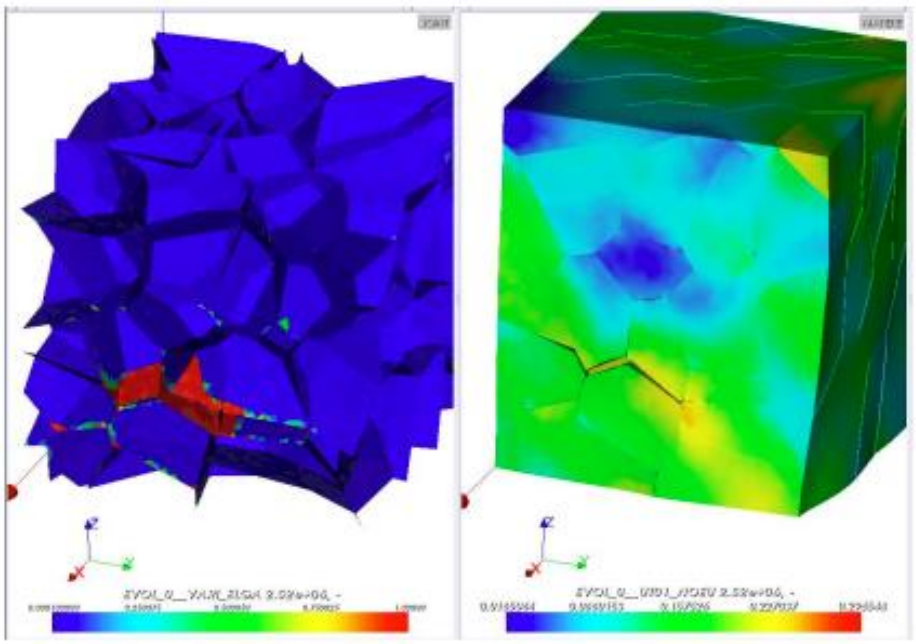


Figure 184: Initiation stage simulated in a 172-grain polycrystal. On the left, cracked grain boundaries are shown in red on the grain boundary network of the metal. On the right, the displacement field is plotted on the cracked polycrystal. Simulated constant elongation rate tensile test ($4\times10\text{-}8\ s^{-1}$) along vertical axis, in primary water at 360°C, $pH_{320°C}$ = 9. Final elongation = 12.6%. Water is in contact of metal on the front side of the model [113].

5. Influence of H_2

As established, the adsorption of hydrogen can cause hydrogen embrittlement in the crack tip regions and may accelerate the SCC crack propagation. Conducting SCC tests in heavy water may help to distinguish this behaviour and it can be incorporated into the model for better predictability.

6. More TKD experiments on evaluating the stress/strain fields at the grain boundaries

The high stress regions in the grain boundaries especially at the metal/oxide interface can be further examined by conducting more experiments to establish a correlation between dislocations and any other defects such as vacancies which could lead to preferential migration of grain boundaries.

Despite the extensive studies and numerous projects, it is still not possible to reliably predict SCC susceptibility and crack growth rates. However, I see this model as a small dot in the process of bigger picture in saying the whole story of SCC in future.

9 APPENDIX

Appendix A: FORTRAN script used in Code_Aster to define the material properties, boundary conditions and applied displacement to the four-point bend test model.

```
#-------------------------------------------------------------------------
--
# 1/2 4/point bending
# 0 < INST < 10 : introduction contraintes résiduelles de surface
# 10 < INST < 20 : serrage à température ambiante
# 20 < INST < 30 : montée à la température d'essai de CSC (290°C)
#-------------------------------------------------------------------------
--
# Fichier : naganand.comm
# Auteur : T. Couvant
#
# Code_Aster   : 12.6
# Unités : mm, N, MPa
#
# Historique :
#  08/02/18 : creation
#-------------------------------------------------------------------------
--

from numpy import tan
import re
import sys
sys.path.append('/home/naganand/Global/Depl5')

# Inputs
depl = 5.

# Code_Aster parameters

subd_pas = 10
subd_niveau = 10
resi_glob_rela = 5.e-5
iter_glob_maxi = 12

#-------------------------------------------------------------------------
--
DEBUT(PAR_LOT='NON',);

MA=LIRE_MAILLAGE(FORMAT='MED',);

MACR_INFO_MAIL;

MODE=AFFE_MODELE(MAILLAGE=MA,
                 AFFE=_F(GROUP_MA=('specimen',),
                         PHENOMENE='MECANIQUE',
                         MODELISATION='3D',),);

#-------------------------------------------------------------------------
--
# Behaviour of T265 SA @360°C
```

```
#-------------------------------------------------------------------------
--

E_360 = 200000.0
NU_360 = 0.33
SS_360=DEFI_FONCTION(
                     NOM_PARA='EPSI',
                     VALE=(
                         0.001,   150.,
                         0.0015,  175.,
                         0.003120127, 208.8043269,
                         0.009346188, 246.7570323,
                         0.015686324, 271.6901054,
                         0.021795738, 293.9529896,
                         0.028499989, 313.1843746,
                         0.035058216, 333.1702892,
                         0.04130028,  350.7286058,
                         0.04739872,  367.0696569,
                         0.053019304, 382.6031269,
                         0.058594327, 396.324335,
                         0.065478704, 414.1738315,
                         0.070724039, 428.5709565,
                         0.077109178, 444.0288492,
                         0.083720551, 461.7785635,
                         0.089150338, 475.0570004,
                         0.094186822, 484.2172835,
                         0.099967499, 499.2659888,
                         0.106164692, 509.29829,
                         0.112864292, 523.5721846,
                         0.118222939, 538.3329162,
                         0.124710099, 557.78314,
                         0.130624672, 564.5105846,
                         0.13663532,  578.7606792,
                         0.142349895, 587.7537277,
                         0.148506208, 597.9869308,
                         0.154629137, 607.1365731,
                         0.160071687, 620.1095427,
                         0.171795519, 640.6668531,
                         0.184344509, 666,
                         0.195792909, 686,
                         0.203022473, 699.1551462,
                         0.215756333, 714.3190154,
                         0.221638419, 724.5816646,
                         0.23,    736,
                         0.245034193, 756.7708077,
                         0.255420985, 773.5106112,
                         0.258522278, 781.3921277,
                         0.26520254 , 785.2255269,
                         0.273094946, 795.2883615,
                         0.27477159,  797.2303862,
                          ),
                     PROL_DROITE='LINEAIRE',
                     PROL_GAUCHE='LINEAIRE',);

#-------------------------------------------------------------------------
----
# Behaviours
#-------------------------------------------------------------------------
----

MATE=DEFI_MATERIAU(ELAS=_F(E=E_360,
```

```
                              NU=NU_360,),
                    TRACTION=_F(SIGM=SS_360,),);


#-------------------------------------------------------------------------
-
# Mechanical properties are defined to the volume groups
#-------------------------------------------------------------------------
-

MAT=AFFE_MATERIAU(MAILLAGE=MA,
                  AFFE=(_F(GROUP_MA=('specimen',),
                           MATER=MATE,),
                        #_F(GROUP_MA=('vis',),
                        #   MATER=MATE,),
                        ), );

ZERO=DEFI_FONCTION(
                     NOM_PARA='INST',
                     VALE=(0.0, 0.0,
                           10.0, 0.0,
                           ),);

#-------------------------------------------------------------------------
---
# Boundary conditions
#-------------------------------------------------------------------------
---

FIX=AFFE_CHAR_MECA(MODELE=MODE,
                       DDL_IMPO=(_F(GROUP_MA='sym',
                                    DX=0.0,),
                                 _F(GROUP_NO='line_up',
                                    DY=0.0,),
                                    ),);

DEPL_Y=DEFI_FONCTION(
                     NOM_PARA='INST',
                     VALE=(0.0, 0.0,
                           10.0, depl,
                           ),);

DEPL=AFFE_CHAR_MECA_F(MODELE=MODE,
                       DDL_IMPO=_F(GROUP_NO='line_down',
                                   DY=DEPL_Y,
                                   DZ=ZERO),);

#-------------------------------------------------------------------------
--
# Automatic adjustement of displacement to reach convergence
#-------------------------------------------------------------------------
--

PAS=DEFI_LIST_REEL(DEBUT=0.0,
                    INTERVALLE=_F(JUSQU_A=10.0,
                                  NOMBRE=10,),);

PAS_SUBD=DEFI_LIST_INST(DEFI_LIST=_F(METHODE='MANUEL',
                                     LIST_INST=PAS,),
                    ECHEC=_F(SUBD_PAS=subd_pas,
                             SUBD_NIVEAU=subd_niveau,),);
```

```
#-----------------------------------------------------------------------
--
# Calculation
#-----------------------------------------------------------------------
--

RESU=STAT_NON_LINE(MODELE=MODE,
                   CHAM_MATER=MAT,
                   EXCIT=(_F(CHARGE=FIX,),
                          _F(CHARGE=DEPL,),),
                   COMPORTEMENT=(
                                _F(RELATION='VMIS_ISOT_TRAC',
                                DEFORMATION='PETIT',
                                RESI_CPLAN_RELA=resi_glob_rela,
                                GROUP_MA=('specimen'),),),
                   INCREMENT=_F(LIST_INST=PAS_SUBD,
                                INST_FIN=10),
                   NEWTON=_F(PREDICTION='ELASTIQUE',
                             MATRICE='TANGENTE',
                             REAC_ITER=1,),
                   CONVERGENCE=_F(RESI_GLOB_RELA=resi_glob_rela,
                                  ITER_GLOB_MAXI=iter_glob_maxi,),
                   SOLVEUR=_F(METHODE='MUMPS',),
                   ARCHIVAGE=_F(INST=(0.0, 5.0, 10.0),),);



#-----------------------------------------------------------------------
---------------
# Calculs contraintes/déformations
#-----------------------------------------------------------------------
---------------

RESU=CALC_CHAMP(reuse =RESU,
                RESULTAT=RESU,
                CONTRAINTE=('SIEF_NOEU',),
                DEFORMATION=('EPSI_NOEU',),
                CRITERES=('SIEQ_NOEU',
                          'EPEQ_NOEU',),
                VARI_INTERNE='VARI_NOEU',);


#-----------------------------------------------------------------------
--------------
# Extractions for control before SCC simulation
#-----------------------------------------------------------------------
--------------

IMPR_RESU(FORMAT='MED',
          UNITE=80,
          RESU=(_F(RESULTAT=RESU,
                   NOM_CHAM=('DEPL',
                             'SIEF_NOEU',
                             'EPSI_NOEU',
                             'SIEQ_NOEU',
                             'EPEQ_NOEU',
                             'VARI_NOEU',),
                   INST=(0., 10.,),),
                   ),);
```

```
#-------------------------------------------------------------------------
--------------
# Extraction of strain and stress (all components of tensors) for
Code_Coriolis
#-------------------------------------------------------------------------
--------------

eps2=POST_RELEVE_T(ACTION=_F(OPERATION='EXTRACTION',
                             INTITULE='Strain',
                             RESULTAT=RESU,
                             NOM_CHAM='EPSI_NOEU',
                             INST=10.0,
                             GROUP_NO=('specimen'),
                             TOUT_CMP='OUI',),);

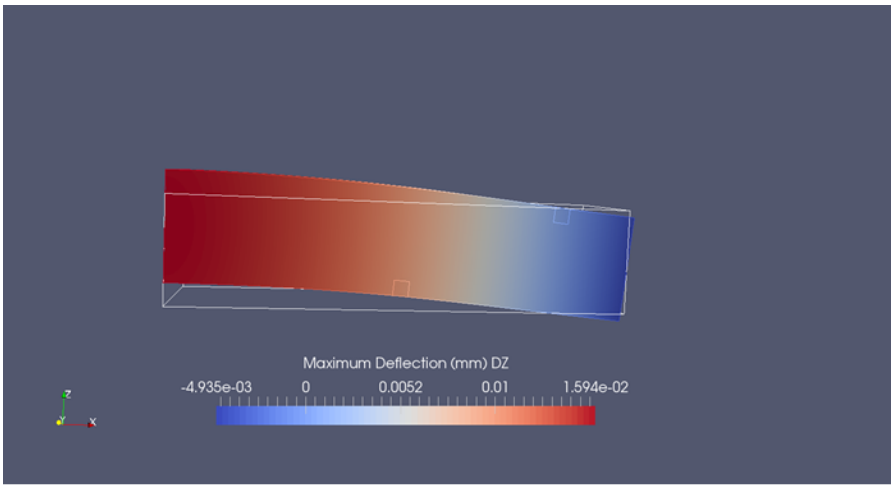
IMPR_TABLE(TABLE=eps2,
           FORMAT='TABLEAU',
           UNITE=8,);

sig2=POST_RELEVE_T(ACTION=_F(OPERATION='EXTRACTION',
                             INTITULE='Stress',
                             RESULTAT=RESU,
                             NOM_CHAM='SIEF_NOEU',
                             INST=(10.),
                             GROUP_NO=('specimen'),
                             TOUT_CMP='OUI',),);

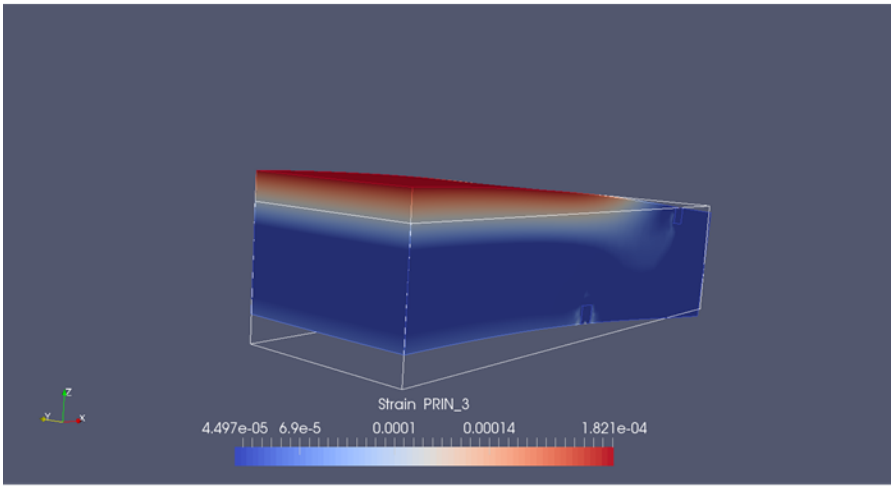
IMPR_TABLE(TABLE=sig2,
           FORMAT='TABLEAU',
           UNITE=8,);

FIN();
```

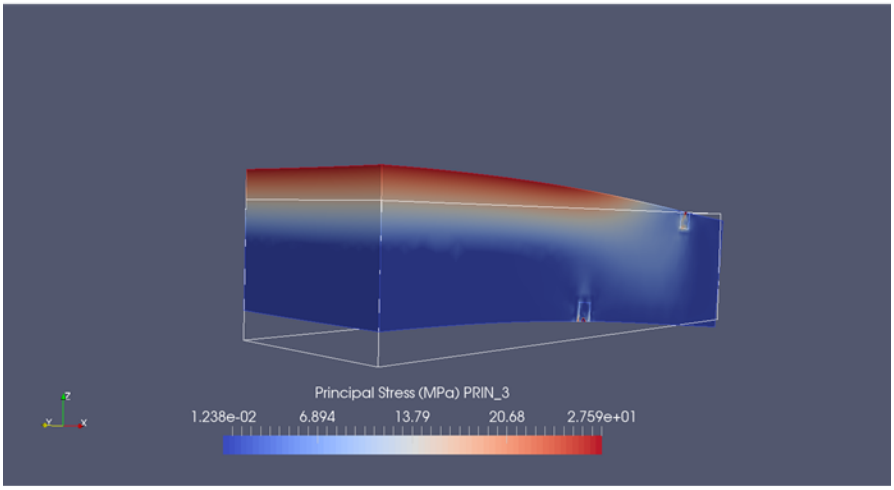
Appendix B:



(a) Deflection of the beam (mm)

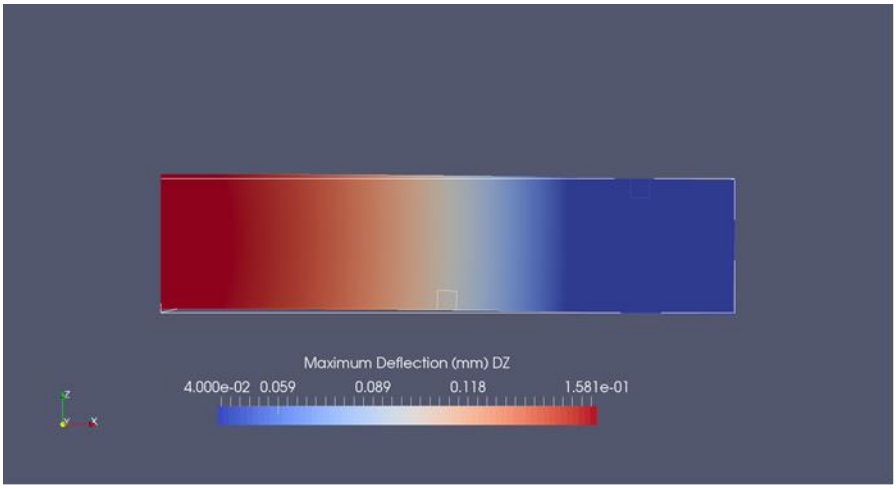


(b) Strain

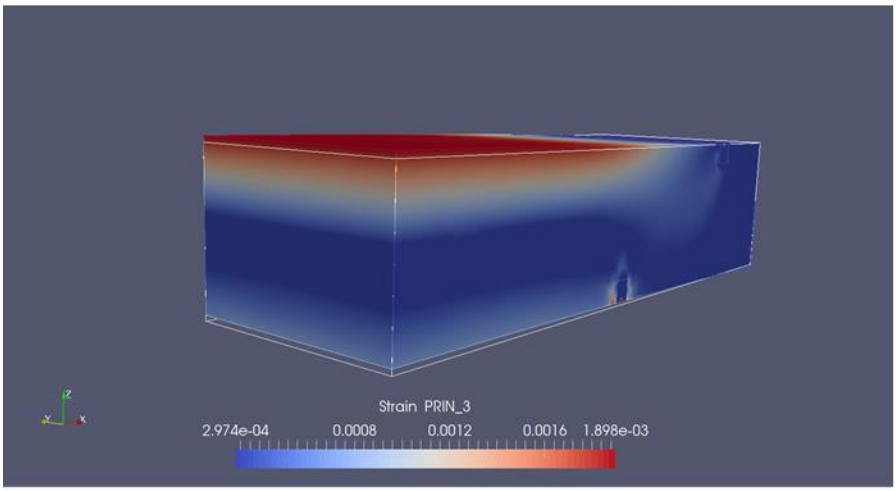


(c) Principle Stress (MPa)

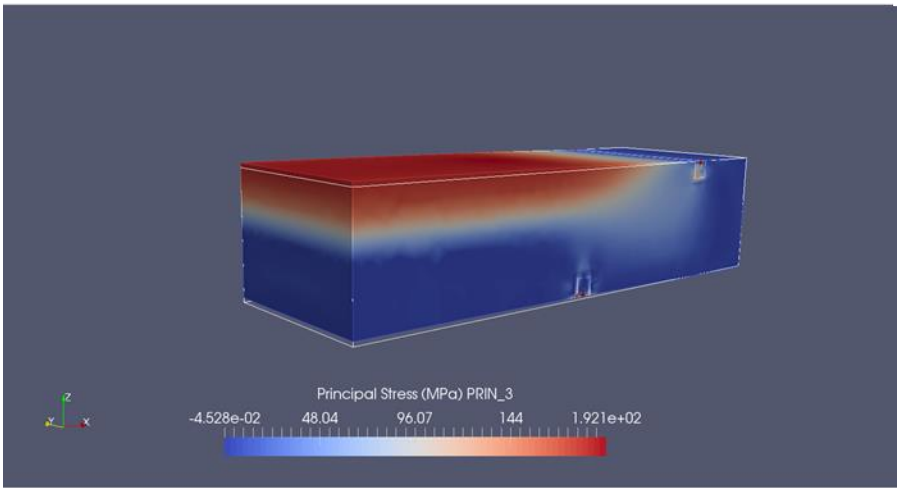
FEM results for 0.01 mm displacement of push rods.



(a) Deflection of the beam (mm)

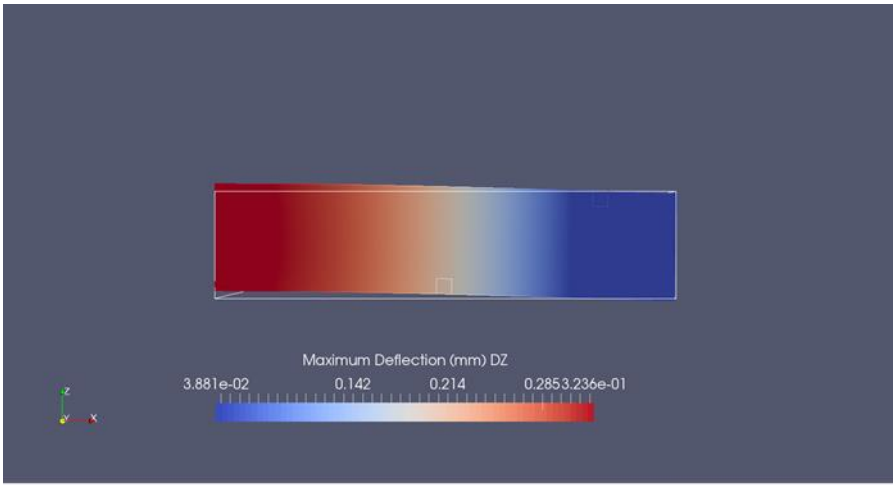


(b) Strain

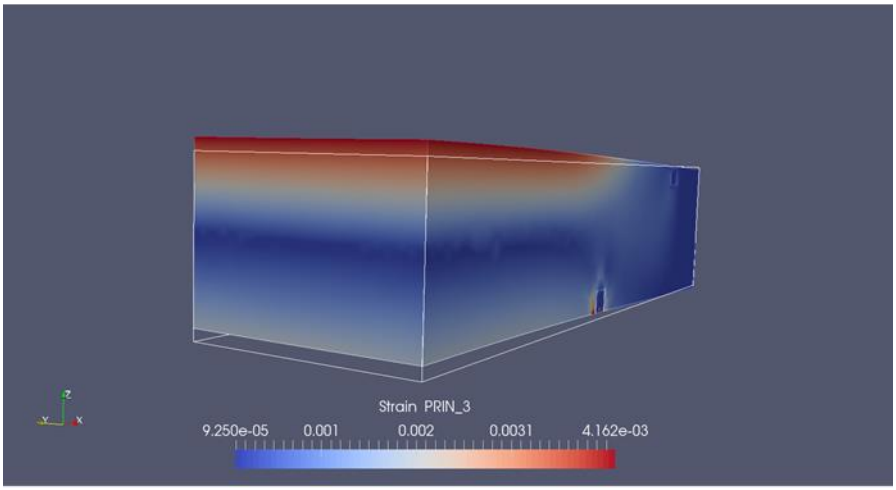


(c) Principle Stress (MPa)

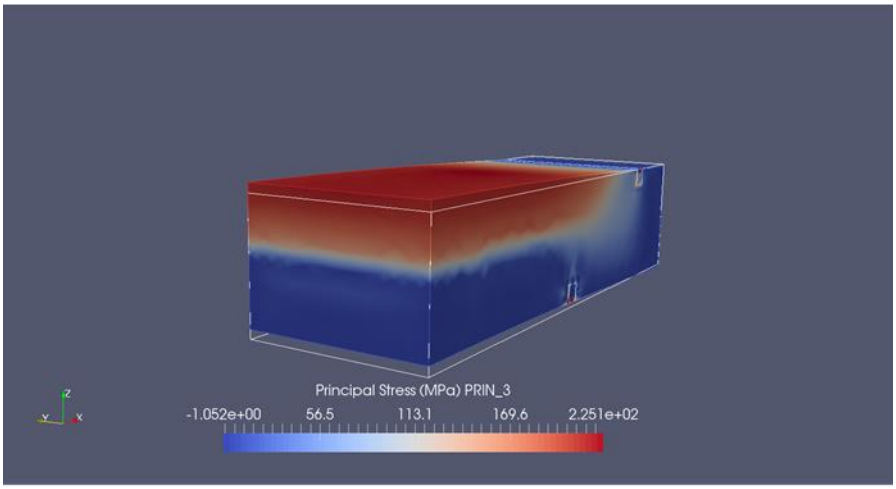
FEM results for 0.1 mm displacement of push rods.



(a) Deflection of the beam (mm)

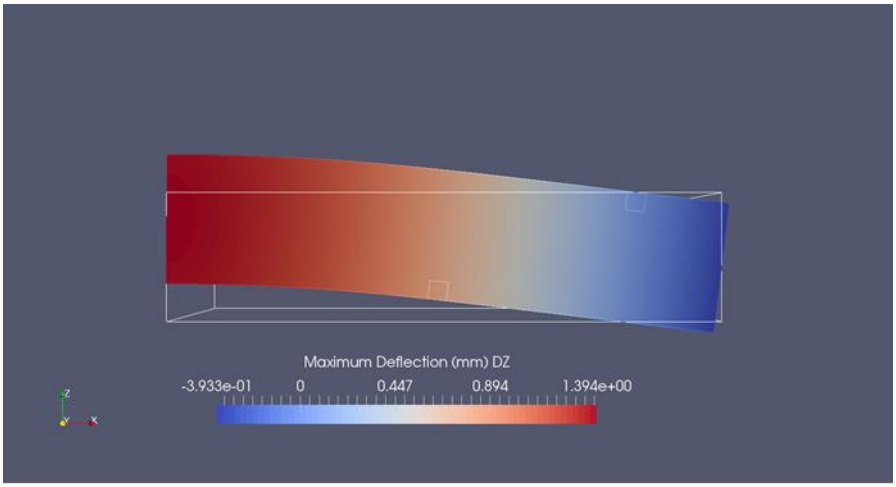


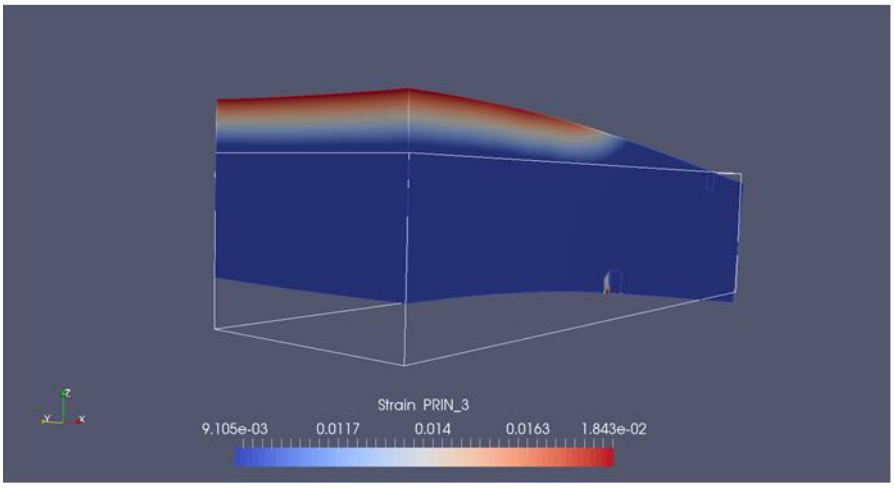
(b) Strain

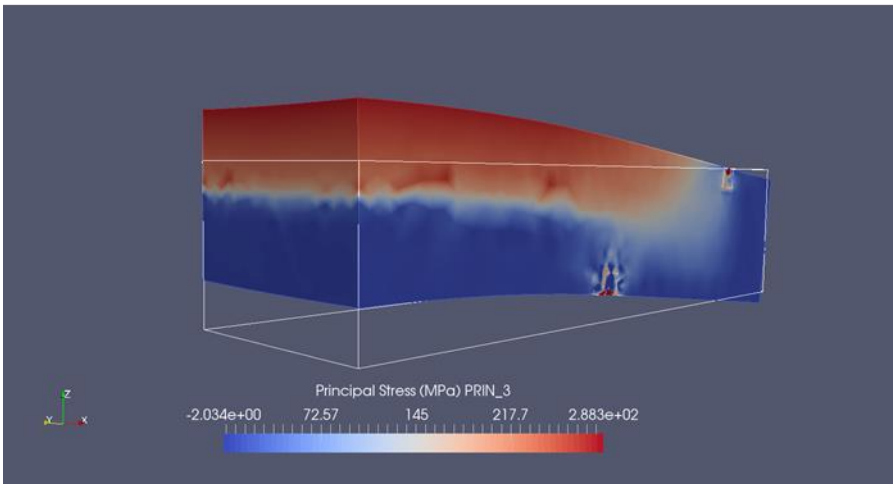


(c) Principle Stress (MPa)

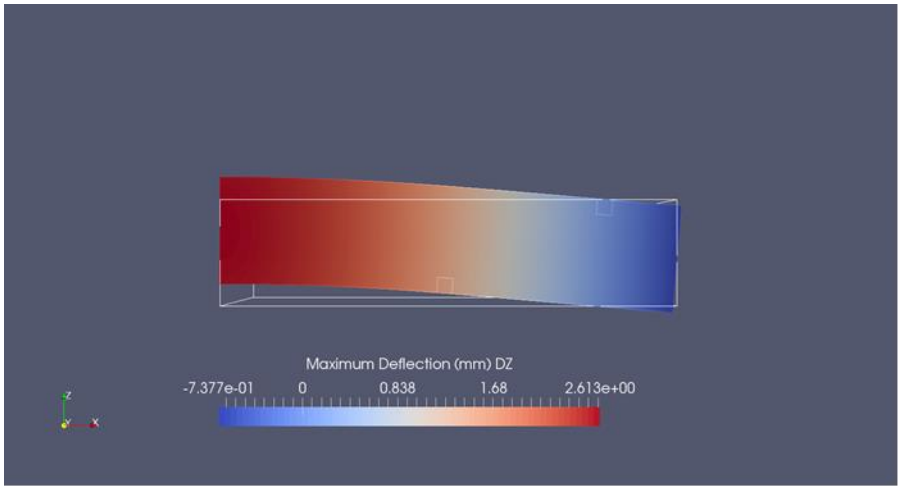
FEM results for 0.2 mm displacement of push rods.



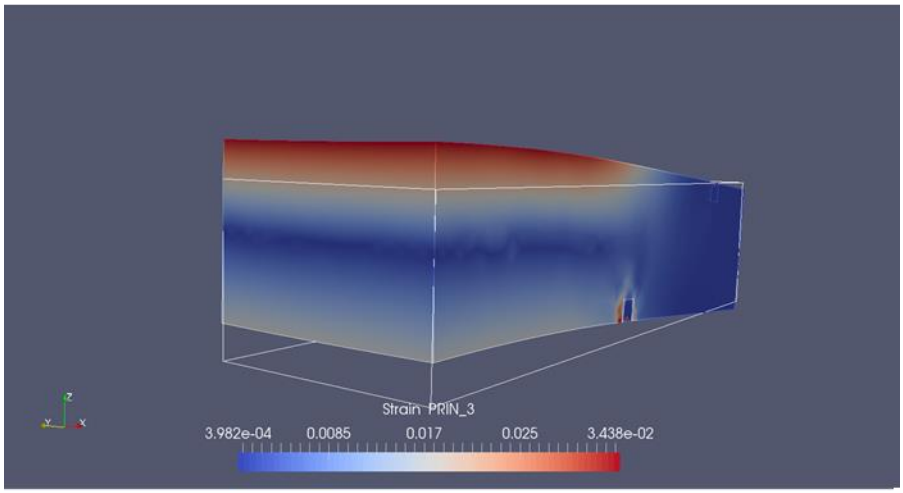




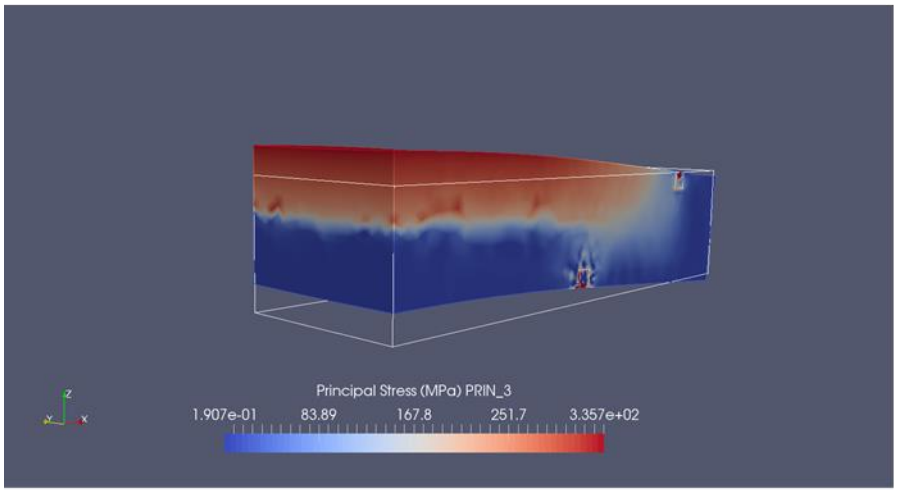
FEM results for 0.8 mm displacement of push rods.



(a) Deflection of the beam (mm)

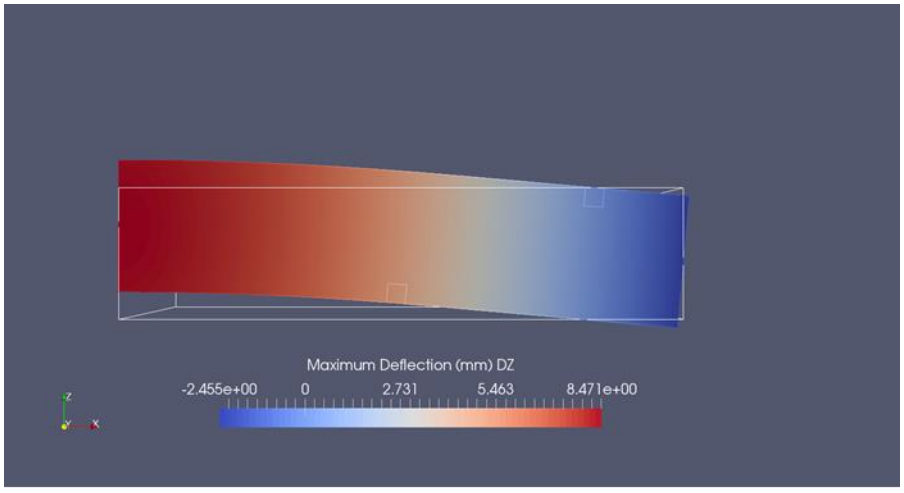


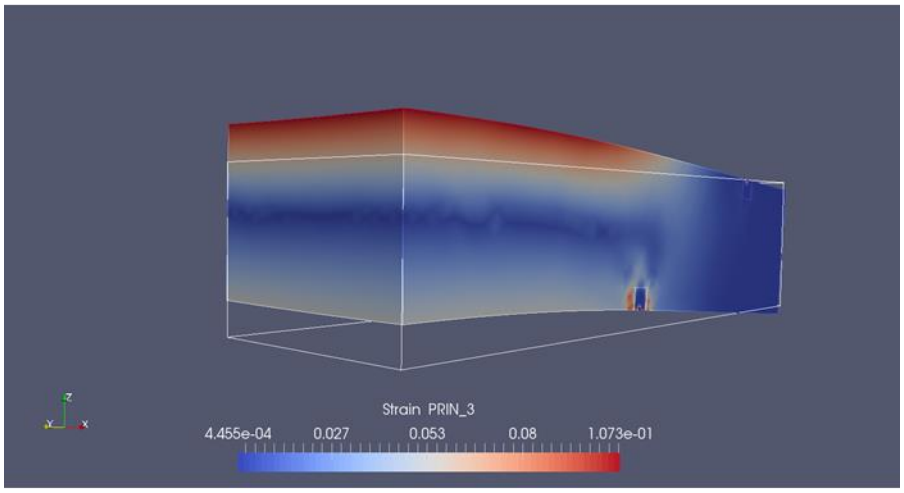
(b) Strain

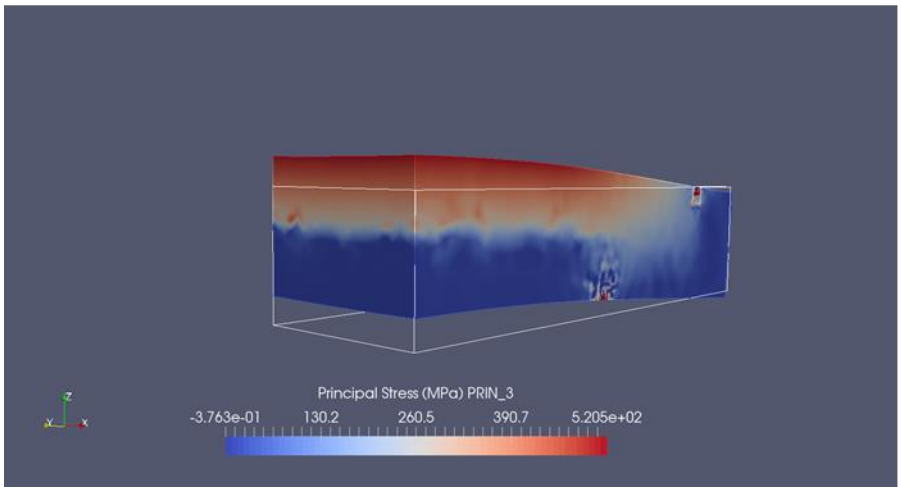


(c) Principle Stress (MPa)

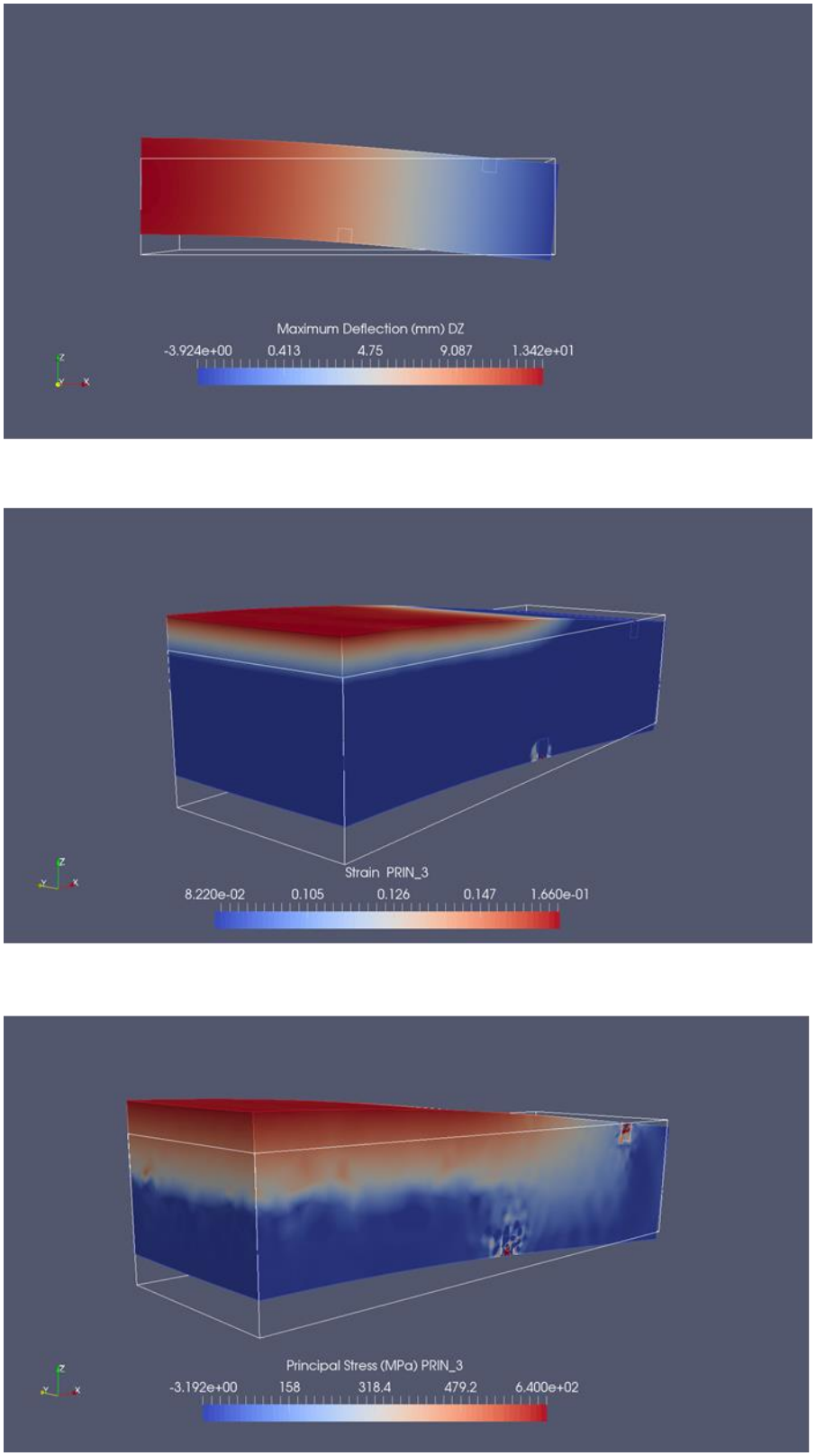
FEM results for 1.5 mm displacement of push rods.



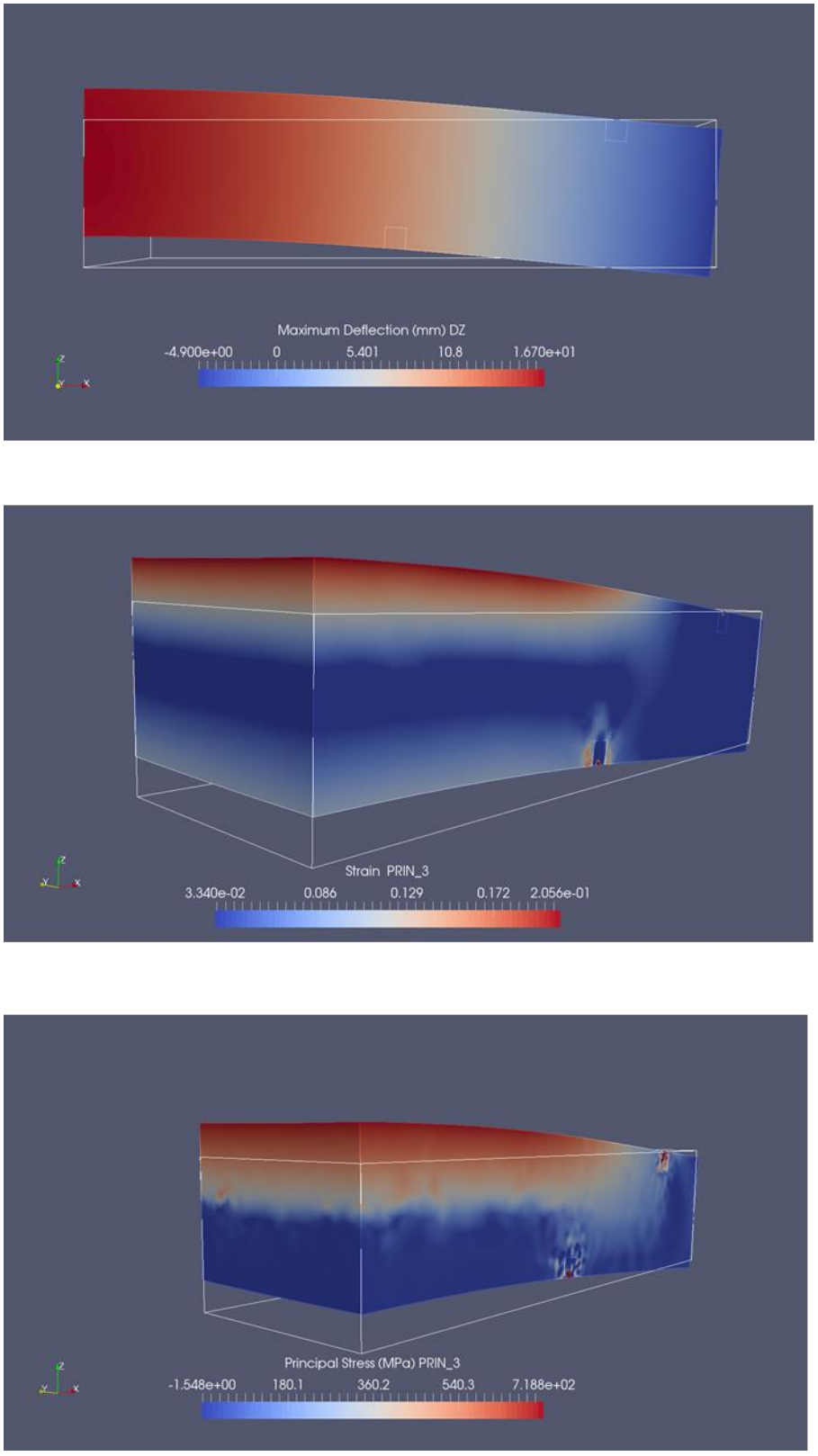




FEM results for 5 mm displacement of push rods.



FEM results for 8 mm displacement of push rods.



FEM results for 10 mm displacement of push rods.

Appendix C

C.1: Python script to convert .inp (abaqus format) to .mesh

```
#!/usr/bin/python
# -*- coding: utf-8 -*-

import readline
import rlcompleter
readline.parse_and_bind('tab: complete')


filename = "mesh"

inpFilePath = "./mesh/" + filename + ".inp"

#---------------------------------------------------------------------------
----
F_in = open(inpFilePath, "r")
L1 = F_in.readlines()
F_in.close()


idxgroup = []
for idx, line in enumerate(L1) :
    if "*Node" in line :
        idxnode = idx
    if "*ELEMENT" in line :
        idxelem = idx
    if "*ELSET" in line :
        idxgroup.append(idx)

#---------------------------------------------------------------------------
----
# creating a dictionary
# in key: the name of the group
# in value: the list of elements of the group
D_Group = {}
for Idx, groupIdx in enumerate(idxgroup[:-1]) :
    groupName = L1[groupIdx].strip().split("=Feature")[1]
    L_lines = L1[idxgroup[Idx] + 1:idxgroup[Idx+1]]
    L_lines = [t.strip() for t in L_lines]
    L_ElemS = ", ".join(L_lines)
    L_Elem = L_ElemS.split(', ')
    D_Group[groupName] = L_Elem

groupIdx = idxgroup[-1] + 1
groupName = L1[groupIdx -1].strip().split("=Feature")[1]
L_lines = L1[groupIdx:]
L_lines = [t.strip() for t in L_lines]
L_ElemS = ", ".join(L_lines)
L_Elem = L_ElemS.split(', ')
D_Group[groupName] = L_Elem

#---------------------------------------------------------------------------
----
# building an inverted dictionary
# in key: the element number
# in value: the group number
```

```
D_ElemGrp = {}
for group in D_Group.keys() :
    L = D_Group[group]
    for elem in L :
        D_ElemGrp[elem] = group.replace('Grain', '')

#-------------------------------------------------------------------------
----
# We build the list of nodes that we translate in ".mesh" format
L_Node = [line for line in L1[idxnode + 1:idxelem]]
L_Node = ['\t'.join(line.strip().split(', ')[1:] + ['0']) + '\n' for line
in L_Node]
L_Node = [line.replace(',', '.') for line in L_Node]
L_Node = [" Vertices\n", "\t%s\n" %len(L_Node)] + L_Node

#-------------------------------------------------------------------------
----
# We build meshes (type TRI3)
L_Elem = [line for line in L1[idxelem + 1:idxgroup[0]]]
L_Elem2 = []
for Idx, line in enumerate(L_Elem) :
#    print 'Idx : %s' %Idx
    L_Elem2.append('\t'.join(line.strip().split(', ')[1:] +
[D_ElemGrp[str(Idx)],]) + '\n')

L_Elem2 = [" Triangles\n", "\t%s\n" %len(L_Elem2)] + L_Elem2 + ["End"]

entete = ["MeshVersionFormatted 2\n", "Dimension\n", "\t3\n"]


F_out = open ("./mesh/" + filename + ".mesh", "w")
F_out.writelines(entete)
F_out.writelines(L_Node)
F_out.writelines(L_Elem2)
F_out.close()
```

C.2: Python script to convert .mesh to .med format

```
#!/usr/bin/python
# -*- coding: utf-8 -*-

import readline
import rlcompleter
readline.parse_and_bind('tab: complete')

import MEDLoader as ML
#from MEDLoader import MEDLoader as ML
import MEDCoupling as MC

#MedInFilePath = "testpostyams10.med"
MedOutFilePath = "tet.med"
MeshInFilePath = "big.mesh"

F_in = open(MeshInFilePath, "r")
L1 = F_in.readlines()
F_in.close()

#--------------------------------------------------------------------------
----
#Nodes
for idx, line in enumerate(L1) :
    if "Vertices" in line :
        idxstart = idx + 2
        break

for idx, line in enumerate(L1[idxstart:]) :
    if  line == "\n" :
        idxend = idx + idxstart
        break

L_Nodes = L1[idxstart:idxend]
L_Nodes = [line.strip().split()[:-1] for line in L_Nodes]
L_nodesGlob = []
NbNodes = len(L_Nodes)
for node in L_Nodes :
    L_nodesGlob += node

coords = [float(val) for val in L_nodesGlob]

#--------------------------------------------------------------------------
----
#Meshes
for idx, line in enumerate(L1) :
    if "Tetrahedra" in line :
        idxstart = idx + 2
for idx, line in enumerate(L1[idxstart:]) :
    if  line == "\n" :
        idxend = idx + idxstart
        break

#    if "# Set of corners" in line :
#        idxend = idx - 1

L_Elem = L1[idxstart:idxend]
NbCells = len(L_Elem)
L_Elem = [line.strip().split()[:-1] for line in L_Elem]
#L_ElemGlob = []
```

```
for idx, elem in enumerate(L_Elem) :
    L_Elem[idx] = [int(val) - 1 for val in elem]

#-------------------------------------------------------------------------
----
# Creating mesh
mesh3D = MC.MEDCouplingUMesh.New("meshVol", 3)
mesh3D.allocateCells(NbCells)

for cell in L_Elem :
    mesh3D.insertNextCell(MC.NORM_TETRA4, 4, cell)

mesh3D.finishInsertingCells()

myCoords = MC.DataArrayDouble.New(coords, NbNodes, 3)
myCoords.setInfoOnComponents(["X [m]","Y [m]","Z [m]"])
mesh3D.setCoords(myCoords)

ML.WriteUMesh(MedOutFilePath,mesh3D,True)

#-------------------------------------------------------------------------
----
# Getting the groups
for idx, line in enumerate(L1) :
    if "Tetrahedra" in line :
        idxstart = idx + 2

for idx, line in enumerate(L1[idxstart:]) :
    if  line == "\n" :
        idxend = idx + idxstart
        break

#    if "# Set of corners" in line :
#        idxend = idx - 1

L_Elem = L1[idxstart:idxend]
D_group = {}
for Idx, line in enumerate(L_Elem) :
    D_group[Idx] = line.strip().split()[-1]

L_group = list(set(D_group.values()))
#L_group.sort()

D_group2 = {}
for group in L_group :
    D_group2["GR%s" %group] = []

for Cell in D_group.keys() :
    D_group2["GR%s" %D_group[Cell]].append(Cell)

MLMesh = ML.MEDFileMesh.New(MedOutFilePath)

L_arrGroup = []
for group in D_group2.keys() :
    DarrayGrain = MC.DataArrayInt(D_group2[group])
    DarrayGrain.setName(group)
    L_arrGroup.append(DarrayGrain)

MLMesh.setGroupsAtLevel(0, L_arrGroup)

MLMesh.write(MedOutFilePath, 0)
```

C.3: Python script to assign the correct orientation to the grains

```
#!/usr/bin/env python2
# -*- coding: utf-8 -*-

F_in = open("mesh/orientations_centroids.txt", "r")
L1 = F_in.readlines()
F_in.close()

# Orientation for grain  .31

L_Angles_Euler = []
for i,line in enumerate(L1[+2:]):

    angles = line.split()[+3:+6]
    angles = str(float(angles[0])*57.3) + "," + str(float(angles[1])*57.3)
+ "," + str(float(angles[2])*57.3)
    L_Angles_Euler.append(angles)

# 57.3 conversion rad/deg

L_ori = []
L_ori.append("orielem = AFFE_CARA_ELEM(INFO=1,\n")
L_ori.append("                         MASSIF=(")


for i in range(len(L_Angles_Euler)):
    L_ori.append("\n                                  _F(ANGL_EULER=(" +
L_Angles_Euler[i] + ",),\n")
    L_ori.append("
GROUP_MA='GR"+str(i+1)+"'),")

L_ori.append("),\n")
L_ori.append("                         MODELE=mo,\n")
L_ori.append("                         );")




F_out = open ("mesh/orientation.31", "w")
F_out.writelines(L_ori)
F_out.close()



# grains for phase .21

L_Phase = []
for i,line in enumerate(L1[+2:]):

    phase = line.split()[6]
    L_Phase.append(phase)

L_aus = []
L_fer = []

for i in range(len(L_Phase)):
    if L_Phase[i] == '1':
```

```
        L_aus.append(i)
    elif L_Phase[i] == '2':
        L_fer.append(i)
    else:
        print 'Ni phase 1 ni phase 2'

L_group_phase = []
L_group_phase.append("mail=DEFI_GROUP(reuse =mail,\n")
L_group_phase.append("                MAILLAGE=mail,\n")
L_group_phase.append("                CREA_GROUP_MA=(_F(NOM='vol',\n")
L_group_phase.append("                                  TOUT='OUI',\n")
L_group_phase.append("
TYPE_MAILLE='3D',\n")
L_group_phase.append("                                  ),\n")
L_group_phase.append("                                _F(NOM='fer',\n")
L_group_phase.append("                                  UNION=(")

L_group_phase.append("'GR" + str(L_fer[0]+1) + "'")

for i in range(len(L_fer)-1):
    L_group_phase.append(",'GR" + str(L_fer[i+1]+1) + "'")

L_group_phase.append("),\n")


L_group_phase.append("                                  ),\n")
L_group_phase.append("                                _F(NOM='aus',\n")
L_group_phase.append("                                  UNION=(")

L_group_phase.append("'GR" + str(L_aus[0]+1) + "'")

for i in range(len(L_aus)-1):
    L_group_phase.append(",'GR" + str(L_aus[i+1]+1) + "'")

L_group_phase.append("),\n")

L_group_phase.append("                                  ),\n")
L_group_phase.append("                              ),\n")
L_group_phase.append("                   );\n")


F_out = open ("mesh/phase.21", "w")
F_out.writelines(L_group_phase)
F_out.close()
```

C.4 : Calculating Misorientation based on Euler Angles

```
% FROM EULER ANGLES TO MISORIENTATION
%Calculation of rotation matrices from euler angles of 2 grains (g1 and g2)
for the determination of the misorientation matrix and Misorientation Angle
% STEP1: Converting Euler Angles from Degrees to Radiants
% Grain 1 (g1)
g1_phi_1 = deg2rad(165)
g1_phi = deg2rad(22)
g1_phi_2 = deg2rad(230)
% STEP2: Definition of rotations for g1 in matrix form (sample reference to
crystal reference frame). Rotation around z,x_new and z_new axis (Bunge
notation)
z_new_g1 = [cos(g1_phi_2) sin(g1_phi_2) 0; -sin(g1_phi_2) cos(g1_phi_2) 0;
0 0 1]
x_new_g1 = [1 0 0; 0 cos(g1_phi) sin(g1_phi); 0 -sin(g1_phi) cos(g1_phi)]
z_g1 = [cos(g1_phi_1) sin(g1_phi_1) 0; -sin(g1_phi_1) cos(g1_phi_1) 0; 0 0
1]
% STEP3: Definition of rotation matrix R for g1
r_g1 = z_new_g1 * x_new_g1 * z_g1

%Repeat for 2nd grain
% Grain 2 (g2)
g2_phi_1 = deg2rad(44)
g2_phi = deg2rad(35)
g2_phi_2 = deg2rad(270)

% Definition of rotations for g2 in matrix form (sample reference to
crystal reference frame). Rotation around z,x_new and z_new axis (Bunge
notation)
z_new_g2 = [cos(g2_phi_2) sin(g2_phi_2) 0; -sin(g2_phi_2) cos(g2_phi_2) 0;
0 0 1]
x_new_g2 = [1 0 0; 0 cos(g2_phi) sin(g2_phi); 0 -sin(g2_phi) cos(g2_phi)]
z_g2 = [cos(g2_phi_1) sin(g2_phi_1) 0; -sin(g2_phi_1) cos(g2_phi_1) 0; 0 0
1]
% Definition of rotation matrix R for g2
r_g2 = z_new_g2 * x_new_g2 * z_g2
% Calculation of the Misorientation matrix between the two grains (g1 and
g2)
% Misorientation Matrix M_delta_g of r_g1 and r_g2
M_delta_g = r_g1 * inv(r_g2)

% 24 symmetry operators for cubic systems
ops = [1 0 0; 0 1 0; 0 0 1];
ops(:,:,2) = [0 0 -1; 0 -1 0; -1 0 0];
ops(:,:,3) = [0 0 -1; 0 1 0; 1 0 0];
ops(:,:,4) = [-1 0 0; 0 1 0; 0 0 -1];
ops(:,:,5) = [0 0 1; 0 1 0; -1 0 0];
ops(:,:,6) = [1 0 0; 0 0 -1; 0 1 0];
ops(:,:,7) = [1 0 0; 0 -1 0; 0 0 -1];
ops(:,:,8) = [1 0 0; 0 0 1; 0 -1 0];
ops(:,:,9) = [0 -1 0; 1 0 0; 0 0 1];
ops(:,:,10) = [-1 0 0; 0 -1 0; 0 0 1];
ops(:,:,11) = [0 1 0; -1 0 0; 0 0 1];
ops(:,:,12) = [0 0 1; 1 0 0; 0 1 0];
ops(:,:,13) = [0 1 0; 0 0 1; 1 0 0];
ops(:,:,14) = [0 0 -1; -1 0 0; 0 1 0];
ops(:,:,15) = [0 -1 0; 0 0 1; -1 0 0];
ops(:,:,16) = [0 1 0; 0 0 -1; -1 0 0];
ops(:,:,17) = [0 0 -1; 1 0 0; 0 -1 0];
```

```
ops(:,:,18) = [0 0 1; -1 0 0; 0 -1 0];
ops(:,:,19) = [0 -1 0; 0 0 -1; 1 0 0];
ops(:,:,20) = [0 1 0; 1 0 0; 0 0 -1];
ops(:,:,21) = [-1 0 0; 0 0 1; 0 1 0];
ops(:,:,22) = [0 0 1; 0 -1 0; 1 0 0];
ops(:,:,23) = [0 -1 0; -1 0 0; 0 0 -1];
ops(:,:,24) = [-1 0 0; 0 0 -1; 0 -1 0];

% Determination of number of operators (e.g. 24 for cubic system)
number_of_elements = size(ops); %(3,3,24)
number_of_elements = number_of_elements(3); %24
% Application of 24 symmetry operators to M_delta_g
ops_result = zeros(3,3,number_of_elements);
for i = 1:number_of_elements
s_i = ops(:,:,i);
ops_result(:,:, i) = s_i * M_delta_g;
end

% Calculate misorientation angle gamma for all 24 misorientation matrices
gamma_result = zeros(number_of_elements);
for i = 1:number_of_elements
matrix = ops_result(:,:,i);
gamma = acos((trace(matrix)-1) / 2);
gamma_result(i) = gamma;
end
% Find minimum Gamma --> Misorientation angle
minimum = min(gamma_result)
% Transform gamma from radiant to degree
gamma_degrees = radtodeg(minimum)
```

10 REFERENCES

[1] A. Rising, World Nuclear Performance Report, World Nucl. Assoc. (2019) 1–36. https://www.world-nuclear.org/getmedia/d77ef8a1-b720-44aa-9b87-abf09f474b43/performance-report-2019.pdf.aspx.

[2] F. Cattant, D. Crusset, D. Féron, Corrosion issues in nuclear industry today, Mater. Today. 11 (2008) 32–37. https://doi.org/10.1016/S1369-7021(08)70205-0.

[3] T. Allen, J. Busby, M. Meyer, D. Petti, Materials challenges for nuclear systems, Mater. Today. 13 (2010) 14–23. https://doi.org/10.1016/S1369-7021(10)70220-0.

[4] P.M. Scott, 2000 F. N. Speller award lecture: Stress corrosion cracking in pressurized water reactors - Interpretation, modeling, and remedies, Corrosion. 56 (2000) 771–782. https://doi.org/10.5006/1.3280580.

[5] R.J.-C.-N. ASSOCIATION, U. 1993, Corrosion Experience in US Light Water Reactors-A NACE 50th Anniversary Perspective, NACE. (n.d.).

[6] Basic Principles Objectives IAEA Nuclear Energy Series Stress Corrosion Cracking in Light Water Reactors: Good Practices and Lessons Learned, in: n.d. http://www.iaea.org/Publications/index.html (accessed December 21, 2019).

[7] J. Pack, Z. Fu, F. Aydogan, Modeling primary and secondary coolant of a nuclear power plant system with a unique framework (MCUF), Prog. Nucl. Energy. 83 (2015) 197–211. https://doi.org/10.1016/j.pnucene.2015.03.008.

[8] D. Feron, R. Staehle, Stress Corrosion Cracking of Nickel Based Alloys in Water-cooled Nuclear Reactors: The Coriou Effect, 2016. https://books.google.co.uk/books?hl=en&lr=&id=5f6zBwAAQBAJ&oi=fnd&pg=PP1

&dq=Stress+Corrosion+Cracking+of+Nickel+Based+Alloys+in+Water-Cooled+Nuclear+Reactors:+The+Coriou+Effect&ots=fY0ne0-iyf&sig=djKAEic1itQEJa1jWl7EFJSZB4Q (accessed March 13, 2020).

[9] No Title, (n.d.). https://www.nrc.gov/reading-rm/basic-ref/students/animated-pwr.html.

[10] R.W. Staehle, J.A. Gorman, Quantitative assessment of submodes of stress corrosion cracking on the secondary side of steam generator tubing in pressurized water reactors: Part 1, Corrosion. 59 (2003) 931–994. https://doi.org/10.5006/1.3277522.

[11] P.M. Scott, An overview of materials degradation by stress corrosion in PWRs, 2007.

[12] S.J. Patel, A century of discoveries, inventors, and new nickel alloys, J. Miner. Met. Mater. Soc. 58 (2006) 18–20. https://doi.org/10.1007/s11837-006-0076-y.

[13] J.R. Davis, Nickel, Cobalt, and Their Alloys, 2000. https://doi.org/10.1361/ncta2000p013.

[14] R.W. Staehle, Quantitative Micro-Nano (QMN) approach to SCC mechanism and prediction-starting a third meeting, in: 15th Int. Conf. Environ. Degrad. Mater. Nucl. Power Syst. React. 2011, 2011: pp. 1452–1542. https://doi.org/10.1007/978-3-319-48760-1_95.

[15] J.J. Kai, C.H. Tsai, G.P. Yu, The IGSCC, sensitization, and microstructure study of Alloys 600 and 690 *, 1993.

[16] A. Aguilar, J.L. Albarran, H.F. Lopez, L. Martinez, Microstructural response on the cracking resistance of alloy 600, Mater. Lett. 61 (2007) 274–277. https://doi.org/10.1016/j.matlet.2006.04.086.

[17] G.P. Airey, Microstructural aspects of the thermal treatment of Inconel alloy 600,

Metallography. 13 (1980) 21–41. https://doi.org/10.1016/0026-0800(80)90020-8.

[18] J.M. Park, W.S. Ryu, Y.H. Kang, DSC study on carbide precipitation reaction in Inconel 600, J. Nucl. Mater. 209 (1994) 221–225. https://doi.org/10.1016/0022-3115(94)90255-0.

[19] S.M. Bruemmer, G.S. Was, Microstructural and microchemical mechanisms controlling intergranular stress corrosion cracking in light-water-reactor systems, J. Nucl. Mater. 216 (1994) 348–363. https://doi.org/10.1016/0022-3115(94)90020-5.

[20] P.H. Hoang, A. Gangadharan, S.C. Ramalingam, Primary water stress corrosion cracking inspection ranking scheme for alloy 600 components, Nucl. Eng. Des. 181 (1998) 209–219. https://doi.org/10.1016/s0029-5493(97)00346-4.

[21] H. Coriou, L. Grall, P. Olivier, H. Willermoz, Influence of Carbon and Nickel Content on Stress-Corrosion Cracking of Austenitic Stainless Alloys in Pure or Chloride Containing Water at 350^{o}C., (1969).

[22] H.R. Copson, S.W. Dean, Effect of Contaminants on Resistance To Stress Corrosion Cracking Of Ni-Cr Alloy 600 in Pressurized Water, Corrosion. 21 (1965) 1–8. https://doi.org/10.5006/0010-9312-21.1.1.

[23] R.W. Staehle, J.A. Gorman, Quantitative assessment of submodes of stress corrosion cracking on the secondary side of steam generator tubing in pressurized water reactors: Part 2, Corrosion. 60 (2004) 5–63. https://doi.org/10.5006/1.3299232.

[24] R.W. Staehle, Introduction to initiation., in: Work. Detect. Avoid. Mech. Model. Predict. SCC Initiat. Watercooled Nucl. React. Plants, 2008.

[25] S. Le Hong, Influence of Surface Condition on Primary Water Stress Corrosion Cracking Initiation of Alloy 600, CORROSION. 57 (2001) 323–333.

https://doi.org/10.5006/1.3290356.

[26] H. Coriou, L. Grall, P. Olivier, … H.W. conference fundamental aspect of S., undefined 1969, Hydrogen transport of deuterium trapping at dislocation and grain boundaries in palladium, (n.d.).

[27] H. Coriou, L. Grall, C. Mahieu, M. Pelas, Sensitivity to Stress Corrosion and Intergranular Attack of High-Nickel Austenitic Alloys, Corrosion. 22 (1966) 280–290. https://doi.org/10.5006/0010-9312-22.10.280.

[28] J. Gorman, V. Moroney, G. White, Alloy 800 steam generator tube performance, (2009). https://inis.iaea.org/search/search.aspx?orig_q=RN:46041019 (accessed March 11, 2020).

[29] K. Arioka, T. Yamada, T. Terachi, R.W. Staehle, Intergranular stress corrosion cracking behavior of austenitic stainless steels in hydrogenated high-temperature water, Corrosion. 62 (2006) 74–83. https://doi.org/10.5006/1.3278254.

[30] K. Arioka, T. Miyamoto, T. Yamada, T. Terachi, Formation of cavities prior to crack initiation and growth on cold-worked carbon steel in high-Temperature Water, in: Corrosion, 2010: pp. 0150081–01500814. https://doi.org/10.5006/1.3318289.

[31] R.W. Staehle, J.A. Gorman, Quantitative assessment of submodes of stress corrosion cracking on the secondary side of steam generator tubing in pressurized water reactors: Part 3, Corrosion. 60 (2004) 115–180. https://doi.org/10.5006/1.3287716.

[32] T. Yonezawa, N. Sasaguri, K. Onimura, Effects of metallurgical factors on stress corrosion cracking of Ni-base alloys in high temperature water, (1988).

[33] M. Meisnar, A. Vilalta-Clemente, M. Moody, K. Arioka, S. Lozano-Perez, A mechanistic study of the temperature dependence of the stress corrosion crack growth

rate in SUS316 stainless steels exposed to PWR primary water, Acta Mater. 114 (2016) 15–24. https://doi.org/10.1016/j.actamat.2016.05.010.

[34] M. Meisnar, A. Vilalta-Clemente, A. Gholinia, M. Moody, A.J. Wilkinson, N. Huin, S. Lozano-Perez, Using transmission Kikuchi diffraction to study intergranular stress corrosion cracking in type 316 stainless steels, Micron. 75 (2015) 1–10. https://doi.org/10.1016/j.micron.2015.04.011.

[35] Z. Shen, M. Meisnar, K. Arioka, S. Lozano-Perez, Mechanistic understanding of the temperature dependence of crack growth rate in alloy 600 and 316 stainless steel through high-resolution characterization, Acta Mater. 165 (2019) 73–86. https://doi.org/10.1016/j.actamat.2018.11.039.

[36] H. Nagano, H. Kajimura, Clarification of stress corrosion cracking mechanism on nickel base Alloys in Steam Generators for their Long Lifetime Assurance, in: Seventh Int. Symp. Environ. Degrad. Mater. Nucl. Power Syst. React., 1995. https://inis.iaea.org/search/search.aspx?orig_q=RN:27043608 (accessed March 12, 2020).

[37] F. Delabrouille, B. Viguier, L. Legras, E. Andrieu, Materials at High Temperatures Effect of the chromium content on the corrosion of nickel based alloys in primary water of pressurised nuclear reactors Effect of the chromium content on the corrosion of nickel based alloys in primary water of pressurised nuclear reactors, (n.d.). https://doi.org/10.1179/mht.2005.033.

[38] K. Arioka, T. Yamada, T. Terachi, G. Chiba, Influence of carbide precipitation and rolling direction on intergranular stress corrosion cracking of austenitic stainless steels in hydrogenated high-temperature water, Corrosion. 62 (2006) 568–575. https://doi.org/10.5006/1.3280670.

[39] K. Arioka, T. Yamada, T. Miyamoto, T. Terachi, Dependence of stress corrosion cracking of Alloy 690 on temperature, cold work, and carbide precipitation - Role of diffusion of vacancies at crack tips, Corrosion. 67 (2011). https://doi.org/10.5006/1.3563640.

[40] T. Terachi, T. Yamada, T. Miyamoto, K. Arioka, K. Fukuya, Corrosion Behavior of Stainless Steels in Simulated PWR Primary Water-Effect of Chromium Content in Alloys and Dissolved Hydrogen, J. Nucl. Sci. Technol. 45 (2012) 975–984. https://doi.org/10.1080/18811248.2008.9711883.

[41] G. Was, T. Angeliu, J.S.- Workshop, Deformation and intergranular cracking behavior of Ni-Cr-Fe alloys at high temperature, in: Proc. an EPRI Airlie 1993, , 1993.

[42] F. Vaillant, J.D. Mithieux, O. De Bouvier, D. Vançon, G. Zacharie, Y. Brechet, F. Louchet, Influence of chromium content and microstructure on creep and PWSCC resistance of nickel base alloys, in: Proc. Ninth Int. Symp. Environ. Degrad. Mater. Nucl. Power Syst. - Water React. -, 1999: pp. 251–260. https://doi.org/10.1002/9781118787618.ch26.

[43] T.M. Angeliu, The Effect of Chromium, Carbon, and Yttrium on the Oxidation of Nickel-Base Alloys in High Temperature Water, J. Electrochem. Soc. 140 (1993) 1877. https://doi.org/10.1149/1.2220732.

[44] S. Lozano-Perez, T. Yamada, T. Terachi, M. Schröder, C.A. English, G.D.W. Smith, C.R.M. Grovenor, B.L. Eyre, Multi-scale characterization of stress corrosion cracking of cold-worked stainless steels and the influence of Cr content, Acta Mater. 57 (2009) 5361–5381. https://doi.org/10.1016/j.actamat.2009.07.040.

[45] R. Bandy, D. van Rooyen, Quantitative examination of stress corrosion cracking of alloy 600 in high temperature water, Nucl. Eng. Des. 86 (1985) 49–56.

https://doi.org/10.1016/0029-5493(85)90208-0.

[46] T. Couvant, L. Legras, C. Pokor, F. Vaillant, Y. Brechet, J.M. Boursier, P. Moulart, Investigations on the mechanisms of PWSCC of strain hardened austenitic stainless steels, in: 13th Int. Conf. Environ. Degrad. Mater. Nucl. Power Syst. 2007, Canadian Nuclear Society, 2007: pp. 19–23.

[47] J.M. Boursier, D. Desjardins, F. Vaillant, The influence of the strain-rate on the stress corrosion cracking of alloy 600 in high temperature primary water, Corros. Sci. 37 (1995) 493–508. https://doi.org/10.1016/0010-938X(94)00158-3.

[48] G. Webb, M. Burke, Stress corrosion cracking behavior of Alloy 600 in high temperature water, in: 7th Int. Symp. Environ. Degrad. Mater. Nucl. Power Syst. Water React., 1995.

[49] N. Totsuka, T. Terachi, T. Yamada, M. Ozawa, K. Nakata, Effect Of Metallurgical Factors On Pwscc Growth Rate Of Ni-Based Alloys, Corrosion. (2008).

[50] J. Giovanna Caballero Hinostroza, C. Duhamel, J. Crepin, T. Couvant, Intergranular oxidation of alloy 600 exposed to simulated PWR primary water, in: 17th Int. Conf. Environ. Degrad. Mater. Nucl. Power Syst. React. , n.d.

[51] B. Ter-Ovanessian, J. Deleume, J.M. Cloué, E. Andrieu, Quantitative assessment of intergranular damage due to PWR primary water exposure in structural Ni-based alloys, Corros. Sci. 67 (2013) 11–19. https://doi.org/10.1016/j.corsci.2012.09.048.

[52] C. Guerre, P. Laghoutaris, J. Chêne, L. Marchetti, R. Molins, C. Duhamel, M. Sennour, Stress Corrosion Cracking of Alloy 600 in PWR Primary Water: Influence of Chromium, Hydrogen and Oxygen Diffusion, in: 15th Int. Conf. Environ. Degrad. Mater. Nucl. Power Syst. React., John Wiley & Sons, Inc., Hoboken, New Jersey,

Canada, 2012: pp. 1477–1488. https://doi.org/10.1002/9781118456835.ch154.

[53] H. Dugdale, D.E.J. Armstrong, E. Tarleton, S.G. Roberts, S. Lozano-Perez, How oxidized grain boundaries fail, Acta Mater. 61 (2013) 4707–4713. https://doi.org/10.1016/j.actamat.2013.05.012.

[54] S. Lozano-Perez, J.M. Titchmarsh, TEM investigations of intergranular stress corrosion cracking in austenitic alloys in PWR environmental conditions, Mater. High Temp. 20 (2003) 573–579. https://doi.org/10.1179/mht.2003.066.

[55] T. Moss, G.S. Was, Accelerated Stress Corrosion Crack Initiation of Alloys 600 and 690 in Hydrogenated Supercritical Water, Metall. Mater. Trans. A Phys. Metall. Mater. Sci. 48 (2017) 1613–1628. https://doi.org/10.1007/s11661-016-3898-4.

[56] K. Norring, J. Engström, P. Norberg, Intergranular stress corrosion cracking in steam generator tubing. Testing of Alloy 690 and Alloy 600 tubes, in: Third Int. Conf. Environ. Degrad. Mater. Nucl. Power Syst. – Water React., n.d.: pp. 587–593.

[57] F. Hernández, Influence of product type on stress corrosion cracking of alloy 600, Corrosion. 55 (1999) 248–258. https://doi.org/10.5006/1.3283985.

[58] Y. Yi, G.S. Was, IGSCC behavior during constant load tests of alloy 600 in primary water, in: Tenth Int. Conf. Environ. Degrad. Mater. Nucl. Power Syst. – Water React., 2001.

[59] S.M. Bruemmer, L.A. Charlot, C.H. Henager, Microstructure and microdeformation effects on IGSCC of Alloy 600 steam generator tubing, Corrosion. 44 (1988) 782–788. https://doi.org/10.5006/1.3584948.

[60] G. Bertali, F. Scenini, M.G. Burke, The effect of residual stress on the Preferential Intergranular Oxidation of Alloy 600, Corros. Sci. 111 (2016) 494–507.

https://doi.org/10.1016/j.corsci.2016.05.022.

[61] G. Bertali, F. Scenini, M.G. Burke, P. Gilles, Solution-annealed and thermally-treated Alloy 600 preferential intergranular oxidation: a comparison, in: 17th Int. Conf. Environ. Degrad. Mater. Nucl. Power Syst. – Water React., 2015. https://www.researchgate.net/publication/303882145 (accessed March 13, 2020).

[62] P.M. Scott, A review of environment-sensitive fracture in water reactor materials, Corros. Sci. 25 (1985) 583–606. https://doi.org/10.1016/0010-938X(85)90001-0.

[63] J.R. Scully, Intergranular Corrosion, in: Encycl. Electrochem., Wiley-VCH Verlag GmbH & Co. KGaA, 2007. https://doi.org/10.1002/9783527610426.bard040403.

[64] P.L.. Andresen, M.M.. Morra, J.. Hickling, A.. Ahluwalia, J. Wilson, PWSCC of Alloys 690, 52 and 152, in: 13th Int. Conf. Environ. Degrad. Mater. Nucl. Power Syst. , Canadian Nuclear Society, 2007.

[65] T. Watanabe, S. Kitamura, Karashima S, Grain boundary hardening and segregation in alpha Iron-Tin alloy, Acta Metall. (1980). https://www.sciencedirect.com/science/article/pii/0001616080901352 (accessed March 13, 2020).

[66] T. Watanabe, Grain boundary design and control for high temperature materials, Mater. Sci. Eng. A. 166 (1993) 11–28. https://doi.org/10.1016/0921-5093(93)90306-Y.

[67] T. Watanabe, S.I. Kimura, S. Karashima, S.I. Kimura, S. Karashima, The effect of a grain boundary structural transformation on sliding in <1010>-tilt zinc bicrystals, Philos. Mag. A Phys. Condens. Matter, Struct. Defects Mech. Prop. 49 (1984) 845–864. https://doi.org/10.1080/01418618408236566.

[68] H. Grimmer, W. Bollmann, D.H. Warrington, Coincidence-site lattices and complete

pattern-shift in cubic crystals, Acta Crystallogr. Sect. A. 30 (1974) 197–207. https://doi.org/10.1107/S056773947400043X.

[69] M.L. Kronberg, F.H. Wilson, Secondary Recrystallization in Copper, JOM. 1 (1949) 501–514. https://doi.org/10.1007/bf03398387.

[70] B. Alexandreanu, B. Capell, G.S. Was, Combined effect of special grain boundaries and grain boundary carbides on IGSCC of Ni-16Cr-9Fe-xC alloys, Mater. Sci. Eng. A. 300 (2001) 94–104. https://doi.org/10.1016/S0921-5093(00)01705-6.

[71] B. Alexandreanu, B.H. Sencer, V. Thaveeprungsriporn, G.S. Was, The effect of grain boundary character distribution on the high temperature deformation behavior of Ni-16Cr-9Fe alloys, Acta Mater. 51 (2003) 3831–3848. https://doi.org/10.1016/S1359-6454(03)00207-6.

[72] B. Alexandreanu, G.S. Was, The role of stress in the efficacy of coincident site lattice boundaries in improving creep and stress corrosion cracking, Scr. Mater. 54 (2006) 1047–1052. https://doi.org/10.1016/j.scriptamat.2005.11.051.

[73] V.Y. Gertsman, S.M. Bruemmer, Study of grain boundary character along intergranular stress corrosion crack paths in austenitic alloys, Acta Mater. 49 (2001) 1589–1598. https://doi.org/10.1016/S1359-6454(01)00064-7.

[74] E.M. Lehockey, G. Palumbo, P. Lin, A.M. Brennenstuhl, On the relationship between grain boundary character distribution and intergranular corrosion, Scr. Mater. 36 (1997) 1211–1218. https://doi.org/10.1016/S1359-6462(97)00018-3.

[75] E.M. Lehockey, G. Palumbo, P. Lin, Grain boundary structure effects on cold work embrittlement of microalloyed steels, Scr. Mater. 39 (1998) 353–358. https://doi.org/10.1016/S1359-6462(98)00172-9.

[76] H. Kokawa, M. Shimada, Y.S. Sato, Grain-boundary structure and precipitation in sensitized austenitic stainless steel, JOM. 52 (2000) 34–37. https://doi.org/10.1007/s11837-000-0159-0.

[77] M. Michiuchi, H. Kokawa, Z. Wang, Y. Sato, K Sakai, Twin-induced grain boundary engineering for 316 austenitic stainless steel, Acta Mater. (2006). https://www.sciencedirect.com/science/article/pii/S1359645406004769 (accessed March 13, 2020).

[78] H. Kokawa, M. Shimada, M. Michiuchi, Z.J. Wang, Y.S. Sato, Arrest of weld-decay in 304 austenitic stainless steel by twin-induced grain boundary engineering, Acta Mater. 55 (2007) 5401–5407. https://doi.org/10.1016/j.actamat.2007.06.005.

[79] P. Lin, G. Palumbo, K.T. Aust, Experimental assessment of the contribution of annealing twins to CSL distributions in FCC materials, Scr. Mater. 36 (1997) 1145–1149. https://doi.org/10.1016/S1359-6462(97)00010-9.

[80] V. Thaveeprungsriporn, G.S. Was, The role of coincidence-site-lattice boundaries in creep of Ni-16Cr-9Fe at 360 °C, Metall. Mater. Trans. A Phys. Metall. Mater. Sci. 28 (1997) 2101–2112. https://doi.org/10.1007/s11661-997-0167-6.

[81] V. Thaveeprungsriporn, G.S. Was, Grain boundary properties of Ni-16Cr-9Fe at 360 °C, Scr. Mater. 35 (1996) 1–8. https://doi.org/10.1016/1359-6462(96)00094-2.

[82] G.S. Was, V. Thaveeprungsriporn, D.C. Crawford, Grain boundary misorientation effects on creep and cracking in Ni-based alloys, JOM. 50 (1998) 44–49. https://doi.org/10.1007/s11837-998-0249-y.

[83] A. Stratulat, D.E.J. Armstrong, S.G. Roberts, Micro-mechanical measurement of fracture behaviour of individual grain boundaries in Ni alloy 600 exposed to a

pressurized water reactor environment, Corros. Sci. 104 (2016) 9–16. https://doi.org/10.1016/j.corsci.2015.10.019.

[84] H. Li, Twinning structure of M23C6 carbide precipitated at twin-related grain boundaries in Alloy 600, Http://Dx.Doi.Org/10.1080/14786435.2016.1143127. 96 (2016) 551–559. https://doi.org/10.1080/14786435.2016.1143127.

[85] Y.S. Lim, H.P. Kim, H.D. Cho, H.H. Lee, Microscopic examination of an Alloy 600/182 weld, Mater. Charact. 60 (2009) 1496–1506. https://doi.org/10.1016/J.MATCHAR.2009.08.005.

[86] J.A. Gorman, E.S. Hunt, Critical factors assessment for U-bend and transition cracking, in: Proc. 1985 Work. Primary-Side Stress Corros. Crack. o f PWR Steam Gener. Tubing, 1987.

[87] K. Norring, J. Engström, Initiation of SCC in nickel base alloys in primary PWR environment: Studies at Studsvik since mid 1980s, in: Energy Mater. Mater. Sci. Eng. Energy Syst., Taylor & Francis, 2008: pp. 113–118. https://doi.org/10.1179/174892408X394227.

[88] S. Lozano-Perez, K. Kruska, I. Iyengar, T. Terachi, T. Yamada, The role of cold work and applied stress on surface oxidation of 304 stainless steel, Corros. Sci. 56 (2012) 78–85. https://doi.org/10.1016/j.corsci.2011.11.021.

[89] F. Meng, Z. Lu, T. Shoji, J. Wang, E. hou Han, W. Ke, Stress corrosion cracking of uni-directionally cold worked 316NG stainless steel in simulated PWR primary water with various dissolved hydrogen concentrations, Corros. Sci. 53 (2011) 2558–2565. https://doi.org/10.1016/j.corsci.2011.04.013.

[90] R. Bandy, D. Van Rooyen, Stress corrosion cracking of Inconel Alloy 600 in high

temperature water—an update., Corrosion. 40 (1984) 425–430. https://doi.org/10.5006/1.3593950.

[91] R.B. Rebak, Z. Xia, Z. Szklarska-Smialowska, Effect of temperature and cold work on the crack growth rate of alloy 600 in primary water, Corrosion. 51 (1995) 689–697. https://doi.org/10.5006/1.3293632.

[92] N. Totsuka, Z. Szklarska-Smialowska, Effect of electrode potential on the hydrogen-induced IGSCC of alloy 600 in an aqueous solution at 350 C., Corrosion. 43 (1987) 734–738. https://doi.org/10.5006/1.3583860.

[93] J. Hou, Q.J. Peng, T. Shoji, J.Q. Wang, E.H. Han, W. Ke, Effects of cold working path on strain concentration, grain boundary microstructure and stress corrosion cracking in Alloy 600, Corros. Sci. 53 (2011) 2956–2962. https://doi.org/10.1016/j.corsci.2011.05.037.

[94] J. Hou, Q.J. Peng, Z.P. Lu, T. Shoji, J.Q. Wang, E.H. Han, W. Ke, Effects of cold working degrees on grain boundary characters and strain concentration at grain boundaries in Alloy 600, Corros. Sci. 53 (2011) 1137–1142. https://doi.org/10.1016/j.corsci.2010.11.022.

[95] T. Terachi, T. Yamada, G. Chiba, K. Arioka, Influence of Cold Work on IGSCC of 316 Stainless Steel in Hydrogenated High-Temperature Water, (2007).

[96] K. Arioka, T. Terachi, Cold Work and Temperature Dependence of Stress Corrosion Crack Growth of Austenitic Stainless Steels in Hydrogenated and Oxygenated High-Temperature Water SCC of austenitic stainless steel View project long term SCC initiation, low temperature lattice diffusion, stress enhanced lattice diffusion View project, Corrosion. 63 (2007) 1114–1123. https://doi.org/10.5006/1.3278329.

[97] J.N. Wanklyn, P.J. Jones, The aqueous corrosion of reactor metals, J. Nucl. Mater. 6 (1962) 291–329. https://doi.org/10.1016/0022-3115(62)90006-5.

[98] T. Couvant, P. Moulart, L. Legras, P. Bordes, J. Capelle, Y. Rouillon, T. Balon, PWSCC of austenitic stainless steels of heaters of pressurizers, in: 13th Int. Conf. Environ. Degrad. Mater. Nucl. Power Syst. React., 2007. https://ci.nii.ac.jp/naid/10030136625/ (accessed March 14, 2020).

[99] T. Shoji, Quantification of Yield Strength Effects on IGSCC of Austenitic Stainless Steels in High Temperature Water, Proc. 11th Int. Symp. Environ. Degrad. Mater. Nucl. Power Syst. React. 2003. (2003).

[100] T. Shoji, K. Sakaguchi, Z. Lu, S. Hirano, Y. Hasegawa, T. Kobayashi, K. Fujimoto, Y. Nomura, Effects of cold work and stress on oxidation and SCC behavior of stainless steels in PWR primary water environments, Rev. Générale Nucléaire. (2011) 50–62. https://doi.org/10.1051/RGN/20111050.

[101] K. Arioka, T. Yamada, T. Terachi, T. Miyamoto, Dependence of stress corrosion cracking for cold-worked stainless steel on temperature and potential, and role of diffusion of vacancies at crack tips, Corrosion. 64 (2008) 691–706. https://doi.org/10.5006/1.3278507.

[102] W. Bamford, J.H. Reactors, A review of Alloy 600 cracking in operating nuclear plants: historical experience and future trends, in: 11th Int. Symp. Environ. Degrad. o f Mater. Nucl. Power Syst. - Water React., 2003.

[103] S. Lozano-Perez, D. Saxey, T. Terachi, T. Yamada, L. Cervera-Gontard, 3-D characterization of SCC in cold worked stainless steels, 14th Int. Conf. Environ. Degrad. Mater. Nucl. Power Syst. Water React. 2009. 2 (2009).

[104] G.P. Airey, Optimization of metallurgical variables to improve the stress corrosion resistance of Inconel 600, 1980.

[105] E. Richey, D. Morton, R. Etien, SCC initiation testing of nickel-based alloys in high temperature water, in: Work. Detect. Avoid. Mech. Model. Predict. SCC Initiat. Water-Cooled Nucl. React. Plants, 2008. https://www.osti.gov/etdeweb/biblio/21109114 (accessed March 14, 2020).

[106] W.C. Moshier, C.M. Brown, Effect of cold work and processing orientation on the SCC behavior of Alloy 600, West Mifflin, PA, 1999. https://doi.org/10.2172/329549.

[107] W.C. Moshier, Effect of cold work and processing orientation on stress corrosion cracking behavior of alloy 600, Corrosion. 56 (2000) 307–320. https://doi.org/10.5006/1.3287659.

[108] P. Andresen, M. Morra, J. Hickling, A Ahluwalia, Effect of Deformation and Orientation on SCC of Alloy 690, NACE Int. Corros. 2009. (2009). https://www.onepetro.org/conference-paper/NACE-09412 (accessed March 14, 2020).

[109] T. Couvant, S.M. Bruemmer, Strain localization and stress corrosion cracking., in: Int. Conf. Plant Mater. Degrad. - Appl. to Stress Corros. Crack. Ni-Base Alloy., 2008: p. 49.

[110] T. Couvant, L. Legras, A. Herbelin, A. Musienko, G. Ilbevare, D. Delafosse, G. Cailletaud, J. Hickling, al De-, T. Couvant, L. Legras, A. Herbelin, A. Musienko, G. Ilevbare, D. Delafosse, G. Cailletaud, Stainless Steels Exposed to Primary Environment, Curran Associates, Inc. 57 Morehouse Lane Red Hook, NY 12571 USA, 2010. https://hal-emse.ccsd.cnrs.fr/emse-01063619 (accessed March 14, 2020).

[111] O.K. Chopra, W.K. Soppet, W.J. Shack, M.B. Mcneil, Effects of Alloy Chemistry,

Cold Work, and Water Chemistry on Corrosion Fatigue and Stress Corrosion Cracking of Nickel Alloys and Welds (NUREG/CR-6721), 2001.

[112] V. Raja, T. Shoji, Stress corrosion cracking: theory and practice, Woodhead Publishing, 2011. https://books.google.com/books?hl=en&lr=&id=C3xwAgAAQBAJ&oi=fnd&pg=PP1&dq=Stress+Corrosion+Cracking:+Theory+and+Practice.&ots=UkkklSHMcQ&sig=opln7bQrYuYvveJV4t6Wj8dFpag (accessed March 16, 2020).

[113] T. Couvant, D. Haboussa, S. Meunier, G. Nicolas, E. Julan, A simulation of IGSCC of austenitic stainless steels exposed to primary water, in: 17th Int. Conf. Environ. Degrad. Mater. Nucl. Power Syst. React., 2015.

[114] K. Norring, B. Rosborg, J. Engström, Influence of LiOH and H2 on primary side IGSCC of alloy 600 steam generator tubes, in: Int. Symp. II, SFEN, Paris, 1990. https://inis.iaea.org/search/search.aspx?orig_q=RN:22069554 (accessed March 14, 2020).

[115] R. Jacko, C. Wood, Lithium and boron effects on PWSCC of alloy 600, in: Contrib. Mater. Investig. to Resolut. Probl. Encount. PWR Plants., 1990. https://inis.iaea.org/search/search.aspx?orig_q=RN:22069555 (accessed March 14, 2020).

[116] Z. Szklarska-Smialowska, Z. Xia, R.R. Valbuena, Mechanism of crack growth in alloy 600 in high-temperature deaerated water, Corrosion. 50 (1994) 676–681. https://doi.org/10.5006/1.3293543.

[117] R.J. Jacko, R.E. Gold, Crack growth rates in primary side materials in elevated pH PWR water, in: Twelfth Int. Conf. Environ. Degrad. Mater. Nucl. Power Syst. – Water React., 2005. https://ci.nii.ac.jp/naid/10030136636/ (accessed March 14, 2020).

[118] T. Couvant, F. Vaillant, O. De Bouvier, Deforge, Effect of a high Li chemistry on Alloy 600 PWSCC susceptibility, in: 14th Int. Conf. Environ. Degrad., 2009.

[119] T. Cassagne, P. Combrade, M. Foucault, A. Gelpi, The influence of mechanical and environmental parameters on the crack growth behaviour of alloy 600 in PWR primary water, in: Twelfth Scand. Corros. Congr. Eurocorr'92, 1992: pp. 55–67.

[120] R. Cowan, G. Gordon, Intergranular SCC and grain boundary composition of Fe-Ni-Cr Alloys, in: SCC Hydrog. Embrittlement Iron Base Alloy. NACE, 1997.

[121] T.S. Bulischeck, D. Van Rooyen, Effect of environmental variables on the stress corrosion cracking of Inconel 600 steam generator tubing., in: Nucl. Technol., 1980: pp. 383–393. https://doi.org/10.13182/nt55-383.

[122] K. Arioka, T. Yamada, T. Miyamoto, M. Aoki, Intergranular stress corrosion cracking growth behavior of Ni-Cr-Fe alloys in pressurized water reactor primary water, Corrosion. 70 (2014) 695–707. https://doi.org/10.5006/1205.

[123] P.L. Andresen, Effects of temperature on crack growth rate in sensitized type 304 stainless steel and alloy 600, Corrosion. 49 (1993) 714–725. https://doi.org/10.5006/1.3316104.

[124] G. Economy, R.J. Jacko, F.W. Pement, IGSCC behavior of Alloy 600 steam generator tubing in water or steam tests above 360° C, Corrosion. 43 (1987) 727–734. https://doi.org/10.5006/1.3583859.

[125] P.L. Andresen, P.W. Emigh, M.M. Morra, Effects of PWR Primary Water Chemistry and Deaerated Water on SCC, Corros. . (2005).

[126] G. Economy, R. Jacko, J. Begley, Influence of hydrogen partial pressure on the IGSCC behavior of alloy 600 tubing in 360 C water or 400 C steam, Corrosion. (1987).

[127] C.H. Shen, P.G. Shewmon, A mechanism for hydrogen-induced intergranular stress corrosion cracking in alloy 600, Metall. Trans. A. 21 (1990) 1261–1271. https://doi.org/10.1007/BF02698254.

[128] Steven A. Attanasio, David S. Morton, Measurement of the Nickel/Nickel Oxide Transition in Ni-Cr-Fe Alloys and Updated Data and Correlations to Quantify the Effect of Aqueous Hydrogen on Primary Water SCC, Niskayuna, NY, 2003. https://doi.org/10.2172/821507.

[129] F. Scenini, The effect of surface preparation on the oxidation and SCC behaviour of alloy 600 and 690 in hydrogenated steam., University of Manchester, 2006.

[130] H.L. Logan, Film-Rupture Mechanism of Stress Corrosion, 1952.

[131] R.N. Parkins, Predictive approaches to stress corrosion cracking failure, Corros. Sci. 20 (1980) 147–166. https://doi.org/10.1016/0010-938X(80)90128-6.

[132] R.N. Parkins, Factors influencing stress corrosion crack growth kinetics., Corrosion. 43 (1987) 130–139. https://doi.org/10.5006/1.3583125.

[133] F.P. Ford, Quantitative Prediction of Environmentally Assisted Cracking, Corros. 52 (1996) 375–395. https://doi.org/10.5006/1.3292125.

[134] F.P. Ford, P.L. Andresen, Corrosion mechanisms in theory and practice, in: Corros. Nucl. Syst. Environ. Assist. Crack. Light Water React., New York, 2002: pp. 399–450.

[135] R.C. Newman, Developments in the slip-dissolution model of stress corrosion cracking, Corrosion. 50 (1994) 682–686. https://doi.org/10.5006/1.3293544.

[136] R.C. Newman, Dependence of stress corrosion crack velocity on strain rate for a binary noble-metal alloy, Corrosion. 63 (2007) 1048–1050. https://doi.org/10.5006/1.3278320.

[137] R.C. Newman, C. Healey, Stability, validity, and sensitivity to input parameters of the slip-dissolution model for stress-corrosion cracking, Corros. Sci. 49 (2007) 4040–4050. https://doi.org/10.1016/j.corsci.2007.05.001.

[138] M.M. Hall, An alternative to the Shoji crack tip strain rate equation, Corros. Sci. 50 (2008) 2902–2905. https://doi.org/10.1016/j.corsci.2008.07.011.

[139] M.M. Hall, Film rupture model for aqueous stress corrosion cracking under constant and variable stress intensity factor, Corros. Sci. 51 (2009) 225–233. https://doi.org/10.1016/j.corsci.2008.08.052.

[140] M.M. Hall, Critique of the Ford-Andresen film rupture model for aqueous stress corrosion cracking, Corros. Sci. 51 (2009) 1103–1106. https://doi.org/10.1016/j.corsci.2009.02.022.

[141] P.L. Andresen, Conceptual similarities and common predictive approaches for SCC in high temperature water systems, in: NACE Corros. Conf., 1996.

[142] R.B. Rebak, Z. Szklarska-Smialowska, The mechanism of stress corrosion cracking of alloy 600 in high temperature water, Corros. Sci. 38 (1996) 971–988. https://doi.org/10.1016/0010-938X(96)00183-7.

[143] Ford FP, Mechanisms of environmentally-assisted cracking, Int. J. Press. Vessel. Pip. (1989). https://inis.iaea.org/search/search.aspx?orig_q=RN:21059155 (accessed March 19, 2020).

[144] D.D. Macdonald, On the modeling of stress corrosion cracking in iron and nickel base alloys in high temperature aqueous environments, Corros. Sci. 38 (1996) 1003–1010. https://doi.org/10.1016/0010-938X(96)00048-0.

[145] P. Combrade, P. Scott, M. Foucault, Andrieu E, Oxidation of Ni base alloys in PWR

water: oxide layers and associated damage to the base metal, in: 2th Int. Conf. Environ. Degrad. Mater. Nucl. Power Syst. Water React., 2005.

[146] M. Vankeerberghen, G. Weyns, S. Gavrilov, B. Martens, J. Deconinck, Crack propagation rate modelling for 316SS exposed to PWR-relevant conditions, J. Nucl. Mater. 384 (2009) 274–285. https://doi.org/10.1016/j.jnucmat.2008.11.034.

[147] D.A. Vermilyea, A Theory for the Propagation of Stress Corrosion Cracks in Metals, J. Electrochem. Soc. 119 (1972) 405. https://doi.org/10.1149/1.2404217.

[148] E.M. Gutman, An inconsistency in “film rupture model” of stress corrosion cracking, Corros. Sci. 49 (2007) 2289–2302. https://doi.org/10.1016/j.corsci.2006.10.023.

[149] S. Lozano-Perez, J. Dohr, M. Meisnar, K. Kruska, SCC in PWRs: Learning from a Bottom-Up Approach, Metall. Mater. Trans. E. 1 (2014) 194–210. https://doi.org/10.1007/s40553-014-0020-y.

[150] J.R. Galvele, Surface mobility mechanism of stress-corrosion cracking, Corros. Sci. 35 (1993) 419–434. https://doi.org/10.1016/0010-938X(93)90175-G.

[151] J.R. Galvele, A stress corrosion cracking mechanism based on surface mobility, Corros. Sci. 27 (1987) 1–33. https://doi.org/10.1016/0010-938X(87)90117-X.

[152] K. Sieradzki, F.J. Friedersdorf, Notes on the surface mobility mechanism of stress-corrosion cracking, Corros. Sci. 36 (1994) 669–675. https://doi.org/10.1016/0010-938X(94)90072-8.

[153] E.M. Gutman, Notes on the discussion concerning the “surface mobility mechanism” of stress corrosion cracking, Corros. Sci. 45 (2003) 2105–2117. https://doi.org/10.1016/S0010-938X(03)00041-6.

[154] E.M. Gutman, An inconsistency in “surface mobility mechanism” of stress corrosion

cracking, Corrosion. 61 (2005) 197–200. https://doi.org/10.5006/1.3280629.

[155] J.R. Galvele, Comments on “notes on the surface mobility mechanism of stress-corrosion cracking”, by K. Sieradzki and F. J. Friedersdorf, Corros. Sci. 36 (1994) 901–910. https://doi.org/10.1016/0010-938X(94)90178-3.

[156] J.R. Galvele, Reply to “Notes on the discussion concerning ‘surface mobility mechanism’ of stress corrosion cracking”, by E.M. Gutman, Corros. Sci. 45 (2003) 2119–2128. https://doi.org/10.1016/s0010-938x(03)00042-8.

[157] W.H. Johnson, On some remarkable changes produced in iron and steel by the action of hydrogen and acids, Nature. 11 (1875) 393. https://doi.org/10.1038/011393a0.

[158] J.P. Hirth, Effects of hydrogen on the properties of iron and steel, Metall. Trans. A. 11 (1980) 861–890. https://doi.org/10.1007/BF02654700.

[159] R.A. Oriani, Hydrogen Embrittlement of Steels, Annu. Rev. Mater. Sci. 8 (1978) 327–357. https://doi.org/10.1146/annurev.ms.08.080178.001551.

[160] R.A. Oriani, The diffusion and trapping of hydrogen in steel, Acta Metall. 18 (1970) 147–157. https://doi.org/10.1016/0001-6160(70)90078-7.

[161] D.M. Symons, Hydrogen embrittlement of Ni-Cr-Fe alloys, Metall. Mater. Trans. A Phys. Metall. Mater. Sci. 28 A (1997) 655–663. https://doi.org/10.1007/s11661-997-0051-4.

[162] D.M. Symons, The effect of carbide precipitation on the hydrogen-enhanced fracture behavior of alloy 690, Metall. Mater. Trans. A Phys. Metall. Mater. Sci. 29 (1998) 1265–1277. https://doi.org/10.1007/s11661-998-0253-4.

[163] F.H. Hua, R.B. Rebak, The role of hydrogen and creep in intergranular stress corrosion cracking of Alloy 600 and Alloy 690 in PWR primary water environments - a review,

in: Environ. Crack. Mater., Elsevier Ltd, 2008: pp. 123–141. https://doi.org/10.1016/B978-008044635-6.50052-2.

[164] R.. Troiano, The Role of Hydrogen and Other Interstitials in the Mechanical Behavior of Metals, Trans. ASM. 52 (1960) 54–80.

[165] C.D. Beachem, A new model for hydrogen-assisted cracking (hydrogen "embrittlement"), Metall. Trans. 3 (1972) 441–455. https://doi.org/10.1007/BF02642048.

[166] S.P. Lynch, Environmentally assisted cracking: Overview of evidence for an adsorption-induced localised-slip process, Acta Metall. 36 (1988) 2639–2661. https://doi.org/10.1016/0001-6160(88)90113-7.

[167] S.P. Lynch, Mechanisms and kinetics of environmentally assisted cracking: Current status, issues, and suggestions for further work, in: Metall. Mater. Trans. A Phys. Metall. Mater. Sci., Springer, 2013: pp. 1209–1229. https://doi.org/10.1007/s11661-012-1359-2.

[168] H.W. Liu, A unified model of environment-assisted cracking, Acta Mater. 56 (2008) 4339–4348. https://doi.org/10.1016/j.actamat.2008.05.001.

[169] S.P. Lynch, Comments on "A unified model of environment-assisted cracking," Scr. Mater. 61 (2009) 331–334. https://doi.org/10.1016/j.scriptamat.2009.02.031.

[170] H.K. Birnbaum, P. Sofronis, Hydrogen-enhanced localized plasticity-a mechanism for hydrogen-related fracture, 1994.

[171] T.M. Angeliu, The intergranular cracking behavior of NI-CR-FE-low C alloys at 360Ċ, University of Michigan, 1993.

[172] R. Magnin, D. Delafosse, B. Baule, C. Bosch, Overview of corrosion - deformation

interactions in stress corrosion fatigue., (2002) 563–576.

[173] H. Birnbaum, I. Robertson, P. Sofronis, Mechanisms of hydrogen related fracture--a review, in: Second Int. Conf. Corros. Interact., 1996.

[174] G. Was, D. Paraventi, J. Hertzberg, Mechanisms of environmentally-enhanced deformation and intergranular cracking of Ni-16 Cr-9 Fe alloys, in: Second Int. Conf. Corros. Interact., 1996.

[175] D.J. Paraventi, T.M. Angeliu, G.S. Was, Effect of hydrogen on creep in high-purity Ni-16Cr-9Fe alloys at 360°C, Corrosion. 58 (2002) 675–686. https://doi.org/10.5006/1.3287697.

[176] A. Kimura, H.K. Birnbaum, Hydrogen induced grain boundary fracture in high purity nickel and its alloys-Enhanced hydrogen diffusion along grain boundaries, Acta Metall. 36 (1988) 757–766. https://doi.org/10.1016/0001-6160(88)90109-5.

[177] E. Sirois, H.K. Birnbaum, Effects of hydrogen and carbon on thermally activated deformation in nickel, Acta Metall. Mater. 40 (1992) 1377–1385. https://doi.org/10.1016/0956-7151(92)90438-K.

[178] C.F. Barth, E.A. Steigerwald, Evaluation of hydrogen embrittlement mechanisms, Metall. Trans. 1 (1970) 3451–3455. https://doi.org/10.1007/BF03037878.

[179] S.L. Lee, D.J. Unger, A decohesion model of hydrogen assisted cracking, Eng. Fract. Mech. 31 (1988) 647–660. https://doi.org/10.1016/0013-7944(88)90107-5.

[180] I. Scheider, M. Pfuff, W. Dietzel, Simulation of hydrogen assisted stress corrosion cracking using the cohesive model, Eng. Fract. Mech. 75 (2008) 4283–4291. https://doi.org/10.1016/j.engfracmech.2007.10.002.

[181] N.R. Raykar, S.K. Maiti, R.K. Singh Raman, Modelling of mode-I stable crack growth

under hydrogen assisted stress corrosion cracking, Eng. Fract. Mech. 78 (2011) 3153–3165. https://doi.org/10.1016/j.engfracmech.2011.07.013.

[182] T. Magnin, R. Chieragatti, R. Oltra, Mechanism of brittle fracture in a ductile 316 alloy during stress corrosion, Acta Metall. Mater. 38 (1990) 1313–1319. https://doi.org/10.1016/0956-7151(90)90203-S.

[183] D.A. Jones, A unified mechanism of stress corrosion and corrosion fatigue cracking, Metall. Trans. A. 16 (1985) 1133–1141. https://doi.org/10.1007/BF02811682.

[184] T. Magnin, A. Chambreuil, B. Bayle, The corrosion-enhanced plasticity model for stress corrosion cracking in ductile fcc alloys, Acta Mater. 44 (1996) 1457–1470. https://doi.org/10.1016/1359-6454(95)00301-0.

[185] D. Delafosse, T. Magnin, Hydrogen induced plasticity in stress corrosion cracking of engineering systems, Eng. Fract. Mech. 68 (2001) 693–729. https://doi.org/10.1016/S0013-7944(00)00121-1.

[186] F. Foct, O. De Bouvier, T. Magnin, Stress Corrosion Cracking Mechanisms of Alloy 600 Polycrystals and Single Crystals in Primary Water-Influence of Hydrogen, n.d.

[187] P.M. Scott, M. Le Calver, Some possible mechanisms of intergranular stress corrosion cracking of Alloy 600 in PWR primary water, in: Sixth Int. Symp. Environ. Degrad. Mater. Nucl. Power Syst. - Water React., 1993.

[188] B.M. Capell, G.S. Was, Selective internal oxidation as a mechanism for intergranular stress corrosion cracking of Ni-Cr-Fe alloys, Metall. Mater. Trans. A Phys. Metall. Mater. Sci. 38 (2007) 1244–1259. https://doi.org/10.1007/s11661-007-9124-7.

[189] P. Laghoutaris, J. Chêne, C. Guerre, O. Raquet, M. Sennour, R. Molins, F. Vaillant, P. Scott, Contribution to understanding of stress corrosion cracking of Alloy 600 in PWR

primary water, Energy Mater. Mater. Sci. Eng. Energy Syst. 3 (2008) 119–125. https://doi.org/10.1179/174892408X394236.

[190] S. Lozano-Perez, M. Meisnar, J. Dohr, K. Kruska, Reviewing the internal oxidation mechanism as a plausible explanation for SCC in PWR primary water., in: 16th Int. Conf. Environ. Degrad. Mater. Nucl. Power Syst. — Water React. , 2013. https://www.researchgate.net/publication/311512327 (accessed March 20, 2020).

[191] K. Fujii, T. Miura, H. Nishioka, K. Fukuya, Degradation of grain boundary strength by oxidation in alloy 600, in: 15th Int. Conf. Environ. Degrad. Mater. Nucl. Power Syst. React. 2011, Springer, Cham, 2011: pp. 1369–1380. https://doi.org/10.1007/978-3-319-48760-1_89.

[192] F. Scenini, R.C. Newman, R.A. Cottis, R.J. Jacko, Effect of surface preparation on intergranular stress corrosion cracking of Alloy 600 in hydrogenated steam, Corrosion. 64 (2008) 824–835. https://doi.org/10.5006/1.3279916.

[193] M.G. Burke, G. Bertali, E. Prestat, F. Scenini, S.J. Haigh, The application of in situ analytical transmission electron microscopy to the study of preferential intergranular oxidation in Alloy 600, Ultramicroscopy. 176 (2017) 46–51. https://doi.org/10.1016/j.ultramic.2016.11.014.

[194] G. Bertali, F. Scenini, M.G. Burke, Advanced microstructural characterization of the intergranular oxidation of Alloy 600, Corros. Sci. 100 (2015) 474–483. https://doi.org/10.1016/j.corsci.2015.08.010.

[195] P.M. Scott, 2000 F. N. Speller award lecture: Stress corrosion cracking in pressurized water reactors - Interpretation, modeling, and remedies, Corrosion. 56 (2000) 771–782. https://doi.org/10.5006/1.3280580.

[196] P. Combrade, P. Scott, F. Vaillant, Overview of the various possible mechanisms of PWSCC of alloy 600., in: Int. Conf. Plant Mater. Degrad. - Appl. to Stress Corros. Crack. Nibase Alloy., Moret–Sur–Loing, France, 2008: pp. 62–83.

[197] P. M. Scott, P. Combrade, On the mechanism of stress corrosion crack initiation and growth in alloy 600 exposed to PWR primary water, in: Elev. Int. Conf. Environ. Degrad. Mater. Nucl. Power Syst. – Water React., Stevenson, Washington, 2003. https://ci.nii.ac.jp/naid/10015414336/ (accessed April 1, 2020).

[198] R.A. Cottis, P. Combrade, F. Vaillant, P.M. Scott, Overview of SCC modelling for Ni-alloys., in: Int. Conf. Plant Mater. Degrad. - Appl. to Stress Corros. Crack. Ni-Base Alloy., Moret–Sur–Loing, France, 2008: p. 60.

[199] P.. Scott, Benhamou C, An overview of recent observations and interpretations of IGSCC in nickel base alloys in PWR primary water, in: Tenth Int. Conf. Environ. Degrad. Mater. Nucl. Power Syst. – Water React., TMS (The Minerals, Metals & Materials Society)., Lake Tahoe, Nevada, 2001.

[200] P.M. Scott., An overview of materials degradation by stress corrosionin PWRs., in: D. Féron, J.-M. Olive (Eds.), Corros. Issues Light Water React. Stress Corros. Crack., European Federation of Corrosion Publications, 2007: pp. 3–11.

[201] F. Vaillant, F. Carrette, R. Cottis, F. Léonard, J.Q. da Fonseca, J. Marrow, G. Ilevbare, Development of a predictive model for SCC initiation of alloy 600 in primary water, in: Work. Detect. Avoid. Mech. Model. Predict. SCC Initiat. Water-Cooled Nucl. React. Plants, Beaune,France, 2008.

[202] I. De Curières, M.-C. Meunier, Prediction of PWSCC initiation in steam generator alloy 600 tubes by the Index Model: comparison between model and experience., in: Work. Detect. Avoid. Mech. Model. Predict. SCC Initiat. Water-Cooled Nucl. React.

Plants, Beaune,France, 2008.

[203] T. Couvant, M. Wehbi, C. Duhamel, J. Crépin, R. Munier, ., Development of a “Local” Model to Predict SCC: Preliminary Calibration of Parameters for Nickel Alloys Exposed to Primary Water, in: 17th Int. Conf. Environ. Degrad. Mater. Nucl. Power Syst. – Water React., Ottawa, Ontario, Canada, 2015.

[204] M. Wehbi, C. Duhamel, T. Couvant, J. Crépin, Grain Boundary Oxidation of Nickel Base Welds 182/82 in Simulated PWR Primary Water, in: 17th Int. Conf. Environ. Degrad. Mater. Nucl. Power Syst. – Water React., Ottawa, Ontario, Canada, 2015.

[205] T. Couvant, J. Caballero, C. Duhamel, J. Crépin, T. Maeguchi, Calibration of the local igscc engineering model for alloy 600, in: 18th Int. Conf. Environ. Degrad. Mater. Nucl. Power Syst. – Water React., Springer International Publishing, 2017: pp. 1511–1533. https://doi.org/10.1007/978-3-030-04639-2_101.

[206] T. Couvant, Prediction of igscc as a finite element modeling post-analysis, in: 18th Int. Conf. Environ. Degrad. Mater. Nucl. Power Syst. – Water React., Springer International Publishing, 2017: pp. 1535–1550. https://doi.org/10.1007/978-3-030-04639-2_102.

[207] T. Couvant, Tests globaux du Code_Coriolis v2, Moret–Sur–Loing, France, 2017.

[208] J. Delmas, A. Assire, Salome-Meca : une plate-forme au service de la simulation mécanique, n.d. https://hal.archives-ouvertes.fr/hal-01413149 (accessed November 26, 2020).

[209] Code_Aster, (n.d.). www.code-aster.org.

[210] C. Durand, Free Software for Computational Mechanics: EDF’s choice, n.d. www.code-aster.org (accessed November 26, 2020).

[211] J. Goldstein, D. Newbury, J. Michael, N. Ritchie, Scanning electron microscopy and X-ray microanalysis, 4th ed., Springer, 2017. https://books.google.com/books?hl=en&lr=&id=D0I_DwAAQBAJ&oi=fnd&pg=PR5&dq=Scanning+Electron+Microscopy+and+X-ray+microanalysis&ots=35SJ9kFqsh&sig=rr9qB4lAQVur7-5dvqrFCgS6F9o (accessed April 2, 2020).

[212] I. Utke, S. Moshkalev, P. Russell, Nanofabrication using focused ion and electron beams: principles and applications, 2012. https://books.google.com/books?hl=en&lr=&id=GBVpAgAAQBAJ&oi=fnd&pg=PP1&dq=The+Histrical+Development+to+Electron+Beam+Induced+Deposition+and+Etching:+From+Carbonaceous+to+Functional+Materials&ots=f5G7NFsJ_L&sig=4CcFCygAQVhQWr3CARDf4R2ay_o (accessed April 2, 2020).

[213] ZEISS Crossbeam 350 and Crossbeam 550, (n.d.). https://www.zeiss.com/microscopy/int/products/fib-sem-instruments/crossbeam.html (accessed October 22, 2018).

[214] F.A. Stevie, L.A. Giannuzzi, B.I. Prenitzer, The focused ion beam instrument, in: Introd. to Focus. Ion Beams Instrumentation, Theory, Tech. Pract., Springer US, 2005: pp. 1–12. https://doi.org/10.1007/0-387-23313-X_1.

[215] L.A. Giannuzzi, F.A. Stevie, Introduction to focused ion beams: Instrumentation, theory, techniques and practice, Springer US, 2005. https://doi.org/10.1007/b101190.

[216] N. Ni, S. Lozano-Perez, J.M. Sykes, G.D.W. Smith, C.R.M. Grovenor, Focussed ion beam sectioning for the 3D characterisation of cracking in oxide scales formed on commercial ZIRLO^{TM} alloys during corrosion in high temperature pressurised water, Corros. Sci. 53 (2011) 4073–4083. https://doi.org/10.1016/j.corsci.2011.08.013.

[217] S. Lozano-Perez, A guide on FIB preparation of samples containing stress corrosion crack tips for TEM and atom-probe analysis, Micron. 39 (2008) 320–328. https://doi.org/10.1016/j.micron.2007.12.003.

[218] A. Cerezo, P.H. Clifton, M.J. Galtrey, C.J. Humphreys, T.F. Kelly, D.J. Larson, S. Lozano-Perez, E.A. Marquis, R.A. Oliver, G. Sha, K. Thompson, M. Zandbergen, R.L. Alvis, Atom probe tomography today, Mater. Today. 10 (2007) 36–42. https://doi.org/10.1016/S1369-7021(07)70306-1.

[219] J. Liu, High Resolution Structural Analysis of Irradiated Zirconium Alloys, University of Oxford, 2019.

[220] C. Carter, D. Williams, Transmission Electron Microscopy: A Textbook for Materials Science. Diffraction. II, 1996.

[221] R. by P.D. Brown, Transmission Electron Microscopy-A Textbook for Materials Science, by David B. Williams and C. Barry Carter, Microsc. Microanal. 5 (1999) 452–453. https://doi.org/10.1017/s1431927699990529.

[222] R. Keyse, Introduction to scanning transmission electron microscopy, 2018.

[223] A.J. Schwartz, M. Kumar, B.L. Adams, F.P. David, Electron Backscatter Diffraction in Materials Science Second Edition , 2nd ed., Springer, 2009. https://link.springer.com/content/pdf/10.1007/978-0-387-88136-2.pdf (accessed April 2, 2020).

[224] D. Dingley, Progressive steps in the development of electron backscatter diffraction and orientation imaging microscopy, in: J. Microsc., 2004: pp. 214–224. https://doi.org/10.1111/j.0022-2720.2004.01321.x.

[225] P.W. Trimby, Orientation mapping of nanostructured materials using transmission

Kikuchi diffraction in the scanning electron microscope, Ultramicroscopy. 120 (2012) 16–24. https://doi.org/10.1016/j.ultramic.2012.06.004.

[226] A.J. Wilkinson, T. Ben Britton, Strains, planes, and EBSD in materials science, Mater. Today. 15 (2012) 366–376. https://doi.org/10.1016/S1369-7021(12)70163-3.

[227] A.J. Wilkinson, G. Meaden, D.J. Dingley, High-resolution elastic strain measurement from electron backscatter diffraction patterns: New levels of sensitivity, Ultramicroscopy. 106 (2006) 307–313. https://doi.org/10.1016/j.ultramic.2005.10.001.

[228] S. Zaefferer, On the formation mechanisms, spatial resolution and intensity of backscatter Kikuchi patterns, Ultramicroscopy. 107 (2007) 254–266. https://doi.org/10.1016/j.ultramic.2006.08.007.

[229] R.R. Keller, R.H. Geiss, Transmission EBSD from 10 nm domains in a scanning electron microscope, J. Microsc. 245 (2012) 245–251. https://doi.org/10.1111/j.1365-2818.2011.03566.x.

[230] K.P. Rice, R.R. Keller, M.P. Stoykovich, Specimen-thickness effects on transmission Kikuchi patterns in the scanning electron microscope, J. Microsc. 254 (2014) 129–136. https://doi.org/10.1111/jmi.12124.

[231] J. Liu, S. Lozano-Perez, A.J. Wilkinson, C.R.M. Grovenor, On the depth resolution of transmission Kikuchi diffraction (TKD) analysis, Ultramicroscopy. 205 (2019) 5–12. https://doi.org/10.1016/j.ultramic.2019.06.003.

[232] N. Saravanan, P. Karamched, J. Liu, E. Burger, F. Scenini, S. Lozano-Perez, Using local GND density to study SCC initiation, 2020.

[233] S.M. Bruemmer, L. Thomas, Insights into Stress Corrosion Cracking Mechanisms from High-Resolution Measurements of Crack-tip Structures and Compositions, MRS

Proc. 1264 (2010) 1264-BB01-09. https://doi.org/10.1557/PROC-1264-BB01-09.

[234] C. Guerre, O. Raquet, E. Herms, S. Marie, M. Le Calvar, SCC crack growth rate of cold-worked austenitic stainless steels in PWR primary water conditions, Can. Nucl. Soc. - 13th Int. Conf. Environ. Degrad. Mater. Nucl. Power Syst. 2007. 1 (2007) 676–699.

[235] F. Vaillant, J.M. Boursier, Y. Rouillon, T. Couvant, C. Amzallag, O. Raquet, Stress corrosion cracking of cold worked austenitic stainless steels in laboratory primary PWR environment, in: Am. Soc. Mech. Eng. Press. Vessel. Pip. Div. PVP, 2004: pp. 51–63. https://doi.org/10.1115/PVP2004-3057.

[236] S. Lozano-Perez, L.C. Gontard, Understanding stress corrosion cracking with electron tomography, Microsc. Microanal. 14 (2008) 642–643. https://doi.org/10.1017/S1431927608084687.

[237] M. Meisnar, A. Vilalta-Clemente, A. Gholinia, M. Moody, A.J. Wilkinson, N. Huin, S. Lozano-Perez, Using transmission Kikuchi diffraction to study intergranular stress corrosion cracking in type 316 stainless steels, Micron. 75 (2015) 1–10. https://doi.org/10.1016/j.micron.2015.04.011.

[238] U. Ehrnstén, T. Saukkonen, W. Karlsen, H. Hänninen, Deformation localisation and EAC in inhomogenous microstructures of austenitic stainless steels, in: 14th Int. Conf. Environ. Degrad. Mater. Nucl. Power Syst. Water React. 2009th Int. Conf. Environ. Degrad. Mater. Nucl. Power Syst., 2009: pp. 910–919.

[239] W. Karlsen, G. Diego, B. Devrient, Localized deformation as a key precursor to initiation of intergranular stress corrosion cracking of austenitic stainless steels employed in nuclear power plants, J. Nucl. Mater. 406 (2010) 138–151. https://doi.org/10.1016/j.jnucmat.2010.01.029.

[240] K. Sasaki, M. Kamaya, T. Miura, K. Fukuya, Correlation between Microstructural Scale Plastic Strain and Misorientation, J. Japan Inst. Met. 74 (2010) 467–474. https://doi.org/10.2320/jinstmet.74.467.

[241] G.O. Ilevbare, T. Couvant, Effect of Localized Strain Deformation on SCC Initiation of Stainless Steels in Simulated PWR Primary Water, Corrosion. (2014).

[242] S. Zaefferer, J. Konrad, D. Raabe, 3D-orientation microscopy in a combined focused ion beam (FIB)-scanning electron microscope: A new dimension of microstructure characterisation, in: Microsc. Conf., 2005. https://pure.mpg.de/pubman/faces/ViewItemOverviewPage.jsp?itemId=item_2017544 (accessed April 2, 2020).

[243] S. Zaefferer, S.I. Wright, D. Raabe, Three-dimensional orientation microscopy in a focused ion beam-scanning electron microscope: A new dimension of microstructure characterization, Metall. Mater. Trans. A Phys. Metall. Mater. Sci. 39 (2008) 374–389. https://doi.org/10.1007/s11661-007-9418-9.

[244] S. Zaefferer, S.I. Wright, Three-dimensional orientation microscopy by serial sectioning and EBSD-based orientation mapping in a FIB-SEM, in: Electron Backscatter Diffr. Mater. Sci., Springer US, 2009: pp. 109–122. https://doi.org/10.1007/978-0-387-88136-2_8.

[245] T.L. Burnett, R. Kelley, B. Winiarski, L. Contreras, M. Daly, A. Gholinia, M.G. Burke, P.J. Withers, Large volume serial section tomography by Xe Plasma FIB dual beam microscopy, Ultramicroscopy. 161 (2016) 119–129. https://doi.org/10.1016/j.ultramic.2015.11.001.

[246] S. Zaefferer, P. Konijnenberg, Advanced analysis of 3D EBSD data obtained from FIB-EBSD tomography, Microsc. Microanal. 18 (2012) 520–521.

https://doi.org/10.1017/S143192761200445X.

[247] A. Khorashadizadeh, D. Raabe, S. Zaefferer, G.S. Rohrer, A.D. Rollett, M. Winning, Five-parameter grain boundary analysis by 3D EBSD of an ultra fine grained CuZr alloy processed by equal channel angular pressing, Adv. Eng. Mater. 13 (2011) 237–244. https://doi.org/10.1002/ADEM.201000259.

[248] S. Licheron, Etude de la relaxation à 20 et 350 ◦C de l'alliage 600 et de l'alliage 800 utilisés pour la fabrication de tubes de générateurs de vapeur et comparaison avec l'acier inoxydable austénitique 18–10 au molybdène., 1979.

[249] Z. Shen, K. Arioka, S. Lozano-Perez, A mechanistic study of SCC in Alloy 600 through high-resolution characterization, Corros. Sci. 132 (2018) 244–259. https://doi.org/10.1016/j.corsci.2018.01.004.

[250] J. Liu, S. Lozano-Perez, P. Karamched, J. Holter, A.J. Wilkinson, C.R.M. Grovenor, Forescattered electron imaging of nanoparticles in scanning electron microscopy, Mater. Charact. 155 (2019) 109814. https://doi.org/10.1016/j.matchar.2019.109814.

[251] D. Dingley, Progressive steps in the development of electron backscatter diffraction and orientation imaging microscopy, J. Microsc. 213 (2004) 214–224. https://doi.org/10.1111/j.0022-2720.2004.01321.x.

[252] W.A. Jesser, D. Kuhlmann-Wilsdorf, Glide and climb stresses on secondary slip systems in F.C.C. crystals due to isolated primary edge and screw dislocations, Mater. Sci. Eng. 51 (1981) 31–37. https://doi.org/10.1016/0025-5416(81)90103-8.

[253] J.F. Nye, Some geometrical relations in dislocated crystals, Acta Metall. 1 (1953) 153–162. https://doi.org/10.1016/0001-6160(53)90054-6.

[254] A.J. Wilkinson, D. Randman, D. Randmany, Philosophical Magazine Determination of

elastic strain fields and geometrically necessary dislocation distributions near nanoindents using electron back scatter diffraction Determination of elastic strain fields and geometrically necessary dislocation distributions near nanoindents using electron back scatter diffraction, Philos. Mag. 90 (2010) 1159–1177. https://doi.org/10.1080/14786430903304145.

[255] A. Prokhodtseva, B. Décamps, A. Ramar, R. Schäublin, Impact of He and Cr on defect accumulation in ion-irradiated ultrahigh-purity Fe(Cr) alloys, Acta Mater. 61 (2013) 6958–6971. https://doi.org/10.1016/j.actamat.2013.08.007.

[256] J.C. Haley, F. Liu, E. Tarleton, A.C.F. Cocks, G.R. Odette, S. Lozano-Perez, S.G. Roberts, Helical dislocations: Observation of vacancy defect bias of screw dislocations in neutron irradiated Fe–9Cr, Acta Mater. 181 (2019) 173–184. https://doi.org/10.1016/j.actamat.2019.09.031.

[257] J. Schindelin, I. Arganda-Carreras, E. Frise, V. Kaynig, M. Longair, T. Pietzsch, S. Preibisch, C. Rueden, S. Saalfeld, B. Schmid, J.Y. Tinevez, D.J. White, V. Hartenstein, K. Eliceiri, P. Tomancak, A. Cardona, Fiji: An open-source platform for biological-image analysis, Nat. Methods. 9 (2012) 676–682. https://doi.org/10.1038/nmeth.2019.

[258] J. Liu, N. Saravanan, J.C. Haley, H. Yu, P. Karamched, A.J. Wilkinson, S. Lozano-Perez, On the effects of step size on measurements of geometrically necessary dislocation density using transmission Kikuchi diffraction, 2020.

[259] R.K. Ham, The determination of dislocation densities in thin films, Philos. Mag. 6 (1961) 1183–1184. https://doi.org/10.1080/14786436108239679.

[260] T. Malis, S.C. Cheng, R.F. Egerton, EELS log-ratio technique for specimen-thickness measurement in the TEM, J. Electron Microsc. Tech. 8 (1988) 193–200.

https://doi.org/10.1002/jemt.1060080206.

[261] A. Varambhia, L. Jones, A. London, D. Ozkaya, P.D. Nellist, S. Lozano-Perez, Determining EDS and EELS partial cross-sections from multiple calibration standards to accurately quantify bi-metallic nanoparticles using STEM, Micron. 113 (2018) 69–82. https://doi.org/10.1016/j.micron.2018.06.015.

[262] M.F. Ashby, The deformation of plastically non-homogeneous materials, Philos. Mag. 21 (1970) 399–424. https://doi.org/10.1080/14786437008238426.

[263] G.E. Dieter, D.J. Bacon, Mechanical metallurgy, McGraw-Hill, 1988.

[264] A. Parslow, A. Cardona, R.J. Bryson-Richardson, Sample drift correction following 4D confocal time-lapse Imaging, J. Vis. Exp. (2014) e51086. https://doi.org/10.3791/51086.

[265] Y. Luo, J. Liu, W. Guo, Q. Yu, S. Li, Dislocation Slip Behavior of Ni Single Crystal Under Dynamic Compression, J. Dyn. Behav. Mater. 2 (2016) 223–233. https://doi.org/10.1007/s40870-016-0060-8.

[266] G.I. Taylor, Plastic strain in metals, Inst. Met. 62 (1938) 307–324.

[267] M.D. McMurtrey, G.S. Was, Role of slip behavior in the irradiation assisted stress corrosion cracking in austenitic steels, 15th Int. Conf. Environ. Degrad. Mater. Nucl. Power Syst. React. 2011. 2 (2011) 1309–1320. https://doi.org/10.1007/978-3-319-48760-1_85.

[268] Z. Jiao, G.S. Was, Impact of localized deformation on IASCC in austenitic stainless steels, J. Nucl. Mater. 408 (2011) 246–256. https://doi.org/10.1016/j.jnucmat.2010.10.087.

[269] M.D. McMurtrey, G.S. Was, L. Patrick, D. Farkas, Relationship between localized

strain and irradiation assisted stress corrosion cracking in an austenitic alloy, Mater. Sci. Eng. A. 528 (2011) 3730–3740. https://doi.org/10.1016/j.msea.2011.01.073.

[270] J. Mayer, L.A. Giannuzzi, T. Kamino, J. Michael, TEM sample preparation and FIB-induced damage, MRS Bull. 32 (2007) 400–407. https://doi.org/10.1557/MRS2007.63.

[271] J. Jiang, T.B. Britton, A.J. Wilkinson, Measurement of geometrically necessary dislocation density with high resolution electron backscatter diffraction: Effects of detector binning and step size, Ultramicroscopy. 125 (2013) 1–9. https://doi.org/10.1016/J.ULTRAMIC.2012.11.003.

[272] J. Liu, S. Lozano-Perez, A.J. Wilkinson, C.R.M. Grovenor, On the depth resolution of transmission Kikuchi diffraction (TKD) analysis, Ultramicroscopy. 205 (2019) 5–12. https://doi.org/10.1016/J.ULTRAMIC.2019.06.003.

[273] A. Arsenlis, D.M. Parks, Crystallographic aspects of geometrically-necessary and statistically-stored dislocation density, Acta Mater. 47 (1999) 1597–1611. https://doi.org/10.1016/S1359-6454(99)00020-8.

[274] P. Karamched, N. Saravavan, A. Wilkinson, S. Lozano-Perez, Effect of sample thinning on strains and lattice rotation measurements, in: RMS EBSD, 2019.

[275] J. Dohr, Micromechanical testing of oxidized grain boundaries, University of Oxford, 2016.

[276] R. Krakow, R.J. Bennett, D.N. Johnstone, Z. Vukmanovic, W. Solano-Alvarez, S.J. Lainé, J.F. Einsle, P.A. Midgley, C.M.F. Rae, R. Hielscher, On three-dimensional misorientation spaces, Proc. R. Soc. A Math. Phys. Eng. Sci. 473 (2017). https://doi.org/10.1098/rspa.2017.0274.

[277] C. Geuzaine, J.-F. Remacle, Gmsh: A 3-D finite element mesh generator with built-in

pre- and post-processing facilities, Int. J. Numer. Methods Eng. 79 (2009) 1309–1331. https://doi.org/10.1002/nme.2579.

[278] L. Renversade, Experimental and numerical analysis of single grain plasticity in an aluminium polycrystal deformed in uniaxial tension., Université de Lyon, 2016.

[279] MeshGems-SurfOpt: The automatic surface remeshing tool of the MeshGems R Suite User Manual MeshGems-SurfOpt Version: 1.1 Documentation Revision: 1.1, 2013. www.ckube.fr (accessed May 1, 2020).

[280] MeshGems-Cleaner: The automatic mesh fixing tool User Manual MeshGems-Cleaner Version: 1.1 Documentation Revision: 1.1, 2013.

[281] MeshGems-Tetra – Volume Tetrahedral Mesh Generation | MeshGems suite, (n.d.). http://www.meshgems.com/volume-meshing-meshgems-tetra.html (accessed May 1, 2020).

[282] J. Dohr, D.E.J. Armstrong, E. Tarleton, T. Couvant, S. Lozano-Perez, The influence of surface oxides on the mechanical response of oxidized grain boundaries, Thin Solid Films. 632 (2017) 17–22. https://doi.org/10.1016/j.tsf.2017.03.060.

[283] K. Fujii, T. Miura, K. Fukuya, Measurement of GB Strength, Oxidized GBs in Ni-base alloys, in: QMM-2, Sun Valley, Idaho, 2011.

[284] J.C. Hinostroza, Modélisation de l'amorçage de la Corrosion sous Contrainte en milieu primaire de l'alliage 600., PSL Research University, 2016.

[285] Z. Zhai, M.B. Toloczko, M.J. Olszta, S.M. Bruemmer, Stress corrosion crack initiation of alloy 600 in PWR primary water, Corros. Sci. 123 (2017) 76–87. https://doi.org/10.1016/J.CORSCI.2017.04.013.

[286] A. Stratulat, J.A. Duff, T.J. Marrow, Grain boundary structure and intergranular stress

corrosion crack initiation in high temperature water of a thermally sensitised austenitic stainless steel, observed in situ, Corros. Sci. 85 (2014) 428–435. https://doi.org/10.1016/J.CORSCI.2014.04.050.

[287] S. Das, H. Yu, E. Tarleton, F. Hofmann, Hardening and Strain Localisation in Helium-Ion-Implanted Tungsten, Sci. Reports 2019 91. 9 (2019) 1–14. https://doi.org/10.1038/s41598-019-54753-3.

[288] S. Das, F. Hofmann, E. Tarleton, Consistent determination of geometrically necessary dislocation density from simulations and experiments, Int. J. Plast. 109 (2018) 18–42. https://doi.org/10.1016/J.IJPLAS.2018.05.001.